ALMA MATER STUDIORUM · UNIVERSITÀ DI BOLOGNA

Scuola di Scienze
Dipartimento di Fisica e Astronomia
Corso di Laurea Magistrale in Fisica

Feasibility study of the MUonE experiment: measuring the leading hadronic contribution to the muon g-2 via space-like data.

Relatore:
Prof. Domenico Galli

Correlatori:
Dott. Giovanni Abbiendi
Dott. Umberto Marconi

Presentata da:
Antonio Principe

Anno Accademico 2019/2020

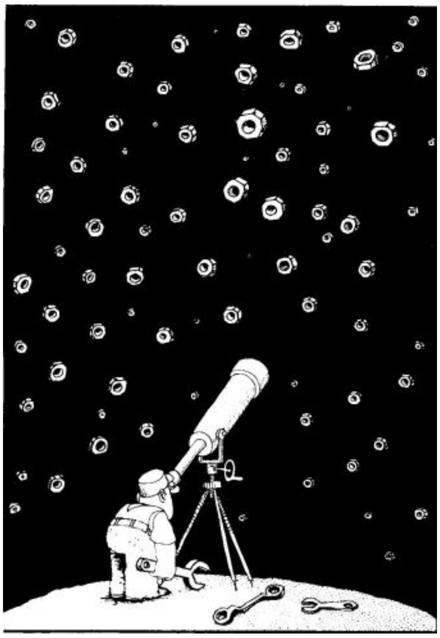

(*Quino*)

I giorni e le notti
suonano
in questi miei nervi d'arpa
Vivo
di questa gioia malata
d'universo
e soffro
per non saperla accendere
nelle mie parole.

(*Giuseppe Ungaretti*)

Sommario

Esiste una discrepanza a livello di 3.5–4 σ tra la misura del momento magnetico anomalo del muone $a_\mu = (g-2)/2$ e la sua previsione basata sul Modello Standard. La previsione teorica, di precisione relativa pari a 0.4 ppm, è limitata dagli effetti dell'interazione forte, i quali sono valutati in base alle misure time-like, agli acceleratori e^+e^- [1]. Il contributo adronico al prim'ordine a_μ^{HLO}, noto con precisione relativa dello 0.4%, è quello che contribuisce maggiormente all'errore teorico [2]. Si ritiene che il metodo basato su misure di annichilazione e^+e^- abbia raggiunto il suo limite di precisione.

Alla misura realizzata dal Brookhaven National Laboratory, di errore relativo di 0.54 ppm [3], si aggiungerà la misura dell'esperimento E989, in corso al Fermilab [4]. L'obiettivo è di ridurre l'incertezza di un fattore 4 (0.14 ppm).

Affinché il confronto tra teoria ed esperimento possa essere in futuro maggiormente affidabile e solido, è necessario ridurre l'incertezza teorica dovuta al contributo adronico.

L'esperimento MUonE propone un metodo innovativo ed indipendente per misurare a_μ^{HLO}. Come recentemente proposto in letteratura [5, 6], è possibile ottenere a_μ^{HLO} tramite la misura del contributo adronico al running dell'accoppiamento elettromagnetico $\Delta\alpha_{had}$ in regione space-like. Il processo di scattering individuato è quello elastico muone su elettrone a riposo. Usando i muoni della linea di fascio M2 del CERN [7] da 150 GeV su bersagli sottili, è possibile in 2 anni, con un unico esperimento, ottenere una precisione statistica dello 0.3%. La sfida teorica e sperimentale consiste nel contenere i sistematici allo stesso livello di precisione. Data l'entità dell'effetto da misurare ($\Delta\alpha_{had} \sim 10^{-3}$), è necessario contenere gli errori sistematici entro 10^{-5} (10 ppm), per poter competere con le misure tradizionali.

Obiettivo della Tesi è stato realizzare lo studio della fattibilità di questa proposta. A questo scopo, sono stati realizzati due test beam, nel 2017 e nel 2018, per analizzare rispettivamente il multiple Coulomb scattering su bersagli sottili e la correlazione elastica tra gli angoli di scattering di muone ed elettrone. L'attività di Tesi ha coperto tutte le fasi dell'analisi,

dall'allineamento dei sensori fino alle analisi finali di fisica per rivelare gli eventi elastici μe. I risultati sono oggetto di pubblicazione [8, 9].

Per quanto concerne il primo test beam, sono stati ottenuti risultati originali sull'accordo tra dati e Monte Carlo. Utilizzando fasci di elettroni da 12 e 20 GeV su bersagli di spessore variabile (8, 20 mm di grafite), abbiamo misurato la deflessione angolare dovuta al MCS usando il telescopio di precisione della collaborazione CERN UA9 [10], di risoluzione intrinseca ~ 0.015 mrad. L'accordo ottenuto tra dati e simulazione, che ho contribuito a costruire, è a livello del percento. Ho inoltre ideato e testato algoritmi di tracciamento e pattern recognition che hanno permesso la prima ricostruzione degli eventi di scattering elastico μe.

Visto l'utilizzo per l'allineamento di run pioni e muoni ad energie elevate (80, 160, 180 GeV), si è misurato il profilo della risoluzione angolare dell'apparato in funzione dell'energia. Basandomi su questa misura, ho proposto un modello parametrico della risposta di un modulo di rivelazione. Esso ha consentito la costruzione di una simulazione Monte Carlo veloce (fast-MC), di cui ho collaborato allo sviluppo, che permette di aggirare il limite della statistica necessaria. Per raggiungere lo 0.3% di errore relativo su a_μ^{HLO}, è richiesto un numero di eventi di segnale elastico μe molto elevato, dell'ordine di 10^{12}. Ottenere tale statistica, con una simulazione completa del detector, richiederebbe risorse di calcolo proibitive.

Ho contribuito inoltre all'analisi del secondo test beam. L'apparato è costituito da tracciatori con risoluzione intrinseca di $\sim$ 0.1-0.05 mrad [11] ed una DAQ automatizzata che ha permesso di estendere la presa dati per diversi mesi. In particolare, mi sono occupato dello studio della risoluzione angolare dai dati e del confronto con l'apparato UA9, usato nel precedente test beam. Dai risultati, è emersa la necessità di vincolare la risoluzione intrinseca del setup finale MUonE ad un valore inferiore a 0.03 mrad, ottenibile con moduli di braccio 1 m e sensori con risoluzione spaziale di almeno $20\,\mu$m.

Infine, ho studiato una prima strategia di misura per ottenere a_μ^{HLO}, basandomi su fast-MC ed inoltre ho proposto un metodo generale per quantificare l'impatto dei sistematici, che ha confermato le precedenti stime.

Nonostante il notevole obiettivo di precisione, i risultati della Tesi non hanno mostrato impedimenti riguardo alla fattibilità della misura.

La proposta di esperimento MUonE è stata inserita all'interno del comitato CERN Physics Beyond Colliders [12, 13]. La collaborazione ha recentemente presentato una Letter of Intent [14] al comitato di SPS.

Abstract

The present discrepancy between the theoretical prediction and the measurement of the muon anomalous magnetic moment $a_\mu = (g-2)/2$ is at level of 3.5-4 σ. The Standard Model prediction has relative precision of 0.4 ppm. The error is dominated by the hadronic contributions because of the non perturbative caracter of the QCD. The leading order hadronic contribution a_μ^{HLO} is the main source of the theoretical error [2]. a_μ^{HLO} has been evaluated with time-like measurements obtained with e^+e^- annihilation in hadrons [1]. This method seems to reach its precision limit.

The error of the existing measurement performed at BNL is 0.54 ppm [3]. New measurement of the muon g-2 is ongoing at Fermilab [4]. Aim of the measurement is to reduce the uncertainty by a factor 4 (0.14 ppm).

It is necessary to reduce the theoretical uncertainty due to hadronic contribution to the anomaly.

MUonE proposed a new method to determine a_μ^{HLO}. As recently proposed in literature [5, 6], it is possible to measure a_μ^{HLO} by means of the hadronic contribution to the electromagnetic effective coupling $\Delta\alpha_{had}$ in the space-like region. The scattering process is the muon elastic scattering on electron at rest. Using the CERN M2 muon beam [7] of 150 GeV on thin targets, it is possible in 2 years, with a single experiment, to obtain a statistical accuracy of 0.3% on a_μ^{HLO}. The theoretical and experimental challenge is to keep the systematics at the same level of precision. The effect to be measured is $\Delta\alpha_{had} \sim 10^{-3}$ so the systematic errors must be contained within 10^{-5} (10 ppm) in order to be competitive with the traditional measurements.

The aim of the Thesis was the feasibility study of the MUonE proposal. On the purpose we performed two test beam in 2017 and 2018 to measured the multiple scattering effect on thin targets and to detect elastic μe events measuring the scattering angles of muons and electrons. The Thesis covered all the aspect of the test beam analysis, from the sensors alignment to the analysis to select the μe elastic events. The results are been submitted for publication [8, 9].

Aim of the first test beam has been to compare GEANT4 predictions

of the MCS effects with data. We used 12 and 20 GeV electron beams hitting on graphite target of different thickness. We measured the angular deflection to the MCS, used the UA9 telescope [10] operating of intrinsic angular resolution of 0.015 mrad. The agreement within MC simulation and data has been verified at the percent level. I developed and used the tracking and the patter recognition also that allowed me to reconstruct μe scattering events.

Exploiting the alignment runs performed with high energy pions and muons (80, 160, 180 GeV), I measured the angular resolution of the detector as a function on the energy. I proposed to use an analytical representation of the resolution function to develop a fast MC. I used this instrument to generate high statistics data samples. Considered that in order to reach the statistical precision of 0.3% on a_μ^{HLO}, the number of elastic events is huge, of the order of 10^{12}.

Such a high statistics cannot be reached with the full simulation within a reasonable time even with large computing farm. I then contributed to the analysis of the result of the second test beam. The main result is that MUonE cannot work with an intrinsic angular resolution worst than 0.03 mrad.

I studied the workflow to get a_μ^{HLO} using the fast MC. I proposed a method to evaluate the effect of the main systematics uncertainties on a_μ^{HLO}. The main result of the Thesis is that there are not limitation preventing MUonE to perform the performed experiment.

The MUonE proposal has been made part of the CERN Physics Beyond Colliders committee [12, 13]. The collaboration has recently presented a Letter of Intent [14] to the SPS Committee.

Contents

Chapter 1

The muon anomalous magnetic moment

In this chapter we will introduce the puzzle of the muon anomalous magnetic moment and therefore the physics case underlying the MUonE proposal [5, 6]. This quantity, together with the corresponding electron anomalous magnetic moment, is one of the most precise measurements in the whole physics landscape. Tracing its history means to cover that of the particle physics, from the Dirac's prediction to the modern quantum field theory.

1.1 Magnetic moments

In classical mechanics, the magnetic moment of an electrically charged particle determines the mechanical interaction with the magnetic field. In the case of a charge e that orbits around an axis in a magnetic field $\vec{B}$, we define the magnetic moment (orbital):

$$\mu = i \cdot A = \frac{ev}{2\pi r}\pi r^2 = \frac{e \cdot mvr}{2m}, \tag{1.1}$$

where i is the current due to the charge motion, A is the area defined by this motion, v is the tangent velocity, r is the orbit ratio and m is the particle mass. In vector notation:

$$\vec{\mu} = g_l \frac{e}{2m}\vec{L}, \qquad g_l = 1, \tag{1.2}$$

where g_l is the gyromagnetic factor defined as the ratio between magnetic and angular momentum $\vec{L}$ (properly normalized), in this case identically equal to the unit. The magnetic field $\vec{B}$ has a mechanical action on the charge, because of the magnetic moment, through a torque:

$$\vec{M} = \vec{\mu} \times \vec{B}. \tag{1.3}$$

These considerations hold for any angular momentum, even for what quantum mechanics (QM) intrinsically assigns to each particle, i.e. the spin. This quantity has suggested the idea that particles are like "spinning top", with an intrinsic rotation. This image, as useful as it is, is wrong: the spin is a quantum property of matter that has no classical counterpart.

In non-relativistic quantum mechanics, as well as in the Hamiltonian formalism, the orbital angular momentum is an operator with a complete set of eigenvectors for an electron that moves for example in a central field like the one of the nucleus [15]:

$$\begin{cases} \hat{H}u = E_n u \\ \hat{L}^2 u = \hbar^2 l(l+1)u \\ \hat{L}_z u = m_z \hbar u \end{cases} \tag{1.4}$$

The possible values of the magnetic quantum number m_z are $2l+1$. The definition of magnetic moment is still valid, but it is usual to introduce the Bohr's magneton: for a generic angular momentum $\vec{J}$

$$\vec{\mu} = g_j \frac{\mu_B}{\hbar} \vec{J}, \qquad \mu_B = \frac{e\hbar}{2m}. \tag{1.5}$$

The gyromagnetic factor g is simply called "g-factor". The first evidence of the spin dates back to the famous experiment of Stern and Gerlach (1922) with electrons. The discovery of the fourth degree of freedom for an electron is however attributed to Uhlenbeck and Goudsmith (1932) [16]: according to the Pauli exclusion principle, the spin allowed to explain in a natural way the atomic spectra under study. In particular the Zeeman effect, caused by the interaction between the external magnetic field and the angular momentum $\vec{L}$ (orbital) and $\vec{S}$ (intrinsic), that is the so-called spin-orbit coupling. For a particle with spin, the magnetic moment is an intrinsic property and is obtained by replacing the angular momentum operator $\vec{L}$ with the spin $\vec{S}$:

$$\vec{S} = \frac{\vec{\sigma}}{2}, \tag{1.6}$$

where σ_i $(i = 1, 2, 3)$ are Pauli matrices. The extension of the $\vec{L}$ operator properties to the spin $\vec{S}$ was immediate:

$$\begin{cases} \hat{S}^2 u = \hbar^2 s(s+1)u \\ \hat{S}_z u = m_s \hbar u \end{cases} \tag{1.7}$$

together with the definition of the intrinsic magnetic moment:

$$\vec{\mu}_s = g_s \frac{\mu_B}{\hbar} \vec{S}. \tag{1.8}$$

From the observations, the possible values of the spin quantization had to be only 2, which implies $s = 1/2$ according to the relation $2s + 1 = 2$. Moreover unlike the angular contribution (g_l =1), the one related to the spin had to satisfy:

$$g_s = 2, \tag{1.9}$$

to explain the experimental observations.

The theoretical explanation of this empirical fact is included in the Dirac's theory [17]. In the non-relativistic limit, the Dirac equation for an electron interacting in an electromagnetic field

$$A^\mu = (\phi, \vec{A}), \tag{1.10}$$

gives the Pauli equation:

$$i\hbar \frac{\partial}{\partial t} \phi = \Big(\frac{(\vec{p} - e\vec{A})^2}{2m_e} - \frac{e}{m_e} \vec{S} \cdot \vec{B} + e\phi \Big), \tag{1.11}$$

where in the right, the first factor represents the kinetic term, the second is the coupling between the spin and the magnetic field, and the last one is the electrical potential. Comparing the second contribution with (1.8), the theory predicts for the spin g-factor $g_s = 2$, as well as for all the point-like particles of spin $s = 1/2$. As intrinsic property of matter, the spin arises naturally from Dirac's field equation and is one of its most remarkable achievement. As Dirac said: “my equation proved to be more intelligent than me”.

1.2 QED virtual process: g-2 anomaly

This is not the end of the story. Later on it was discovered that proton and neutron have magnetic moments that differ significantly from those expected for point particles and that was one of the first indications they are fermions with an internal structure, i.e. interacting substructures, quarks and gluons as we know. Even for electron and muon a slight difference was discovered for the g-factor from the predicted value. This is still related to the existence of interactions that occur with the fermions, but not due to internal structure: the virtual processes of quantum electrodynamics (QED). Quantum fields theory predicts a deviation from Dirac's prediction. We will now go into more detail on this subject.

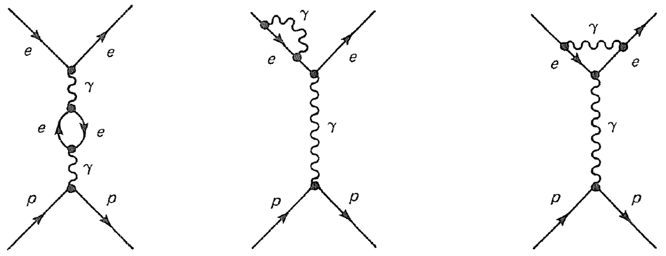

Vacuum polarization Electron mass renormalization Anomalous magnetic moment

Figure 1.1: The main QED radiative contributions to the Lamb shift.

1.2.1 Renormalization and running coupling constants

The Standard Model predictions, cross sections and decay widths, are obtained by a perturbative method, that is calculating Feynman diagrams at subsequent orders of a series expansion in powers of the coupling constant: the calculation converges, that is it gives finite results, if the successive contributions tend to zero quickly enough [18].

Each single diagram is calculated by integrating over all possible momenta of the virtual particles that are present: it was immediately realized, from the QED perturbative calculations, that already the first diagrams of higher order are divergent when the momentum becomes high. The solution to handle the infinites arrived with the analysis of the Lamb shift [19] (fig. 1.1): the breakup in the degeneration between two hydrogen lines, unexpected in the Dirac's theory. To account for this problem, the simplest radiative correction was calculated, consisting in the emission and absorption of a virtual photon γ: the energy levels are slightly modified by a kind of self-energy of the bound electrons.

The calculation is divergent for $E_\gamma \to E_\gamma^{max}$, the upper energy limit in the integral, that is it depends on the cut chosen to make the result finite, a situation obviously inconsistent. In 1947, Bethe proposed that also the free electron should bring a self-energy contribution, that is it could interact with the electromagnetic field created by itself, and that therefore its kinetic energy should be modified [20]. Here is the fundamental step: he inserted this modification in a redefinition of the observed mass

$$m_{obs} \approx \left(1 + \alpha_{EM}\frac{4E_\gamma^{max}}{3\pi mc^2}\right) \cdot m \quad \Rightarrow \quad m_{obs} = m_{obs}(E_\gamma^{max}), \tag{1.12}$$

where m is interpreted as the so-called bare mass of the electron, that is the one that would be measured without any virtual process occurring. The remarkable consequence of this procedure, called renormalization, is that the mass (renormalized), which can be measured, depends on the energy scale of the observation. From that moment, this procedure was considerably developed: by redefining the theory parameters, in particular the particle mass and charge, it was possible to obtain finite results[1].

The interaction strength depends on the energy/distance scale at which we probe the microscopic world. The closer we get to a charged particle, the greater the observed effect of the virtual processes that take place around it, which screen the charge, modify its value and therefore modify that of the electromagnetic coupling, which in particular increases with energy.

The renormalization of the charge e can therefore be expressed in terms of running of the electromagnetic coupling $\alpha = e^2/4\pi$. From the theory:

$$\alpha(q^2) = \frac{\alpha}{1 - \Delta\alpha(q^2)} \tag{1.13}$$

where q^2 is the energy scale. The different contributions to the running of α come from the 3 charged leptons and 5 quarks (neglecting the top, too heavy to contribute significantly). This statement will be explained in detail below: the MUonE experiment is essentially aimed at measuring the hadronic contribution to this running, in a region of space-like transferred momenta suitable to estimate the muon anomaly.

1.2.2 Schwinger calculus: first QED result

Fig. 1.2 shows the first order contribution to the magnetic moment by the virtual vacuum polarization processes of QED. In 1948 Schwinger calculated the impact of this diagram to the electron g-factor [21]. Recalling the eq. (1.8), it is possible to define the anomaly a_μ as the deviation from Dirac's prediction:

$$g_\mu = 2(1 + a_\mu) \;\Rightarrow\; a_\mu = \frac{g_\mu - 2}{2}. \tag{1.14}$$

Hence the expression "g-2" becomes a synonym for anomalous magnetic moment. Schwinger's famous QED calculation predicts at first order [21]:

$$a_\mu = \frac{\alpha}{2\pi} \sim 0.001161 \;\Rightarrow\; g_\mu^{th} = 2 \cdot 1.001161, \tag{1.15}$$

so:

$$\vec{\mu}_s = g\frac{\mu_B}{\hbar}\vec{S} = 2\left(1 + \frac{\alpha}{2\pi}\right)\frac{\mu_B}{\hbar}\vec{S} \tag{1.16}$$

---

[1] In 1971 Veltman and 't Hooft demonstrate the renormalizability of non-abelian gauge theories with spontaneous symmetry breaking, i.e. of Glashow-Weinberg-Salam's electroweak theory. A few years later quantum chromodynamics was inserted as SU(3) gauge theory, definitively building the Standard Model as the renormalizable theory of fundamental interactions.

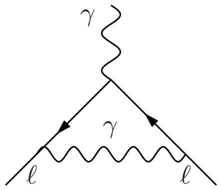

Figure 1.2: Lowest order QED contribution to the muon anomalous magnetic moment.

In the same year, Kusch and Foley (1948) [22] obtained experimentally:

$$g_\mu^{exp} = 2\,(1.00119 \pm 0.00005). \tag{1.17}$$

This result is in agreement with the Schwinger's prediction and is one of the first QED triumphs. The brilliant confirmation of the perturbative method has given the start to the calculation of higher orders and fixed the standard framework within which most of the future calculations of the radiative corrections will be obtained. From the ∼5 significant figures of the Kusch and Foley measurement, we have moved on to the 9 of the BNL measure (sec. 1.4).

1.3 Muon g-2 in the Standard Model

In the Standard Model, the anomaly a_μ can be expressed as the sum of three contributions:

$$a_\mu^{SM} = a_\mu^{QED} + a_\mu^{EW} + a_\mu^{\mathrm{had}}. \tag{1.18}$$

As the theory is renormalizable, a precise and unambiguous prediction of this quantity is possible, so the anomalous magnetic moment has become one of the best observables to test it. The first two terms, electromagnetic and weak, can be calculated with extreme precision by perturbative calculation. The hadronic one, instead, must rely on experimental data and for that reason presents the biggest uncertainty. The g-2 is a low energy observable and in this region it is not possible the perturbative QCD treatment, because of the confinement. The issue of the hadronic contribution will be addressed in the following paragraphs.

1.3.1 QED contribution

In QED, the anomaly a_μ becomes a perturbative expansion in α/π:

$$a_\mu = \Sigma_j C_j \left(\frac{\alpha}{\pi}\right)^j. \tag{1.19}$$

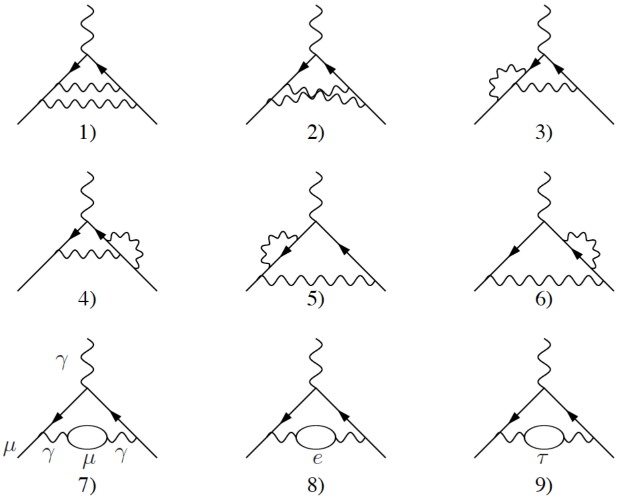

Figure 1.3: Second-order QED diagrams that contribute to anomaly.

To date, theoretical calculations have reached the fifth perturbative order. Below the successive contributions and the main authors of the relative calculations [23, 24]:

$$\begin{aligned} a_\mu^{QED} = &\frac{1}{2}\frac{\alpha}{\pi} && \text{[Schwinger 1948]} \\ &+ 0.765857426(16)\left(\frac{\alpha}{\pi}\right)^2 && \text{[Sommerfield 1957]} \\ &+ 24.05050988(28)\left(\frac{\alpha}{\pi}\right)^3 && \text{[Remiddi, Laporta 1995, 1996]} \\ &+ 130.8796(63)\left(\frac{\alpha}{\pi}\right)^4 && \text{[Kinoshita 1981, 2012]} \\ &+ 753.29(1.04)\left(\frac{\alpha}{\pi}\right)^5 && \text{[Kinoshita 2004]} \end{aligned} \tag{1.20}$$

If we add these five contributions, which are dominated by the first order calculated by Schwinger (1.15), we get:

$$a_\mu^{QED} = 0.00116584718951(22)(77) \tag{1.21}$$

or:

$$a_\mu^{QED} = 11658471.8951(0.0022)(0.0077)\cdot 10^{-10}. \tag{1.22}$$

The first error arises from the coefficients of the perturbative development, the second from the fine structure constant α, measured with Rubidium nuclei, which provides a new determination of the constant independent of the electron magnetic anomaly a_e, from which α was traditionally extracted [25].

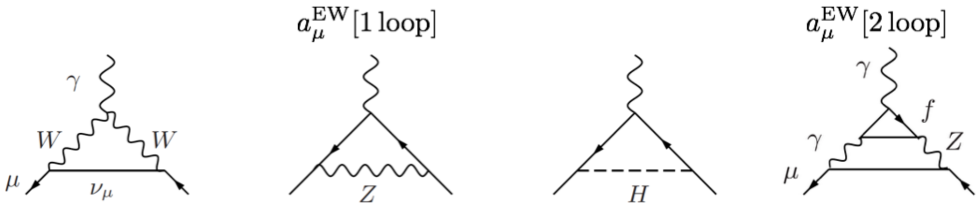

Figure 1.4: Electroweak contributions to the muon anomalous magnetic moment.

1.3.2 Electroweak contribution

The electroweak contribution is the smallest one, as it is suppressed by the factor $(m_\mu/M_W)^2$, compared to the QED: it involves the massive bosons $W^\pm$, Z^0 and the Higgs one (fig. 1.4). One-loop calculation leads to [26]:

$$\begin{aligned} a_\mu^{EW}[1\,{\rm loop}] &= \frac{5G_\mu m_\mu^2}{24\sqrt{2}\,\pi^2}\left[1+\frac{1}{5}\left(1-4\sin^2\theta_W\right)^2 + \mathcal{O}\left(\frac{m_\mu^2}{M_{Z,W,H}^2}\right)\right] \\ &= 19.48\times 10^{-10}, \end{aligned} \tag{1.23}$$

where $\sin^2\theta_W = 1 - M_W^2/M_Z^2 \approx 0.223$ is the electroweak angle and $G_\mu \approx 1.166\times 10^{-5}$ GeV^{-2} is the Fermi coupling constant. The contribution to two loops also contains an hadronic part and must be included as it is not negligible (and negative). Using the new Higgs boson mass value $M_H = (125.6 \pm 1.5)$ GeV, one can get:

$$a_\mu^{EW}[2\,{\rm loop}] = -4.12(0.10)\times 10^{-10}, \tag{1.24}$$

where the error essentially depends on the hadronic loop uncertainties. Adding up the two terms, one obtain:

$$a_\mu^{EW} = 15.36(0.10)\times 10^{-10}. \tag{1.25}$$

1.3.3 Hadronic contribution: time-like approach

Strong interactions allow perturbative calculations only for energy scales higher than few GeV, where one enters the regime of asymptotic freedom. The hadronic bubble in fig. 1.5 cannot be calculated with the same method used for the first two contributions, EM and EW. Fortunately most of the hadronic effects are vacuum polarization corrections, divided as usual into leading order and next-to-leading[2]:

$$a_\mu^{\rm had\,VP} = a_\mu^{\rm HLO} + a_\mu^{\rm HNLO}. \tag{1.26}$$

---

[2] The hadronic contribution to a_μ consists of a further contribution in addition to the one from vacuum polarization (VP), the Light-by-Light which will be discussed later.

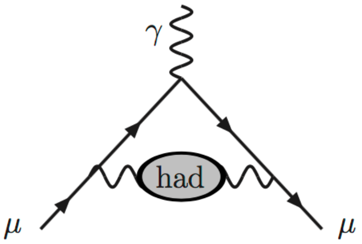

Figure 1.5: Hadronic contribution at leading order (HLO) to the muon anomalous magnetic moment.

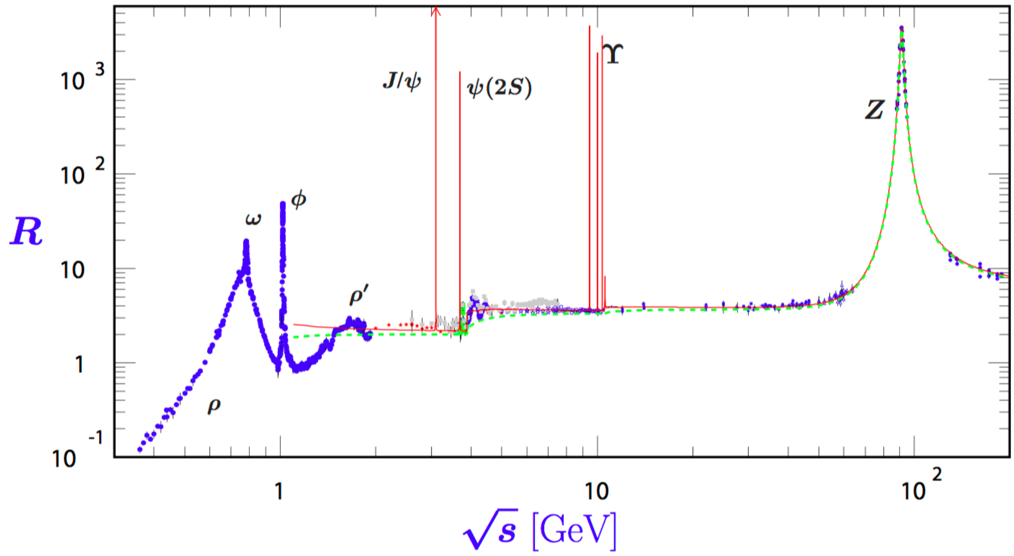

Figure 1.6: Hadronic ratio R from PDG [26]: this plot shows the whole range from m_π to 200 GeV

The hadronic contribution to the vacuum polarization is calculated by exploiting the analyticity (causality) and the unitarity of the theory (optical theorem). Experimental measurements of the annihilation cross section of e^+e^- to hadrons are used to extract the hadronic contribution to the anomaly a_μ. The vacuum polarization effects can be calculated by replacing the free photon propagator with the “dressed” one:

$$\frac{1}{q^2} \Rightarrow \int_0^\infty \frac{\mathrm{d}s}{s} \frac{1}{q^2 - s} \frac{1}{\pi} \mathrm{Im}\Pi_{had}(s), \tag{1.27}$$

The imaginary part of the $\Pi_{had}(s)$ function, the photon self-energy, is traditionally determined through the optical theorem from low energy measurements of the total cross section of hadronic production in e^+e^- annihilation:

$$\sigma(s)(e^+e^- \to \gamma^* \to \text{had}) = \frac{4\pi^2\alpha}{s}\frac{1}{\pi}\mathrm{Im}\Pi_{had}(s). \tag{1.28}$$

The hadronic leading order contribution is shown in figure 1.5 and corresponds to the exchange of a "massive photon" of mass $\sqrt{s}$, according to the 1.28. In general, the anomaly a_μ can be determined with the following dispersion integral and the associated kernel function $K(s)$:

$$a_\mu^{\mathrm{HLO}} = \frac{\alpha}{\pi}\int_0^\infty \frac{\mathrm{d}s}{s}\frac{1}{\pi}\mathrm{Im}\Pi_{had}(s)K(s), \quad K(s) = \int_0^1 \mathrm{d}x\frac{x^2(1-x)}{x^2+s/m_\mu^2(1-x)}\,. \tag{1.29}$$

The time-like method relies on the use of the optical theorem and the well-known R hadronic ratio, normalized to the cross section $e^+e^- \to \mu^+\mu^-$ (figg. 1.6, 1.8):

$$R(s) \equiv \frac{\sigma^{(0)}\left(e^+e^- \to \gamma^* \to \text{hadrons}\right)}{4\pi\alpha^2/3s}, \tag{1.30}$$

which shows that the hadronic leading order contribution[3] a_μ^{HLO} can be obtained from the following dispersion integral:

$$a_\mu^{\mathrm{HLO}} = \left(\frac{\alpha m_\mu}{3\pi}\right)^2\left(\int_{m_{\pi^0}^2}^{E_{\mathrm{cut}}^2}\frac{R^{\mathrm{data}}(s)\hat{K}(s)}{s^2}\mathrm{d}s + \int_{E_{\mathrm{cut}}^2}^{\infty}\frac{R^{\mathrm{pQCD}}(s)\hat{K}(s)}{s^2}\mathrm{d}s\right), \tag{1.31}$$

where E_{cut} is the energy up to which the data must be used and from where it is safe to use the perturbative QCD (pQCD); the rescaled kernel function $\hat{K}(s) = 3s/m_\mu^2 K(s)$ is a smooth function rising from 0.39 for $s = m_{\pi^0}^2$ to 1 for $s \to \infty$. The hadronic ratio R is shown in fig. 1.6 and in particular in fig. 1.8, together with the relative contributions of the different energies. It is clear that the low-energy region is largely dominated by mesonic resonances that cannot be treated perturbatively. The ρ meson region is the one that makes the biggest contribution $\sim 75\%$ (figg. 1.7 and 1.9): the dispersive integral is in fact controlled by the $1/s^2$ factor, so the low energy regions are dominant on the other ones. Time-like e^+e^- data can be used up to about 40 GeV, where interference $\gamma - Z^0$ comes into play. However the pQCD becomes reliable from ≈ 5 GeV, after the J/ψ resonances, even though this region accounts only for a few percent in the final a_μ^{HLO} account.

It is important to note the hadronic blob we want to know is not what we measure, i.e. it is not a physical observable: in reality the insertions with virtual photons attached to the hadronic bubbles are "dressed" photons

---

[3] The following notations are used in literature: a_μ^{HLO}, $a_\mu^{\mathrm{had\,LO}}$ o $a_\mu^{\mathrm{had\,VP}}$.

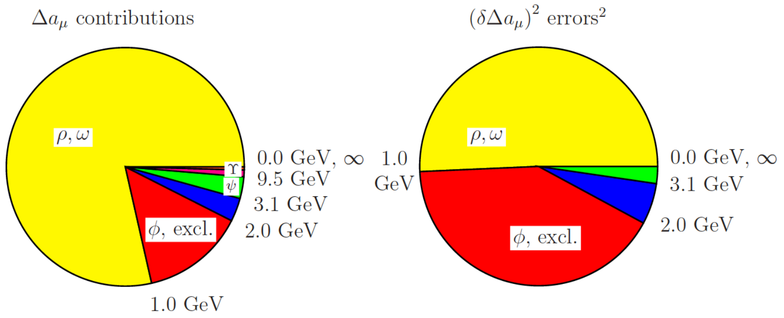

Figure 1.7: Contributions and error squares from different energy regions. Different evaluations of the available datasets may lead to slight differences in the relative contributions.

(propagators with all possible radiative corrections). The dispersive method requires the bare ("undressed") cross section $\sigma^{(0)}(s)$ (1.30). The physical cross section (measured / dressed) is proportional to e^4 or $\alpha^2 = \alpha^2(s)$, due to the running of the charge e. The bare cross section is obtained by replacing the running $\alpha(s)$ with the classic $\alpha = \alpha(0)$ and subtracting all radiative corrections not present in the hadronic blob line:

$$\sigma^{(0)}\left(e^+e^- \to \text{hadrons}\right) = \sigma\left(e^+e^- \to \text{hadrons}\right)\left(\frac{\alpha(0)}{\alpha(s)}\right)^2 . \tag{1.32}$$

The standard measurement of σ_{had} (and therefore indirectly of $\sigma_{had}^{(0)}$) is obtained as a set of experimental points corresponding to a scan for variable energy of the beams. However KLOE at DAΦNE (Frascati) has introduced a novel mode, the so-called radiative return (RR) method, which is particularly interesting for machines that work on-resonance like ϕ and B factories, illustrated in fig. 1.10: it consists in extracting the measurement itself using one of the contributions (ISR=initial state radiation) which must in any case be subtracted to obtain the wanted quantity, that is the hadronic bubble.

In fig. 1.11, all the recent evaluations of a_μ^{HLO} are shown. The latest results consist in a complete re-evaluation of all the measurements. The two most recent evaluations are the least conservative about the error. One of these is the current value (2018) reported by the PDG [26]:

$$a_\mu^{\text{HLO}} = 693.1(3.3)(0.7) \cdot 10^{-10}, \tag{1.33}$$

where the first error is experimental and dominated by systematic uncertainties, while the second one is due to the pQCD used at intermediate and higher energies, to predict the contribution of the continuum quark-antiquark. Previous results with a more conservative evaluation of the uncertainties ended

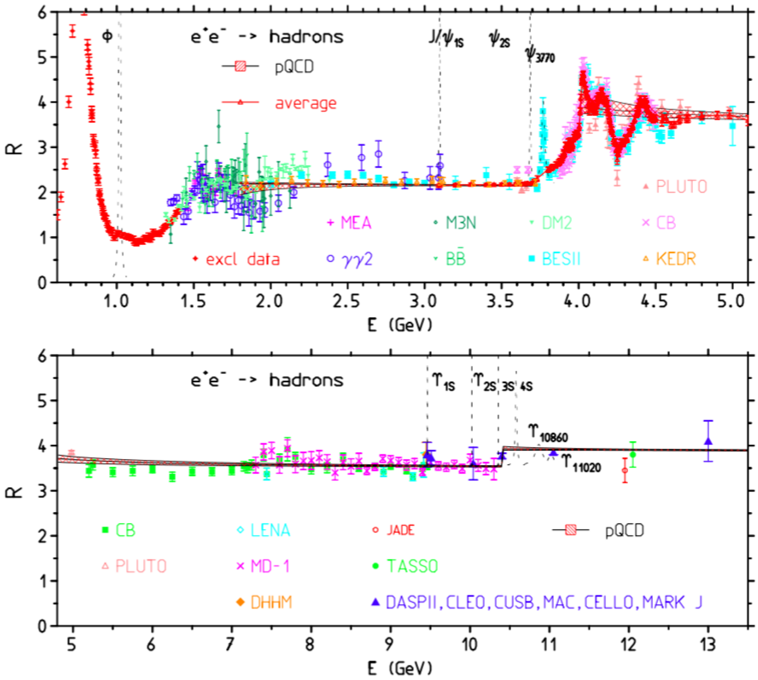

Figure 1.8: Hadronic R ratio from data obtained at the various e^+e^- storage rings, in the region of interest. New data of KEDR detector (Novosibirsk) are shown between 1.84 and 3.72 GeV. The perturbative prediction of quark-antiquark production cross-section (pQCD) is also displayed [2].

up to an uncertainty of 4-5 $\cdot 10^{-10}$. These errors should be compared with the total errors of the perturbative contributions QED and EW, respectively of $0.008 \cdot 10^{-10}$ and $0.10 \cdot 10^{-10}$.

The next-to-leading hadronic contributions are relevant. The next orders of vacuum polarization (shown in figure 1.12) are determined from the data using the same dispersive method (NLO, NNLO). The Light-by-Light contributions (HLbL, NLO and NNLO) can be estimated at present only theoretically:

$$a_\mu^{\text{had}} = \underbrace{a_\mu^{\text{HLO}} + a_\mu^{\text{HNLO}}}_{\text{VP}} + a_\mu^{\text{HLbL}}. \tag{1.34}$$

In tab. 1.1, some of the most recent estimations for the hadronic contributions. The LbL term contributes only marginally to the central value (at the same level of the EW), but has a large uncertainty, comparable with that of the leading order contribution. It produces a tension between the different total hadronic estimates, depending on its evaluation. There is the

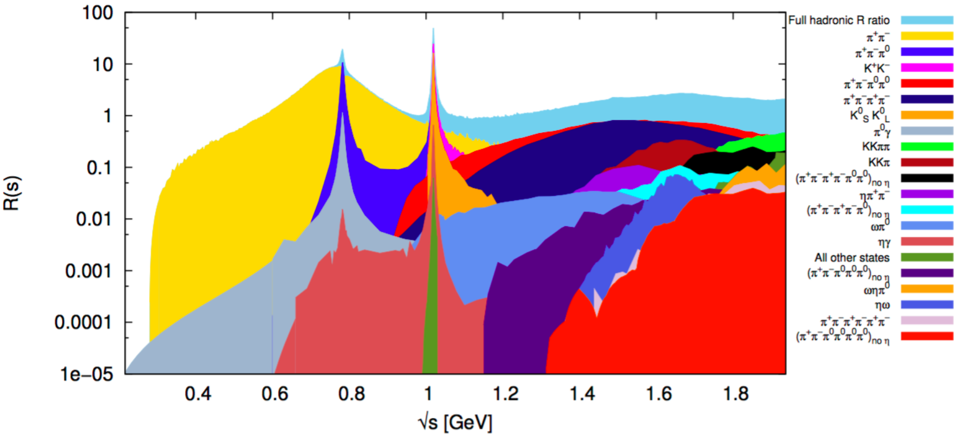

Figure 1.9: Contributions of different decay channels at hadronic R ratio: up to 2 GeV more than 30 exclusive channels must be measured [27]. The dominant channel is $e^+e^- \to \pi^+\pi^-$.

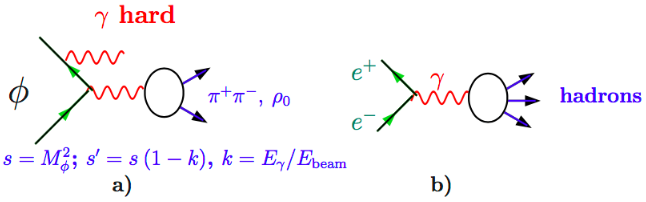

Figure 1.10: a) Principle of the radiative return. b) Standard measurement [1].

so-called "Glashow consensus" on the HLbL NLO part [31]. Recently a dispersive approach has been proposed for the calculation of this contribution which could allow reduce the uncertainty in the future: according to first estimations one could hope for a reduction of the LbL error contribution to the level of 1×10^{-10}, so the expectation is to reduce the relative error to 10%.

In recent years, considerable progress has been made on the Lattice QCD (LQCD) in particular in the numerical calculation of the $a_\mu^{\rm HLO}$ from first principles. However, the current precision of LQCD calculation is still non competitive (fig. 1.11): most of the uncertainties arise from the need for extrapolations (finite volume, lattice spacing). To date, LQCD estimates reach the level of 3% error on $a_\mu^{\rm HLO}$, against 0.4-0.5% error of e^+e^- measurements. Substantial improvements are expected in the next decade on this front.

Progress in traditional time-like measurements was expected in these years [31], just up to the level of the most recent one (KNT18 [27]), that

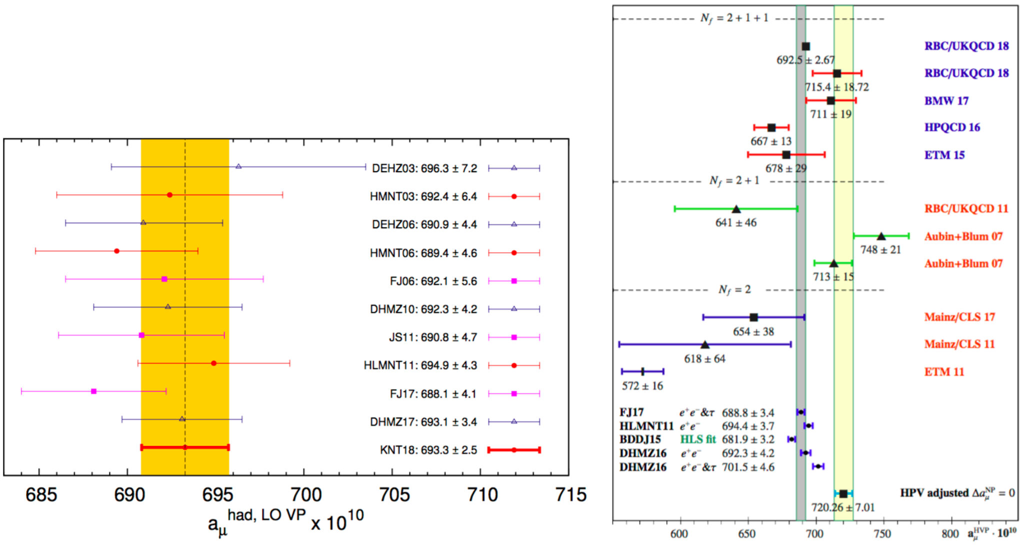

Figure 1.11: Left: recent time-like evaluations of a_μ^{HLO} [27]. Right: summary of recent lattice QCD results for the leading order a_μ^{HLO} , in units 10^{-10} [2, 28]. The gray vertical band represents Jegerlhener evaluation [29, 30]. The yellow band represents the required hadronic vacuum polarization such that theory matches the experimental BNL result. Some recent time-like estimates are shown for comparison.

reduced the absolute error on a_μ^{HLO} below 3×10^{-10} ($<$0.4%). Further reduction in the error on the leading contribution is considered unlikely. Many of the estimates reported in the tab. 1.1 are already judged not to be "conservative". According to S. Eidelman, the time-like method, through the e^+e^- annihilation measurements, could have reached the limit by now.[4].

1.3.4 Running of α

As mentioned the virtual effects of vacuum polarization can be absorbed in a redefinition of the fine structure constant, resulting in an electromagnetic coupling that depends on the q^2 energy scale:

$$\alpha(q^2) = \frac{\alpha(0)}{1 - \Delta\alpha(q^2)} = \frac{\alpha(0)}{1 - \Delta\alpha_{lep}(q^2) - \Delta\alpha_{had}(q^2)}, \tag{1.35}$$

Vacuum polarization derives from loops where leptons and hadrons (quarks) are included. The leptonic shift $\Delta\alpha_{lep}(q^2)$, with $q^2 = t < 0$ for space-like momenta or $q^2 = s > 0$ for time-like, is well known and can be calculated

---

[4] Private communication.

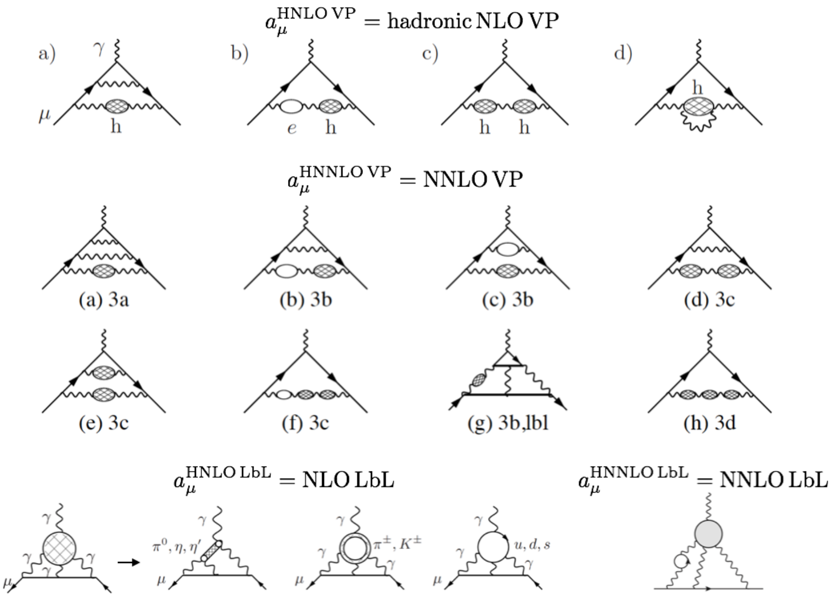

Figure 1.12: Next-to-leading order hadronic contributions to the muon anomalous magnetic moment.

order-by-order in perturbation theory: it's known up to 3-loops in QED (4-loops in some regions). From [34]:

$$\Delta\alpha_{lep}\left(q^2\right) = -\mathrm{Re}\overline{\Pi}_{lep}\left(q^2\right), \tag{1.36}$$

that develops in a perturbative series of α/π, similar to the leptonic contribution to the anomaly a_μ:

$$\overline{\Pi}_{lep}\left(q^2\right) \propto \Sigma_k \left(\frac{\alpha}{\pi}\right)^k \overline{\Pi}^{(k)}_{lep}\left(q^2\right), \tag{1.37}$$

with k perturbative order: $k = 1$ (1 loop), $k = 2$ (2 loops) and so on. Fig. 1.13 shows the corrections to the propagator with one and two loops.

The hadronic shift $\Delta\alpha_{had}$, i.e. the quark blobs, cannot be determined in the same way, due to the quark confinement in low-energy QCD. It is traditionally determined as a_μ^{HLO}, that is by low-energy e^+e^- annihilation measurements ($q^2 = s > 0$). What is used is always the hadronic ratio R (eq. (1.30)), from which the running of $\alpha(s)$ can be obtained as [35]:

$$\left|\frac{\alpha(s)}{\alpha(0)}\right|^2 = \frac{d\sigma_{data}(R)/d\sqrt{s}}{d\sigma^0_{MC}/d\sqrt{s}}, \tag{1.38}$$

where $d\sigma^0_{MC}/d\sqrt{s}$ is the MC cross section with running "off", i.e. $\alpha = \alpha(0)$ and where $E_{CM} = \sqrt{s}$ is the e^+e^- center-of-mass energy. Fig. 1.14 shows

a_μ contributions	value ($\times 10^{10}$)	rel. error	ref.
QED (5-loops)	11658471.895 ± 0.008	$7 \cdot 10^{-10}$	[26]
EW (2-loops)	15.36 ± 0.10	0.65%	[26]
Hadronic			
LO VP	$\mathbf{693.1 \pm 3.4}$	0.49%	DMHZ17 [32, 26]
	688.1 ± 3.4	0.49%	FJ17 [29]
	693.3 ± 2.5	0.36%	KNT18 [27]
NLO VP	-9.87 ± 0.09	0.91%	[26]
	-9.82 ± 0.04	0.41%	KNT18 [27]
NNLO VP	1.24 ± 0.01	0.81%	[26]
NLO LbL	$\mathbf{10.5 \pm 2.6}$	25%	[26]
	9.8 ± 2.6	27%	[33]
NNLO LbL	0.3 ± 0.2	67%	[26]
SM total	11659182.3 ± 4.3	0.37 ppm	DMHZ17 [32, 26]
	11659177.6 ± 4.4	0.38 ppm	FJ17 [29]
	11659182.1 ± 3.6	0.31 ppm	KNT18 [27]
Experimental	11659209.1 ± 6.3	0.54 ppm	BNL [3, 26]
Δa_μ(exp - SM)	$26.8 \pm 7.6\,(3.5\,\sigma)$		DMHZ17
	$31.5 \pm 7.7\,(4.1\,\sigma)$		FJ17
	$27.0 \pm 7.3\,(3.7\,\sigma)$		KNT18

Table 1.1: Standard Model evaluation of the muon anomaly, with the experimental measurement. The final goal of the new experiment at Fermilab is $1.6 \cdot 10^{-10}$ as absolute error on a_μ (sez. 1.4).

the results of a KLOE analysis measuring the running of α extraction in the time-like region of the ρ-ω resonances. As mentioned above, the MC cross section must be corrected for other radiative effects than those to be determined (in the case of KLOE, for final state photon radiation [35, 1]).

1.4 Muon g-2: measurements

This section describes the principles underlying the direct measurement of the muon anomalous magnetic moment. CERN has carried out three experiments to measure a_μ, with increasing accuracy: CERN I (1965, 4300 ppm), CERN II (1968, 270 ppm) and CERN III (1979, 7 ppm). Currently the reference measurement is the one made in Brookhaven (BNL) by the experiment E821 with an accuracy of 0.54 ppm (1999) [36, 3]. The new experiment E989 "g-2" at Fermilab (FNAL) is in the running phase with the aim of improving the accuracy by a factor of 4, to 0.14 ppm [37]. A

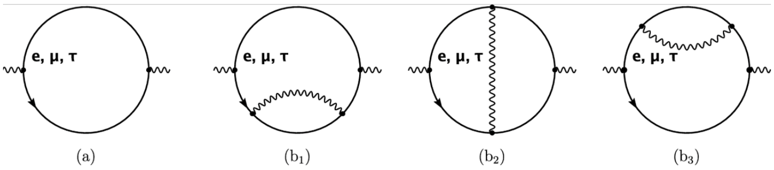

Figure 1.13: One and two loops contributions to the running of α [34].

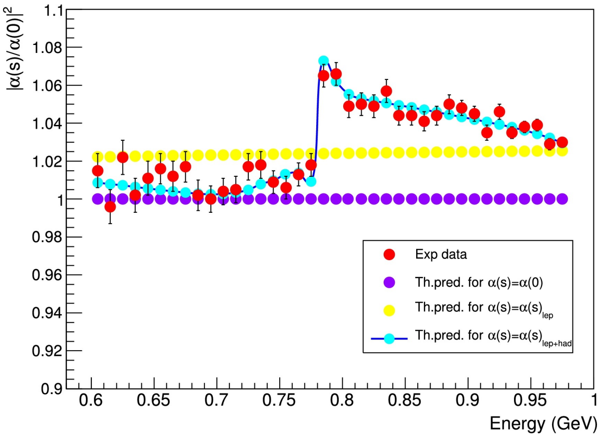

Figure 1.14: Recent KLOE measurements (red points) of ratio $|\alpha(s)/\alpha(0)|^2$ (eq. (1.38)): evidence of the hadronic contribution to the $\alpha(s)$ in the ρ-ω resonance region [35].

complementary experiment is planned in Japan, at J-PARC [38], with the same precision goal.

1.4.1 Muon storage rings: CERN, BNL, FNAL

The experiments carried out at CERN and Brookhaven, as well as the current Fermilab experiment (fig. 1.16), have used muons of relatively high energy in storage rings. Polarized muons moving on a circular orbit under the action of a uniform magnetic field are subject to the effect of the anomaly a_μ which causes a Larmor precession. The spin precedes along the orbit around the motion direction, that is around the momentum vector, with an anomalous frequency ω_a which depends on the fact that $a_\mu \neq 0$.

Protons incident on target produce large quantities of charged pions. By considering as reference the positive pions, they decay through the weak process:

$$\pi^+ \to \mu_L^+ + \nu_{\mu L} \tag{1.39}$$

This decay violates in a maximum way the parity (fig. 1.15): the neutrino

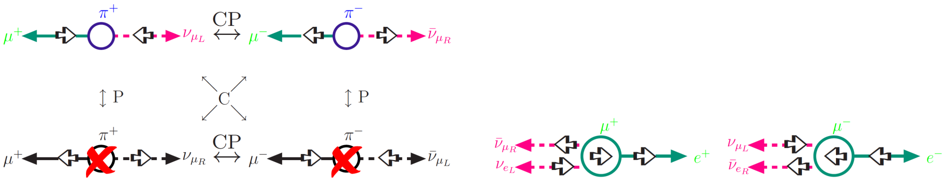

Figure 1.15: Pion and muon CP violation decays.

must be left-handed, therefore since the pion spin is zero, the positive muon must also be left-handed, as illustrated in figure. Its spin is opposite to the momentum since it is emitted back-to-back with respect to the neutrino in the pion rest frame. Opposite helicity is obtained for negative muons, from negative pion decay. Muons have therefore "wrong" helicity and this is why the pion decay into electron is suppressed. By exploiting this parity-violating process, highly polarized muon beams are obtained, i.e. with a well-defined spin direction. This is the first necessary ingredient.

The positive / negative muons decay in turn into positrons / electrons, through weak decay in which an analogous violation of the parity occurs (fig. 1.15):

$$\mu_L^+ \to e_R^+ + \nu_{eL} + \bar{\nu}_{\mu R} \tag{1.40}$$

Responsible of the violation are always the neutrinos / antineutrinos in left/right-handed state: they are both present after the decay, therefore the muon spin is correlated to the helicity of the emitted positron, that is to its direction. High-energy positrons are preferentially emitted along the positive muon spin direction. The tracking and energy measurement of decay positrons therefore provides a measure of the spin direction of the parent muon: this is another key point to observe the induced precession from a_μ along the orbit.

The third element is the muon storage ring in which they can orbit for long enough to observe their decay, in relation to the relativistic factor γ ($\gamma\tau_\mu \approx 64.4\,\mu$s): a highly uniform and constant magnetic field provides for circular deflection (fig. 1.17). The muon orbital frequency is the known cyclotron frequency:

$$\vec{\omega}_c = \frac{e\vec{B}}{m_\mu \gamma}. \tag{1.41}$$

The frequency of precession in magnetic field due to the spin includes the well-known Larmor term with the Thomas relativistic term:

$$\vec{\omega}_s = g_\mu \frac{e\vec{B}}{2m_\mu} + (1-\gamma)\frac{e\vec{B}}{m_\mu \gamma}. \tag{1.42}$$

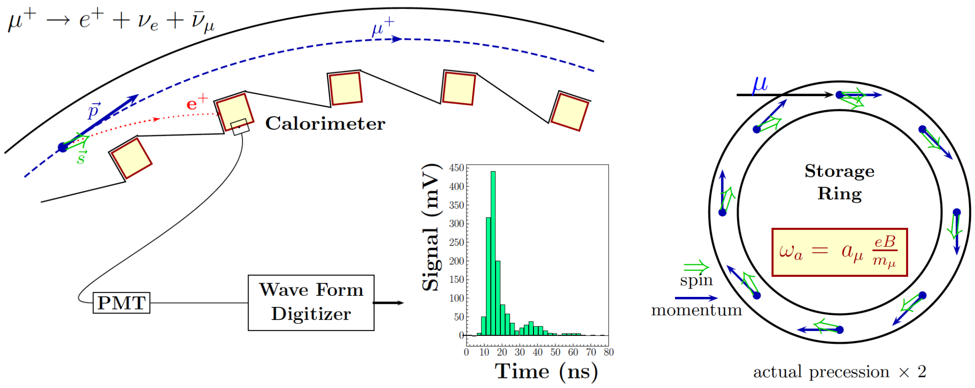

Figure 1.16: Left: BNL / Fermilab measurement scheme. Right: Spin precession.

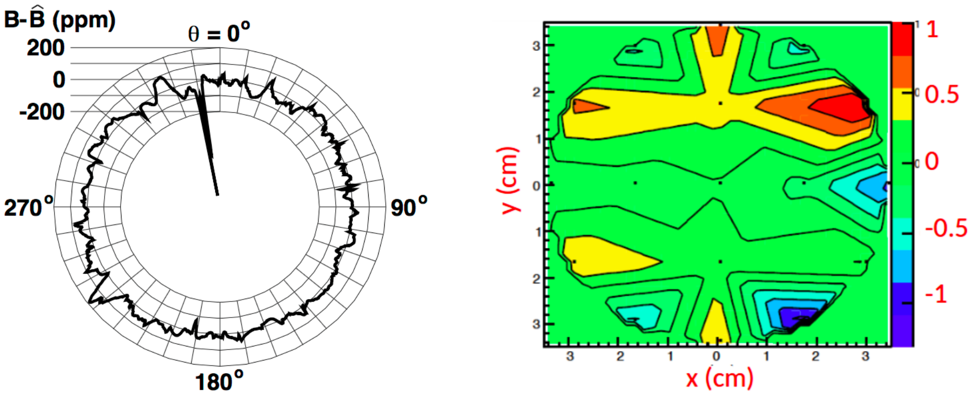

Figure 1.17: Left: BNL magnetic field measured by pNMR probes inside the storage ring [36]. Right: Recent measurement of the magnetic field by a single probe (in ppm, relative to the nominal value).

If $g_\mu = 2$ that is $a_\mu = 0$ (Dirac's prediction), then $\vec{\omega}_s = \vec{\omega}_c$. If the anomaly is not zero, $\omega_s > \omega_c$. The net spin precession frequency along the orbit is defined as the anomalous frequency:

$$\vec{\omega}_a \equiv \vec{\omega}_s - \vec{\omega}_c = a_\mu \frac{e\vec{B}}{m_\mu}. \tag{1.43}$$

In principle from the measurement of ω_a and the knowledge of the magnetic field or rather the field integral experienced by the muon along the orbit, we obtain a measurement of the anomaly a_μ. In the experiments performed at CERN, BNL and now FNAL, a quadrupole electric field is also needed to focus the beam. This electric field is seen by the muon in orbit as another external magnetic field that modifies the anomalous precession frequency:

$$\vec{\omega}_a = \frac{e}{m_\mu}\left[a_\mu \vec{B} - \left(a_\mu - \frac{1}{\gamma^2 - 1}\right)\frac{\vec{\beta} \times \vec{E}}{c}\right]. \tag{1.44}$$

From the CERN III experiment, a special condition has been used called "magic moment", then applied to BNL and FNAL: for $\gamma = 29.3$, that is for $p = 3.094$ GeV$/c$, it is found:

$$\left(a_\mu - \frac{1}{\gamma^2 - 1}\right) \approx 0, \tag{1.45}$$

so as to remove the dependence on the necessary electric field[5] and recover the (1.43). This kind of experiments were and are built to work with muon momenta around the magic one; however they will have a certain beam spread and therefore a small correction is applied to the anomalous frequency to take into account the muon below or above the magic moment. Also modest vertical oscillations, compared to the orbit plane (of betatron) are induced by the electric field and also produce a correction for ω_a [37, 36].

1.4.2 Measuring a_μ

In fig. 1.18, the so-called "wiggle plot" that shows the anomaly in action: the muon exponential decay is overlapped by a modulation with a higher frequency, due to the net frequency of anomalous precession, that is the fact that $g_\mu \neq 2 \Rightarrow a_\mu \neq 0$. As we said the direction of positron emission corresponds to that of spin of the parent muon, therefore the time distribution of the decay positrons (or electrons) is modulated by ω_a and is described by the following function:

$$N(t) = N_0 \exp\left(-t/\gamma\tau_\mu\right)\left[1 + A\cos\left(\omega_a t + \phi\right)\right], \tag{1.46}$$

where N_0 is the normalizing factor, while A and ϕ are fully dependent on the E_{th} threshold energy used to select the decay positrons: for $E_{th} = 2$ GeV, $A \approx 0.4$.

The precise knowledge of the magnetic field is necessary, together with ω_a, to determine a_μ through eq. (1.43): it is obtained through a local sampling along the whole storage ring, carried out through the technique of nuclear magnetic resonance with protons (pNMR) using probes of water or vaseline (fig. 1.17). The proton precession frequency ω_p is proportional to the local

---

[5] At J-PARC [38], in a different way, the muon beam is such that $E = 0 \Rightarrow \vec{\beta} \times \vec{E} = 0$.

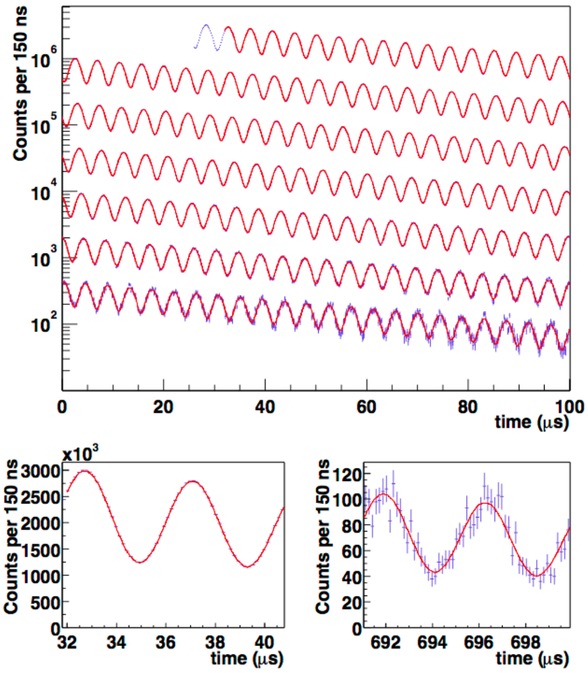

Figure 1.18: Effect of the muon anomaly as seen in the wiggle plot [36]. The high-frequency modulation is fitted with (1.46) to get the Larmor frequency ω_a, due to the anomaly a_μ.

magnetic field. The frequency $\tilde{\omega}_p$ averaged along the ring is therefore the second observable frequency measured, together with ω_a: table 1.2 shows a summary of experimental uncertainties for the BNL muon g-2 measurement and goals for the new experiment at Fermilab. Using:

$$\begin{cases} \omega_a = a_\mu e B / m_\mu \\ B = \hbar \omega_p / 2\mu_p \\ \mu_\mu = (1 + a_\mu) e\hbar / 2m_\mu \end{cases} \tag{1.47}$$

the anomaly a_μ is extracted as a frequency ratio:

$$a_\mu = \frac{\omega_a / \tilde{\omega}_p}{\lambda - \omega_a / \tilde{\omega}_p}, \tag{1.48}$$

where λ is the muon-to-proton magnetic moment ratio:

$$\lambda = \frac{\mu_\mu}{\mu_p} = 3.183345107(84) \quad (26\,\text{ppb}), \tag{1.49}$$

obtained by measurements of the muonium hyperfine structure ($\mu^+ e^-$) from the same E821 experiment [3], recently updated [26].

a_μ incertainty source	BNL E821 (ppb) [3]	FNAL E989 (ppb) [4]
ω_a statistics	480	100
ω_a systematics	180	70
ω_p systematics	170	70
Total	540	140

Table 1.2: Overview of the statistical and systematic uncertainties for the BNL measurement and projections for the Fermilab determination.

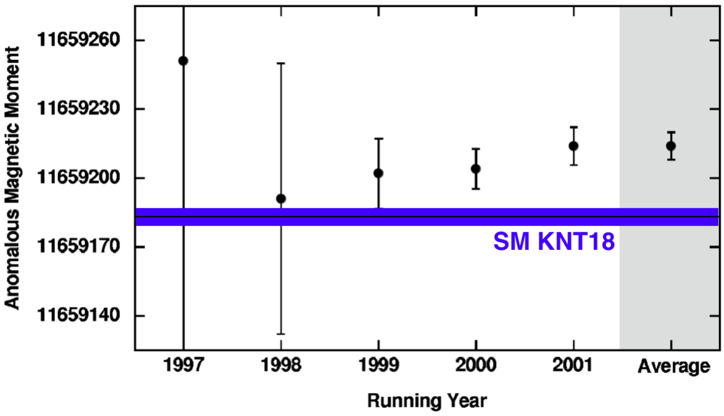

Figure 1.19: Results for the E821 individual measurements of a_μ ($\times 10^{10}$) by running year [3], together with the final average and the last SM prediction (Keshavarzi et al. [27]).

The final a_μ result by BNL is obtained by combining the individual a_μ results from all running periods. All E821 results are plotted in fig. 1.19 together with the final average. With the new value of λ, the updated experimental results for μ^+ and μ^- are [26]:

$$\begin{aligned} a_{\mu^+}^{\text{exp}} &= 11659204(6)(5) \cdot 10^{-10} \\ a_{\mu^-}^{\text{exp}} &= 11659215(8)(3) \cdot 10^{-10}. \end{aligned} \tag{1.50}$$

Assuming CPT invariance and taking into account correlations between systematic uncertainties, one finds for their average

$$a_\mu^{\text{exp}} = 11659209.1(5.4)(3.3) \cdot 10^{-10}, \tag{1.51}$$

where the first errors are statistical and the second systematic: in quadrature, $6.3 \cdot 10^{-10}$ gives 0.54 ppm as relative precision usually quoted for the BNL measurement.

1.5 Discussion about the muon g-2 discrepancy

The discrepancy between the BNL measurement and the Standard Model prediction is at the level of about 3.5-4$\,\sigma$ depending on the theoretical evaluations (tab. 1.1). It constitutes one of the most intriguing issues in the particle physics landscape. There are three possible origins to explain this long-standing discrepancy:

- experimental: it may be the result of statistical fluctuations or underestimation of systematic uncertainties of the E821 experiment;
- theoretical: some ingredients that appear in the theory predictions are not fully understood and cause correlated systematic shifts;
- new physics: the discrepancy is real and can be explained by physics beyond Standard Model (BSM).

Concerning the first point, the Fermilab E989 experiment is expected to publish the first result by 2019, with similar precision as the previous BNL measurement. The final targeted precision is four times better. The other planned measurement of a_μ from J-PARC would be very important, because by means of different technique it should reach the same level of precision. Direct measurements are extremely difficult (proof of this is the fact that the new one will be published almost 20 years after the previous one), but it would be essential to have at least two independent measurements with comparable accuracy.

On the theory side the hadronic corrections dominate the uncertainty of the SM prediction, as shown in tab. 1.1. The traditional estimates seem to have reached their limit precision. Lattice QCD calculations are promising but not yet competitive with them.

To follow the improvement of the experimental accuracy and to ensure that the future theory / data comparisons are reliable, the theoretical predictions are expected to improve. In 2017 the "Muon g-2 theory initiative" was created to facilitate interactions between the different groups and to bring together theorists from the different communities to discuss, assess, and compare the status of the various efforts, and to map out strategies for obtaining the best theoretical predictions for the hadronic corrections.

The MUonE experiment provides an alternative and completely novel way to contribute to the control and improvement of the accuracy of hadronic contribution at the leading order. The final goal, as we will see, is an accuracy of a_μ^{HLO} below the percent, i.e. at level of the traditional measurements.

Recently F. Jegerlehner stated [2] about the time-like measurements combination necessary to obtain a_μ^{HLO}: «There is no unambiguous method to combine systematic errors. Uncertainties are definitely squeezed beyond what can be justified beyond doubt, I think. Therefore, the very different Euclidean approach, lattice QCD and the proposed alternative direct measurement of the hadronic shift $\Delta\alpha(-q^2)$ [5, 6] (MUonE), in the long term will be indispensable as complementary cross-checks.»

About the last point, new physics BSM as an explanation of the discrepancy, we know that the anomaly a_l is an observable sensitive to new physics as [26]:

$$a_l^{NP} \sim \frac{m_l^2}{\Lambda^2} \tag{1.52}$$

where m_l is the lepton mass ($l = e$, μ, τ) and Λ is the energy scale of new physics. The muon anomaly a_μ is a better observable than a_e because of $(m_\mu/m_e)^2 \sim 4 \cdot 10^4$. The BSM explanation is the most fascinating option. The likely candidate is still the supersymmetry with relatively small chargino and neutralino masses. Here the interplay with direct measurements at the LHC is crucial, but so far there is no contradiction between the LHC data and the masses of the supersymmetry particles required to explain the muon anomaly [39].

Chapter 2

MUonE proposal

We have seen that the LO hadronic contribution dominates the uncertainty associated with the theoretical prediction of a_μ^{HLO}. Therefore it has been studied for many years by the theory community of the muon g-2. The MUonE experiment [6] aims to contribute to this effort having proposed a new method to extract a_μ^{HLO}, complementary to the traditional time-like approach.

2.1 Space-like approach to a_μ^{HLO}

The leading-order hadronic contribution (HLO) to the muon g-2 is calculable with the relation introduced in sec. 1.3.3:

$$a_\mu^{\mathrm{HLO}} = \frac{\alpha}{\pi^2} \int_0^\infty \frac{ds}{s} \mathrm{Im}\Pi_{\mathrm{had}}(s) K(s), \tag{2.1}$$

where the kernel $K(s)$ is defined in eq. (1.29) of the previous chapter and α is the fine structure constant. The integral defining a_μ^{HLO} is determined by the optical theorem [40], which links the e^+e^- hadronic production cross section to the imaginary part of $\Pi_{\mathrm{had}}(s)$, the hadronic contribution to the photon vacuum polarization.

This is the heart of the MUonE proposed method [5]: by exchanging the integration order between x and s, to get:

$$a_\mu^{\mathrm{HLO}} = \frac{\alpha}{\pi^2} \int_0^1 dx\, m_\mu^2 x^2 \int_0^\infty \frac{ds}{s} \frac{\mathrm{Im}\Pi_{\mathrm{had}}(s)}{\frac{x^2 m_\mu^2}{1-x} + s}. \tag{2.2}$$

Using this dispersion relation:

$$\overline{\Pi}_{\mathrm{had}}\left[t(x)\right] \equiv \Pi_{\mathrm{had}}(t) - \Pi_{\mathrm{had}}(0) = \frac{t}{\pi} \int_0^\infty \frac{ds}{s} \frac{\mathrm{Im}\Pi_{\mathrm{had}}(s)}{s-t} \tag{2.3}$$

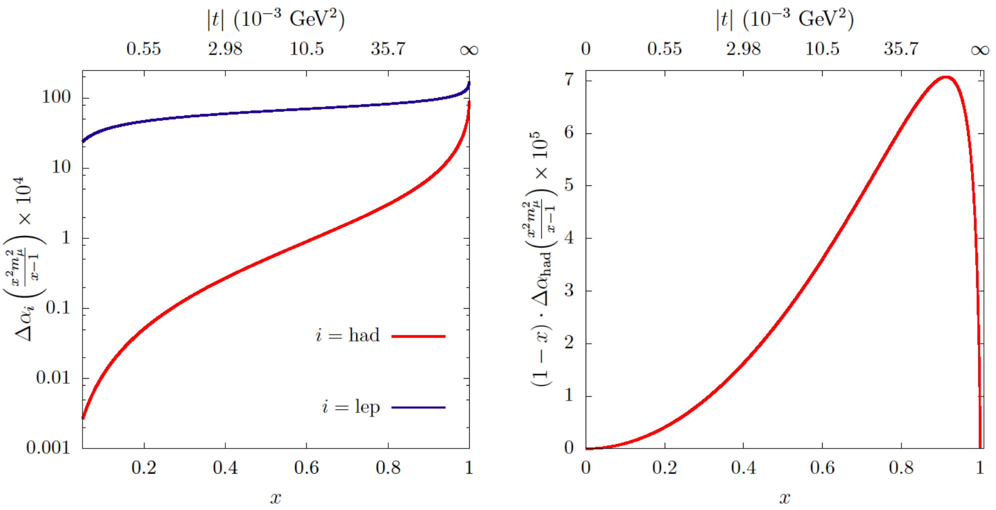

Figure 2.1: (left) Leptonic and hadronic contribution to the running of α. (right) The integrand in eq. (2.8) from which it can be determined $a_\mu^{\rm HLO}$ [6].

and defining the variable t as:

$$t(x) \equiv \frac{x^2 m_\mu^2}{x-1} < 0, \tag{2.4}$$

with $-\infty < t < 0$, eq. (2.2) can be written as:

$$a_\mu^{\rm HLO} = \frac{\alpha}{\pi}\int_0^1 dx (x-1)\overline{\Pi}_{\rm had}\left[t(x)\right]. \tag{2.5}$$

This relation indicates that t can be interpreted as the Mandelstam t variable. As Im$\overline{\Pi}_{had}(t) = 0$ for negative t, eq. (2.5), can be rewritten in the form:

$$a_\mu^{\rm HLO} = \frac{\alpha}{\pi}\int_0^1 dx\,(x-1){\rm Re}\overline{\Pi}_{\rm had}\left[t(x)\right]. \tag{2.6}$$

$\Delta\alpha(t)$ is linked to the photon vacuum polarization by:

$$\Delta\alpha\left[t(x)\right] = -{\rm Re}\overline{\Pi}_{\rm lep}\left[t(x)\right] - {\rm Re}\overline{\Pi}_{\rm had}\left[t(x)\right]. \tag{2.7}$$

So considering $\Delta\alpha_{\rm had}(t)$ we can rewrite (2.6) as:

$$\boxed{a_\mu^{\rm HLO} = \frac{\alpha}{\pi}\int_0^1 dx(1-x)\Delta\alpha_{\rm had}\left[t(x)\right]}. \tag{2.8}$$

This is the master formula underlying the MUonE proposal: it allows to calculate $a_\mu^{\rm HLO}$ on the basis of $\Delta\alpha_{\rm had}(t)$, that is the hadronic contribution to the QED coupling running for space-like transferred momenta.

The "rotation" of the Feynman diagram we have described, from annihilation (s-channel) to scattering (t-channel), simplifies enormously the calculation of the integral for a_μ^{HLO}. The space-like integrand function in eq. (2.8), shown in fig. 2.1, is smooth and free of resonances, contrarily what happens in the time-like approach. Thanks to this feature, it could be possible with a single scattering experiment to determine a_μ^{HLO}.

2.2 MUonE method

2.2.1 Introduction

We can determine $\Delta\alpha_{\mathrm{had}}(t)$ as:

$$\Delta\alpha_{\mathrm{had}}(t) = 1 - \Delta\alpha_{\mathrm{lep}}(t) - \frac{\alpha}{\alpha(t)}, \tag{2.9}$$

since of the well know relation:

$$\alpha(t) = \frac{\alpha}{1 - \Delta\alpha_{\mathrm{lep}}(t) - \Delta\alpha_{\mathrm{had}}(t)}. \tag{2.10}$$

The MUonE experiment proposes to measure the effective electromagnetic coupling $\alpha(t)$ by means of the elastic scattering of high energy muons on electrons at rest. The high intensity CERN M2 muon beam [7] provides 150 GeV muons, allowing to cover most of the master integral (2.8). The MUonE proposal is appealing for the following key points [6]:

- the elastic scattering μ-e is a pure t-channel process, ideal to measure the running of $\alpha(t)$;
- the M2 muon beam at CERN is a high intensity source of high energy muons;
- the highly boosted kinematics allows to cover the whole acceptance with a single and homogenous detector: the angular deflections will be contained within a cone of 50 mrad;
- the kinematics of the $2 \rightarrow 2$ elastic scattering is completely determined by the angular observables. The signal region is identified by the correlation between the muon and electron scattering angles.

However, the clear signature of the elastic scattering is modified by the radiative corrections and by the detector resolution. Radiative corrections to the μ-e cross section requires NLO and NNLO calculations, never performed

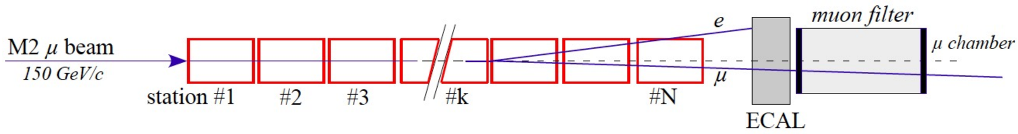

Figure 2.2: Apparatus scheme (not to scale), from the Letter of Intent [14].

until now at the required level of precision [41]. From the experimental side, the scattering occurs in a target and not in vacuum, so the control of the multiple Coulomb scattering is essential. Controlling these two effects to the required precision is the main challenge of the experiment.

The goal of MUonE is to determine a_μ^{HLO} with a relative precision of 0.3% comparable to the time-like traditional approach. Since the hadronic running gives a maximum contribution to the cross section at the permille level for high squared transferred momentum t, the systematics must be kept below 10^{-5} (10 ppm). This requirement is equivalent to measuring the shape of the elastic μ-e differential cross section to 10 ppm.

The effort of the MUonE collaboration in reaching the precision target is therefore twofold, both on the experimental and the theoretical front.

2.2.2 The workflow scheme

The MUonE concept is based on the precise measurement of the scattering angles (θ_e, θ_μ) of the outgoing electrons and muons, with respect to the direction of the incoming muons. Let's see how $\alpha(t)$ can be obtained from the angular measurement, by means of (2.8) and (2.10) and from there how to get a_μ^{HLO}:

$$(\theta_e, \theta_\mu) \;\rightarrow\; \alpha(t) \;\rightarrow\; \Delta\alpha_{\text{had}}(t) \;\rightarrow\; a_\mu^{\text{HLO}}. \tag{2.11}$$

A sketch of the experimental apparatus [14] is shown in fig. 2.2. It consists of a sequence of 40 identical stations. Each station contains a 15 mm Beryllium target and 3 tracking layers, which are placed along a lever arm of about 1 m. The thin targets allows to minimize multiple scattering effects. Angles of the scattered particles are measured by tracking layers. The apparatus is also equipped with an electromagnetic calorimeter (ECAL), placed downstream the stations. It provides particle identification (PID) and possibly a measurement of the electron energy. In order to control the low residual contamination of pions in the muon beam $\sim 10^{-6}$ [42], a muon filter, instrumented with muon chambers will be added, downstream the ECAL.

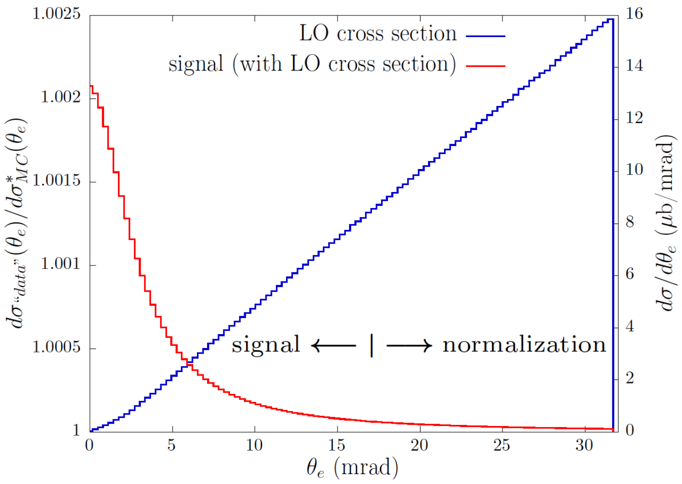

Figure 2.3: In blue, the differential cross section as a function of θ_e at LO. In red, the sensitivity to the hadronic running as defined in eq. (2.12).

To determine $\alpha(t)$, we will measure the following counting ratio:

$$\frac{d\sigma_{\text{data}}/d\theta_i}{d\sigma^0_{\text{MC}}/d\theta_i} = \frac{dN_{\text{data}}/d\theta_i}{dN^0_{\text{MC}}/d\theta_i} = \left|\frac{\alpha(t)}{\alpha}\right|^2 = \frac{1}{|1 - \Delta\alpha_{\text{lep}}(t) - \Delta\alpha_{\text{had}}(t)|^2}, \tag{2.12}$$

where the observables θ_i are the scattering angles θ_μ and θ_e of muons and electrons, $dN_{\text{data}}/d\theta_i$ e $d\sigma_{\text{data}}/d\theta_i$ are the observed counts and the differential cross section respectively; $dN^0_{\text{MC}}/d\theta_i$ e $d\sigma^0_{\text{MC}}/d\theta_i$ are instead counts and differential cross section Monte Carlo (MC) determined assuming as $\alpha(t)$ the value of the fine structure constant α. The method does not rely on the knowledge of the luminosity.

Figure 2.3 shows the signal that MUonE aims to measure (in red), i.e. the ratio $dN_{\text{data}}/dN^0_{\text{MC}}$ defined in (2.12) as a function of θ_e, with the LO differential cross section $d\sigma/d\theta_e$ (in blue) which will be analytically determined in sec. 2.6.2.

The relation (2.12) directly connects $\Delta\alpha_{\text{had}}(t)$ to the counting ratio. In the kinematical range of interest: $\Delta\alpha_{\text{lep}}(t) \lesssim 10^{-2}$ and $\Delta\alpha_{\text{had}}(t) \lesssim 10^{-3}$.

In the complete NLO and NNLO calculations, the ratio of the observed angular distributions $dN_{\text{data}}/d\theta_i$ and the theoretical predictions $dN^0_{\text{MC}}/d\theta_i$ do not have a mathematical expression. They must be evaluated numerically by MC methods.

The extraction of the hadronic contribution $\Delta\alpha_{\text{had}}(t)$ is carried out by a template fit method [14]. It is a powerful tool [43] that allows to fit the parameters of $\Delta\alpha_{\text{had}}(t)$, in the lack of analytical expressions for the cross section at higher orders.

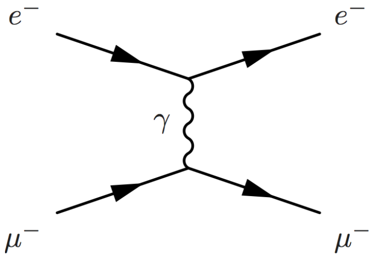

Figure 2.4: Tree level diagram of the μ-e scattering processes.

In the following sections, we will mainly discuss about:

- the elastic scattering kinematics, to establish the fundamental correlation between θ_μ and θ_e;
- the requested luminosity needed to ensure the experiment can achieve a statistical precision on a_μ^{HLO} competitive with respect to the traditional time-like method, in a time scale of about 2 years;
- the CMS Silicon sensors to be used to perform the precise measurement of the angular deflections.
- the DAQ and trigger system foreseen to readout the detector.

The design of ECAL is still under optimization. We will briefly discuss it to describe the required performance. In the last chapter, we will present the first exercise performed to determine a_μ^{HLO} discussing a parametrization of $\Delta\alpha_{\text{had}}(t)$.

2.3 μ-e elastic scattering

2.3.1 Kinematics properties

At Born level the muon-electron elastic scattering 2 → 2 (fig. 2.4) can be represented as:

$$\mu^\pm(p_1) + e^-(p_2) \to \mu^\pm(p_3) + e^-(p_4), \tag{2.13}$$

where p_1 and p_2 are the 4-momenta in the initial state, p_3 and p_4 are the 4-momenta in the final state. In the laboratory system, referring to the fig. 2.5,

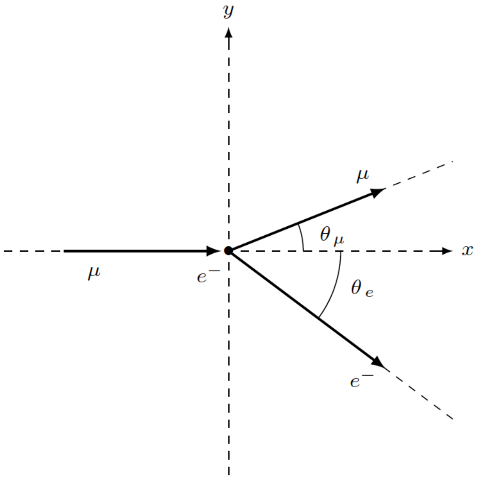

Figure 2.5: μ-e elastic scattering in the laboratory rest frame [44].

the particles 4-momenta are given by:

$$\begin{aligned} p_1 &= (E_\mu, \vec{p}_\mu) = (E_\mu, 0, 0, p_\mu) \\ p_2 &= (E_e, \vec{p}_e) = (m_e, 0, 0, 0) \\ p_3 &= (E'_\mu, \vec{p}'_\mu) = (E'_\mu, p'_\mu \cos\theta_\mu, 0, p'_\mu \sin\theta_\mu) \\ p_4 &= (E'_e, \vec{p}'_e) = (E'_e, p'_e \cos\theta_e, 0, p'_e \sin\theta_e), \end{aligned} \tag{2.14}$$

with m_e and m_μ are the electron and muon mass respectively, $p_\mu = |\vec{p}_\mu|$, $E_\mu = E_\mu^{\text{beam}}$, and after the scattering $p'_\mu = |\vec{p}'_\mu|$ e $p'_e = |\vec{p}'_e|$.

The differential cross section at leading order (LO) in QED is given by [41, 44]:

$$\frac{d\sigma_0}{dt} = \frac{4\pi\alpha_0^2}{\lambda(s, m_e^2, m_\mu^2)} \left[\frac{(s - m_e^2 - m_\mu^2)^2}{t^2} + \frac{s}{t} + \frac{1}{2} \right], \tag{2.15}$$

where $\alpha_0 = \alpha$ is the fine structure constant, s and t are the Mandelstam variables and λ is the Källén function:

$$\begin{aligned} & s \equiv (p_1 + p_2)^2 = (p_3 + p_4)^2 = m_e^2 + m_\mu^2 + 2m_e E_\mu \\ & t \equiv (p_1 - p_3)^2 = (p_2 - p_4)^2 = 2m_e(m_e - E'_e) = 2m_e(E'_\mu - E_\mu) \\ & \lambda(s, m_e^2, m_\mu^2) \equiv (s - m_e^2 - m_\mu^2)^2 - 4m_e^2 m_\mu^2 = 4m_e^2(E_\mu^2 - m_\mu^2). \end{aligned} \tag{2.16}$$

In the LO cross section (2.15), the electromagnetic coupling is an overall factor. The effect of vacuum polarization can be accounted by the running of α as:

$$\frac{d\sigma/dt}{d\sigma_0/dt} = \left| \frac{\alpha(t)}{\alpha} \right|^2 = \frac{1}{|1 - \Delta\alpha(t)|^2}. \tag{2.17}$$

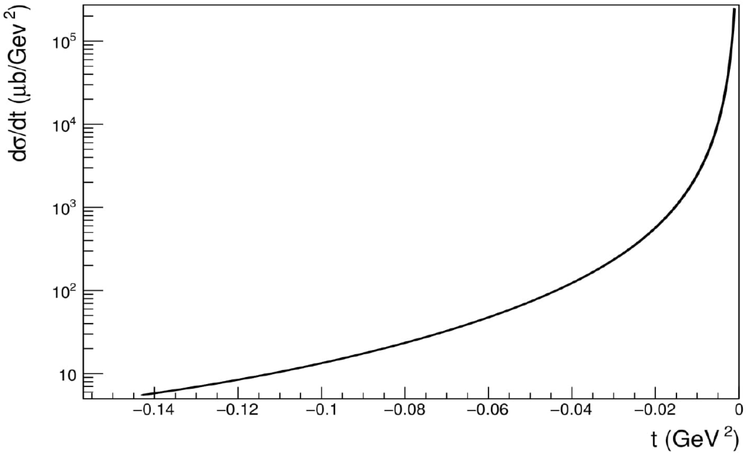

Figure 2.6: LO differential cross section in t for the μ-e elastic scattering [44].

When considering NLO and NNLO radiative corrections (virtual and real photons) $\alpha(t)$ is not more factorizable (see section 2.6.3).

Figure 2.6 shows the cross section as a function of t as defined in eq. (2.15): it is peaked at low values of the squared transferred momentum ($t \to 0$). Note that according to eq. (2.15) $t \propto -E'_e$. It implies that a lower limit on the scattered electron energy corresponds to an upper limit on t.

With good approximation the atomic electrons can be considered as at rest in the laboratory frame. In fact, the center-of-mass (CM) energy is

$$s \approx 0.164463\,\text{GeV}^2 \;\to\; E_{CM} = \sqrt{s} \approx 405.5\,\text{MeV}, \tag{2.18}$$

while the electron binding energy for Beryllium is of the order of a few tens of KeV.

The collision is highly boosted in the forward direction, with respect to the laboratory frame since of the Lorentz factor:

$$\gamma = (E_\mu^{\text{beam}} + m_e)/\sqrt{s} \approx 369.9. \tag{2.19}$$

The integrand function of eq. (2.8), plotted in fig. 2.1, is peaked at $x_{peak} \approx 0.914$ that corresponds to a transferred momentum of:

$$t_{peak} \approx -0.108\,\text{GeV}^2 \approx -(329\,\text{MeV})^2. \tag{2.20}$$

The beam energy $E_\mu = 150$ GeV is large enough to explore the integral beyond the peak, down to:

$$t_{\min} = -\lambda/s_{\text{M2}} \approx -0.142893\,\text{GeV}^2, \tag{2.21}$$

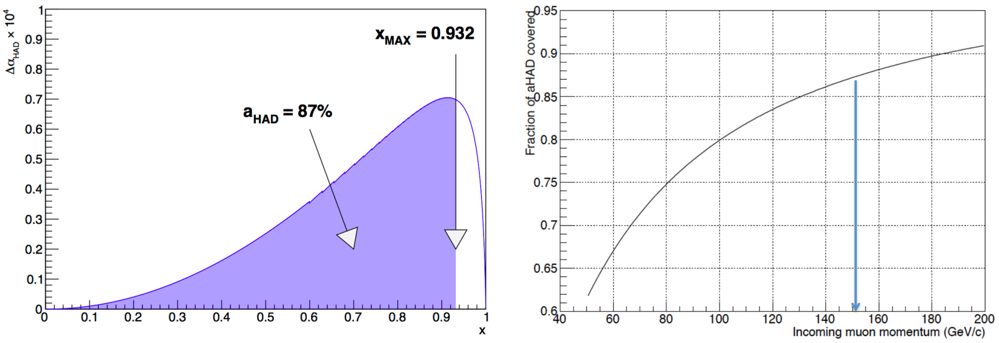

Figure 2.7: (Left) Coverage of $a_\mu^{\rm HLO}$ according to eq. (2.8), for $E_\mu = 150$ GeV. (Right) Fraction of $a_\mu^{\rm HLO}$ as a function of beam energy.

corresponding to $x_{\rm max} \approx 0.93212$. The integral from 0 to $x_{\rm max}$ provides a coverage of 87% for $a_\mu^{\rm HLO}$ (fig. 2.7). In order to obtain the complete value of $a_\mu^{\rm HLO}$, we can extrapolate $\Delta\alpha_{\rm had}(t)$ to the whole x range [0,1], using an appropriate parametrization [14] (see last chapter). Figure 2.7 shows how the integral defining $a_\mu^{\rm HLO}$ depends on the M2 beam energy.

2.3.2 $\theta_\mu - \theta_e$ correlation

Given the energy of the incoming muons and the squared transferred momentum t, by using 4-momentum conservation, all the other kinematic variables can be univocally determined. Moreover, the scattering process is planar, i.e the three vectors of the incoming muon and outgoing electron and muon lie on the same plane.

The fundamental correlation between θ_μ and θ_e can be obtained from the transverse momentum conservation:

$$\sin\theta_\mu = \frac{p'_e \sin\theta_e}{p'_\mu} = \frac{\sqrt{E'^2_e(\theta_e) - m_e^2}\,\sin\theta_e}{\sqrt{(E_\mu + m_e - E'_e(\theta_e))^2 - m_\mu^2}} \tag{2.22}$$

where p'_e and p'_μ are the 3-momenta after the scattering of the electron and muon and $E'_e(\theta_e)$ is the electron energy after the scattering. The electron energy is given by (2.57) of section 2.6.1. Angles θ_e and θ_μ are defined with respect to the direction of the incoming muon. The correlation between the scattering angles is shown in fig. 2.8. This is the main signature to recognize and to select the signal. We call this correlation the "elasticity curve".

The kinematics of the elastic scattering (sec. 2.6.1) limits the muon angle to ~ 5 mrad, while the electron ones are within ~ 50 mrad. The angular acceptance $\Delta\theta$ of 50 mrad can be obtained using a Silicon tracker of

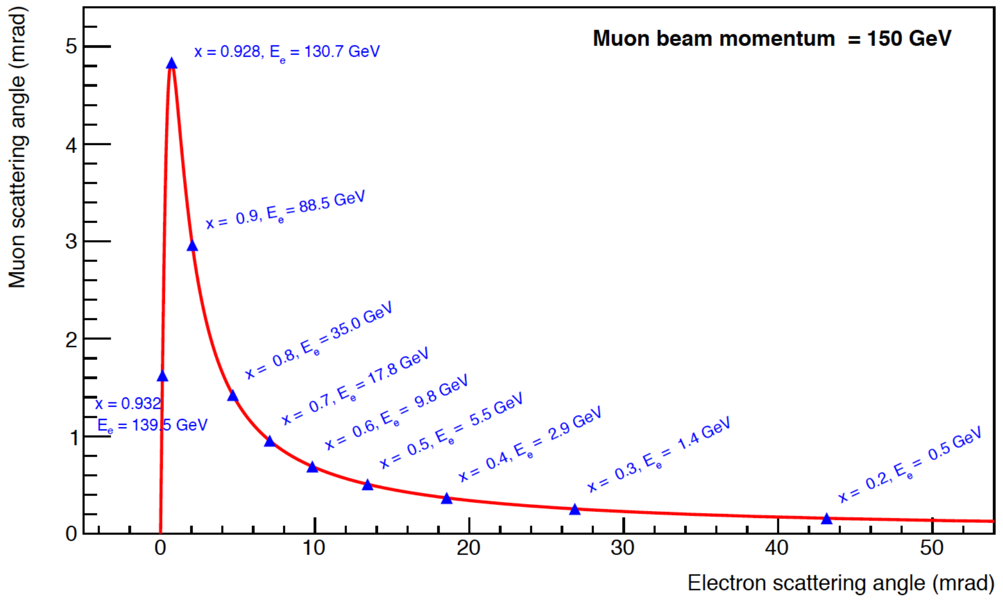

Figure 2.8: Kinematic correlation between θ_μ and θ_e, for $E_\mu = 150$ GeV [6]. In blue the electron energies (2.57) and the corresponding x values.

10 cm × 10 cm and a length of a station $L = 100$ cm:

$$\Delta\theta = \frac{d/2}{L} = \frac{10\,\text{cm}}{2 \cdot 100\,\text{cm}} = 50\,\text{mrad} \tag{2.23}$$

The whole detector acceptance can be covered with a single Si planar sensor: it is a key aspect in order to control the systematic effects.

Figure 2.9 shows the angular correlation corresponding to 3 different beam energies: each beam energy E_μ selects a different curve. To be noticed that the maximum difference between the curves occurs in the low θ_e region. This feature inspired us to define a method based on the kinematics inversion to measure very precisely the beam energy using the both the angles (θ_μ,θ_e). Such a fundamental aspect will be discussed in the last chapter.

2.4 The requested luminosity

The ultimate goal of the experiment is to reach a statistical precision of 0.3% on the value of a_μ^{HLO}. By exploiting the M2 high intensity, it will be possible to obtain this statistical precision in about 2 years.

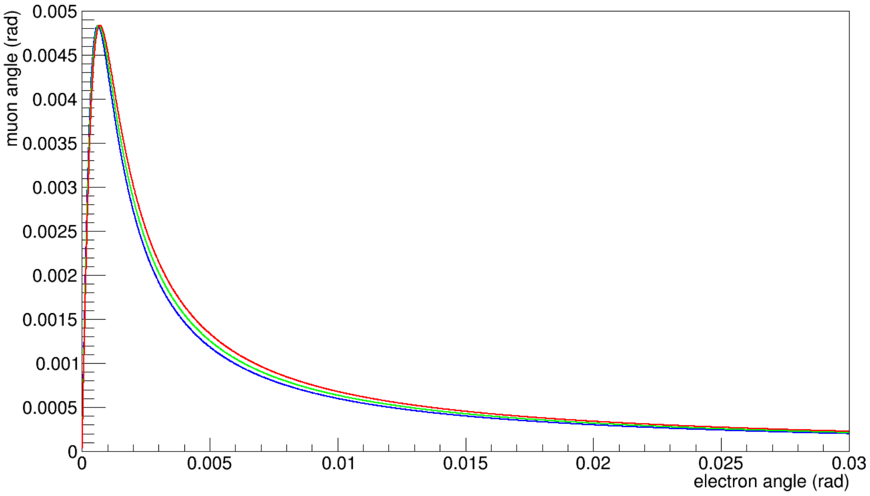

Figure 2.9: Correlation between muon and electron scattering angles, for 3 different energies: red, green, blue for $E_\mu = 150,\ 160,\ 170$ GeV.

2.4.1 Integrated luminosity

To evaluate the required luminosity, we use the error propagation applied to the eq. (2.17). The absolute error on the cross section, affecting $\alpha(t)$, reads:

$$\delta\left(\frac{d\sigma}{dt}\right) = \delta\left(\frac{\alpha^2(t)}{\alpha^2(0)}\,\frac{d\sigma_0}{dt}\right), \tag{2.24}$$

where

$$\delta\left(\frac{\alpha^2(t)}{\alpha^2(0)}\right) = \delta\left(\frac{1}{(1-\Delta\alpha(t))^2}\right) = \frac{2\delta\Delta\alpha(t)}{(1-\Delta\alpha(t))^3}. \tag{2.25}$$

Then the absolute error is

$$\delta\left(\frac{d\sigma}{dt}\right) = \frac{2\,\delta\Delta\alpha_{\rm had}(t)}{(1-\Delta\alpha(t))^3}\,\frac{d\sigma_0}{dt}, \tag{2.26}$$

assuming here that the absolute error on the running $\delta\Delta\alpha(t)$ is entirely due to the hadronic contribution $\delta\Delta\alpha_{\rm had}(t)$.

The relative error on the cross section is:

$$\frac{\delta\sigma}{\sigma} \equiv \frac{\delta(d\sigma/dt)}{d\sigma/dt} = \frac{2\,\delta\Delta\alpha_{\rm had}(t)}{1-\Delta\alpha(t)} \approx 2\,\delta\Delta\alpha_{\rm had}(t), \tag{2.27}$$

so the uncertainty on $\Delta\alpha_{\rm had}(t)$ is given by

$$\boxed{\delta\Delta\alpha_{\rm had}(t) \approx \frac{1}{2}\frac{\delta\sigma}{\sigma}}. \tag{2.28}$$

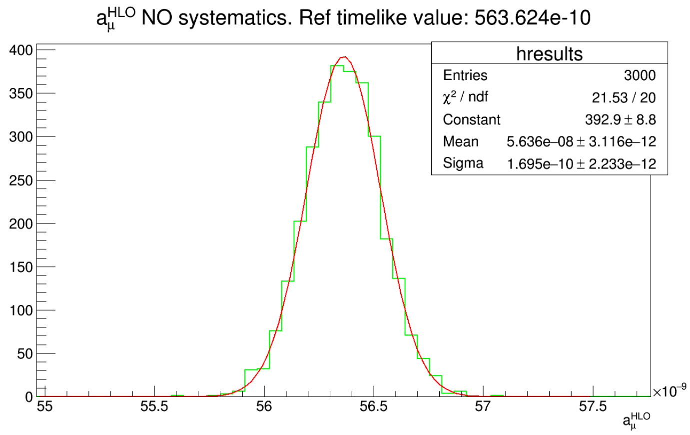

Figure 2.10: Results of 3000 pseudo-experiments to study the statistical accuracy and to determined the required integrated luminosity.

The number of entries N_i in a given i-th bin of the observable distribution is related to the cross section by

$$N_i = \sigma_i \cdot L, \tag{2.29}$$

where σ_i is the integrated cross section in the i-th bin while L is the time integrated luminosity. So the error on the hadronic running can be evaluated as

$$\delta\Delta\alpha_{\text{had},i} \approx \frac{1}{2}\frac{\delta\sigma_i}{\sigma_i} = \frac{1}{2}\frac{\delta N_i}{N_i} = \frac{1}{2}\frac{1}{\sqrt{N_i}} = \frac{1}{2}\frac{1}{\sqrt{\sigma_i \cdot L}}. \tag{2.30}$$

We can now estimate the required luminosity L. According to the available time-like measurements, it is possible to calculate the expected $\Delta\alpha_{\text{had}}(t)$ function in the space-like region, by rotation of the dispersion integral (sec. 2.1). It has been done by using the routines provided us by F. Jegherlener. One can then apply a statistical smearing to the calculated $\Delta\alpha_{\text{had},i}$ according to eq. (2.30). Using a polynomial parametrization of $\Delta\alpha_{\text{had}}(t)$ and the MUonE master formula (2.8), it is possible to estimate the corresponding value of anomaly a_μ^{HLO}. By performing an ensemble of pseudo-experiments [43], it is possible to evaluate the statistical error due to the luminosity L. In fig. 2.10 the results of the pseudo-experiments, with

$$L = 1.5 \cdot 10^7 \,\text{nb}^{-1}. \tag{2.31}$$

Fitting the distribution of a_μ^{HLO} with a gaussian the mean is in perfect agreement with the reference value and the standard deviation is compatible with a statistical precision of about 0.3%.

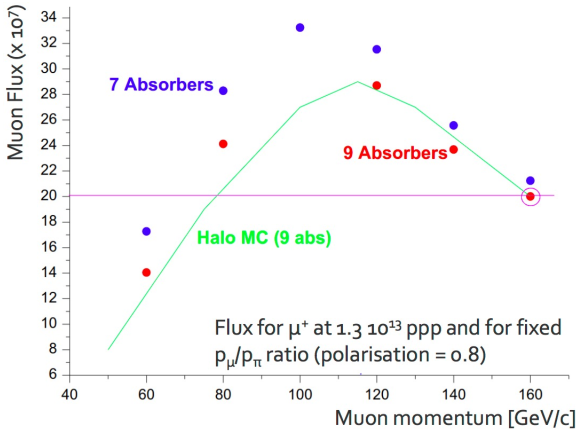

Figure 2.11: The M2 flux per spill for positive muons, from $1.3 \cdot 10^{13}$ protons per cycle extracted from SPS [7]. At 160 GeV, measurements made by COMPASS provide a peak flux of 200 MHz/spill corresponding to $\bar{I}_\mu \sim 13$ MHz of average intensity. The green curve is the result of a Monte Carlo simulation.

2.4.2 The M2 intensity, the target thickness and the event rate

The M2 muon beam is one of the secondary lines provided by SPS and is unique in terms of high energy, high intensity and low contamination. The main characteristics of this facility will be described to calculate the required target thickness.

The CERN SPS beam line M2 can be set to run with high intensity of muon beams, of momenta varying from 60 to 190 GeV/c. M2 is obtained from an intense proton beam, extracted from the SPS at 400 GeV/c, that impinges on a Beryllium target of 50 cm. Secondary particles fly trough the decay tunnel and the hadrons defocusing system. Muons are then selected and focused after a dedicated hadron absorber. The residual hadron contamination is of the order of 10^{-6} [42], to be compared to the typical contamination of secondary beams at the percent level.

The SPS ensures a constant protons flux: the spill duration is 4.8 s, with variable duty cycle (ratio of spill to cycle length). In the so-called “slow extraction” mode, the time of the extraction cycle is 15.6 s. The duty cycle is of about 4.8 s/15.6 s = 31% [7].

Figure 2.11 shows the maximum number of muons per spill versus the beam energy. The average beam intensity for energies at 150 GeV can be estimated in:

$$\bar{I}_\mu = \text{duty cycle} \times I_\mu^{\text{peak}} \sim 0.31 \times 50\,\text{MHz} \sim 1.5 \cdot 10^7\,\mu/\text{s}. \tag{2.32}$$

Assuming a running time Δt_0 per year:

$$\Delta t_0 \sim 2 \cdot 10^7\,\text{s/year (63\% year)}, \tag{2.33}$$

and 2 years of data taking Δt, given $L = 1.5 \cdot 10^7\,\text{nb}^{-1}$, the instantaneous luminosity must be [6]:

$$\mathcal{L}_{\text{request}} = \frac{L}{\Delta t} = \frac{L}{2\,\Delta t_0} \sim 3.8 \cdot 10^{32}\,\text{cm}^{-2}\text{s}^{-1}. \tag{2.34}$$

To determine the thickness of the Beryllium target, one can rely on the expression of the instantaneous luminosity:

$$\mathcal{L} = \bar{I}_\mu \cdot \rho_e\, d = \bar{I}_\mu \cdot \frac{N_A\, \rho_{\text{Be}}\, Z}{W}\, d, \tag{2.35}$$

where ρ_e is the density of the electron scattering centers, ρ_{Be} the Beryllium density, Z and W the atomic number and atomic weight, d the total target thickness and N_A the Avogadro's number.

Assuming the M2 mean intensity $\bar{I}_\mu$ of eq. (2.33), $\rho_{\text{Be}} = 1.85\ \text{g/cm}^3$ and $(Z/W)_{Be} = 0.44$, the target thickness turns out to:

$$d = \frac{W \mathcal{L}_{request}}{N_A\, \rho_{\text{Be}}\, Z} = 60\ \text{cm}. \tag{2.36}$$

Given the leading order total cross section $\sigma_{\mu e} = 245\,\mu\text{b}$ (for $\theta_e < 30$ mrad), the number of required signal events, i.e. the total statistics MUonE must collect, can be estimated as:

$$N_{\text{tot}} = L \cdot \sigma_{\mu e} \sim 3.7 \cdot 10^{12}. \tag{2.37}$$

In conclusion, the high intensity of the M2 beam allows to collect the required statistical precision in a time scale of about 2 years.

In order to evaluate the expected elastic event rate one can rely on the following relation:

$$dp_{\mu e}/dx = \sigma_{\mu e} \cdot \rho_e = 245\,\mu\text{b} \cdot \rho_e \sim 1.21 \cdot 10^{-4}\,/\text{cm}, \tag{2.38}$$

where $dp_{\mu e}/dx$ is the probability of elastic interaction per unit of length, ρ_e is the density of scattering centers (i.e. atomic electrons) for Beryllium, given by

$$\rho_e = \frac{N_A\, \rho_{Be}\, Z_{Be}}{W_{Be}} = 4.95 \cdot 10^{23}\ e^-/\text{cm}^3. \tag{2.39}$$

For a target of 1.5 cm per station, this probability is:

$$p_{\mu e}^{\text{station}} \sim 1.81 \cdot 10^{-4}. \tag{2.40}$$

For a total of 60 cm of Beryllium, we have

$$p_{\mu e}^{\text{tot}} \sim 1.21 \cdot 10^{-4} \cdot 60 \sim 7.26 \cdot 10^{-3}. \tag{2.41}$$

Now it is possible to estimate the expected signal rate per module and the total rate, for $I_\mu^{peak} = 50$ MHz:

$$f_{\mu e}^{\text{station}} = p_{\mu e}^{\text{station}} \cdot I_\mu^{\text{peak}} \sim 7.4\,\text{kHz} \quad \rightarrow \quad f_{\mu e}^{\text{tot}} \sim 450\,\text{kHz}. \tag{2.42}$$

2.5 The detector

We have set a series of fixed points, some of which have been tested in two test beams performed in 2017 and 2018 [8, 9].

The tracking system represents the heart of the detector concept. The requirements are compelling [14]: high intrinsic angular resolution (< 0.03 mrad), large surface area (~ 10 cm side), high uniformity and efficiency ($\sim 100\%$) over the q^2 range of interest, high rate sustainability and easy integration in trigger system. An active area of 10×10 cm^2 for the tracking modules contains all the kinematics of the event.

Muons can be distinguished from electrons using solely the angular information, with the exception of a limited ambiguity region, which is determined by the the angular resolution itself.

Very high and uniform detection efficiency in a high beam rate environment is an important requirement. Silicon detector with high signal-to-noise ratio (S/N ~ 25) as the ones currently developed for use at colliders can achieve detection efficiency close to 100% and sustain high rate (~ 70 MHz).

Given the requested high rate, it was natural to study existing detectors developed for the high-luminosity upgrade at LHC. The focus was mainly on Silicon strip detectors (SSD), with maximum readout rate. We also considered the possibility of pixel detectors. Although a large number of channels and the small sizes, they can provide significant improvements from the point of view of the material budget. In the case of MUonE, occupancy is not a problem, so standard thickness SSDs are appropriate to keep a high S/N ratio.

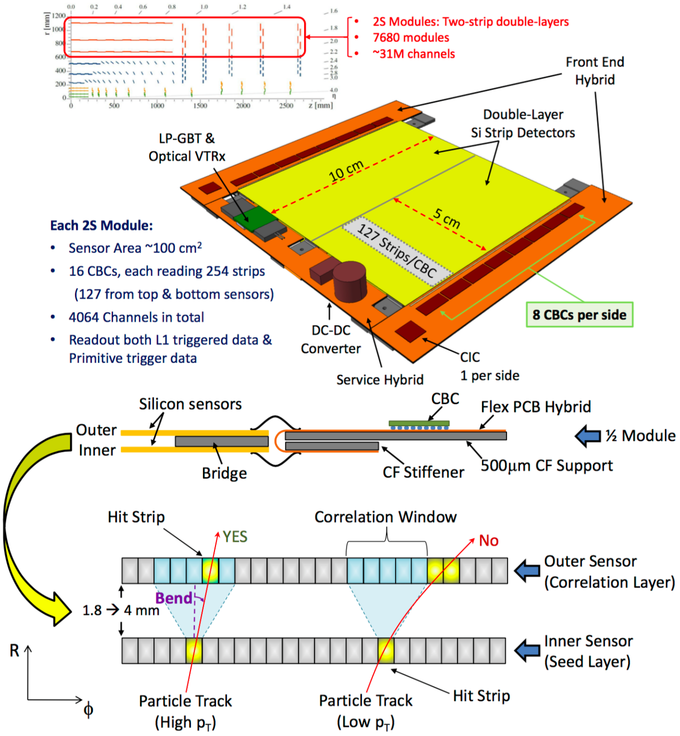

Figure 2.12: S2 module [45].

2.5.1 CMS 2S trackers

Thanks to CMS experts and collaborators, a feasible solution has been found for the trackers: these are the 2S modules trackers with CBC3 readout ASIC [46, 47], developed by CMS for the Hi-Lumi upgrade [48]. These are Silicon strip detectors single-sided, double layer, that have gone through a development phase of at least 10 years. They will be used by CMS as external trackers at a distance of $\sim$ 70-120 cm from the vertex and thanks to the high readout frequency for the first trigger hardware (L1).

The CMS L1 trigger will select high transverse momentum tracks ($p_t >$ 1-2 GeV) and is realized thanks to a double layer system (fig. 2.13): each coordinate x/y is read by two adjacent Si layers, controlled by the CBC3 chips. These ASICs generate at 40 MHz raw track segments (stubs), if the hits of adjacent layer are within a selected correlation window. At 40 MHz MUonE can rely on these stubs to quickly reconstruct the tracks in order to cope the high M2 intensity ($\sim$ 50-60 MHz). The readout is digital to ensure high speed. The pitch readout is 90 μm, for 300 μm thickness for each layer.

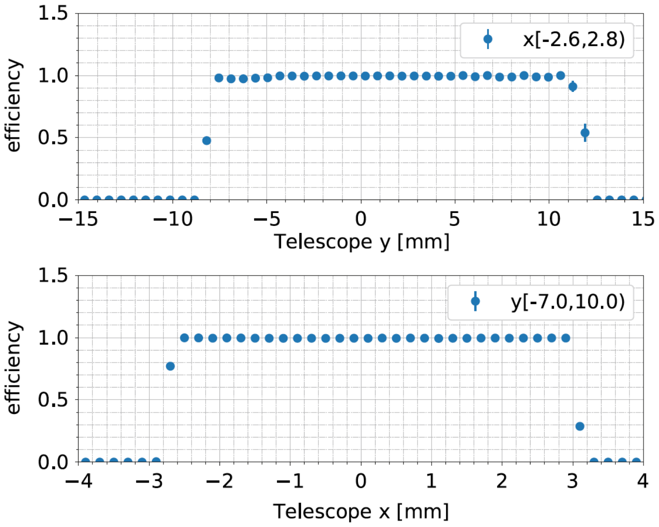

Figure 2.13: Efficiency and uniformity test of CMS 2S trackers [47], recently done by Imperial College group. It shown the response of a single area of the sensor surface read by one ASIC.

These parameters provide an intrinsic point resolution of:

$$\sigma_x = \frac{p}{\sqrt{2}\sqrt{12}} = \frac{90\,\mu\text{m}}{\sqrt{24}} \sim 18\,\mu\text{m} \quad \text{(binary)}. \tag{2.43}$$

The additional factor $\sqrt{2}$ is due to the fact that each coordinate is read by two adjacent layers, so we basically have two measurements of the same coordinate. Given this hit resolution, a single MUonE station could achieve an intrinsic angular resolution of:

$$\Delta\theta_i = \sqrt{2}\,\frac{\sigma_i}{L} = \sqrt{2}\,\frac{18\,\mu\text{m}}{100\,\text{cm}} \sim 0.025\,\text{mrad}. \tag{2.44}$$

The CMS 2S efficiency and uniformity has been measured by the CMS collaboration: recent results are shown in fig. 2.13.

2.5.2 The DAQ concept

The output rate of the MUonE readout system is determined by the intensity of the M2 muon beam and by the induced detector's modules occupancy. The intensity of the beam is rather high, in average of the order of 50-60 MHz. The induced occupancy instead is expected to be quite small, since large fraction of the muons will cross the detector undisturbed. However, although the occupancy of the detector's modules will be small, we

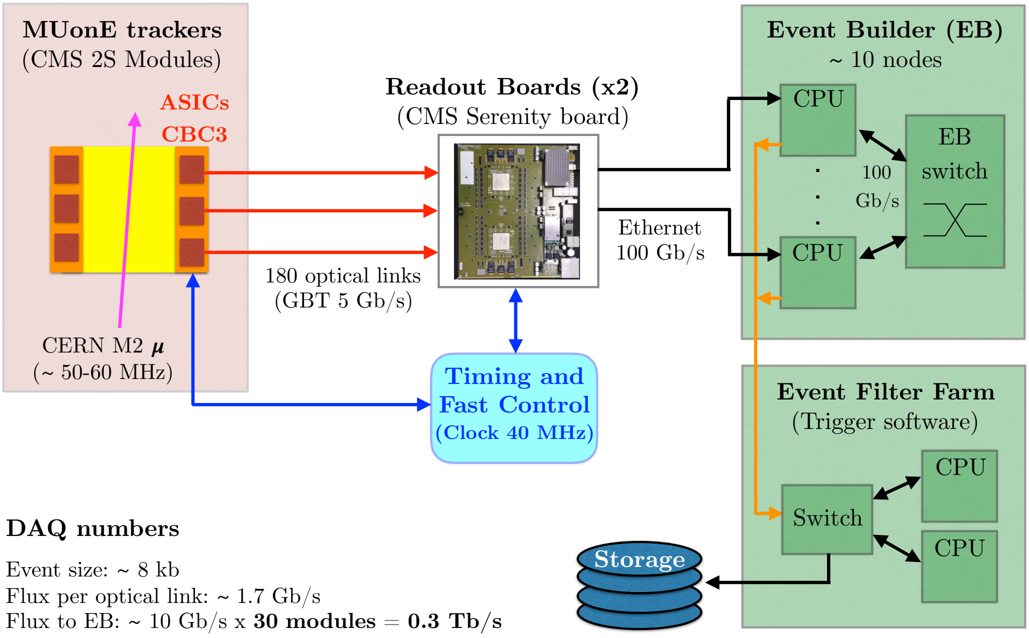

Figure 2.14: DAQ scheme of the MUonE experiment.

aim sampling the detector at 40 MHz, as for the LHC experiments. The high sampling rate will allow us limiting the pileup to just a few overlapping events per clock cycle, easing pattern recognition and tracking.

As a consequence of the small detector occupancy, the DAQ system does not need a custom hardware trigger to reduce the data throughput (fig. 2.14). A triggerless acquisition is therefore planned, as designed for LHCb upgrade [49]. Data will flow at the clock frequency of 40 MHz from the frontend (FE) to the Event Builder (EB). The connection between FE and EB will be made through the electronic interface board Serenity [50], developed by Imperial College (London) for CMS, which we are working with. The board receives optical fiber and transmits via Ethernet protocol.

The dedicated EB will aggregate events fragments recorded in the different modules of the detector to provide the global picture. The functionality of the EB can be obtained with order of 10 servers. Interesting events candidates will be then selected by means of a software trigger, implemented as algorithms running on a Event Filter Farm (EFF).

Thanks to the GEANT4 detailed simulation of the detector, we estimated the data flow produced by a station, in order to evaluate the needs of the acquisition system. The relevant parameters:

- 12 bits for coding a stub;

- The mean number of stubs recorded by a CBC per crossing muon, turns out to be 0.07 (fig. 2.15);
- 16 CBC per tracking station;
- 6 tracking module per station;
- clock frequency at 40 MHz.
- pileup of about 3 events per clock cycle, determined as 60 MHz (M2 frequency) / 40 MHz × 2[1]

From these numbers we can determine the expected rate of the data, flowing from a station to the EB, as:

$$\text{flux} = 12 \times 0.07 \times 16 \times 6 \times 4 \cdot 10^7 \times 3 \sim 10\,\text{Gb/s/station}. \tag{2.45}$$

This flow is sustainable with a network of modest size (∼ 10 servers), relatively easy to implement. The EB network is expected to handle an aggregate amount of data of less than 0.5 Tb/s[2]. A single network switch with 100 Gb/s ports is sufficient. In addition, the Serenity readout boards can be programmed in order to implement a first hardware selection, which could reduce the data flow to the EB, i.e the computing requirements.

The size of the computing farm (EFF) for the online selection of the events can be estimated once knowing the latency of the selection algorithm needed to process an event. The scale of the farm depends on the latency according to the steady state equation. Since the input frequency is 40 MHz, in order to keep n_{CPU} relatively small, we require the processing latency to be of the order of about 10 μs per event:

$$n_{\text{CPU}} \sim \text{latency} \times \text{input frequency} \sim 10\,\mu\text{s} \times 40\,\text{MHz} = 400\,\text{CPU core}. \tag{2.46}$$

The selection criterion cannot simply be based on the hits multiplicity of hits (i.e. at least 2 hits per module produced by scattered μ and e), as it has been shown by simulations. Each track generates 6 stubs per station, i.e. 12 stubs per μe elastic scattering event. The distribution of the registered stubs per station, per passing muon, is shown in fig. 2.16. The probability of obtaining more than 10 stubs per module, a conservative assumption, is

---

[1] The factor 2 depends on the need to extend the signals persistence to at least 2 clock cycles (clock gate), as the MUonE electronics cannot be synchronized with the arrival of the muons produced by the SPS protons, which is intrinsically random [14]. On the other hand, the CMS DAQ is synchronous with the collisions of the LHC bunches.

[2] For comparison, LHCb plans for its upgrade ∼ 400 PCs for the Event Building, for a total of about 30 Tb/s to manage [49]

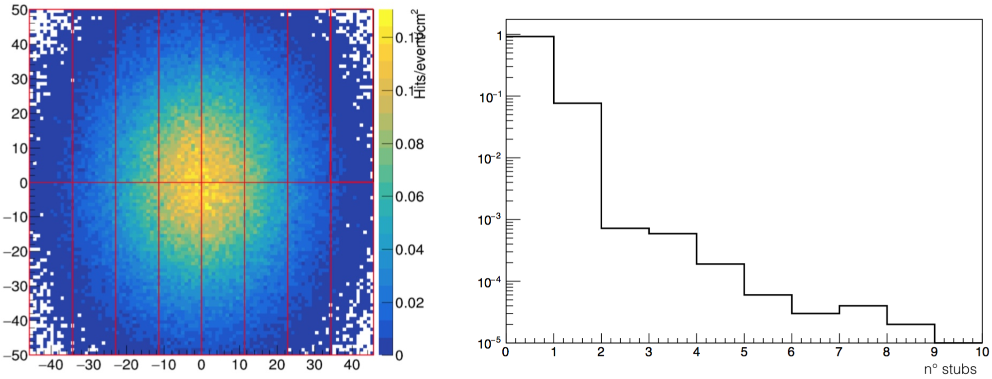

Figure 2.15: (Left) Spot on the sensors plane of the M2 muon beam from GEANT4 simulation. The red boxes are the area readout by the different CBC3 ASIC (8 per side). (Right) Stub fraction on the hottest ASIC [14].

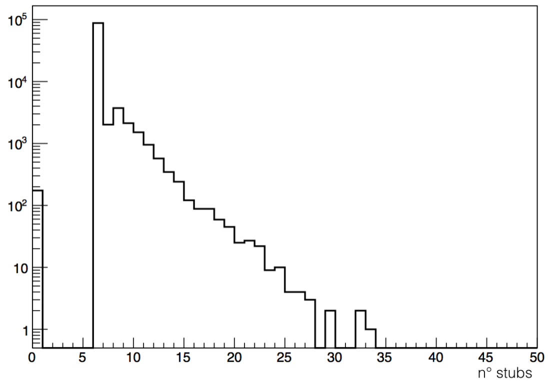

Figure 2.16: Number of stubs per station per passing muon.

estimated by the distribution around 6%. Considering a pileup of 3 events per clock, the probability becomes 18% per station. In the case of the complete detector, on 40 modules the probability of getting this patterns turns to certainty.

In addition, the expected elastic event rate (signal) per module of ~ 7 kHz (sec. 2.4.2) is much lower than the total expected rate:

$$rate\,(\text{signal} + \text{background}) \sim 40\,\text{MHz} \times 18\% \sim 7\,\text{MHz/station}. \qquad (2.47)$$

The signal-to-background ratio is of the order of 1:1000. More sophisticated criteria have to be studied to select interesting events, based on the track χ^2 and on the vertex constraint in the target. The challenge will be to design efficient filters on the signal, with low latency.

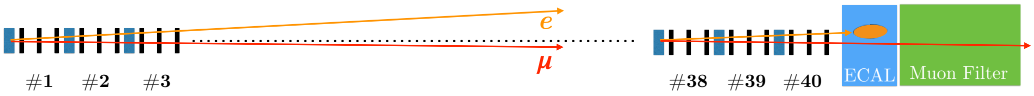

Figure 2.17: Use of the electromagnetic calorimeter (ECAL), assuming 40 tracking stations. The yellow tracks belong to high angle electrons ($\theta_e \gtrsim$ 20-25 mrad).

2.5.3 Preliminary considerations about the calorimeter

The calorimeter is needed to perform the particle ID at small angle, around 2-4 mrad, where electrons and muons cannot been distinguished relying solely on the emission angles [14].

An homogeneous ECAL has been proposed placed downstream all the tracker stations, composed of lead tungstate ($PbWO_4$) crystals, similar to those used by the CMS electromagnetic calorimeter, whose performances are described in [32]. Crystals (section 2.5 x 2.5 cm^2, 23 cm long, 26 X_0) can be readout by solid state sensors (SiPM or APD).

With a surface of 1 m × 1 m, the calorimeter can cover an angular acceptance of about 30 mrad for the closest 15 stations (from station 25 to 40, see fig. 2.17):

$$z = \frac{\Delta y}{\theta_e} = \frac{0.5\,\text{m}}{0.03\,\text{rad}} \sim 15\,\text{m} \tag{2.48}$$

where Δy is half of the transverse size and z is the distance from the calorimeter surface. For an angular acceptance of few mrad, relevant for the PID, the same surface can largely cover the entire detector acceptance. With this surface the calorimeter can been used also to registerer redundant informations useful to study the energy response of the closest tracking stations and account (and correct) for possible background effects all the other stations. The use of a calorimeter of such area (1x1 m^2), with relative readout system, is therefore still under study, as reported in the Letter of Intent [14].

2.6 Theory of $\mu e \to \mu e$ elastic scattering

2.6.1 Kinematics of elastic scattering

The electron is at rest in the laboratory system, so that $|\vec{p}_e| = 0$. The invariant s is set by the energy E_μ of the incoming muons. For an elastic scattering the squared transferred 4-momentum t can be expressed as (with

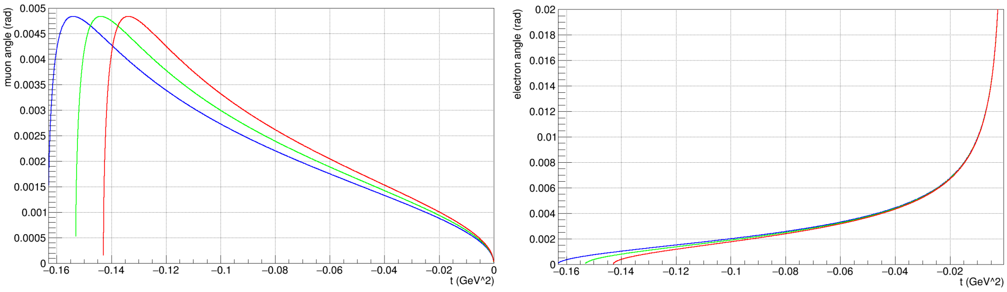

Figure 2.18: Correlations between muon scattering angle and t (left) and between electron scattering angle and t (right) for three different energies: 150 GeV (red), 160 GeV (green), 170 GeV (blue).

the notations of eq. (2.14)):

$$\begin{aligned} t_{\mu\mu} &\equiv (p_1 - p_3)^2 = 2m_e(E'_\mu - E_\mu) \\ t_{ee} &\equiv (p_2 - p_4)^2 = 2m_e(m_e - E'_e). \end{aligned} \tag{2.49}$$

Because of 4-momentum conservation, at leading order it must be:

$$t_{\mu\mu} = t_{ee} = t. \tag{2.50}$$

For a given beam energy E_μ and a given value of t, any other kinematic variable is uniquely defined, namely E'_μ,E'_e and θ_μ,θ_e energies and angles of the scattered particles:

$$E'_\mu = \frac{2m_e E_\mu + t}{2m_e} \tag{2.51}$$

$$E'_e = \frac{2m_e^2 - t}{2m_e}. \tag{2.52}$$

$$\cos\theta_\mu = \frac{2m_e^2(t - 2m_\mu^2) + 2m_e E_\mu(2m_e E_\mu + t)}{\sqrt{\lambda(s, m_e^2, m_\mu^2)}\sqrt{\lambda(s + t, m_e^2, m_\mu^2)}} \tag{2.53}$$

$$\cos\theta_e = \frac{-2m_e(E_\mu + m_e)t}{\sqrt{\lambda(s, m_e^2, m_\mu^2)}\sqrt{t^2 - 4m_e^2 t}}. \tag{2.54}$$

Figure 2.18 shows the electron and muon scattering angles as a function of t as defined in eqq. (2.53) and (2.54): one can notice that the higher the transferred momenta the smaller the electron scattering angles.

It is useful to express the energies in the laboratory frame as a function of the observable scattering angles. For the muon one obtains:

$$E'_\mu(\theta_\mu) = \frac{a \pm b\, p_\mu^2 \cos\theta_\mu}{d}, \tag{2.55}$$

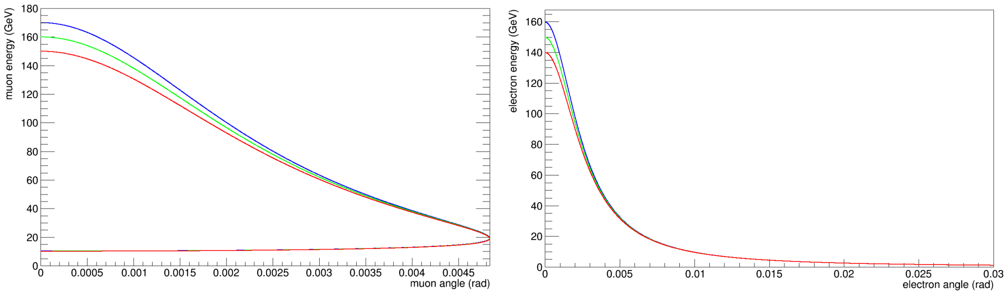

Figure 2.19: Correlations between the energies and the angles for muon (left) and electron (right) for three different energies: 150 GeV (red), 160 GeV (green), 170 GeV (blue).

where

$$\begin{aligned} a &\equiv (E_\mu + m_e)(m_\mu^2 + m_e E_\mu) \\ b = b(\theta_\mu) &\equiv \sqrt{m_e^2 - m_\mu^2 \sin^2\theta_\mu} \\ d = d(\theta_\mu) &\equiv (E_\mu + m_e)^2 - p_\mu^2 \cos^2\theta_\mu . \end{aligned} \tag{2.56}$$

The corresponding relation for the electron is:

$$E_e'(\theta_e) = m_e \frac{(E_\mu + m_e)^2 + p_\mu^2 \cos^2\theta_e}{(E_\mu + m_e)^2 - p_\mu^2 \cos^2\theta_e} = m_e \frac{1 + r^2\cos^2\theta_e}{1 - r^2\cos^2\theta_e} \tag{2.57}$$

with

$$r \equiv \frac{p_\mu}{E_\mu + m_e} = \frac{\sqrt{E_\mu^2 - m_\mu^2}}{E_\mu + m_e}. \tag{2.58}$$

E_μ' and E_e' as a function of the respective scattering angles $\theta_m u$, θ_e are shown in fig. 2.19.

The relation (2.57) can be reverted as:

$$\cos\theta_e = \frac{1}{r}\sqrt{\frac{E_e' - m_e}{E_e' + m_e}}. \tag{2.59}$$

Since $m_e < m_\mu$ the eq. (2.56) shows that

$$\sin\theta_\mu < \frac{m_e}{m_\mu} \quad \to \quad \theta_\mu^{max} = \arcsin\frac{m_e}{m_\mu} \sim 4.83\,\mathrm{mrad} \tag{2.60}$$

so there is a maximum scattering angle θ_μ^{max} for the muon, determined by the ratio between the electron and muon masses.

The physical meaning of the sign ambiguity of eq. (2.55) is clear from fig. 2.19: for each muon angle there are two possible muon energies, corresponding to two different electron scattering angles, expect for the peak.

The electron kinematics does not show this feature: there is a biunivocal relation between the electron energy E'_e and the corresponding scattering angle θ_e.

The relation (2.57) implies there is a maximum energy for the scattering electron, corresponding to $\cos\theta_e = 1$, i.e. $\theta_e = 0$:

$$E_e^{max} = m_e \frac{(E_\mu + m_e)^2 + p_\mu^2}{(E_\mu + m_e)^2 - p_\mu^2}. \tag{2.61}$$

For $E_\mu = 150$ GeV, $E_e^{max} \sim 139.8$ GeV corresponding to a squared momentum transfer $|t| \sim 0.1429$ GeV^2.

2.6.2 Differential cross section

Experimental observables are the scattering angles (θ_μ, θ_e), so it is useful to determine the angular differential cross sections expressed as their function. They can be obtained analytically from the differential cross section express as a function of t (eq. 2.15).

The differential cross section as a function of the electron scattering angle is given by:

$$\frac{d\sigma}{d\theta_e} = \frac{d\sigma}{dt}\frac{dt}{d\theta_e}. \tag{2.62}$$

From the expression of t in lab frame (2.49) and the expression of the energy of scattering electron (2.57), we obtain:

$$\begin{aligned} t = t_{ee} &= 2m_e\left(m_e - E'_e(\theta_e)\right) \\ &= 2m_e^2\left(1 - \frac{1 + r^2\cos^2\theta_e}{1 - r^2\cos^2\theta_e}\right) \\ &= \frac{4m_e^2 r^2\cos^2\theta_e}{r^2\cos^2\theta_e - 1}. \end{aligned} \tag{2.63}$$

So the differential cross section in the electron scattering angle is (fig. 2.20):

$$\frac{d\sigma}{d\theta_e} = \frac{4m_e^2 r^2 \sin 2\theta_e}{\left(r^2\cos^2\theta_e - 1\right)^2}\frac{d\sigma}{dt}. \tag{2.64}$$

In the case of θ_μ there is a complication due to the double value function, as already seen. The differential cross section in θ_μ shown in fig. 2.20 can be calculated as

$$\frac{d\sigma}{d\theta_\mu} = \frac{d\sigma}{dt}\frac{dt}{d\theta_\mu}. \tag{2.65}$$

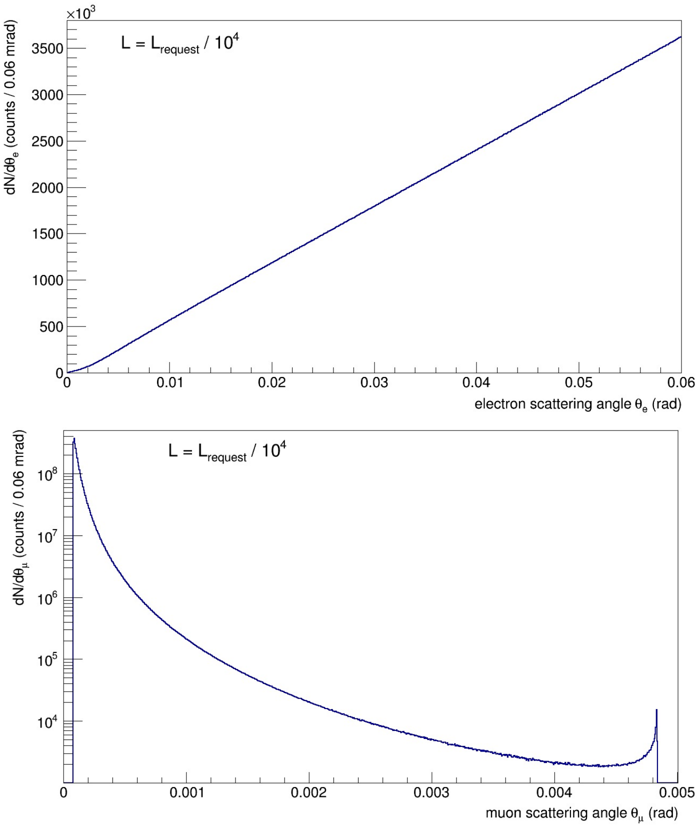

Figure 2.20: Differential cross section at leading order as a function of θ_e (top) and θ_μ (bottom). Here the integrated luminosity L is $1.5 \cdot 10^3$ nb^{-1}, i.e. 10^4 times less the requested luminosity determined in sec. 2.4.

Here we need the expression of t as a function of θ_μ of eq. (2.49) and $E'_\mu(\theta_\mu)$ of eq. (2.55):

$$\begin{aligned} t = t_{\mu\mu} &= 2m_e\left(E'_\mu(\theta_\mu) - E_\mu\right) \\ &= 2m_e\left(\frac{a \pm b\,p_\mu^2\cos\theta_\mu}{d} - E_\mu\right). \end{aligned} \tag{2.66}$$

Coefficients a, $b = b(\theta_\mu)$, $d = d(\theta_\mu)$ are given in the eq. (2.56). The θ_μ derivative of (2.66) in θ_μ is:

$$\begin{aligned} \frac{dt}{d\theta_\mu} = \frac{\pm 2m_e p_\mu^2 \sin\theta_\mu}{d^2 b} &\left\{\mp 2ab\cos\theta_\mu + p_\mu^2\cos^2\theta_\mu(m_\mu^2 - m_e^2)\right. \\ &\left. +(E_\mu + m_e)^2\left[m_\mu^2(1 - 2\cos^2\theta_\mu) - m_e^2\right]\right\}. \end{aligned} \tag{2.67}$$

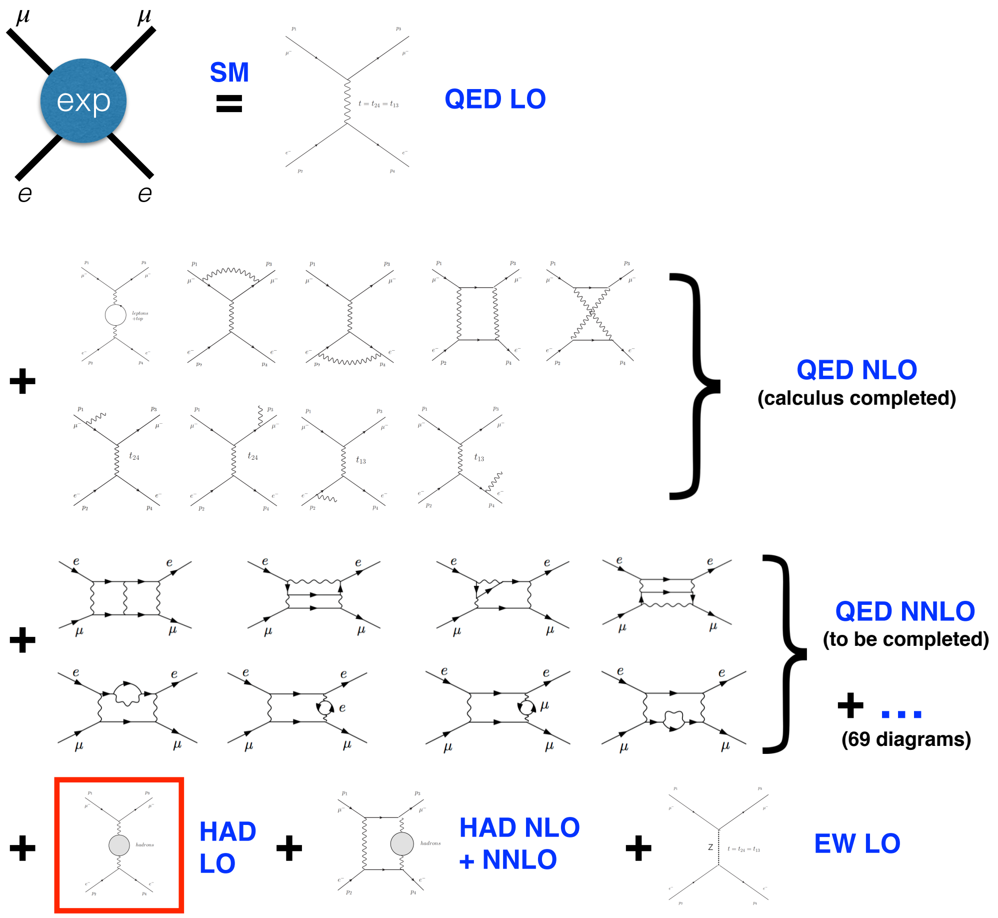

Figure 2.21: Radiative corrections scheme within Standard Model to the μe scattering (from a lecture of M. Passera). The red box includes the contribution that MUonE plans to determine, from the scattering measurement.

2.6.3 Higher-order corrections

The theorist community is engaged in a significant effort aiming to determine all the necessary corrections and the related errors of higher order contributions to the μe elastic scattering.

In the SM, the cross section σ_{exp} can be calculated with perturbative method that involves a large number of terms. It can be schematically represented as it is shown in fig. 2.21:

$$\begin{aligned}\sigma_{exp} \propto\ & \mathrm{LO\,(QED)} + \mathrm{NLO\,(QED)} + \mathrm{NNLO\,(QED)} \\ & + \mathrm{NLO\,(EW)} + \mathrm{NLO\,(had)} + \mathrm{NNLO\,(had)}\end{aligned} \tag{2.68}$$

where LO corresponds to the Born level in eq. (2.15), NLO and NNLO (QED)

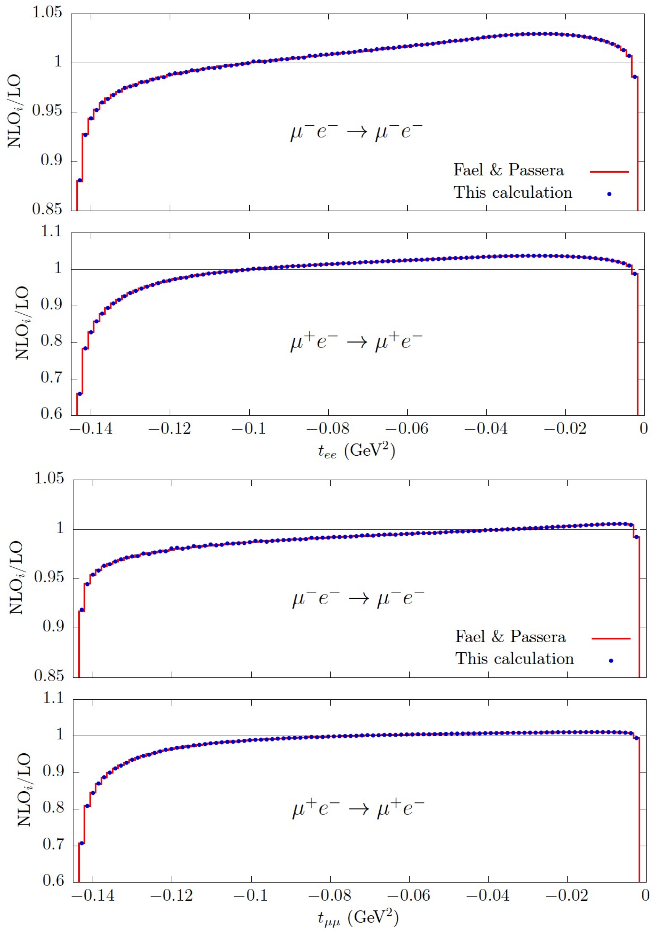

Figure 2.22: Ratio of the NLO and LO cross section in QED of the $\mu^- e^- \to \mu^- e^-$ (first and second upper panels) and $\mu^+ e^- \to \mu^+ e^-$ (third and fourth panels) process, as a function of t_{ee} and $t_{\mu\mu}$ [41].

are the leptonic contributions, NLO (EW) is a small electroweak term. The two last terms are the hadronic contributions: the first one NLO (had) is exactly what MUonE aims to determine by subtraction of the others.

Some of the NLO (QED) contributions are due to vacuum polarization process with one and two loops: as we already said, their effects are accounted by using the effective charge, as an overall factor by the replacement of α with $\alpha(t)$ in the LO cross section.

Recently the full set of the NLO QED corrections has been calculated without any approximation [41]. It has been developed a fully differential Monte Carlo code. The authors also computed the full set of NLO (EW) corrections.

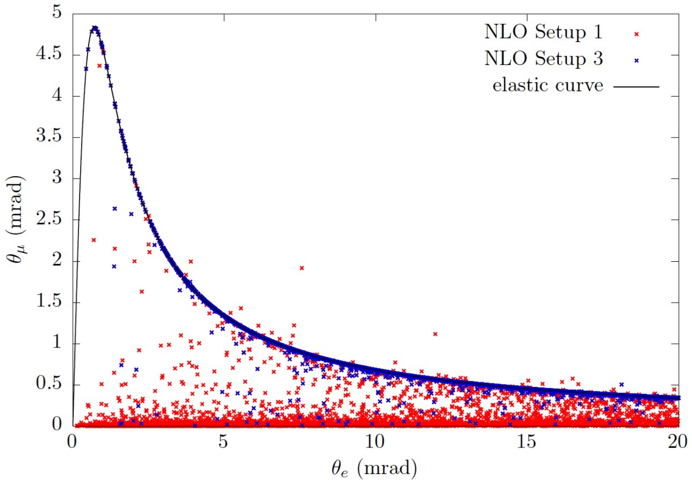

Figure 2.23: The correlation between θ_μ and θ_e for the process at LO (elastic curve) and NLO QED (points), for different selection criteria [41].

The results of these calculations are shown in fig. 2.22. They show the ratio of the NLO (QED) differential cross section with respect to the LO (QED), for both the process $\mu^\pm e^- \to \mu^\pm e^-$, as a function of the squared momentum transfer t_{ee} and $t_{\mu\mu}$ in the electron and muon legs respectively. They are no more the same, because of the radiative process.

Compared to the leading order, the NLO contributions to the cross section are of the order of 5-10% at low electron angle, i.e. they play an important role. In order to study their effects on the measurement strategy, an intensive work with MC simulations has begun, in particular the analysis of the theoretical and experimental cuts, which are necessary to select the signal region of interest.

Figure 2.23 shows the results of a first study perform to evaluate the effect of a cut in acoplanarity for the selection of the elastic events. In this figure, there are not experimental effects (multiple scattering, intrinsic resolution) or backgrounds. The dispersion of the events is due to the radiative corrections: the elastic region therefore is subject to a migration of counts because of NLO, especially towards the muon low angle.

Both the angular distributions of muon and electron will be used the measurement. Muon is more robust, because is subjected to a lower radiation.

This is an important aspect as far as the sensitivity to the running is concerned. The sensitivity can be measured as [14, 41]:

$$R_i = \frac{d\sigma_i(\Delta\alpha_{\text{had}}(t) \neq 0)}{d\sigma_i(\Delta\alpha_{\text{had}}(t) = 0)}. \tag{2.69}$$

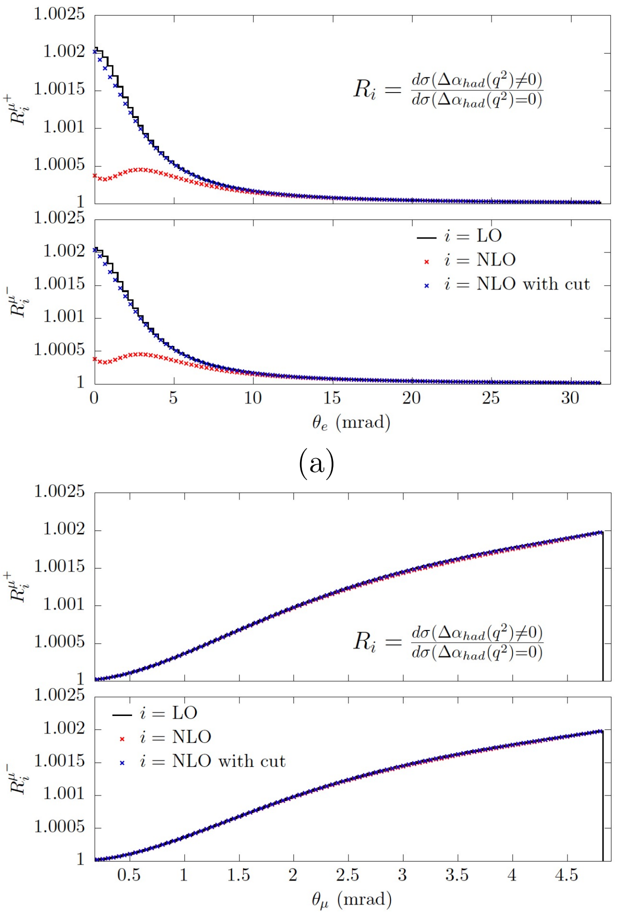

(a)

(b)

Figure 2.24: Sensitivity to the hadronic running as defined in eq. (2.69) as a function of θ_e (a) and θ_μ (b) [41].

the ratio between the cross section with and without the hadronic correction to the running of α.

Figures 2.24 show how the QED corrections affect the ratio R_i for different selection criteria (for the two processes $\mu^\pm e^- \to \mu^\pm e^-$).

In the absence of elasticity cuts, the ratio for the electrons is strongly affected by the QED radiation, especially in the region of small angles, where is the highest sensitivity to the running. This sensitivity is largely recovered by applying an acoplanarity cut, that removes most of the contribution of the radiative processes. On the other hand, the muon ratio appears to be robust to the the radiative corrections and applied cuts.

It is important to note that the distribution of the hadronic running as a function of θ_e is strongly peaked: this naturally makes two regions on θ_e,

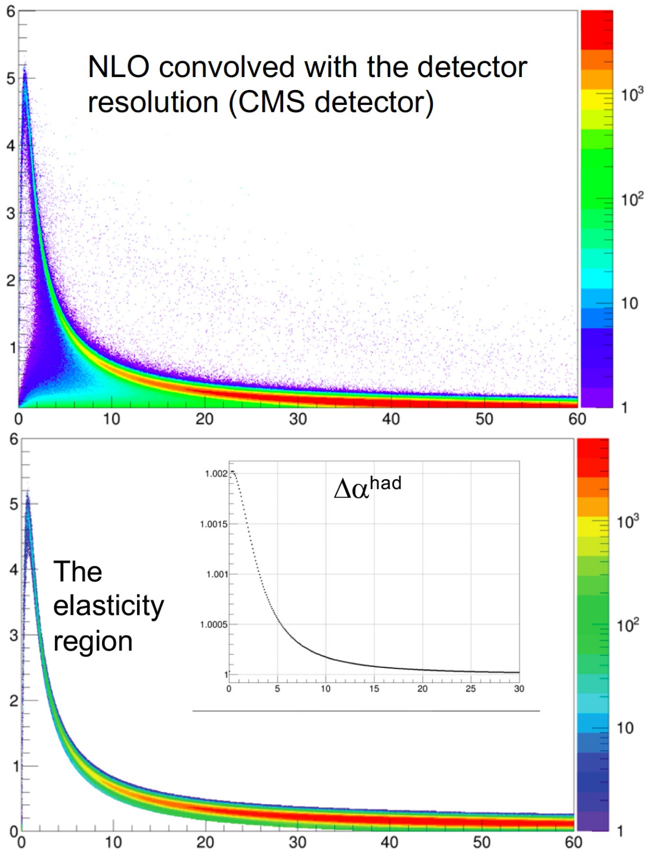

Figure 2.25: Correlation plots $\theta_\mu\theta_e$ in mrad, with the NLO QED effects and experimental smearings. (Top) Without and (bottom) with a cut around the elasticity curve to select the signal.

at high and low q^2, where $\Delta\alpha_{had}$ becomes less than 10^{-5} for $\theta_e \gtrsim 20$ mrad. There is therefore the possibility that the low transferred momenta region can be used as a "normalization" region, i.e. an area where the effect to be measured is less than the required precision, so that it can be considered negligible. This is an important aspect currently under study, as it would allow a better control of some systematics.

Figure 2.25 show the detector resolution on top of MC NLO. The selection of the elasticity region obtained taking into account the effect of detector resolution preserve about 95% of signal events and allows to recover the full sensitivity to the hadronic running.

The calculation of the NNLO QED corrections is in progress [51, 52, 53, 54]. The expected contribution should be of the order of one percent or less. In fig. 2.21, some of the NNLO diagrams are shown.

Chapter 3

Experimental effects and simulations

We have seen that the μe elastic scattering in MUonE will take place in matter, since the scattering centers are the target atomic electrons. Particles crossing the target undergo several interaction processes. We focused the attention on multiple Coulomb scattering (MCS), ionization and bremsstrahlung. MCS is particularly important as it acts as a randomizer of the scattering angles, breaking the exact kinematic correlations between the muon and electron scattering angles.

3.1 Multiple Coulomb scattering

When a charged particle traverses a layer of matter because of MCS it is deflected from the original path (often without appreciable energy loss). The dominant contribution to the MCS is due to the nuclei. The effect of the atomic electrons is the screening of the nuclear electromagnetic field [55]. A detailed theory of the MCS, accounting for the effects of the nuclear potentials and electronic screening, is rather complicated [56, 57, 58]. A great help in evaluated MCS effects came from the Highland theory [59]. However, the only way to treat multiple scattering precisely is with Monte Carlo simulations [60, 61].

Particle propagation through the material is a stochastic process: charged particles follow a random walk, undergoing a very large number of elementary Coulomb scattering with nuclei. As a consequence the direction and the position are random variables. The statistical properties are directly measurable quantity.

For particles moving along the z-axis, perpendicular to a target, MCS can

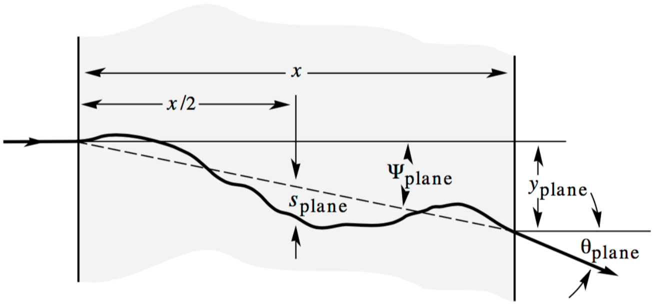

Figure 3.1: Quantities used to describe multiple Coulomb scattering. The particle is incident in the plane of the figure [26].

be measured in two perpendicular planes, xz and yz, by two random variables: the projected angle $\theta_{plane,x}$ by the lateral displacement x, and $\theta_{plane,y}$ by the lateral displacement y (fig. 3.1). In a layer of thickness d, it turns out to be that for relatively small deflections the probability density function of the projected scattering angles θ_{plane} can be described by a gaussian distribution:

$$f(\theta_{plane}) = \frac{1}{\sqrt{2\pi}\theta_{\text{MS}}} \exp\left(-\frac{\theta_{plane}^2}{2\theta_{\text{MS}}^2}\right) \tag{3.1}$$

where the standard deviation

$$\theta_{\text{MS}} = \sqrt{<\theta_{plane}^2>} = \theta_{plane}^{rms} \tag{3.2}$$

is defined by the Highland-Molière formula [26]:

$$\theta_{\text{MS}} = \frac{13.6}{E}\sqrt{\frac{d}{X_0}}\left(1 + 0.038\log\left(\frac{d}{X_0}\right)\right). \tag{3.3}$$

Here E is the particle energy, d the layer thickness and X_0 the radiation length of target material. The MCS is a white noise, as it is unbiased, i.e. the average angular distribution is zero, $<\theta_{plane}>= 0$, and statistically it increases the width of the beam angular distribution by θ_{MS}. This formula (historically obtained as a fit to the [...]) is considered accurate to $\sim$ 10% or better, for $10^{-3} < d/X_0 < 100$. This is a key relation to estimate multiple scattering effects, although as a first approximation. Figure 3.2 shows a result we obtained in a test beam (performed in 2017 [8]), which confirms the behavior of θ_{MS} of eq. (3.3) with the thickness d. Effects of the material are all included in the radiation length X_0, whose approximated value is

$$X_0 \approx \frac{180A}{Z^2}\,\text{g/cm}^2. \tag{3.4}$$

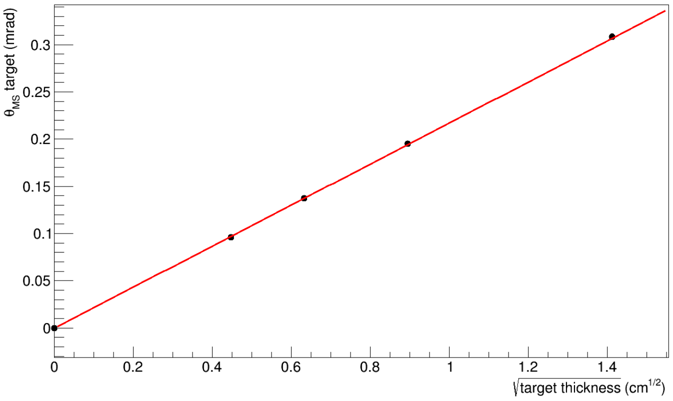

Figure 3.2: Multiple scattering angles as a function of the target thickness, from our 2017 test beam data.

MCS is linearly dependent on Z of the material, and on the inverse of the particle energy. The inverse dependence with the energy is due to the Rutherford cross-section, going as $1/p^2$. The logarithmic correction has been determined with the fit of data sets available to Highland [59].

The probability density function of θ_{space}, i.e. the unprojected angular distribution, is given by:

$$f(\theta_{space}) \equiv f(\theta_x, \theta_y) = f(\theta_x) \cdot f(\theta_y) = \frac{1}{2\pi\theta_{\mathrm{MS}}^2} \exp\left(-\frac{\theta_{space}^2}{2\theta_{\mathrm{MS}}^2}\right). \tag{3.5}$$

Because of the symmetry of the scattering processes with respect to the azimuth angle ϕ the projections of the deflection angles in the zx and zy planes are uncorrelated and identically distributed, that is:

$$< \theta_x^2 > = < \theta_y^2 > = \frac{1}{2} < \theta_{space}^2 > \quad \rightarrow \quad \theta_{space}^2 \approx \theta_x^2 + \theta_y^2. \tag{3.6}$$

It can be shown that the distributions of the x and y variables, corresponding to the hits coordinates measured by a tracker, are related to θ_{plane} by:

$$< y_{plane}^2 > = \frac{1}{3} d^2 < \theta_{plane}^2 > = \frac{1}{3} d^2\, \theta_{\mathrm{MS}}^2 \quad \rightarrow \quad y_{plane}^{rms} = \frac{1}{\sqrt{3}} d\, \theta_{\mathrm{MS}}. \tag{3.7}$$

Note that the lateral displacement is reduced by a factor $\sqrt{3}$ with respect to the track projection $d \times \theta_{\mathrm{MS}}$. To prove this relation we built up a toy-MC, whose results are presented in the appendix A.1.

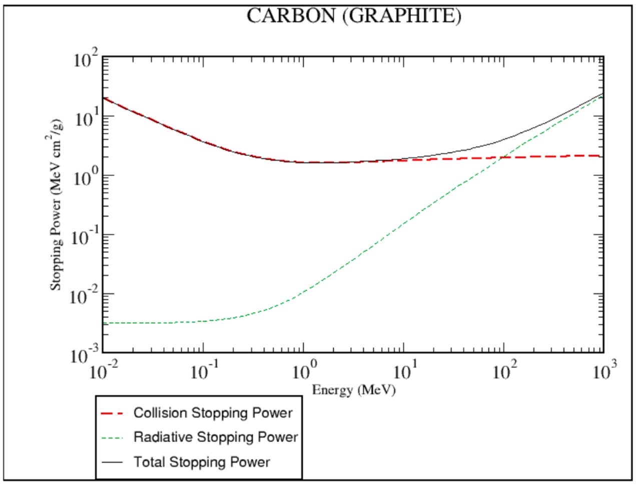

Figure 3.3: Stopping power of electrons in Graphite [62].

3.2 Energy loss for high energy electrons and muons

The probability of large scattering angles in MCS are small and are expected because of the Rutherford cross section [26]. The energy loss due to the bremsstrahlung adds large contribution to the tails of the angular distribution, amounting to about 5-10%.

3.2.1 Electrons

Electrons energies involved in the μ-e elastic scattering vary from few GeV up to about 140 GeV, depending on the energy of the M2 muon beam. In this energy range electrons lose energy by the emission of photons in the electric field of the atomic nucleus. For the electron energies, in the range of interest, the energy loss by bremsstrahlung is by far the dominating process. This energy loss is proportional to the electron energy, while the ionization loss depends logarithmically on it. Figure 3.3 shows the energy loss per unit length of electrons in graphite.

The energy loss per unit length due to the bremsstrahlung is:

$$-\frac{dE}{dx} = k\frac{E}{X_0} \tag{3.8}$$

with an explicit dependence on the radiation length X_0, in turn related to

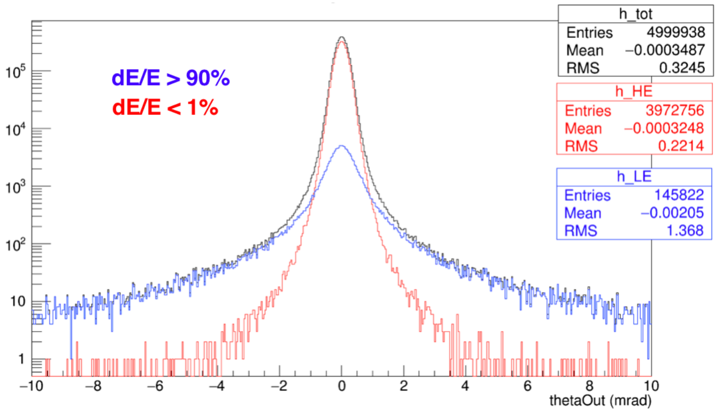

Figure 3.4: Angular deflection of 12 GeV electrons on 8 mm graphite: result of a GEANT4 simulation. In red, the electrons that have lost less than 1% of their initial energy, in blue those that have lost more than 90%.

the material density, the atomic weight W and the atomic number Z:

$$X_0 \propto \frac{W}{\rho\, Z^2} \text{ (cm)}. \tag{3.9}$$

Figure 3.4 shows the result of a GEANT4 simulation. The core of the distribution is due to multiple scattering events occurring without significant energy loss, while the long tails are due to electrons that have lost much of their energy by bremsstrahlung ($dE/E \gtrsim 90\%$). The core of the distribution covers about 90% of the integral and within a few percent can be described by a gaussian. Instead tails instead do not show a gaussian profile.

3.2.2 Muons

The emission probability of bremsstrahlung photons is dependent on the mass m of the particle and is proportional to $1/m^2$. It is not relevant for muon energies up to several hundreds GeV. Muons of these energies can be considered as minimum ionizing particles. The mean stopping power for high-energy muons in a material can be described by [63]:

$$< dE/dx >= a(E) + b(E)E, \tag{3.10}$$

where E is the total energy, $a(E)$ is the electronic stopping power, and $b(E)$ is a term accounting for radiative processes, namely bremsstrahlung, pair production and photonuclear interactions:

$$b(E) \equiv b_{brems}(E) + b_{pair}(E) + b_{nucl}(E). \tag{3.11}$$

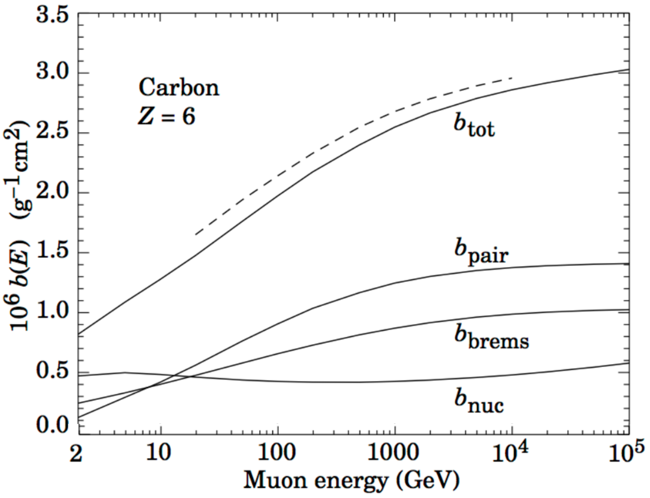

Figure 3.5: Contributions to the muon radiative energy loss as a function of the muon energy [63] according to eq. (3.10).

$a(E)$ and $b(E)$ are slowly varying functions of E. For $E \lesssim 100$ GeV, $b(E)E$ is less than 1% of $a(E)$. Figure 3.5 shows the role of the different radiative muon processes.

The angular deflection for high-energy muons does not present long tails that are typical of electron angular distributions. High energy muons allow to align the detector and to perform a precise scanning of the apparatus needed to measure the detector angular resolution, as explained in the following chapter.

3.3 Detector angular resolution

Electrons and muons will be tracked by means of silicon detectors. Tracking errors are due to MCS and to the detector intrinsic resolution.

The effect of the intrinsic resolution on the hit detection translates in the angular uncertainty $\Delta\theta_i$ of the reconstructed track as:

$$\Delta\theta_i = \sqrt{2}\,\frac{\sigma_x}{L}, \tag{3.12}$$

where σ_x is the hit detector resolution and L is the length of the tracking station, corresponding to the distance between first and last sensor.

The intrinsic resolution is statistically independent from the resolution effect due to MCS. The detector resolution $\Delta\theta_{det}$ is therefore the sum in

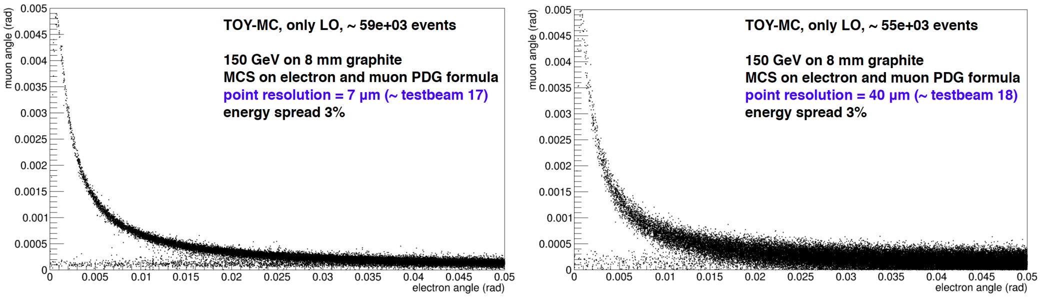

Figure 3.6: Hit resolution comparison for signal events. On the left, the angular correlation between θ_μ and θ_e for $\sigma_x = 7\,\mu$m. On the right the corresponding correlation for $\sigma_x = 40\,\mu$m.

quadrature of intrinsic and multiple scattering:

$$\Delta\theta_{det}(E) = \sqrt{\Delta\theta_i^2 + \theta_{MS}^2(E)}. \tag{3.13}$$

Figures 3.6 show the performance of detectors with different intrinsic resolution[1] of $7\,\mu$m and $35\,\mu$m respectively, for 150 GeV muons colliding on a 8 mm thick graphite target. The resolution effects generate horizontal and vertical counts migrations in the 2D histogram. In particular the vertical migrations, occurring along the muon angle are mainly due to the intrinsic resolution. The intrinsic resolution is relevant for energies greater than 20-30 GeV, depending on the detector material budget.

The resolution model of eq. (3.13) allowed us to develop a fast simulation algorithm used to study the experimental effects on events generated according to the LO (and NLO) cross section (see sec. 3.4). The model includes various experimental effects, as target and trackers multiple scattering, average energy loss in the target, energy spread of the muon beam and intrinsic resolution.

Figures 3.7 show the multiple scattering effect of 2S CMS trackers on the differential LO cross sections. Multiple scattering gives a relevant contribution for high electron and muon angles, where both particles have small energies. The intrinsic resolution of the sensors are included.

The MCS induces a counting migration depending on the shape of the cross section. Event counts accumulate at large angles, where the electron energies are of few GeV, because of the resolution flux due to the detector resolution and the growing of the differential cross section: for a given angular interval, more events migrate from larger angles than from lower ones. In the case of the muon angular distribution, the main effect is in the smearing

---

[1] used in the 2017 and 2018 test beam, as we will discussed in the following chapter.

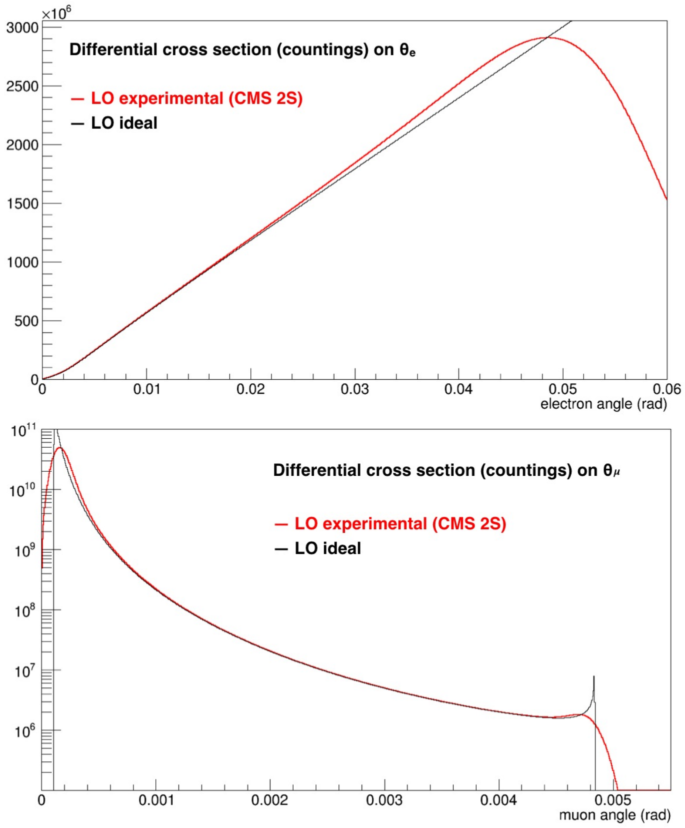

Figure 3.7: The resolution effects on the differential cross sections in the scattering angles θ_e and θ_μ.

of the peak around the maximum $\theta_\mu \sim 4.8$ mrad, where the muon energy is about 20 GeV.

The validity of the resolution model, expressed by the eq. (3.13), has been verified in the 2017 test beam [8].

3.4 Fast simulation

A complete GEANT4 simulation is CPU time consuming. Generate the required large data samples of μe elastic scattering (of the order of 10^{12} events) within a reasonable time interval is prohibitive, even if exploiting farms of several hundreds of servers. To study the detector effects with high statistics, we developed a parametrization of the apparatus response.

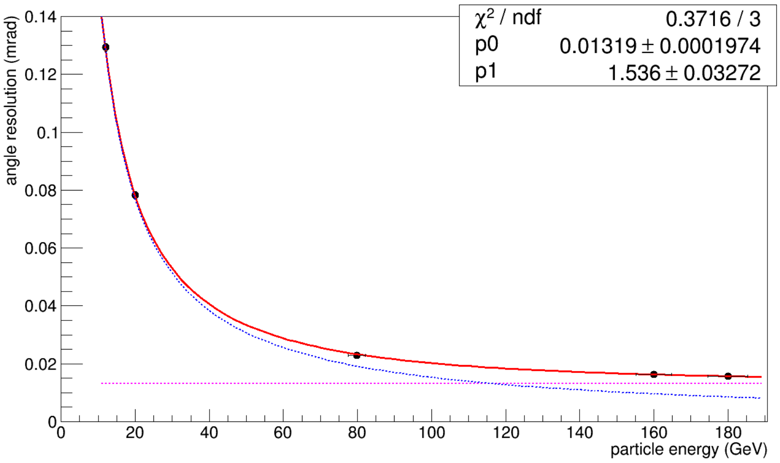

Figure 3.8: Angular resolution as a function of particles energy, as obtained with 2017 test beam data. Fit parameters p0 (in mrad) and p1 (in mrad/GeV) correspond to A and B coefficients in the fit curve (3.14), respectively.

3.4.1 Detector resolution model

Figure 3.8 shows the angular resolution as a function of the particle energy, as measured in the 2017 test beam. Data has been collected with test beam runs with different particle beams: 12 GeV e^- and 20 GeV e^-, 80 GeV π^+, 160 GeV μ^+ and 180 GeV π^+. It shows the width of the gaussian core (90% of the angular deflection distribution) as a function of the particles energy.

Running without target (i.e. without the target MCS effects), made it possible to measure the tracking resolution function at different energies. The fit function:

$$f(E) = \sqrt{A^2 + \left(\frac{B}{E}\right)^2} \tag{3.14}$$

allows to unfold the two resolution effects. The parameters A and B represent the contribution of the intrinsic angular resolution and of the MCS of the tracking apparatus (per unit of energy) respectively. This effective parametric model is a key instrument for the development of the fast simulation, which will be explained in sec. 3.4.2.

As interesting check, the nominal intrinsic resolution turns out to be:

$$\sigma_i = \frac{\sqrt{2}\,\Delta x}{L} \sim \frac{\sqrt{2} \times 7\,\mu\text{m}}{900\,\text{mm}} \sim 0.011\,\text{mrad}, \tag{3.15}$$

to be compared to the fit result $A = 0.013$ mrad obtained from data.

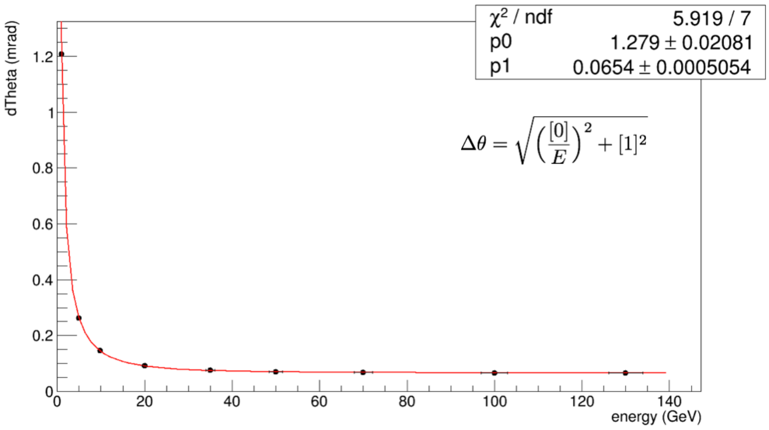

Figure 3.9: Angular resolution as a function of the particle energy.

To validate the parametric model, we performed a GEANT4 resolution scanning for electron energies varying between 1 and 130 GeV. The tracking algorithm, developed for the analysis of test beams data, has been used to reconstruct the simulated events with a length of a tracking station of 50 cm.

Figure 3.9 shows the result of the fit. The resulting fit parameters are:

$$\begin{aligned} A &= p1 = \Delta\theta_i = \sqrt{2}\,\frac{\sigma_i}{L} = \sqrt{2}\,\frac{90\,\mu\mathrm{m}/\sqrt{24}}{40.2\,\mathrm{cm}} \sim 0.065\,\mathrm{mrad}, \\ B &= p0 = \theta_{MS}(1\,\mathrm{GeV}) = 13.6\sqrt{\frac{4\cdot 300\,\mu\mathrm{m}}{X_0(\mathrm{Si})}}\left(1 + 0.038\log\frac{4\cdot 300\,\mu\mathrm{m}}{X_0(\mathrm{Si})}\right) \\ &\sim 1.28\,\mathrm{mrad\,GeV} \end{aligned} \tag{3.16}$$

The simulation confirms the validity of the parametrization.

The complete detector resolution model requires to consider the effect of the target. The parameterization in this case contains $2+1$ parameters:

$$f(E) = \sqrt{A^2 + \left(\frac{B}{E}\right)^2 + \left(\frac{C}{E}\right)^2}, \tag{3.17}$$

where A and B are related to the tracking resolution, while C is due to the multiple scattering in the target, calculated assuming the average collision depth of half the target thickness (uniform depth scattering probability).

Figure 3.10 shows the 6 modules configuration, corresponding to the CMS detector used for the simulation. Figure 3.11 shows the impact of the target material budget in the resolution model. The effect of the detector material budget and of the target are comparable.

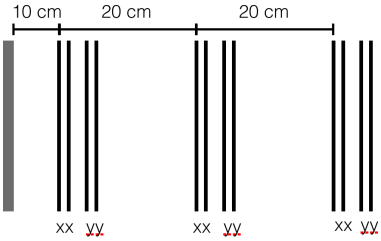

Figure 3.10: CMS 2S module with 2 sensors per view with $L = 50$ cm used in the simulation.

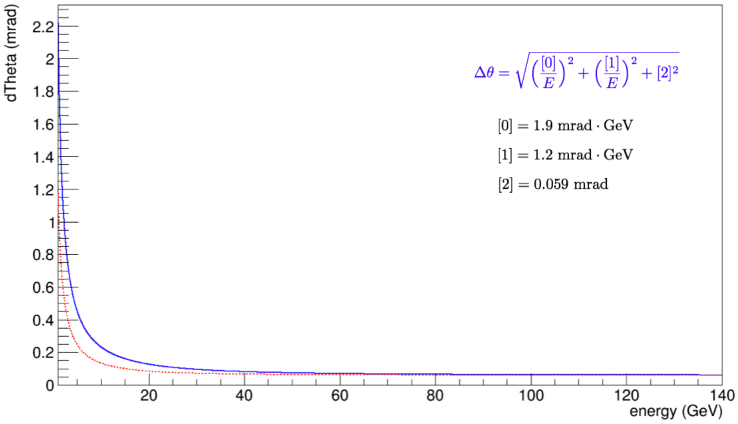

Figure 3.11: Angular resolution of a CMS module: in red and blue the result obtained without and with the target.

3.4.2 The algorithm

The analytic resolution model can be easily interfaced to the LO scattering generator and the recently available NLO generator, to produce the required simulated events in rather a short time. For these studies at large statistics, we have used the computing farm of LHCb Bologna.

Figure 3.12 shows the events distribution generated (in about 3 hours) with the LO cross section generator. The running of the electromagnetic coupling $\alpha(t)$ has been considered. It has been calculated using the routine of prof. F. Jegerlehner [1]. The LO algorithm works similarly to the toy-MC but more efficiently. The main steps of the algorithm used to implement the simulation code are:

- fine sampling of the differential cross section as a function of the electron scattering angle, up to the maximum generation angle of 60 mrad;
- determination of the kinematics variable for the accompanying muon;

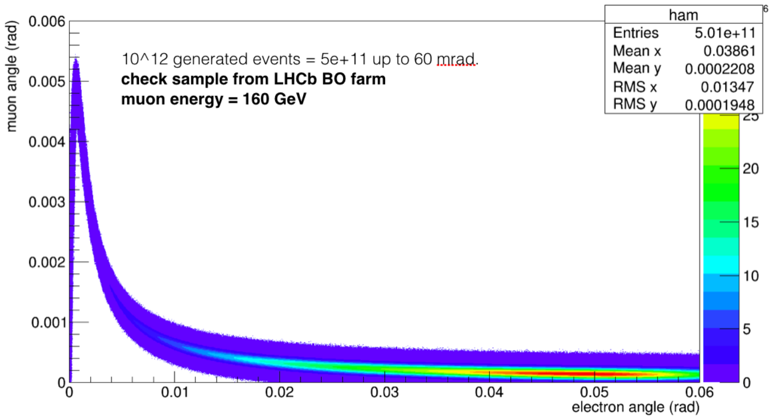

Figure 3.12: Scatter plot θ_μ-θ_e generated with the fast simulation.

- calculation of $t = q^2$, and the corresponding value of $\alpha(t)$;
- smearing of the observable angles, according to the resolution model of eq. (3.17).

The maximum generation angle plays an important role since due to the resolution it creates distortions of the angular spectrum at high angles. However, a trade-off between accuracy of the model and CPU time is needed. Since of the cross section grows linearly with the electron angle, it is necessary to limit the maximum angle.

Figure 3.13 shows two examples obtained cutting the generation of the events at 50 and 60 mrad. Differences of the order of 1% appears with the cuts at 30-35 mrad in the angular distribution, with respect to the case of a cut applied at 100 mrad. The cut at 60 mrad ($E_e > 280$ MeV) has been chosen to consider the electron angular range up to 40 mrad. With this choice the generation efficiency is of about 60%, i.e. the rest of the events produced at high electron angles are useless. The fast-MC idea opened the way for detailed studies to determine a_μ^{HLO}.

3.4.3 Preliminary studies on CMS 2S trackers

We are currently performing studies to assess the performance of a CMS sensors based detector, which has been described in the previous chapter, and to optimize the detector geometry of the final tracker stations. We aim to evaluate the performance with high statistics of this implementation of the MUonE detector, considering the hit resolution of 18 μm and the material budget of the double Silicon layers foreseen for a single CMS 2S

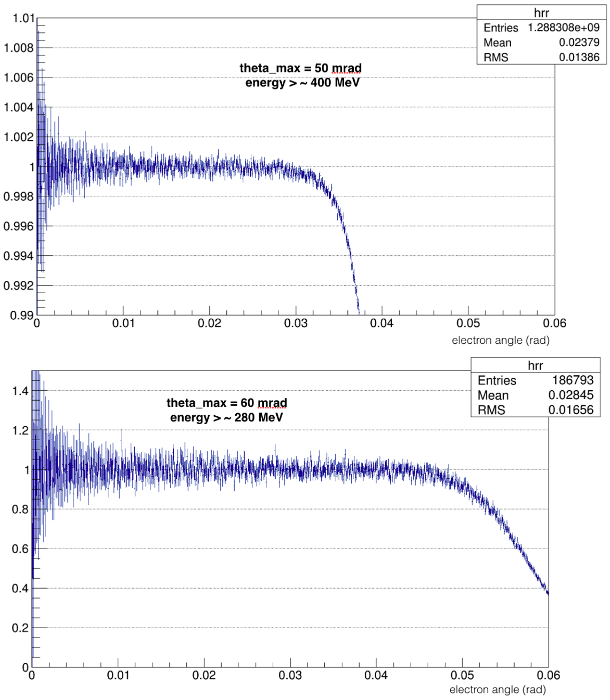

Figure 3.13: Ratio between cross sections with experimental effects for different maximum generated angles, 50 mrad (top), 60 mrad (bottom) with respect to the case of 100 mrad.

module, amounting to $2 \times 300\,\mu$m. We have assumed a length of the station of $L = 50$ cm. Assuming here a measure arm of a station of $L = 50$ cm.

Figures 3.14 show some first high statistics results about the comparison between the CMS trackers and an ideal solution with Si sensors of intrinsic resolution of 10 μm and single layers per view of thickness of 300 μm. In fig. 3.14(top) is shown the ratio of the LO cross sections with and without the resolution effects (MCS and intrinsic resolution). The impact of the experimental resolution on the cross section is evident: at high electron angles there is a counts accumulation of the order of $+2\%$ at $\theta_e = 30$ mrad. There is a difference of maximum 1% at large angles (low electron energy) between CMS and the ideal solution, essentially due to the multiple scattering contribution of the 2S double layers.

Figure 3.14(bottom) shows a zoom at low angle region that corresponds to high electron energy where the intrinsic resolution is the dominant contribution. Therefore the difference due to the CMS double layers is smaller because of lower MCS impact. However, a little bump of the relative order of 10^{-4} emerges for $\theta_e \lesssim 2$ mrad due to the counts accumulation near

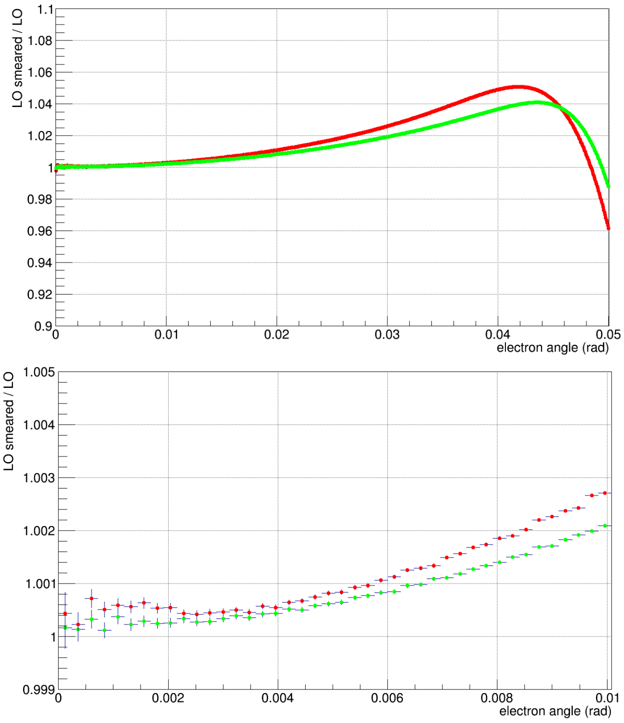

Figure 3.14: Results of the fast simulation: CMS solution (red) in comparison with the best one under analysis (green).

the angle boundary (angular deflections cannot be negative). Thanks to the high statistics provided by fast-MC, we identified this effect as due to the CMS 2S intrinsic resolution of 18 μm against the ideal one of 10 μm, using a configuration with stations of $L = 50$ cm.

Thanks to this preliminary analysis, we have established that a station length of $L = 100$ cm (as quoted in the previous chapter) is required to achieve an angular resolution of about 0.02 mrad with 18 μm of point resolution, equivalent to what could be achieved approximately with 10 μm and $L = 50$ cm.

3.5 Background studies

3.5.1 GEANT4

Monte Carlo simulations have been performed to study the resolution effects due to the target and the detector, and to evaluate the background.

We have developed a GEANT4 simulation code to describe the response of the apparatus[2], used to describe the the two test beam data taking.

A detailed detector simulation is essential to prove we can control the experimental effects with the required precision. We implemented the silicon detectors as homogeneous volumes. This is the most relevant simplification we have adopted. The detailed simulation of the hit formation (clustering) has to be developed.

GEANT4 classes have been edited to get relevant information: tracking angles, hits positions in the silicon volumes, energies and identifiers of the secondary particles, and of the interactions that have produced them[3].

We assumed a gaussian beam energy distribution with a relative spread of 3 relying on measurements performed by CERN accelerator experts.

The angular profile of the beam has been measured directly by recording the incoming particles angles.

Particles incoming directions have been defined in GEANT using the discrete inverse cumulative method.

Particular attention has been dedicated to the comparison of the different electromagnetic physics lists (settings of the relevant interactions) that can be selected and tuned in GEANT4. To describe the multiple scattering, we considered the so called opt3 and opt4 options, which offer two different models describing the multiple scattering. GEANT4 authors declared to be interested in the 2017 test beam results and collaborated with us in tuning the code, because of the lack of MCS experimental data in the literature for electrons in the energy range 10-20 GeV hitting on low Z targets.

Several GEANT4 results about the comparison with the analyzed data will be shown in the next chapter on test beams.

3.5.2 Simulation results

In order to study the background, we performed a GEANT4 simulation of $5 \cdot 10^8$ events[4], with 150 GeV muons colliding on 2 cm thick Beryllium target. We recorded events with the muon and at least one secondary charged particle leaving the target.

This was a preliminary study performed to determine the secondary particle multiplicity, the sources of the physics background and validate GEANT4 settings. In this simulation we considered the interactions of the muon with the target neglecting any detector effects.

---

[2] We started by modifying GEANT4 examples: by studying in particular `TestEm5` and editing the classes `DetectorConstruction`, `TrackingAction` and `SteppingAction`.

[3] One of the main issues with GEANT4 is to extract the interesting information as efficiently as possible.

[4] At the M2 nominal intensity ($\sim$ 50 MHz), this statistics can be achieved in only 10 s.

counts	final track multiplicity	fraction
497537	$m > 1$	$1 \cdot 10^{-3}$ of tot
495084	$m = 2$	99.5% of $m > 1$
2449	$m = 3$	$\sim 0.5\%$ of $m > 1$
4	$m = 4$	$< 10^{-5}$ of $m > 1$

Table 3.1: Counts of the exit charged multiplicity, by using $5 \cdot 10^8$ incoming muons of 150 GeV on 2 cm of Beryllium, for final particle energy $E > 100$ MeV, within 50 mrad.

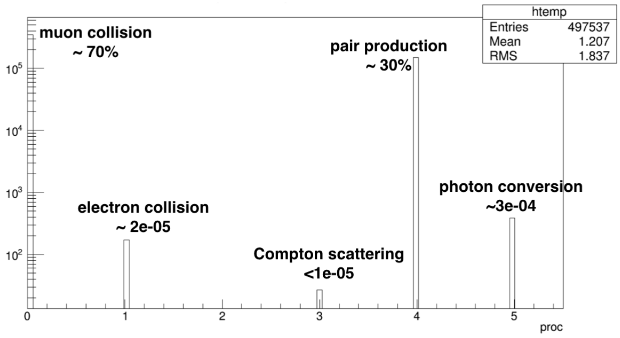

Figure 3.15: GEANT process for the secondary electrons.

We have considered charged particles with $E > 100$ MeV, within the angular acceptance of 50 mrad. This corresponds to the geometrical acceptance of a station of $L = 100$ cm, with a Silicon sensor of 10 cm × 10 cm, as planned for the MUonE detector.

Muons passing the target without detectable secondary are 99.9% of the total. The recorded multiplicities are shown in tab. 3.1.

Figure 3.15 shows the GEANT4 processes that have produced at least one secondary charged particle. 70% of these events are elastic μe scattering ("muon collision"). 30% of them are background events due to pair production: by far the most important source of background. In case one of the two charged particles of a pair is not detected, the event can mimic the elastic scattering.

Figure 3.16(a) shows where these events are located in the (θ_e, θ_μ) plane. Background events have low muon angles. There is a certain degree of contamination of the signal region at large electron angles.

The level of the background obtained selecting the events within the resolution around the elasticity curve is shown in fig. 3.16(b). It can be noticed there is an exponential decrease of the background level (in red) as a function of θ_e and the total contamination of the signal region (in green) at level of

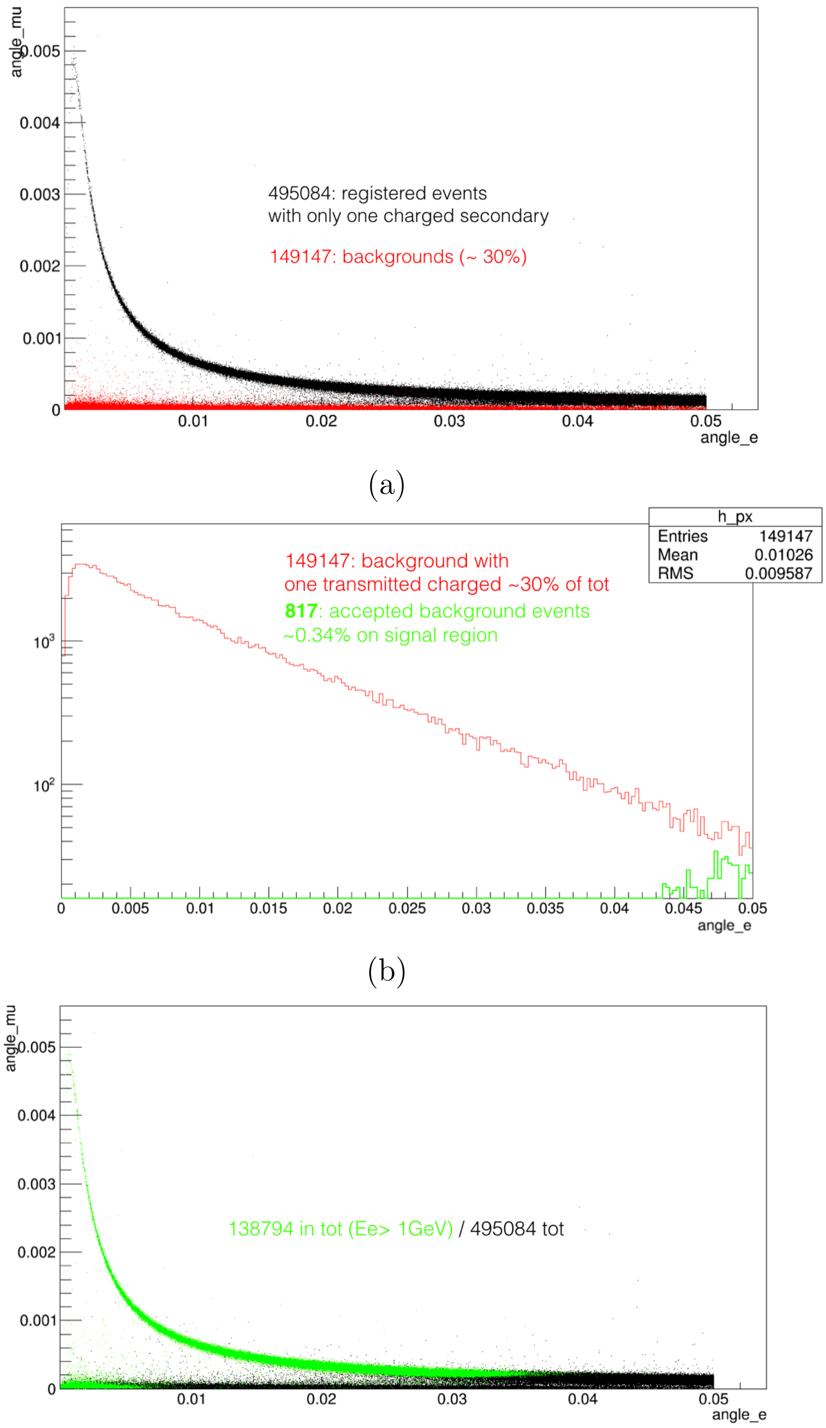

(a)

(b)

(c)

Figure 3.16: (a) Correlation θ_μ-θ_e: in red the background events. (b) The background behavior as a function of θ_e (in red) and the accepted background (in green) in the elastic region. (c) Energy selection for $E_e > 1$ GeV.

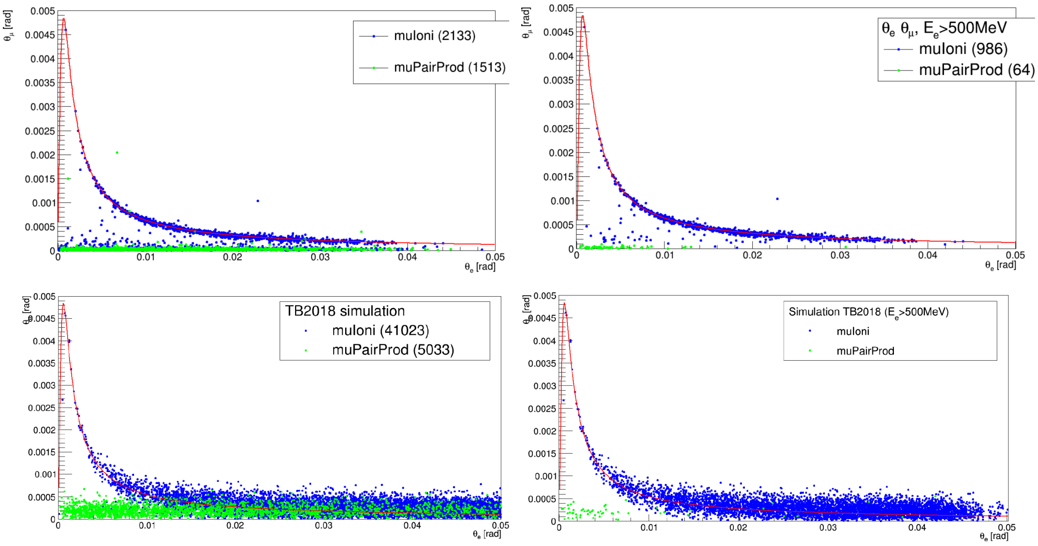

Figure 3.17: Full GEANT4 simulation of 2017 / 2018 test beam [64], without and with an energy cut: E > 500 MeV. (Top) With good resolution of test beam 2017 of 7 μm. (Bottom) With the resolution of test beam 2018 of 35 μm.

$3 \cdot 10^{-3}$, for $\theta_e \gtrsim 40$ mrad.

The differential contamination is of the order of percent level for $\theta_e \gtrsim$ 35-40 mrad and about 10^{-3} at low angle region.

Figure 3.16(c) shows the result of an energy selection requiring $E > 1$ GeV. The residual high energy component is confined at very low muon and electron angles.

To further check GEANT4 settings, we evaluated the rate of μe scattering process within 30 mrad (corresponding to $E_e \gtrsim 1$ GeV). We selected $1.23 \cdot 10^5$ signal events of the initial $5 \cdot 10^8$ incoming muons. The resulting signal rate is $2.46 \cdot 10^{-4}$ in agreement with the theoretical calculation that gives $2.42 \cdot 10^{-4}$ for 2 cm of Beryllium (see sec. 2.4.2). For high order simulations the interface of GEANT to specific NLO generator is needed.

Figures 3.17 explain the role of the intrinsic resolution on the background rejection capabilities. A good intrinsic resolution below 10 μm allows to distinguish signal from background up to 35-40 mrad. As a consequence a simple geometrical cut on the muon angle, for instance $\theta_\mu > 0.1$ mrad remove most of this background, preserving with good efficiency the signal region.

We estimated that with the best angular resolution background is still present in the low electron angular region ($\theta_e \lesssim 10$ mrad), with a differential contamination at the level of about 10^{-3} bin-by-bin.

To control the background contamination at level of 10^{-5} or less, MUonE can count on the combined action of the GEANT4, with a precision of about percent level, and of the use of the calorimeter.

Another important information to control this background is the coplanarity. The coplanarity cut works since the e^+e^- pairs production is not constrained to the same plain of the elastic scattering, determined by the incoming muon and outgoing particles. The χ^2 of the tracks, i.e. the quality of the tracks, is also important, since it can be used to limit the presence of very low energy particles, which are affected by huge MCS effects.

Chapter 4

Test Beams analysis

In 2017 and 2018 two test beams were performed at CERN, the first dedicated to study of the MCS, the second focused on the analysis of elastic scattering events μ-e. In both cases we have performed:

- Silicon trackers alignment;
- studies of data quality for the detectors characterization;
- tracking, with particular attention to the errors treatment;
- construction of pattern reconstruction algorithms to recognize elastic events candidates;
- comparisons between the analysis physics results and GEANT4 simulations.

The analysis of the 2017 test beam data (TB17) has been completed and the results are currently being published, while the 2018 test beam (TB18) is still being analyzed by two different groups.

4.1 The apparatus

4.1.1 Generalities

In both the test beams we used single sided[1] Silicon strip detectors (SSD) with different characteristics and tracking capabilities. During the TB17, we used the telescope by UA9 collaboration [10], built for precision studies of angular deflection of particles. The UA9 has been optimized to provide a very

---

[1] Two layers are needed to read x and y coordinates.

Si strip features	test beam 2017	test beam 2018
Strip pitch	60 μm	242 μm
Floating strip	yes	yes
(Quoted) Point resolution	7 μm	35 μm
Si bulk thickness	320 μm	300 μm
Transverse active area	3.8 x 3.8 cm^2	9.3 x 9.3 cm^2
Single sided	yes	yes
Readout	analogue	analogue
Max readout rate	140 kHz	10 kHz

Table 4.1: Main sensors characteristics used in the test beams.

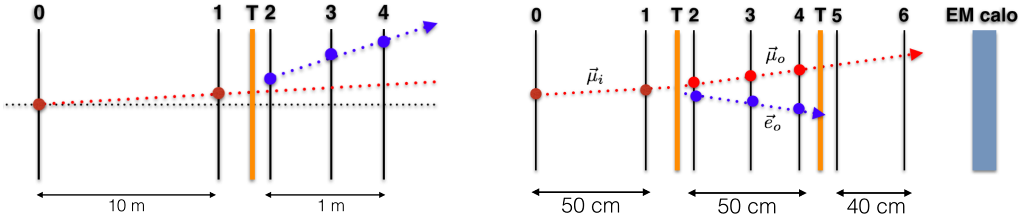

(a) (b)

Figure 4.1: Sketches of the TB setups (not to scale): (a) TB17 and (b) TB18 in the first configuration with two targets and two upstream tracking modules. Detailed descriptions of TB18 apparatus is in ref. [71].

precise hits resolution and to operate at high couting rate with fast readout electronics. The setup consists of a rather long upstream arm of about 10 m, equipped with two tracking stations, and the downstream arm ($\sim$ 0.9 m), equipped with 3 tracking stations (fig. 4.1). Between the two parts we put the target. The beam-line was the H8 of CERN SPS. For these measurements we used electrons and positrons of energies 12 and 20 GeV, muons of 160 GeV, and pions of 80 and 180 GeV (see next sec. 4.4.2). As targets we used graphite tiles of 2, 4, 8 and 20 mm thickness. We aimed at measuring multiple scattering effects to be compared to GEANT4 simulations. Events for MCS studies are selected as single tracks, crossing the whole detector with a single hit per sensor. Analysis of events with multiple tracks have been performed only with muons, looking for elastic collisions on atomic electrons.

The TB18 was a long run, that lasted about 5 months. We used silicon sensors of the AGILE experiment [11, 65] (originally used to the detect gamma rays on satellite). We set an automatic DAQ system remotely controlled and managed by the group of INFN Insubria. The apparatus composed by two modules of about 50 cm each. The setup was placed downstream COMPASS [66], at the M2 muon beam line of the CERN SPS. We detected muons from pion beams hitting on 8 mm graphite targets at energy of about 187 GeV and also M2 muons, according to the COMPASS requests (see next sec. 4.5). Aim of the TB18 has been to track μ-e elastic events. We have foreseen to measure the energy of the scattered particles exploiting a calorimeter located downstream the apparatus. Characteristics of the two setups used in TB17 and TB18 are reported in tab. 4.1 and in fig. 4.1.

In both cases the material budget is similar, since the thickness of the silicon trackers are comparable. Distances between sensors and the hit resolution are quite different, implying different intrinsic angular resolutions:

$$\Delta\theta_i \sim 0.011\,\text{mrad}\ \ (\text{TB17}), \qquad \Delta\theta_i \sim 0.10(0.05)\,\text{mrad}\ \ (\text{TB18}). \tag{4.1}$$

In a second phase of the TB18, the second target has been removed, so a double measure arm was obtained. As a consequence the intrinsic resolution improved.

4.1.2 DAQ

An important difference between the two detectors is in the readout electronics and the data acquisition (DAQ) rate capabilities. The UA9 apparatus (TB17) uses fast electronics developed by CMS. The readout ASIC is the APV25, designed to operate at LHC frequencies of 40 MHz. The maximum operational readout trigger rate was $\nu_m^{\max} = 140$ kHz, suitable to the L1 CMS trigger. When used at the H8 CERN SPS beam line the dead time was about 1% [10].

The dead time measures the fraction of the time the DAQ is busy [55, 67]. It is defined as the product of the DAQ readout frequency ν_m (measured rate) and the acquisition time t_D (processing time):

$$D(\%) \equiv \nu_m \cdot t_D. \tag{4.2}$$

The maximum trigger rate is $\nu_m^{\max} = 1/t_D$. As shown in fig. 4.2, the input or physics rate f is related to the dead time by:

$$\nu_m = f\,(1 - D) \quad \Rightarrow \quad \nu_m = \frac{f}{1 + f\,t_D}, \tag{4.3}$$

and to trigger efficiency ϵ_{trig}:

$$\epsilon_{\text{trig}} = \frac{\nu_m}{f} = 1 - D. \tag{4.4}$$

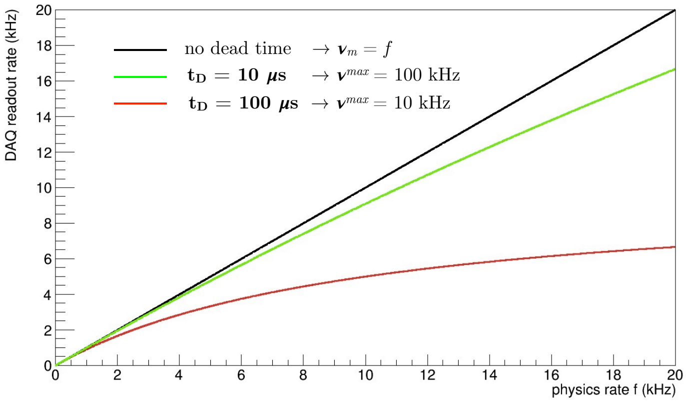

Figure 4.2: DAQ readout frequency ν_m as a function of the input (physics) rate f from eq. (4.3), for different processing times t_D.

Therefore the higher the dead time D the greater the inefficiency of the DAQ system.

In general at relative high frequencies, a DAQ system (i.e. ν_m) progressively loses its ability to follow the input data rate of frequency f as shown in fig. 4.2:

$$\lim_{f\to\infty} \nu_m = 1/t_D = \nu_m^{\max}. \tag{4.5}$$

To circumvent this limitation, pipelines, buffers and multi-level triggers architectures are usually used, in order to reduce or completely remove the dead time.

In this respect, the sensors developed for AGILE and the corresponding readout have been designed with less demanding performance requirements, to run at significant lower frequencies. The maximum readout rate $\nu_m^{\max}$ we managed to run with TB18 hardware is

$$\nu_m^{\max} = 10\,\text{kHz} \quad \Rightarrow \quad t_D = 1/\nu_m^{\max} = 100\,\mu\text{s}, \tag{4.6}$$

to be compared to $\nu_m^{\max} = 140$ kHz for the TB17 acquisition. The intensity of muon rate f was extremely variable during the test beam, tuned to satisfy the COMPASS requests. As a result we recorded data at variable frequencies, from about 5 to 70-80 kHz per SPS spill (4.8 s), so the input frequency was $f = 1 \div 15$ kHz as peak rate.

Considering $f = 15$ kHz, it can be estimated the related dead time and the trigger efficiency of TB18, by using eqq. (4.2)(4.4), from the readout rate

ν_m in eq. (4.3):

$$\begin{aligned} \nu_m &= \frac{15\,\text{kHz}}{1 + 15\,\text{kHz} \times 100\,\mu\text{s}} \sim 6\,\text{kHz} \\ &\Rightarrow D \sim 6\,\text{kHz} \times 100\,\mu\text{s} \sim 60\% \\ &\Rightarrow \epsilon_{\text{trig}} \sim 40\%. \end{aligned} \tag{4.7}$$

The maximum DAQ rate resulted in quite a small trigger efficiency, and the need of a long data taking to collect high statistics data sample.

4.2 Tracking

As envisaged for the MUonE experiment, in both the setups used for test beams, we didn't use any external magnetic field. This makes the reconstruction of charged tracks rather simple since the track model is linear. A global tracking algorithm was then chosen for the track fitting [68]. It minimizes the χ^2 according to the Generalized Least Squares (GLS) method:

$$\chi^2 = \sum_i^n \sum_j^n \left(y_i - f(z_i, \vec{p})\right) (\mathbf{V}^{-1})_{ij} \left(y_j - f(z_j, \vec{p})\right), \tag{4.8}$$

where $f(z_i, \vec{p}) = p_0 + p_1 z_i$ represents the linear fitting function (linear model) calculated at the i-th layer of coordinate z_i along the beam direction, y_i is the hit coordinate recorded at the i-th silicon layer, $\vec{p} = (p_0,\ p_1)$ is the vector of the track parameters, and finally $\mathbf{V}$ is the errors covariance matrix.

In general $\mathbf{V}$ is a non-diagonal matrix. Off-diagonal terms depend on the correlations between hits recorded at successive layers and induced by the multiple Coulomb scattering. The mechanism in place is conceptually simple to describe. MCS effects in the detector plane n.1 induces correlations between the hits recorded at planes 2-3, 2-4, 3-4 and so on, depending on their relative z distances. The V_{ij} element of the covariance matrix is the average track deviation products δx on the layer i, j-th with respect to the incoming direction:

$$V_{ij} \equiv < \delta x_i \delta x_j > = \theta_{\text{MS}}^2 \sum_{k=1}^{i-1} \left((z_i - z_k)(z_j - z_k)\right) \quad \text{for } i \leq j = 1 \ldots n, \tag{4.9}$$

where θ_{MS} is the Highland-Molière dispersion angle. The covariance matrix $\mathbf{V}$ by construction is symmetrical. As we will see off-diagonal terms turns out to be negligible, due to the higher particle energies, because of the $1/E$ MCS dependency.

The χ^2 to be minimized (4.8) can be expressed in matrix notation as:

$$\chi^2 = (\mathbf{Y} - \mathbf{AP})^T \mathbf{V}^{-1} (\mathbf{Y} - \mathbf{AP}), \tag{4.10}$$

where the **Y**, **A** and **P** are the measurement vector (hits), the so-called design matrix and the track parameters vector respectively:

$$\mathbf{Y} = \begin{bmatrix} y_1 \\ y_2 \\ \vdots \\ y_n \end{bmatrix} \quad \mathbf{A} = \begin{bmatrix} 1 & z_1 \\ 1 & z_2 \\ \vdots & \vdots \\ 1 & z_n \end{bmatrix} \quad \mathbf{P} = \begin{bmatrix} p_0 \\ p_1 \end{bmatrix}. \tag{4.11}$$

The problem to solve is linear so it possible to obtain an exact solution, avoiding numerical minimization methods (e.g. Minuit). The criterion of the minimum squares requires that

$$\frac{\partial \chi^2}{\partial \mathbf{P}} = 0 \quad \rightarrow \quad \mathbf{A}^T \mathbf{V}^{-1} (\mathbf{Y} - \mathbf{AP}) = 0, \tag{4.12}$$

By solving it for **A**, we get the fit parameters vector we are interested as:

$$\hat{\mathbf{P}} = (\mathbf{A}^T \mathbf{V}^{-1} \mathbf{A})^{-1} \mathbf{A}^T \mathbf{V}^{-1} \mathbf{Y} \tag{4.13}$$

with errors matrix given by:

$$\mathbf{C} = (\mathbf{A}^T \mathbf{V}^{-1} \mathbf{A})^{-1}. \tag{4.14}$$

A recursive algorithm has been built to solve (4.13): for each track what changes in the iteration step is the hits vector **Y**, while the other matrices are calculated only ab initio, given a certain setup. As a result the procedure of track reconstruction has turned out to be very fast.

4.3 Alignment

High energy pion runs were used for detector alignment in the TB17, while traversing muons were used to align the detectors in TB18. The alignment procedure has been based on a recursive procedure minimizing tracks residuals.

Two translational misalignments can affect a silicon detector: misalignments along the x and y axis, transverse to the beam z axis, and rotational misalignment of the sensors around the z-axis. Peculiar attention has been put in controlling longitudinal shifts of the detector positions with respect to

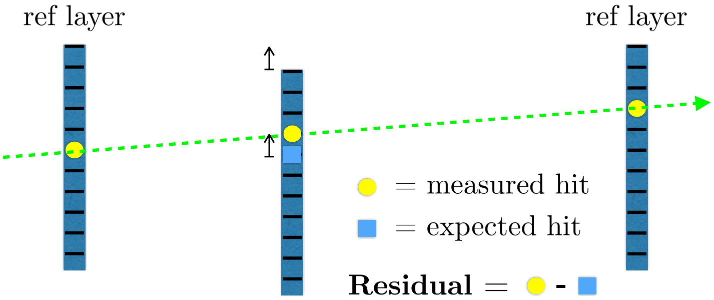

Figure 4.3: Definition of the residual: $r_{x/y}$ in eq. (4.15) are the means of the residual statistical distributions over all the selected tracks.

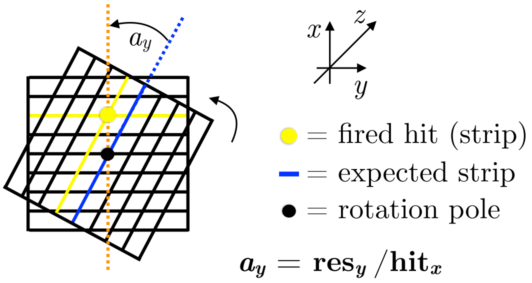

Figure 4.4: Rotational misalignment: a_y is the correction angle to applied at the y hits in eq. (4.15).

the nominal position. Rotation along the x or y axis (tilts) are more difficult to discover and correct, as they are second-order effects.

Only tracks that have released a single hit in each sensor are selected for the alignment. Straight lines have been defined tracking through two reference planes, to get the expected coordinates and measure hits residuals at different planes.

Residuals at a given plane are defined as differences between measured hits coordinates and the estimated positions at plane as shown in fig. 4.3. The mean values of the distributions measure the transverse shift to be corrected. Residual mean values have been iteratively corrected to reach the zero within statistical errors.

Rotations along z-axis induce a correlation (fig. 4.4) between residuals measured along the transverse direction in view x (or y) and the corresponding hits of the same tracking module in the orthogonal view y (or x). Rotational misalignments have been corrected iteratively by minimizing these correlations, independently for the x and y coordinates.

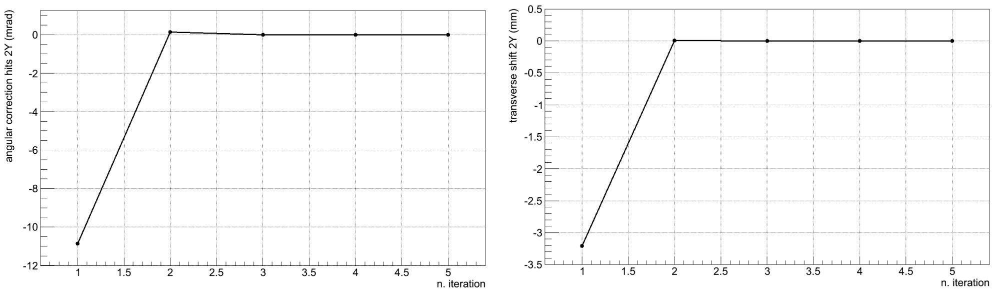

Figure 4.5: Alignment parameters as a function of iteractions, TB17.

Corrections for the alignment have applied to the hits coordinates considering the first order approximation:

$$\begin{cases} x' = x - r_x - a_x \cdot y \\ y' = y - r_y - a_y \cdot x \end{cases} \tag{4.15}$$

where (x,y) and (x',y') indicate the hits coordinates before and after the alignment, (r_x,r_y) and (a_x,a_y) are the parameters related to the transverse translations and rotations along the beam axis respectively, calculated as the summing up what is obtained at each iteration:

$$r_{x,y} \equiv \sum_{i=1}^{n} r^{(i)}_{x,y} \quad a_{x,y} \equiv \sum_{i=1}^{n} a^{(i)}_{x,y}. \tag{4.16}$$

We observed that the procedure converges after just a few iterations and the correction coefficients obtained at each step tend rapidly to zero, as it is shown in fig. 4.5, where both $r^{(i)} \to 0$ and $a^{(i)} \to 0$. The high statistics of the data samples ($N \gtrsim 3 \cdot 10^5$) used for the alignment allows to reach an accuracy in the correction of the transverse offsets of 1 μm and less than 0.1 mrad for the rotational angles, as quoted in [10]. Large corrections may cause non-linearity effects, in this case the alignment procedure may not converge.

Once the alignment parameters have been determined they are used to operate the coordinate transformation (4.15) of the data samples. Correction of the transverse plane rotation correlates the x and y hits: to be applied it requires both the $(x,\ y)$ coordinates of one hit have to be detected. In case one of the two coordinates is missing the hit cannot be corrected and must be discarded. This implies that inefficiencies on a detection layer propagate to the layer measuring the orthogonal coordinate in the same tracking module. In case more than a single hits has been recorded then multiple combinations (pairing) have to be generated to reproduce the true hit combination to be exploited in the pattern reconstruction procedure for track finding.

Residual misalignments may induce systematics effects in the angular observables affecting angular measurements. In particular, any longitudinal misalignments would affect the angular distributions, because the direct proportionality between reconstructed angles and the relative distance between sensors. In both the test beams distances between the layers have been measured with an estimated uncertainty of the order of 1 mm. The longitudinal misalignment turned out to be hard to measure with the data, as we will discuss.

4.4 Test beam 2017 results

4.4.1 Pre-alignment studies

For the alignment we used high-energy pions runs. Figure 4.6 shows the residuals measured at the three downstream planes before and after a preliminary alignment performed from the data with the electron runs without target. Indications of a good alignment procedure can be obtained from the residuals distributions: mean values go to zero within the errors and distribution widths progressively reduce.

We started to test GEANT4 results already at this stage, by applying to the simulated hits the same reconstruction procedure used for real data. Detectors in the simulations are perfectly aligned. Results of the simulations turn out to be in good agreement with the measurements: residuals in the gaussian cores agree quite well. The tails of the residuals distributions are instead asymmetrical along y as visible in fig. 4.6.

Figure 4.7 shows the electron beam spot in the first silicon layer. The electron beam enters the detector hitting the edge of the first upstream sensors creating the asymmetric beam profile we observed. This asymmetry required us to pay attention to the fiducial cuts and to track quality cuts (χ^2) to be applied in order to get reliable comparisons with the MC simulations.

4.4.2 Pion runs and alignment parameters

The pion runs at 80 and 180 GeV have been used to determine the definitive alignment parameters and calibrate the detector. The reference planes chosen for the alignment are the plane 0 and plane 1, since their distance was set to 10 m. The muon runs have been aligned relying on the muons themselves, as an intervention on the setup prevented the still use pions.

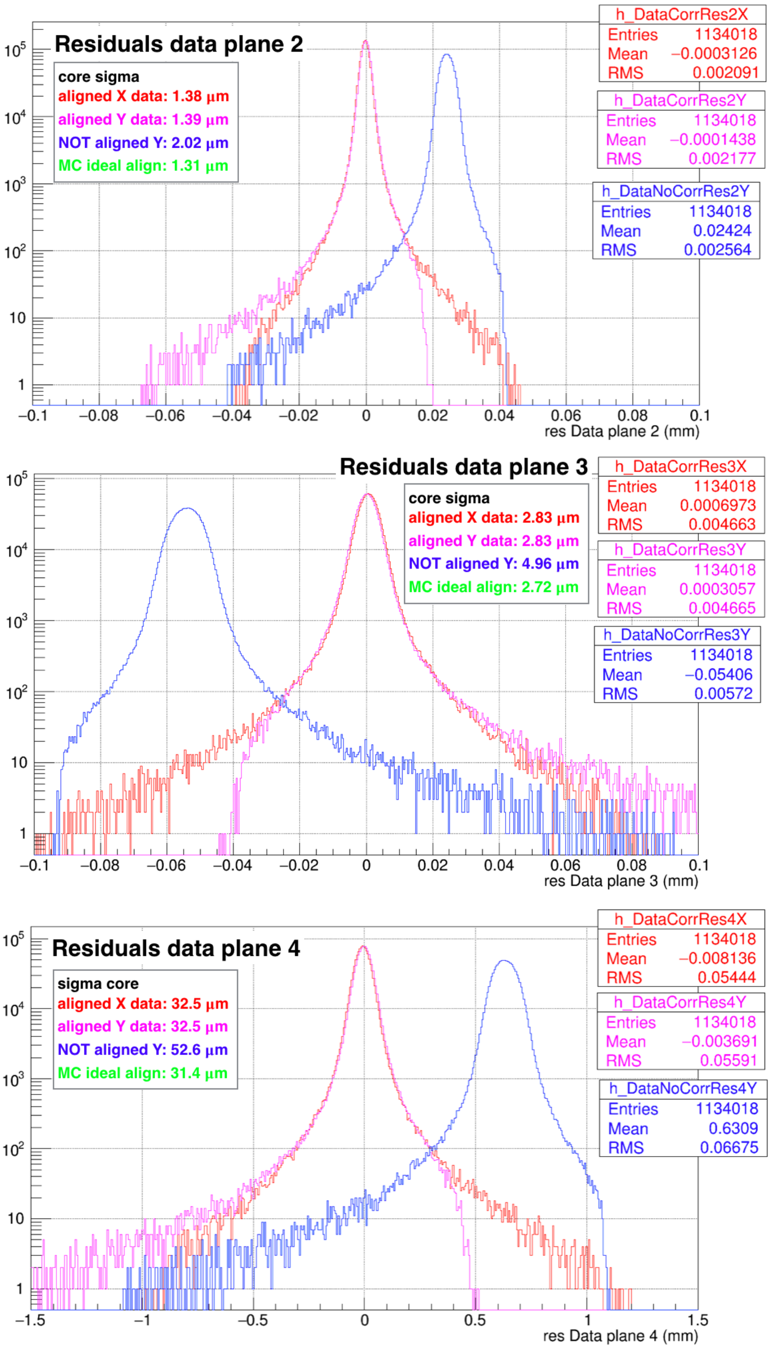

Figure 4.6: Distributions of the residuals from the preliminary alignment using electron runs. From top to bottom, downstream planes 2, 3 and 4, see fig. 4.1(a).

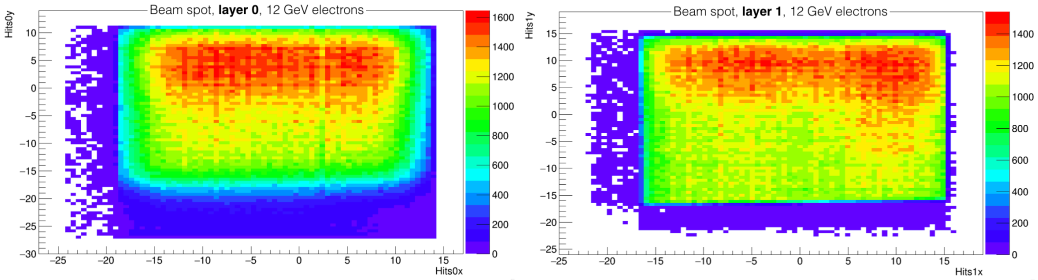

Figure 4.7: Beam spot at first upstream layers 0 and 1: 12 GeV electron run.

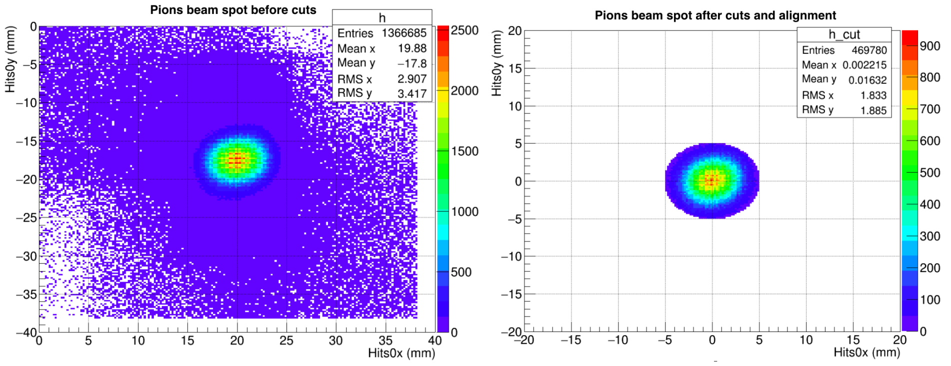

Figure 4.8: Beam spot at first layer of 180 GeV pion runs.

The hits recorded at plane 0 and plane 1 were aligned in the laboratory reference system, eliminating transverse offsets. A fiducial cut centered at the beam axis, of radius 5 mm, was then applied to select events around the beam spot as shown in fig. 4.8. We then aligned the downstream planes 2, 3 and 4, independently in the x and y directions. The quality of the alignment and the quality of the tracking have been checked looking at distribution of the χ^2, calculated for the three downstream planes and for a global fit to all the five planes.

Fig. 4.10(a) shows that χ^2 presents a bump, indicating an excess of tracks with high χ^2. Displays of these events show that they are likely due to noise instead of activities related to the pions. Run with muons is shown in fig. 4.10(b): it confirms the pattern.

The quality alignment seems to be anyway very good. Table 4.2 collects the alignment parameters extracted from the central 180 GeV pion run. During one week we collect 5 runs using 180 GeV pions and possible constants variations in time have been checked: figg. 4.9 show transverse shifts and angles of these runs. Numerous interventions have been made during the test beam, which may have caused slight variations in the sensors positioning.

layer	r_x (mm)	r_y (mm)	a_x (mrad)	a_y (mrad)
0 (ref)	19.882	-17.609	< 0.01	< 0.01
1 (ref)	19.388	-19.162	< 0.01	< 0.01
2	0.408	-3.140	-0.500	-10.647
3	6.023	-7.819	17.803	-29.901
4	4.452	-1.417	5.682	-6.402

Table 4.2: Alignment parameters measured from the central pion run (n=3 in figg. 4.9).

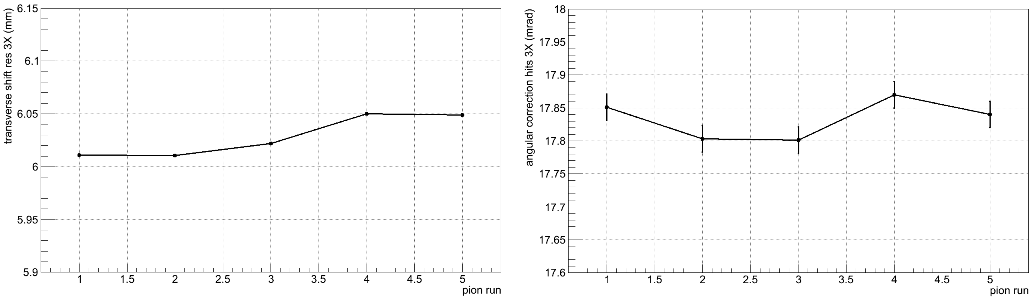

Figure 4.9: Variations of alignment constants as a function of pion runs.

Therefore for the alignment of the electron runs, it was decided to use the single sets of the alignment constants measured from each pion run closest in time.

After few iterations, values of the residual alignment constants are well below the precision goal. Widths of the residual distribution, as expected, are very close to the intrinsic resolution, since the multiple scattering for high energetic pions and muons is small.

Alignment runs allowed us to measure the intrinsic angular resolution of the apparatus. Angular deflections measured without target with 80 GeV and 180 GeV pions runs, and with and without target (8 mm graphite) with 160 GeV muons are shown in figure 4.11.

The observed widths of the angular distributions $\Delta\sigma$ include the intrinsic resolution σ_i and the resolution σ_{MS} due to the MCS:

$$\sigma_i = \sqrt{\Delta\sigma^2 - \sigma_{MS}^2}. \tag{4.17}$$

The contribution due to the intrinsic resolution can be determined calculating σ_{MS} by means of the Highland-Molière formula.

Such a procedure returned the values of the intrinsic resolution of the apparatus of about 0.012 mrad, in agreement with the expectations. As a

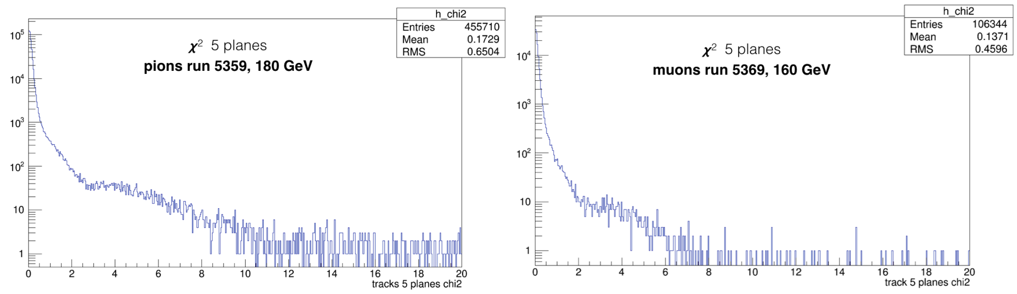

(a) (b)

Figure 4.10: χ^2 distribution of 5 planes fit: (a) pion and (b) muon runs.

further cross-check of the goodness of the alignment, we can observe the angular distributions do not present appreciable offsets.

4.4.3 Tracking electrons

All electron and positron runs have been aligned using constants determined from pion runs.

Figures 4.12 and 4.13 (a) show the incoming (upstream the target) and outgoing (downstream the target) electrons angular distributions for electrons of 12 GeV crossing the detector without target and for 12 GeV electrons colliding on 8 mm thick graphite target, respectively.

Figures 4.12 and 4.13 (b) show the corresponding angular deflections defined as the difference between the downstream and upstream track angles. Note that the distribution of the angular deflections span over 4 to 5 orders of magnitude.

We observe that the information from the third downstream tracking layer turns out to be relatively less important for tracking. Hits coordinates measured at the third plane have relatively large error, because of the cumulative

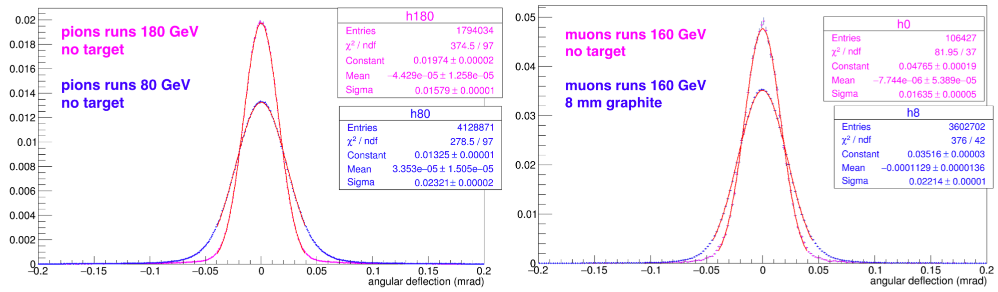

Figure 4.11: Angular resolution from pions (left) and muons (right).

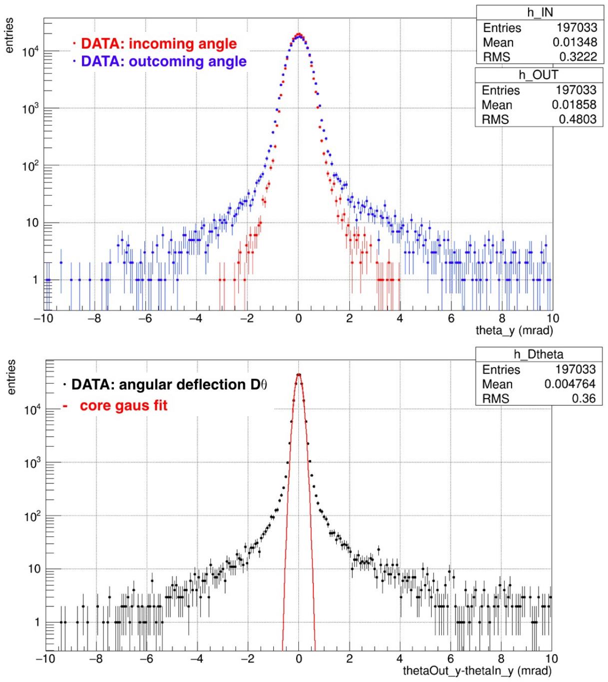

Figure 4.12: Angular distributions from 12 GeV electrons without target. (Top) Incoming and outgoing directions. (Bottom) Deflection distribution.

effect of the multiple scattering.

The hit resolution of the three downstream tracking planes in tab. 4.3 can be obtained from the square root of the diagonal elements of the covariance matrix V of the hits, shown in the following equations for 12 GeV particles:

$$V(12\,\mathrm{GeV}) = \begin{bmatrix} 4.761\cdot 10^{-5} & 0 & 0 \\ 0 & 0.00150 & 0.00263 \\ 0 & 0.00263 & 0.00578 \end{bmatrix} \mathrm{mm}^2 \tag{4.18}$$

and for 20 GeV:

$$V(20\,\mathrm{GeV}) = \begin{bmatrix} 4.761\cdot 10^{-5} & 0 & 0 \\ 0 & 0.000570 & 0.000948 \\ 0 & 0.000948 & 0.00229 \end{bmatrix} \mathrm{mm}^2 \tag{4.19}$$

These matrices was calculated by eq. (4.9) and used in χ^2 minimization for tracking, with the following parameters:

- nominal TB17 layers positions $z = (0, 9390, 9788, 10290, 10698)$ mm,
- MCS contributions θ_{MS} for a single tracking module (0.640 mm of Si) of 0.0759 mrad and 0.0456 mrad, for 12 and 20 GeV respectively.

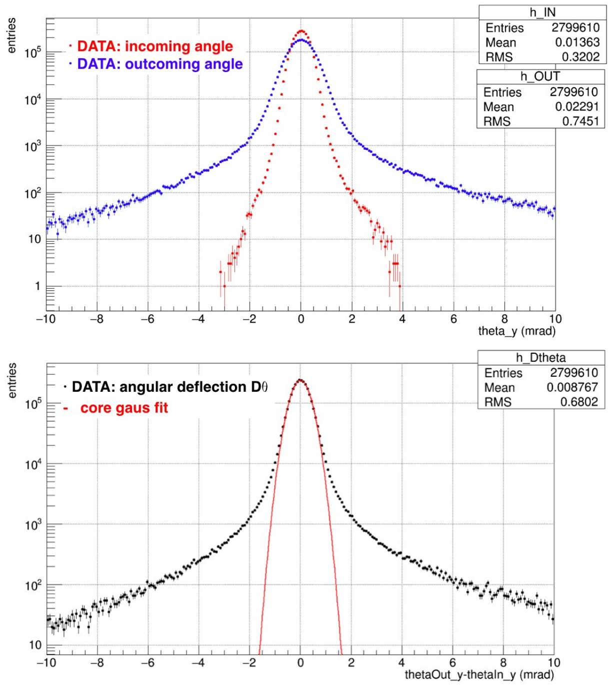

Figure 4.13: Angular distributions from 12 GeV electrons on 20 mm graphite. (Top) Incoming and outgoing directions. (Bottom) Deflection distribution.

The results shown in the figg. 4.12 and 4.13 (b) have been obtained without fiducial cuts on the recorded events. We studied how the distributions possibly vary applying selection cuts to the event used for the analysis.

4.4.4 Fiducial analysis

We observed that the angular deflections are not symmetric, since the electron and muon beams were not well centered. In addition, there may be other source of asymmetry as for instance the contamination in the halo

layer	σ (μm)		
	for 12 GeV	for 20 GeV	for 100 GeV
2	6.9	6.9	6.9
3	39	24	8.3
4	76	48	12

Table 4.3: Hits errors per layer, obtained from covariance matrix V in eq. 4.18. It is shown for comparison the case of 100 GeV particles.

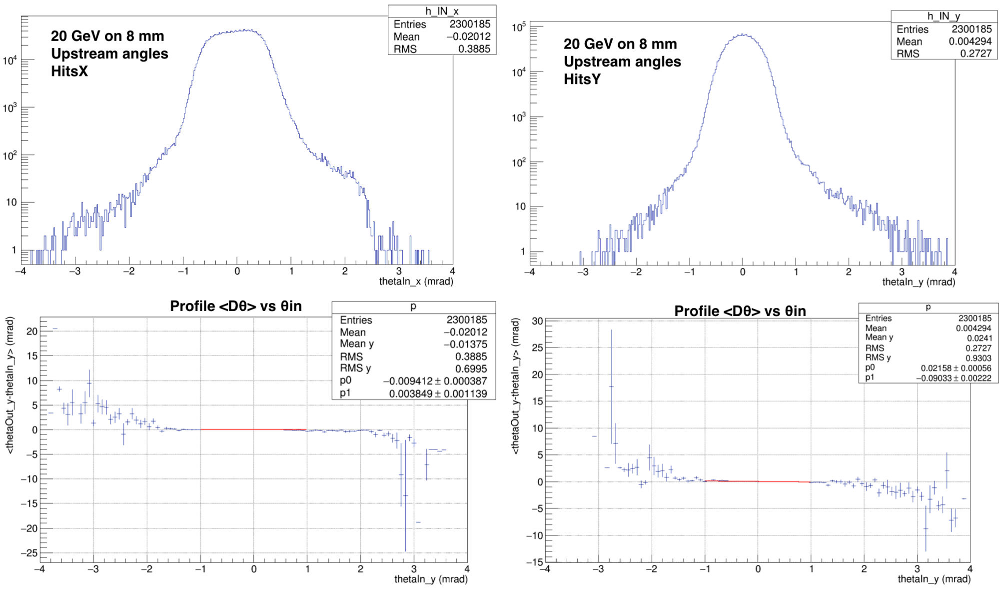

Figure 4.14: First row: x and y incoming angles for 20 GeV electrons. Second row: x and y angular deflection on 8 mm graphite target as a function of the incident angle.

beam. Figures 4.14 and 4.15 confirm that anomalous effects are correlated to the beam halo and are also visible at the edges of sensors. There should be no correlation between the angular deflection and the particle incoming direction. Effects due to the effective path length in the detector caused by the different crossing angles are negligible. Fig. 4.15 in addition shows that the quality of the tracks get progressively worse at the sensor edges.

Fiducial cuts in the upstream sensors have been optimized to get symmetrical angular deflections in the x, y direction.

Figures 4.16 show the effect of the cut applied to the incoming angles:

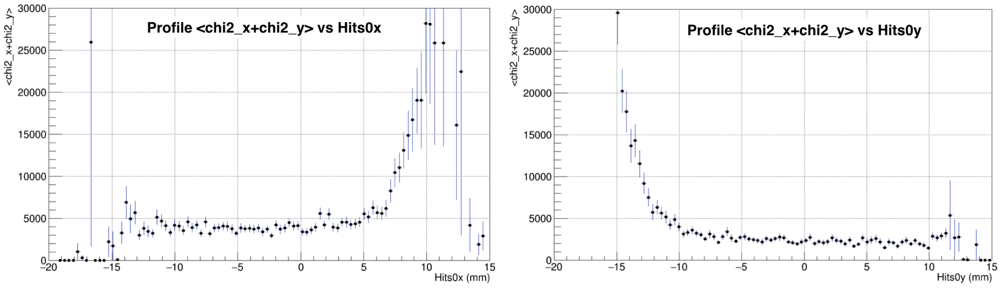

Figure 4.15: χ^2 distribution as a function of the impact point on the sensor.

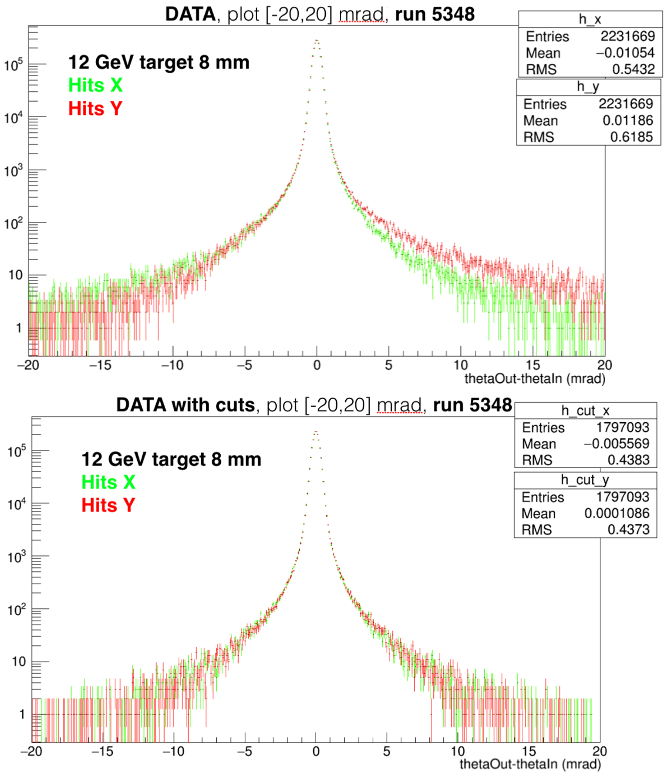

Figure 4.16: Effect of the quality cuts, (top) before and (bottom) after.

σ	res 2 (μm)	res 3 (μm)	res 4 (μm)
DATA	1.33	2.82	33.3
GEANT4	1.27	2.72	32.7

Table 4.4: Core RMS of the tracking residuals: comparison MC - data.

- incoming angle θ between -2 and $+2$ mrad,
- impact point in the first sensor: $-12 < x < 8$ and $-11 < y < 11$ mm,
- loose χ^2 cut: $\chi^2_x + \chi^2_y < 100$; for the final analysis we reduce the cut value to 20 (see next sec. 4.4.7).

Before these cuts were applied, asymmetries in the left / right distributions were at percent level; after having applied the cuts the asymmetries get down below 10^{-3}. This cuts let to preserve the tails of the distributions, for a statistically reliable MC to data comparison. As expected, the combined effects of these quality cuts improve the shape of the distributions in both the x and y directions.

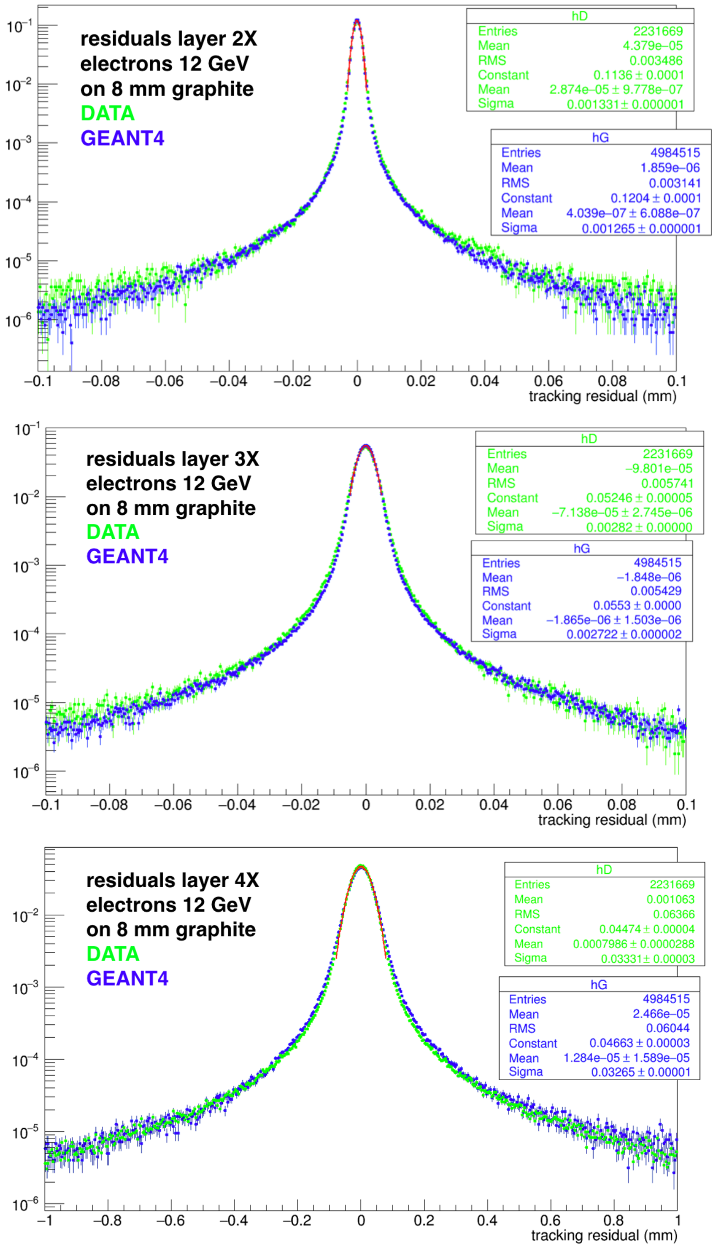

Figure 4.17: Comparison of residuals distributions for 12 GeV electrons hitting on 8 mm graphite. Data in green and GEANT4 in blue. From top to bottom, x view downstream layers 2, 3 and 4.

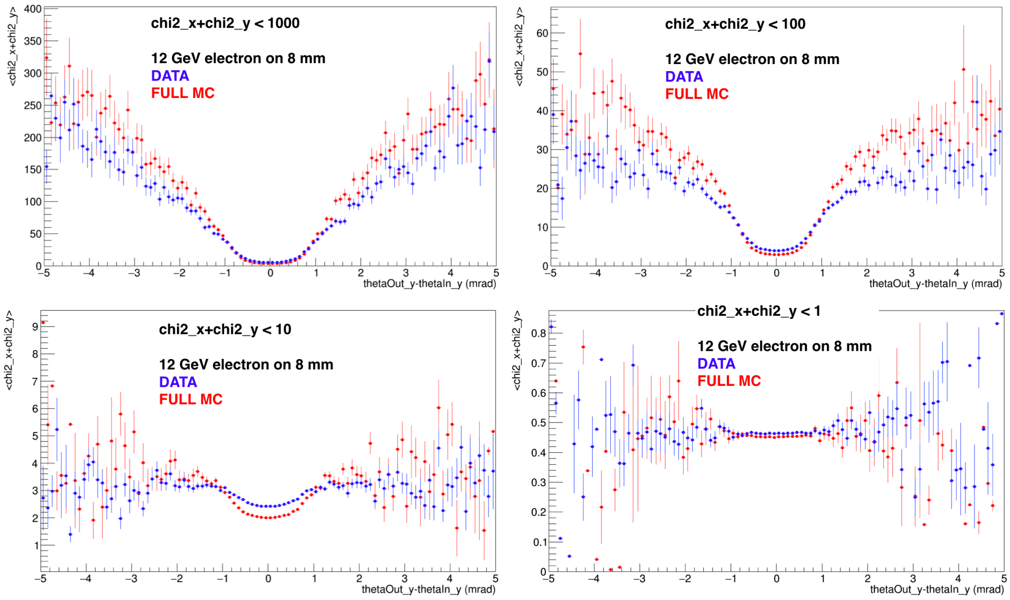

Figure 4.18: Profile histogram of χ^2 as a function of the angular deflection for different maximum χ^2 cuts. Data are in blue, in red are the MC simulations.

Comparison of MC and data residual distributions benefit of these quality cuts, as shown in fig. 4.17. Table 4.4 summarizes the standard deviation of the cores of these distributions. The agreement looks quite good also in the tails. This is an important cross-check of the detailed full simulation.

4.4.5 χ^2 analysis

In the previous chapter we observed that the long tails in the angular deflection are due to electrons that because of the bremsstrahlung have lost most of their energy in the target. To calculate the χ^2 of a track one needs to correctly estimate the errors on the hits measurements. The nominal beam energy is used to estimate the MCS effects and evaluate the covariance matrix.

As a result of the multiple scattering the errors depend on the particles energy. Most of the tracks in the core of the angular distribution (order of 90%) are well reconstructed with a good χ^2 since the particle energy corresponds to the beam energy. Energies of the particles undergoing large deflections are instead much lower than the beam energy and as a result the χ^2 can be largely wrong.

We have observed this effect studying the correlation between the χ^2 and the particles deflection angle. Figures 4.18 show the correlations for

12 GeV electrons hitting on 8 mm graphite, for different χ^2 cutting values, compared to Monte Carlo simulation. As a consequence of the energy loss the χ^2 gets progressively larger with the increasing deflection angles. Strong cut on the χ^2 allows to select particles with the "correct" energy: electrons that keep most of their energy survive the selection. However, tracks that have lost most of their energy can still have a good χ^2 because the minimum deflection angle is always the most probable one.

Our simulation shows the possibility of a good control of the χ^2 variable at different energies, as shown in figg. 4.19(a). Figures 4.19(b) show for MC and data separately how tails due to the bremsstrahlung radiation can be rejected by a χ^2 cut on the track quality, recovering the gaussian behavior of the angular deflection distribution. We stress the need of a detailed simulation of detector response to precisely evaluate the cut efficiency and its possible systematic effect on the final measurement.

4.4.6 Test of the Highland-Moliere formula

Estimates of the MCS performed using the Highland-Molière formula are stated to be reliable at the few percent level (as in the PDG [26]). Data we collected for different particle energies and different target thickness allow to test the validity of this model.

The observed variance can be written in gaussian approximation as:

$$\Delta\sigma^2 = \sigma^2_{\text{target}} + \sigma^2_0. \tag{4.20}$$

We measured both $\Delta\sigma$ and σ_0, with and without the target. σ_0 represents the MCS contribution of the tracking apparatus, downstream the targets. So fitting with a simple gaussian the measured distributions cores of $\Delta\sigma$ and σ_0, we can determine σ_{target} by deconvolution:

$$\sigma_{\text{target}} = \sqrt{\Delta\sigma^2 - \sigma^2_0}. \tag{4.21}$$

These values can be compared to the GEANT4 results, as shown in tab. 4.6, or to the predictions of the Highland-Moliere formula.

Figure 4.20 shows the values of σ_{target} as a function of the target thickness for electron energy of 12 GeV. The curve:

$$\sigma_{\text{target}} = \frac{13.6}{E}\sqrt{\frac{d}{X_0}}(1+B), \tag{4.22}$$

corresponding to the Highland-Moliere formula, fits quite well the data. The fit returns the beam energy, the target radiation length and the correction term B, which result in good agreement with the nominal values

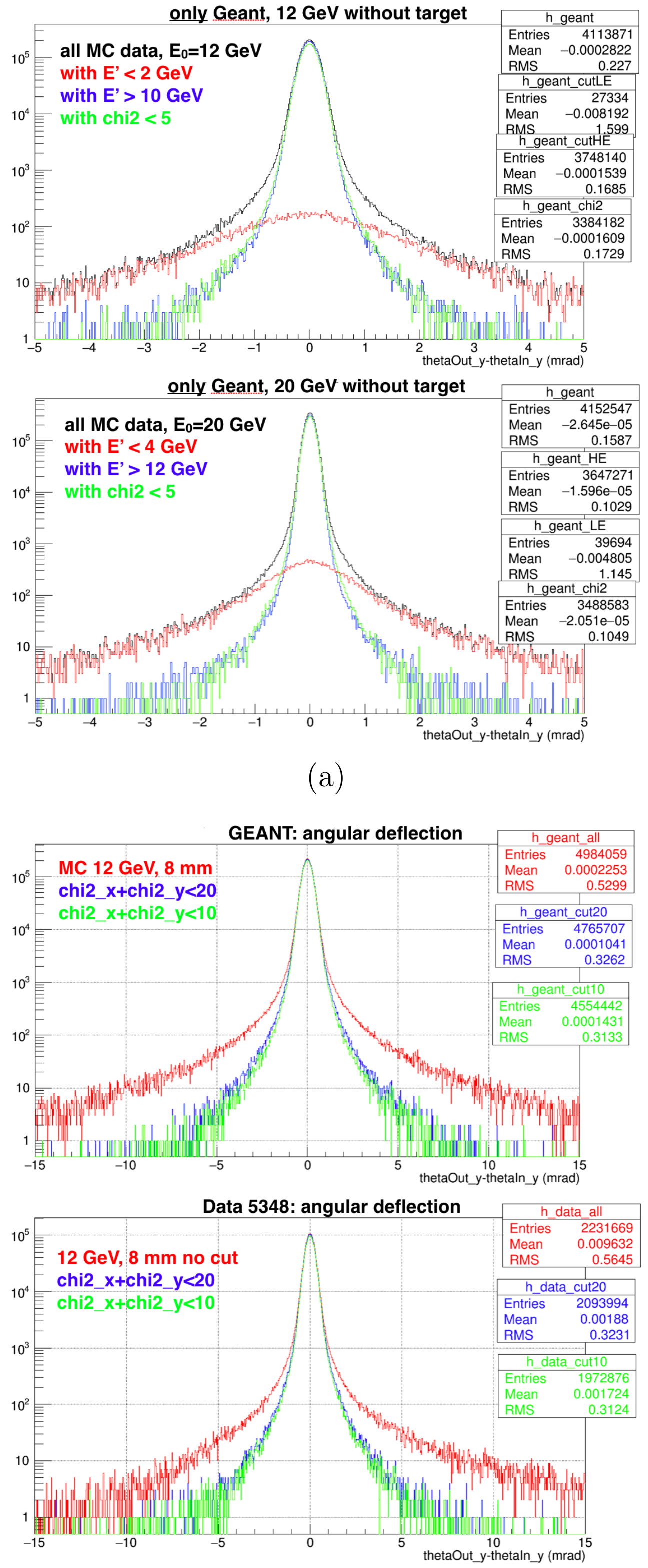

(a)

(b)

Figure 4.19: (a) GEANT4 simulations for 12 and 20 GeV electrons on 8 mm graphite with different χ^2 cuts. (b) Comparison MC-data for 12 GeV electrons on 8 mm graphite.

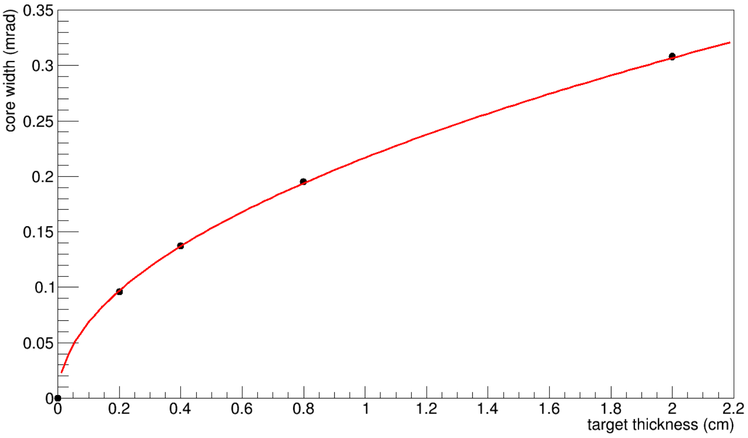

Figure 4.20: Fit with the Highland-Moliere formula of the RMS of the target scattering distributions, obtained with 12 GeV electrons, as a function of the target thickness.

$E_{\text{beam}} = 12$ GeV, $X_0(\text{C}^2) = 23.3$ cm with B negative and around the percent:

- $E = (11.9 \pm 0.4)$ GeV,
- $X_0 = (23.1 \pm 0.7)$ cm,
- $B = -0.04 \pm 0.01$.

Although high relative errors, these results provide another cross-check of our analysis method.

4.4.7 Comparison MC-data

Different GEANT4 versions and different physics lists has been carried out, since of the known differences in the models adopted to simulate multiple scattering.

Figure 4.21 allows to compare the effects of the selection cuts on data and on the full MC simulations. The plot covers the whole angular range to evaluate the distribution including the extreme tails. The result looks quite good. A gaussian fit of the distribution shows the agreement between the standard deviations are within 3.5%. The agreement of the cores of the distributions, although crucial as they covering 90% of the angular distributions is at the percent level. A much more compelling method for the comparison is based on bin-by-bin ratios, between normalized data and MC histograms.

---

[2] The target material is a particular graphite of $\rho = 1.83$ g/cm^3 and $X_0 = 23.32$ cm.

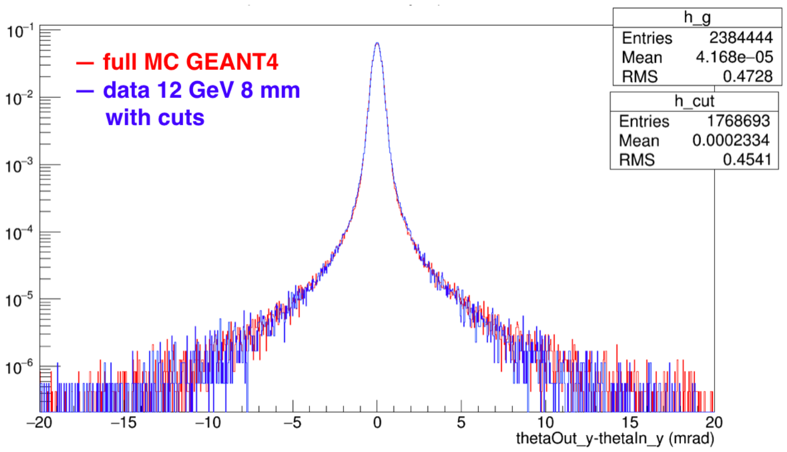

Figure 4.21: Comparison MC-data: 12 GeV electrons hitting on 8 mm graphite. Data in blue and MC in red.

Figures 4.22 show the results of the comparisons between data and full GEANT4 simulations about the electron runs of (a) 12 GeV hitting on 20 mm, (b) 12 GeV on 8 mm and (c) 20 GeV on 8 mm of graphite respectively. For all samples (data and MC) we applied a quality cut corresponding to $\chi^2_x + \chi^2_y < 20$. Table 4.5 summarizes the corresponding results of the gaussian fits of the angular distribution cores. The data systematic errors are estimated according to ref. [8]. The main source is related to the beam scale energy: it is at level of 1%.

We tested the GEANT4 physics lists [61] “opt3” and “opt4” for comparison. It can be seen that in the region nearby the core data values lies between the two GEANT4 distribution. The bin-by-bin ratios show discrepancy are larger in the tails region.

Decreasing the target thickness the agreements look progressively worse, especially in the tail region. We interpreted the disagreement as due to the bad modeling of trackers. The good agreement obtained with 12 GeV electrons on 20 mm hides the inaccurate apparatus simulation. Discrepancies gradually emerges decreasing the target thickness since target effects get comparable to those due to the downstream tracking modules.

In order to directly compare data, full MC previsions and the Highland formula predictions, tab. 4.6 reports the angular distributions cores due to the target contribution only, obtained by using eq. (4.21). Data and MC are in agreement within 2-3%. The Highland predictions present a discrepancy, uniform on the samples, of about 8.5%. This discrepancy is in agreement with as stated in the PDG [26].

To overcome the lack of an accurate simulation of the sensors, we devel-

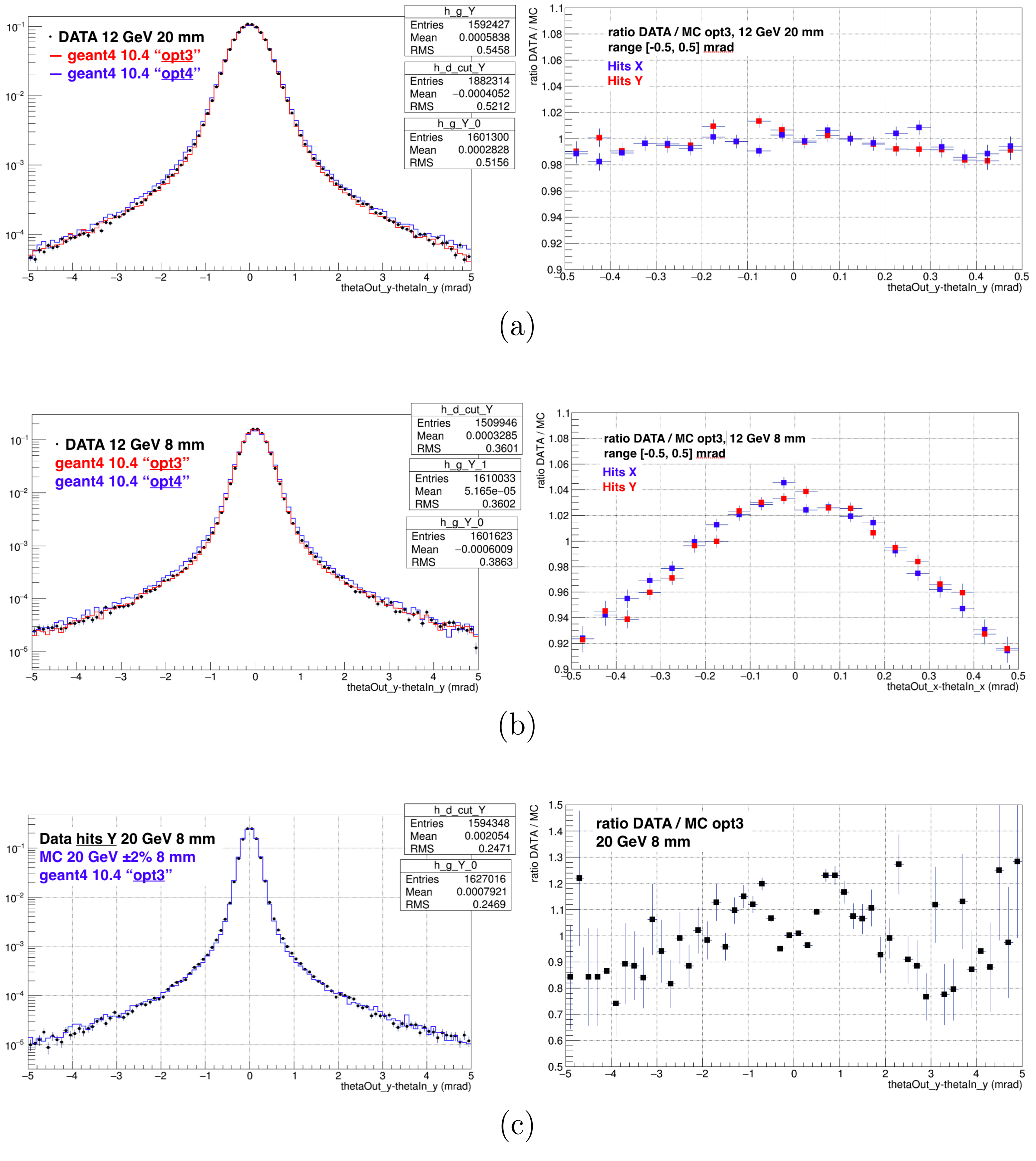

(a)

(b)

(c)

Figure 4.22: Comparison between data and full GEANT4 simulation with bin-by-bin ratio data/MC. (a) 12 GeV electrons hitting on 20 mm graphite. (b) 12 GeV electrons hitting on 8 mm graphite. (c) 20 GeV electrons hitting on 8 mm graphite. Different GEANT4 physics lists are shown (see text).

e^- sample with target	$\Delta\sigma$ (mrad) DATA	GEANT4	Δ(exp-MC)
12 GeV 8 mm	$0.2392 \pm 0.0002 \pm 0.003$	0.2488 ± 0.0001	-3.8%
20 GeV 8 mm	$0.1441 \pm 0.0001 \pm 0.002$	0.1485 ± 0.0001	-3.0%
12 GeV 20 mm	$0.3538 \pm 0.0003 \pm 0.005$	0.3564 ± 0.0001	-0.7%
e^- sample no target	σ_0 (mrad) DATA	GEANT4	Δ(exp-MC)
12 GeV	$0.1314 \pm 0.0004 \pm 0.002$	0.1542 ± 0.0001	-15%
20 GeV	$0.0803 \pm 0.0002 \pm 0.001$	0.0928 ± 0.0001	-13%

Table 4.5: RMS of the core region (90% of the events) of the angular deflections $\Delta\sigma$ with target and σ_0 without target. For data, the first uncertainty is statistical, the second systematic corresponding to 1.3% [8]. For MC the uncertainties are statistical only.

Sample	σ_{target} (mrad) DATA	GEANT4	Highland
12 GeV e^- 8 mm	0.200 ± 0.003	0.1952 ± 0.0001	0.1831
20 GeV e^- 8 mm	0.120 ± 0.002	0.1158 ± 0.0001	0.1099
12 GeV e^- 20 mm	0.329 ± 0.005	0.3213 ± 0.0001	0.3011

Table 4.6: Target MCS contribution σ_{target} obtained deconvolving the measured apparatus resolution σ_0 from the measured angular deflection $\Delta\sigma$ with targets, by using eq. (4.21) and the values in tab. 4.5.

oped a method to combine the GEANT simulation of the target $T_{\text{MC}}(E_0, \theta)$ with the apparatus resolution function $A_{\text{data}}(E_0, \theta)$ measured with data. The response of the apparatus has been obtained from the measurements performed without targets. On this basis one can compare the effect of the target as determined with GEANT4 to the deflection distributions measured with real data [8]:

$$f^{(0)}_{\text{MC}}(E_0, \theta) = T_{\text{MC}}(E_0, \theta) \otimes A_{\text{data}}(E_0, \theta), \tag{4.23}$$

where E_0 is the nominal beam energy.

This method requires a correction since the resolution function A_{data} does not take into account effects of energy loss in the target. This correction is particularly important to compare the tails of the distribution, as they are populated by electrons that have lost much of their energy for bremsstrahlung, as we have already pointed out.

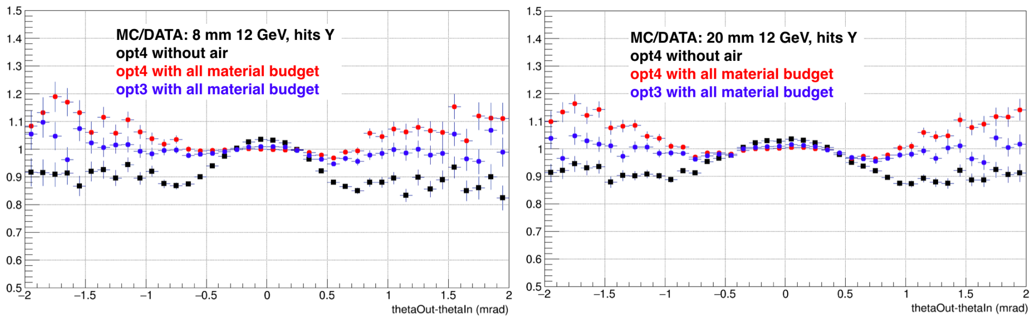

Figure 4.23: Comparisons data with the results of the convolution method (see text). (Left) 12 GeV electron hitting on 8 mm graphite. (Right) 12 GeV electron on 20 mm graphite. The effect of the air is particularly evident in the black dot distribution obtained without air in the detector simulation.

The corrected model to be compared with the data can be written as:

$$f_{\mathrm{MC}}(E_0, \theta) = f^{(0)}_{\mathrm{MC}}(E_0, \theta) \otimes f^{\mathrm{corr}}_{\mathrm{MC}}(E_0, \theta) \tag{4.24}$$

where f^{corr} is:

$$f^{\mathrm{corr}}_{\mathrm{MC}}(E_0, \theta) = \frac{S_{\mathrm{MC}}(E_0, \theta)}{T_{\mathrm{MC}}(E_0, \theta) \otimes A_{\mathrm{MC}}(E_0, \theta)}. \tag{4.25}$$

where S_{MC} is the complete simulation (target plus apparatus), T_{MC} and A_{MC} represent the MC simulation of the target and the apparatus respectively.

Moreover, we have observed that energy losses in the air cannot be neglected, due to the long upstream part of the detector of 10 m. It is necessary therefore to consider all the upstream and downstream material budget.

In figure 4.23 a bin-by-bin comparison between data and the simulations obtained with the convolution method in the different cases: without air, and with the two physics lists. With the model we proposed the agreement appears remarkable.

Figures 4.24 show the comparison of the core distribution between the convolution model f_{MC} and data of different samples. Considering the bin-by-bin ratios, the agreements looks very good, within the percent level. Comparing the gaussian width of the distributions, data and MC are in agreement below 1%.

We tried to slightly modify the GEANT4 detector model, varying the density and thickness of the material budge without significant differences in the simulation results. We then studied how uncertainties in the distances between sensors propagate their effects on the observable angular distributions. During the alignment stage, we attempted to evaluate possible z shift

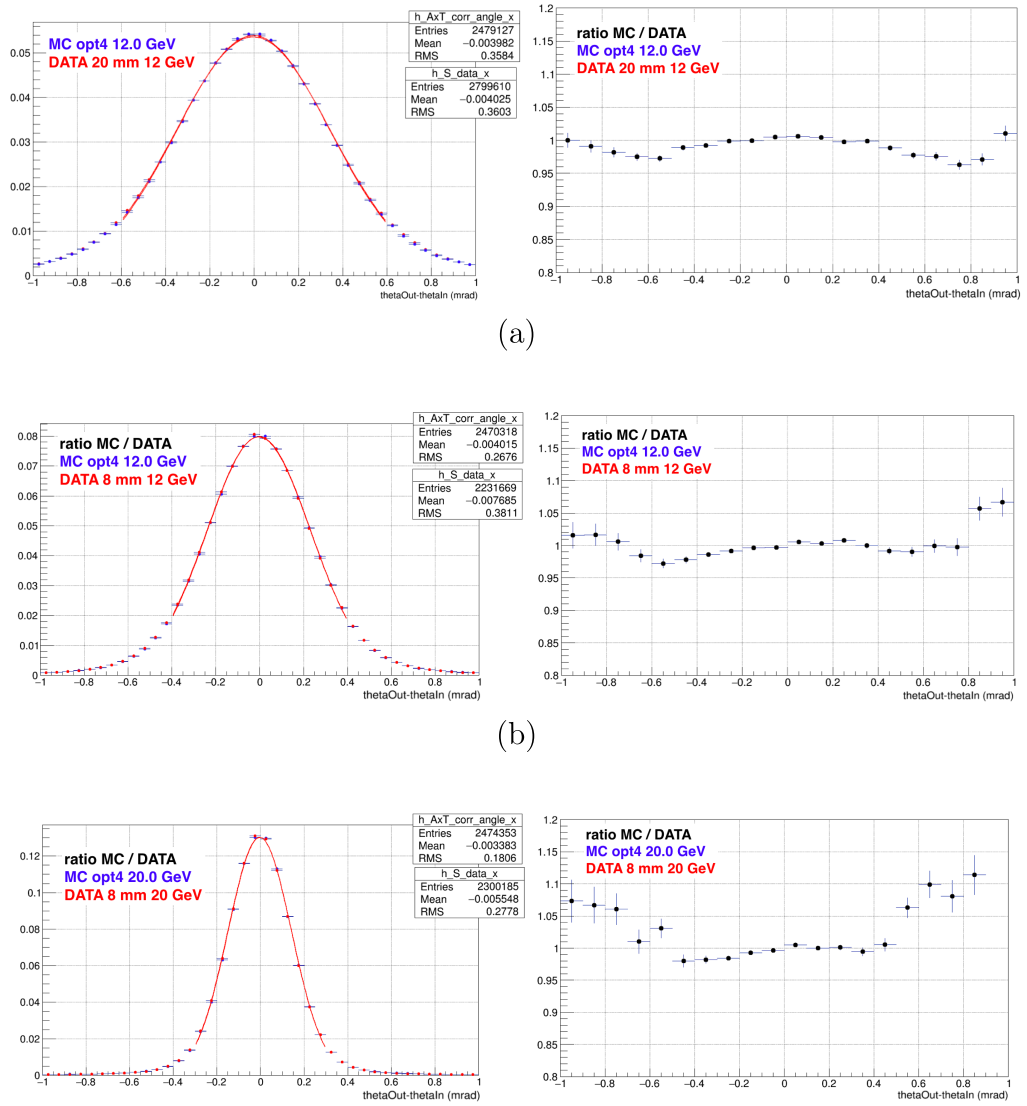

(a)

(b)

(c)

Figure 4.24: Comparison between data and the results of convolution method (see text) with bin-by-bin ratio MC/data. (a) 12 GeV electrons hitting on 20 mm graphite. (b) 12 GeV electrons hitting on 8 mm graphite. (c) 20 GeV electrons hitting on 8 mm graphite. The RMS of the core regions of MC and data are in agreement within 0.7%, 0.8% and 0.5% respectively.

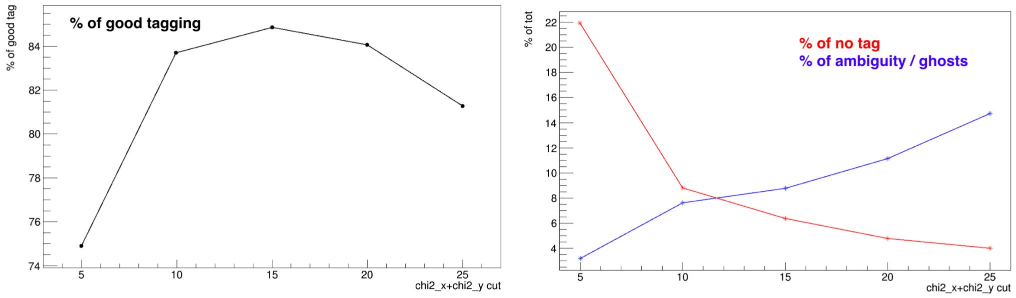

Figure 4.25: (Left) The efficiency of the tagging procedure performing PID using χ^2 selection. (Right) Fraction of events without tagging in red and tagged ambiguously in blue as a function of χ^2 values.

of the layers positions, with respect to the the nominal positions, but with ambiguous results. Therefore we decided to rely on the nominal distances.

4.4.8 μ-e correlation

We collected data colliding 160 GeV muon colliding on 8 mm target. The goal was to gather events to study the correlation between the muon and electron elastic scattering angles, to be able to test the pattern recognition algorithm and to make preliminary studies of the background and of possible selection variables.

The UA9 apparatus used for this test beam had no stereo planes for x,y disambiguation. The ambiguities generates ghosts that made the pattern reconstruction difficult. We have chosen to test an algorithm with a minimum requirement, of two and only two hits per plane.

Angular measurements requires tracking the incoming muons with the upstream modules, and tracking the two outgoing muon and electron. The upstream section allowed tracking with very good resolution. No particle ID detectors were available to distinguish the scattered particles.

A pattern recognition algorithm had been developed with track finding capabilities and for track fitting. A procedure for tracking the scattered muon based the best track χ^2 has been developed. It acts selecting the best track candidate as the muon my means of the sum of the χ^2 in both views, a choice that proved to be very powerful:

- we have selected a downstream topology of 2 and only 2 hits per layer, to identify elastic candidates. The χ^2 requires at least 3 hits per track, and in this case there were just 3 downstream layers;

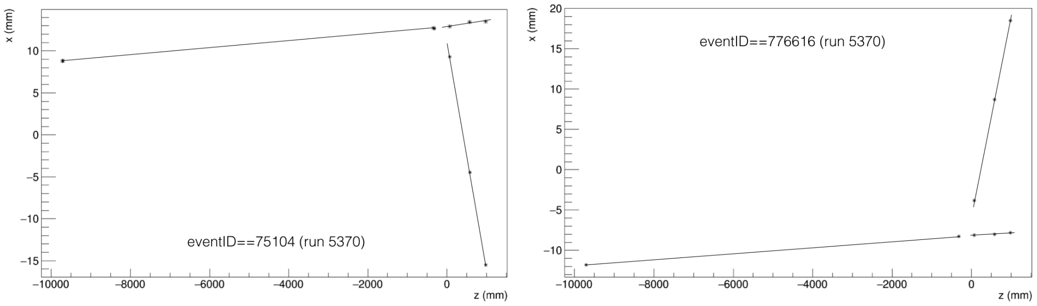

Figure 4.26: Event displays of selected μe scattering candidates.

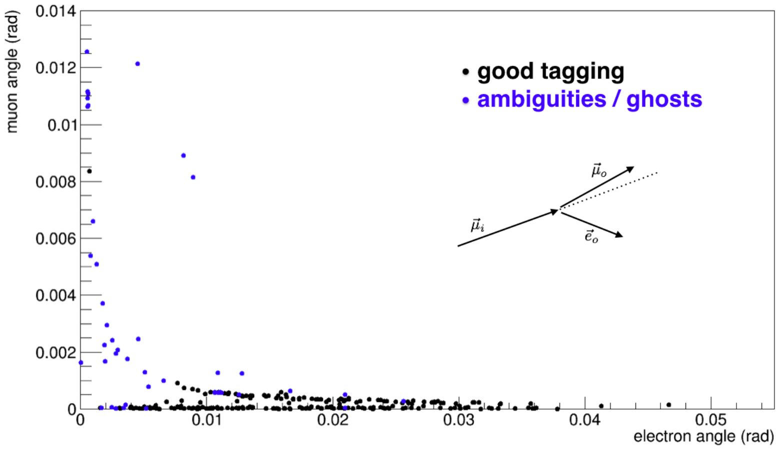

Figure 4.27: First angular θ_μ-θ_e correlation plot.

- all the possible hits combinations have been used to determination the track parameters and χ^2 on separate x and y views;

- we have chosen the best track pairs among all the combinations as the best χ^2, lower than a given threshold;

- in case of ambiguities, i.e. several good pairs are selected, events were further analyzed to understand their patterns.

Figures 4.25 show the results of the study performed to determine the optimal values of the χ^2. As expected a loose selection increases the number of ambiguous tracks combination, while a tight cut minimizes the ambiguity, but increasing the probability of an untagged event. A good condition is found for $\chi_x^2 + \chi_y^2$ around a value of 15.

Some of the event displays of the $2 \rightarrow 2$ selected candidates are shown in the fig. 4.26. The track fitting has been performed by tracking in the two

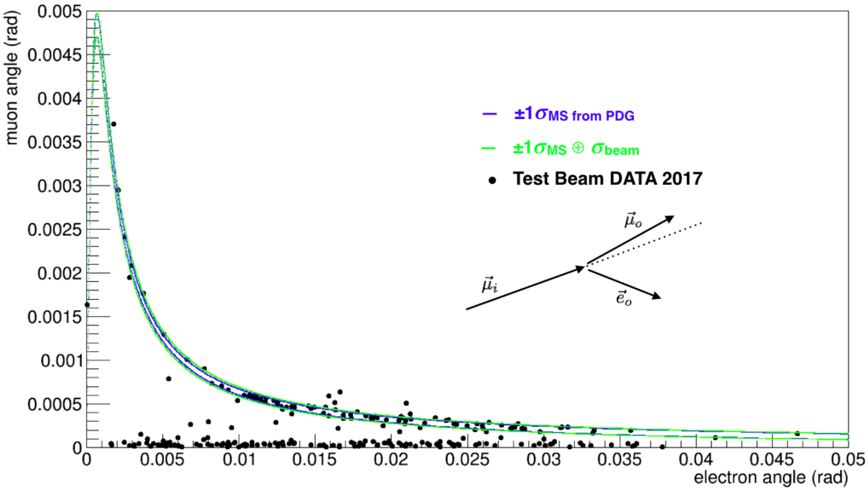

Figure 4.28: Angular correlation θ_μ-θ_e. There are about 250 selected events. It is shown the kinematics prediction convoluted with the multiple scattering effect and the beam energy spread.

separate views and constructing the angular deflection α in space through:

$$\cos\alpha = \frac{m_{ix}m_{ox} + m_{iy}m_{oy} + 1}{\sqrt{(m_{ix}^2 + m_{iy}^2 + 1)(m_{ox}^2 + m_{oy}^2 + 1)}}, \tag{4.26}$$

here m_i and m_o are the slopes of the incoming and outgoing tracks respectively in the x and y views.

We found 251 events surviving the selection. Figure 4.27 shows the expected angular correlation. Many events are close to the predicted elasticity curve. Few points in the horizontal band are expected as background from e^+e^- pairs and from high order radiative processes.

In blue we indicates the ambiguous combinations, classified by the algorithm [numeri] They have been found mostly where they are expected: in the region where the angles and energies of muon and electron are approximately the same. In this region both the tracks χ^2 are good (particles have high energies), so a discrimination algorithm based on χ^2 is not able to identify the muon and the electrons. This important aspect will be further explored in data analysis of the 2018 test beam.

Figure 4.28 shows the foreseen region for multiple scattering and beam spread effect: the experimental points seem very well contained within the resolution function.

Considering the low statistics it is impossible to perform a quantitative study of the selection efficiency of the selection of cuts. However, we have

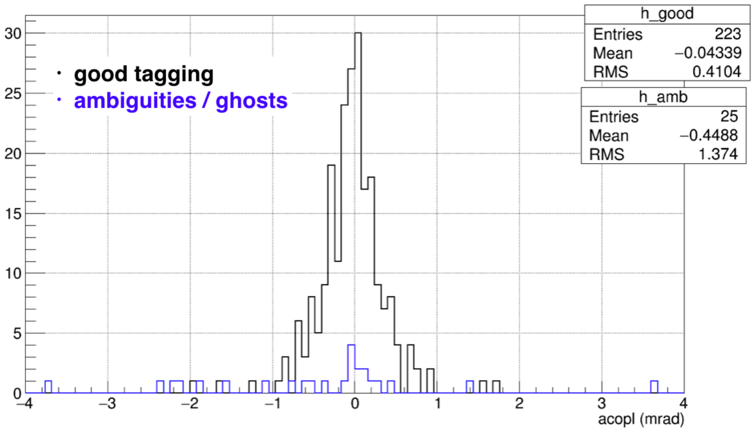

Figure 4.29: Acoplanarity distribution, with the definition in eq. (4.27).

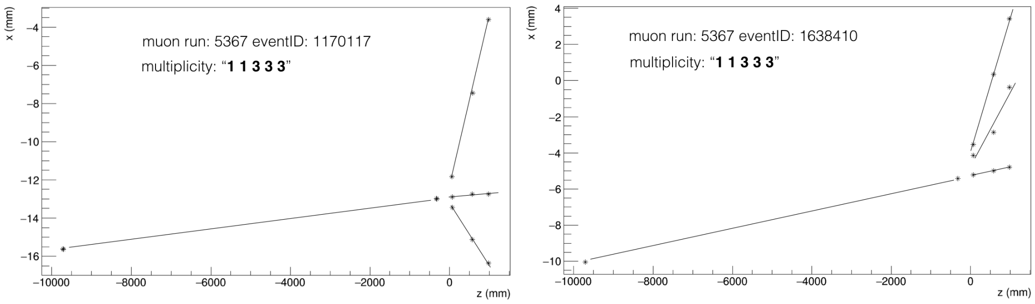

Figure 4.30: Displays of events with higher multiplicity: 1 → 3 events.

tested the effects of the acoplanarity cut. The input and output tracks should belong to the same plane, because of the momentum conservation. Coplanarity is violated because of experimental effects (multiple scattering and intrinsic resolution) and because of the radiative corrections. Here we used the following definition:

$$A_1 = \frac{\pi}{2} - \arccos \frac{\vec{\mu}_i \cdot (\vec{\mu}_o \times \vec{e}_o)}{|\vec{\mu}_i||\vec{\mu}_o \times \vec{e}_o|} \tag{4.27}$$

As shown in fig. 4.29, the expected events are distributed around zero, which corresponds to the ideal coplanarity condition, defined by the outgoing directions $\vec{\mu}_o$ and $\vec{e}_o$. This definition does not seem very selective and in the next section we tested a second definition more efficient to reject background. Finally some event displays corresponding to three particles final state are shown fig. 4.30. Most probably these events are due to e^+e^- couple background, see sec. 3.5.2.

The results of the 2017 are currently being published [8]. The analysis

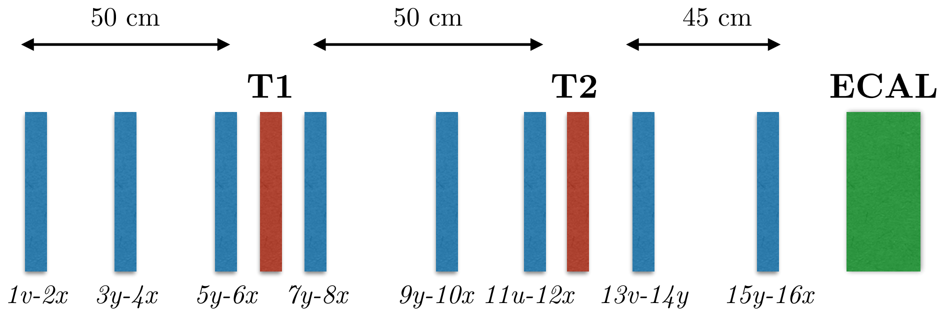

Figure 4.31: TB18 setup layers (not to scale).

of the scattering events shows that signal clearly appears with the expected characteristics, although the apparatus was not optimally designed to accomplish this task.

4.5 Test beam 2018 results

The 2018 test beam was dedicated to the study of μ-e elastic scattering events. On this purpose we used two modules prototype, similar to those foreseen for final apparatus: length of the module 50 cm and 1 m in the second part of the test beam, high sensors transverse dimension of 10×10 cm^2, muon energy around 180 GeV and also an electromagnetic calorimeter located downstream the modules. The test beam has been executed parasitically, putting the detector downstream COMPASS.

This test was a proof-of-concept of the measurement, performed in order to verify the experimental constraints that will have to be addressed by the MUonE apparatus. Results about data quality, alignment and the preliminary physics analysis will be shown. The analysis instead is still ongoing. Details about the hardware and the DAQ system have been given in [9].

Aim of this section is not report in detail all the setups used in the test beam: the technical details together with an independent analysis are reported in [71]. We present the results on the quality analysis of the sensors, how we coped with the encountered problems and how these aspects have affected the final physics analysis.

4.5.1 Data quality analysis

First we studied the hits quality. Then by performing a preliminary alignment and a strictly analysis of each layer residuals distribution, we realized

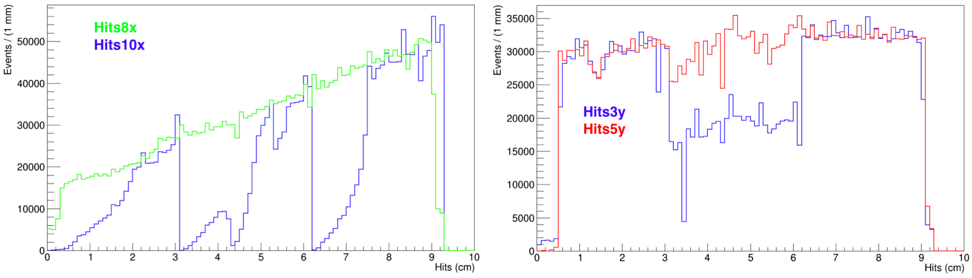

Figure 4.32: Hits profile of some problematic layers ($3y$, $10x$) in comparison with $5y$ and $4x$ that no show hits inefficiencies.

that several sensors have serious problems:

- partial or total inefficiencies, i.e. suppression of hits counting, by single readout ASICs;
- severe systematic shifts of the readout positions of entire blocks of strips;
- dead strips at the boundaries of the region covered by different ASICs;
- non-uniform point resolution along the sensor.

A sketch of the apparatus is shown in fig. 4.31. The strips are read by 3 ASICs. Figure 4.32 shows the typical structure of the detected inefficiencies. They are clearly due to the read-out system of the silicon sensors. These problems overlap and modify the measured beam profile which looks like uniform in y (as visible from the $5y$ hits distribution in red) and almost linearly in x (from the $4x$ distribution in green).

Most serious inefficiencies, such as $10x$ layer, led to the replacement of the related sensors during the beam test. Thanks to the collaboration with the Insubria group, more moderate problems, such as the one presented by $5y$ layer, have been quickly interpreted as due to the high intensity of the incoming muons, with regards to the front-end electronics. The electronics appears to be beyond the limit, as stated in sec. 4.1.2. from the point of view of dead time. Therefore, some ASICs, especially those at the beginning of the apparatus, suffer from the high counting rate especially when COMPASS has requested a higher muon rate.

We have aligned the sensors, using the procedure already described. To construct the residuals we used the first sensor of the upstream module and the last one of the downstream module. They were selected to maximize the distance. For this test beam were used $\sim$ 187 GeV muons only. Muons themselves had been employed for the detectors alignment.

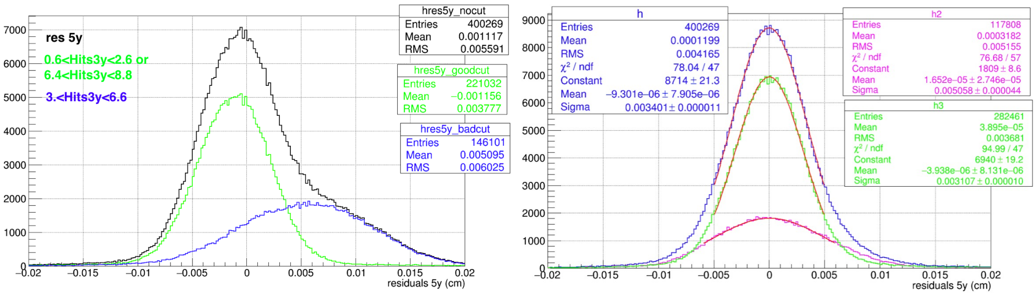

Figure 4.33: Residual distribution for $5y$ layer, with a cut on $3y$ to select the ASIC 1 and 3 (green) or the central one (blue). (Left) Before correction, (right) after correction.

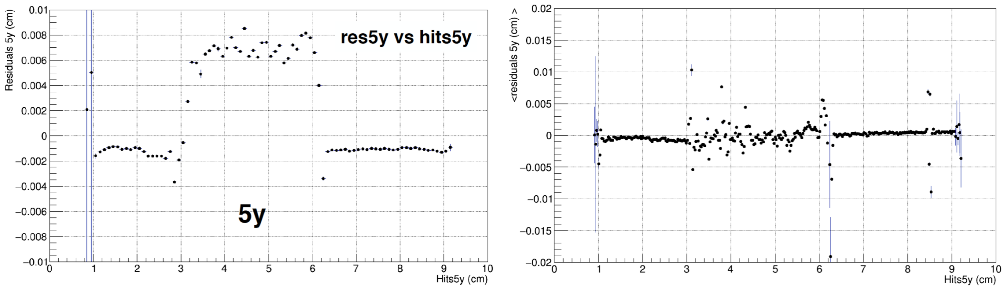

Figure 4.34: Profile of $5y$ residuals as a function of the same $5y$ hits, (left) before and (right) after the systematic shift correction of about $+65\,\mu$m.

The preliminary evaluations of the residuals have allowed us to detect further problems. Figure 4.33 (left) shows the residuals of $5y$ layer that present a bump. We have detected two components generating it, by selecting different regions on the $3y$ sensor as reference. The alignment algorithm automatically tried to mediate between the two components. By using only as reference the hits readout by the outer ASIC (first and third) of $3y$ layer, the $5y$ residuals distribution looks like as should be as shown in fig. 4.33 (right): a gaussian shape well aligned without bumps or other structures, with a width in agreement with the quoted intrinsic resolution.

The central ASIC clearly does not work properly: it can be noticed limits in the read-out capabilities of the central ASIC. For $5y$ layer we measured a systematic shift on the measured hits of $+65\,\mu$m, as shown in fig. 4.34 (left), while for $3y$ sensors it is $-25\,\mu$m (fig. 4.37). These shifts were identified as due to the high counting rate. They were corrected during the offline analysis stage by applying the corresponding offsets: see fig. 4.34 (right) and the related fig. 4.35.

Dead strips were found in all the layers. They have caused further prob-

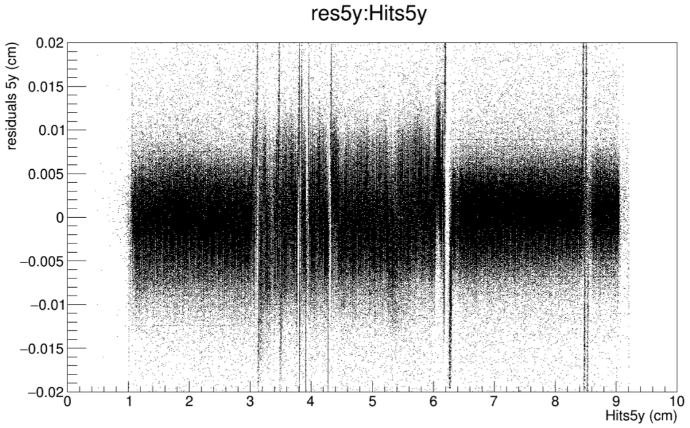

Figure 4.35: Scatter plot of $5y$ residuals as a function of $5y$ hits, after systematic shift correction of the central ASIC.

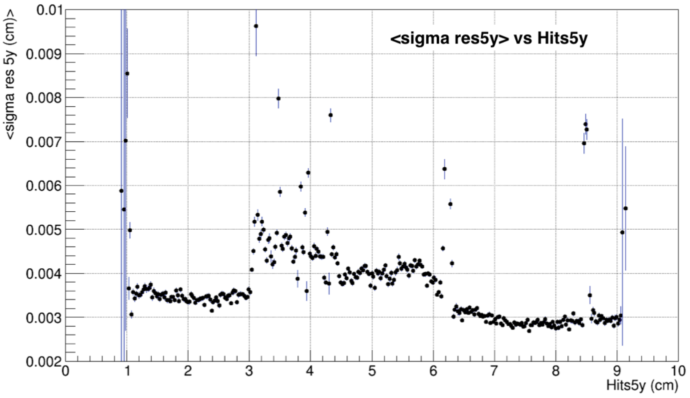

Figure 4.36: Profile of the residuals RMS of $5y$ layer as a function of $5y$ hits.

lems. As we can see in figg. 4.37 and 4.38, these inactive strips generate systematic shifts in the neighboring ones. In fact, because of the analogue readout, dead strip affects clusters measurement since the hits positions are reconstructed using the centre of gravity method (see appendix C.2). If a strip does not read the deposited charge, the clustering algorithm takes in account only signals of the adjacent ones, producing a systematic bias (up to ~ 100 μm) higher than the intrinsic precision that needs to be corrected.

The points dispersion in the residuals scatter plots as a function of the hits should be correspond to the hit intrinsic resolution ($\sim$ 30-35 μm), given the high energy muons. Considering the high statistics samples used for the alignment ($N > 10^5$), the residuals means must be around zero within the errors because they scale as $\sqrt{N}$.

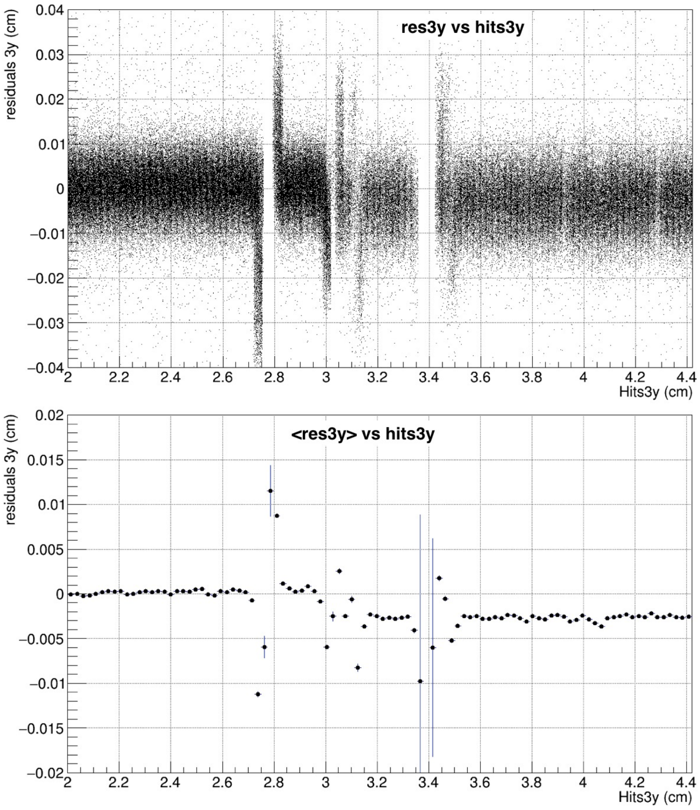

Figure 4.37: (Top) Scatter plot of $3y$ residuals as a function of $3y$ hits. (Bottom) Corresponding profile plot. To notice the systematic shift of about $-25\,\mu$m in the measured hits by the central ASIC ($\gtrsim$ 3.1 cm).

Figures 4.36 and 4.38 show the point resolution analysis of individual strips as a function of their position. A detailed analysis of the residuals width enables to scan the uniformity of the sensors response. It is a fine-grained "muography", strip by strip, allowed by high energy muons.

In addition to the problems already discussed, fig. 4.36 shows that $5y$ sensor presents also a serious problem of resolution uniformity. Strips read from the central ASIC have a significant lower precision than those read by the others: 40-45 μm in comparison to 30-35 μm of first and third ASICs. Figg. 4.38 show the same analysis performed on $13y$ sensor, one of the layers with less hits efficiency problems. Although it should be notice they are several dead strips at the ASIC boundaries and also a non-uniform resolution which appears to be changing (in 2 cm range) from 25 to 30 μm.

We can analyze the direct impact of this resolution uniformity problems on the angular deflections. Figure 4.39 (top) shows the angular deflection

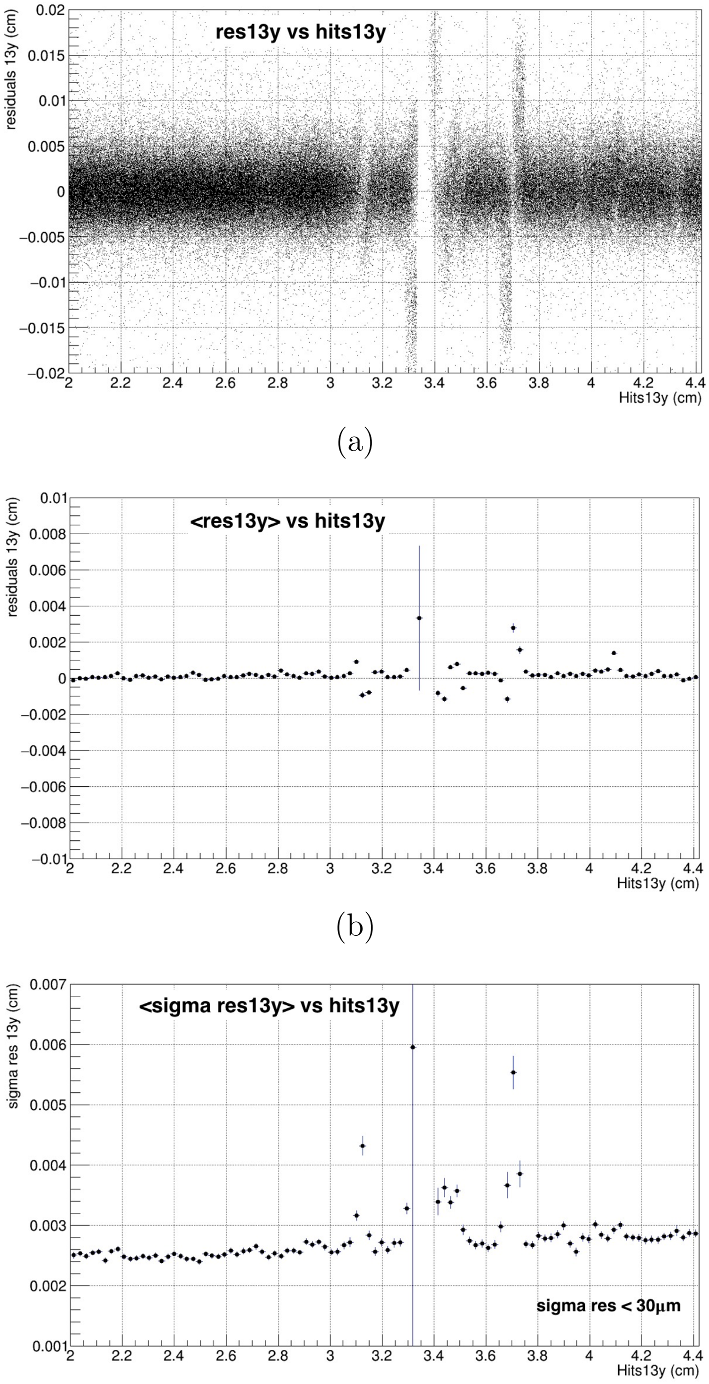

(a)

(b)

(c)

Figure 4.38: Residual analysis of 13y, one of best layer of the setup: zoom at the boundary between the first and second ASICs. (a) Scatter plot of residuals as a function of hits. (b) Corresponding profile plot. (c) Profile plot of the corresponding residuals width.

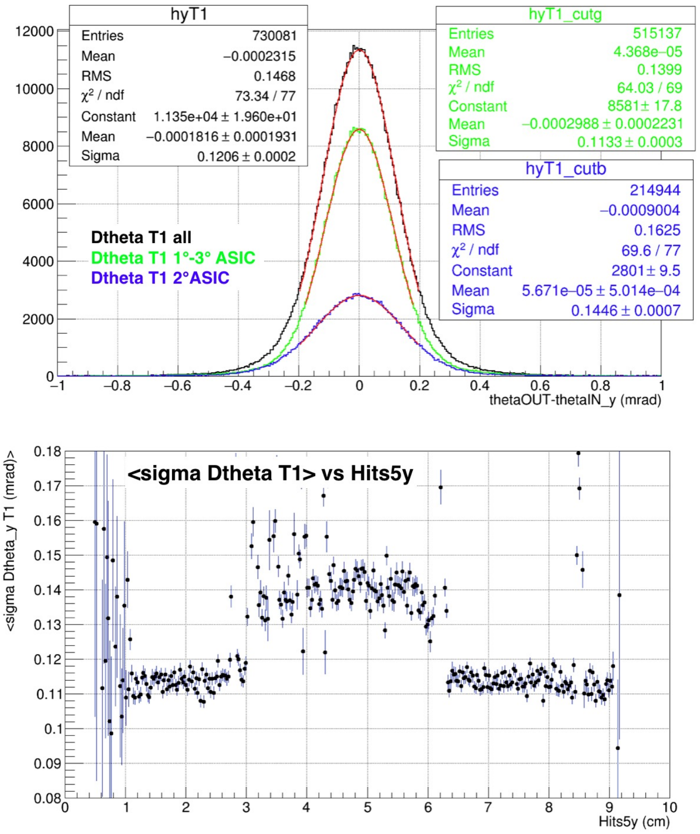

Figure 4.39: (Top) Angular deflection of passing muons of 187 GeV through a first graphite target of 8 mm, selecting different hits of the $5y$ layer. (Bottom) Profile of the angular resolution as a function of the $5y$ sensor: ~ 0.11 mrad is how we expect for the intrinsic angular resolution of the two targets configuration of TB18.

of the passing muons $\theta_{\mathrm{OUT}} - \theta_{\mathrm{IN}}$ (due to the intrinsic resolution) produced through the first target, explicitly taken the problematic $5y$ hits to construct the incoming tracks. Selecting different groups of hits corresponding to the different ASIC, the distributions appear well aligned thanks to the bias correction already explained.

However, one can notice that the angular deflection widths are significantly different: 0.113 mrad (first and third ASICs) versus 0.145 mrad (central ASIC), with a difference of about 22%. This discrepancy perfectly matches the difference between the hits resolution seen in fig. 4.36: a mean of 33 μm (first and third ASICs) in comparison with 43 μm, with a difference of $\sim$ 23%. Therefore an uniformity scansion of the hits resolution, as a function of the sensor surface, can be perform also on the angular deflection, by using

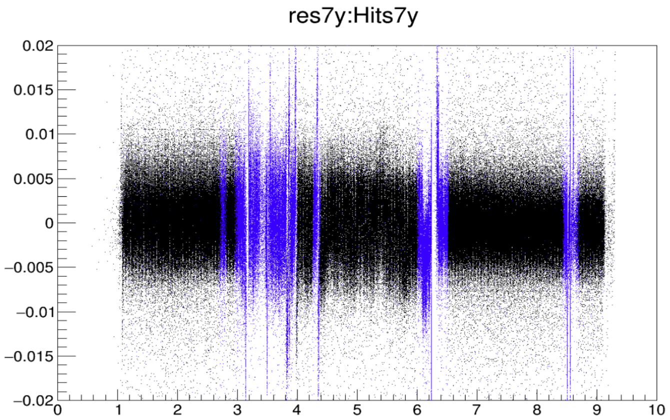

Figure 4.40: Scatter plot of residuals as a function of hits (in cm) for the $7y$ layer, to explain the action of the fiducial mask, in blue.

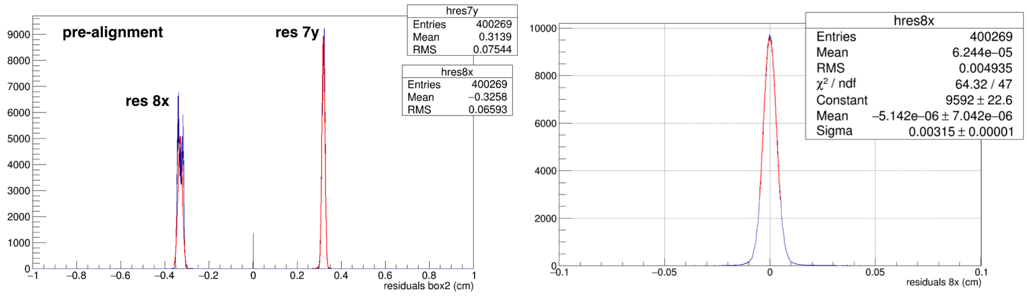

Figure 4.41: Residuals before ($8x$ and $7y$ planes) and after the alignment ($8x$ plane).

the huge data samples of passing muons as shown in fig. 4.39 (bottom). This is an important analysis which will have to perform on the definitive sensors of the MUonE apparatus.

Due to the limited availability of spare sensors, all these problems led us to create quality mask to remove the groups of bad strips and to cope with the imperfections. The figure 4.40 shows the actions of this mask on a single layer. No hits were eliminated, but those identified as problematic were tagged with a flag, available to the analysts. In tab. 4.7, we reported the fractions of the critical hits encountered per layer with respect to the total.

4.5.2 Alignment

Figures 4.41 and 4.42 show the corrections to the transverse shifts and rotations with respect to the z axis of the beam. As in the case of the 2017

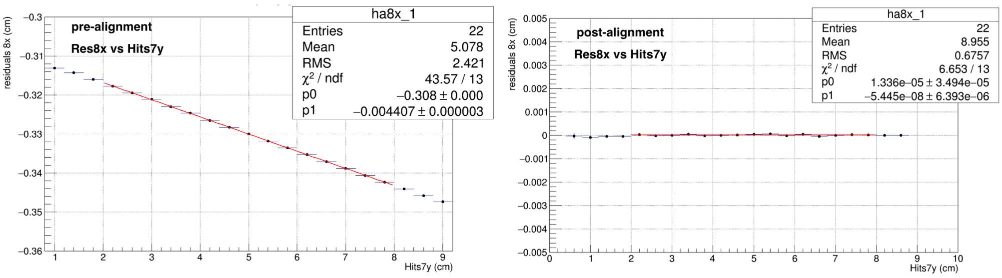

Figure 4.42: Correlation between residuals of a layer as a function of the one in the same box.

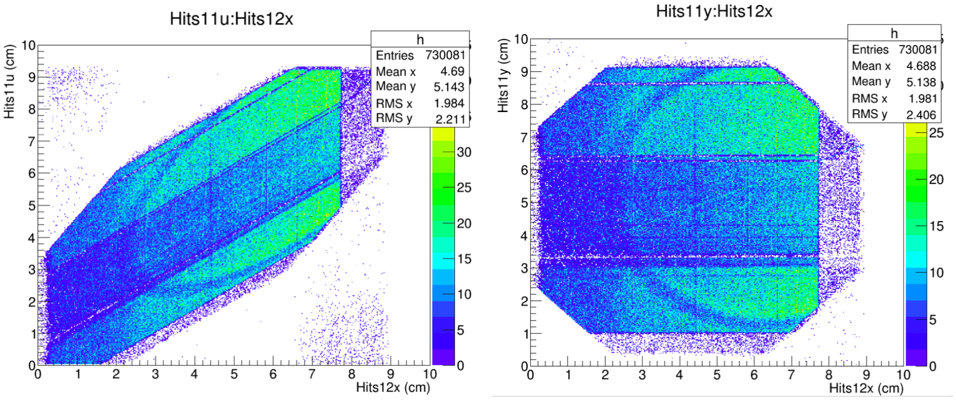

Figure 4.43: Sensor images reconstructed from $11u$ and $12x$ hits (left) and after the rotation of stereo $11u$ hits (right).

test beam, the first ones had been corrected within 1 μm, while rotations had been corrected within 0.1 mrad.

In this setup there are also stereo planes, useful to disambiguate multiple hits patterns, typically produced by strip detectors. As a preliminary step, the hits of all the planes have been rotated and aligned in the same way as the others (fig. 4.43). The discrimination power was used in the next pattern recognition phase. To notice that the xy planes, obtained from stereo layers, are “blunted” because of the lack of the corresponding coordinate in one view x or y.

From an accurate evaluation of the interdistances between sensor layers, we discovered the presence of tilts with respect to the x axis. Particularly relevant this appearing in the $9y$ plane. Although it is a second order effect, we were able to identify and correct it from the data thanks to the wide open muon beam. Figure 4.44 (right) shows the tilt scheme; on the left, the incoming beam angular profile in y view. In figg. 4.45 we report the correlation between the $9y$ residuals as a function of the same hits, before

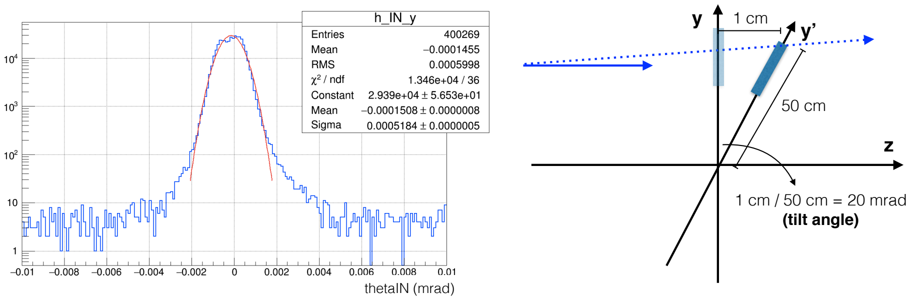

Figure 4.44: (Left) Incoming beam angular profile in y view. (Right) Estimated tilt along x axis of $9y$ layer (figure not to scale).

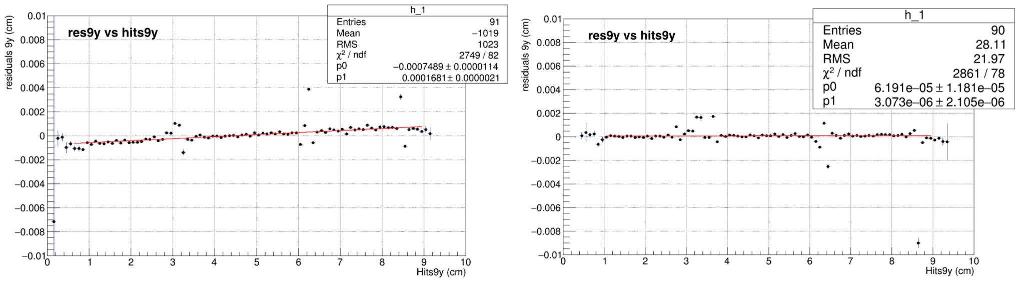

Figure 4.45: Tilt of $9y$ layer, from correlation between residuals and hits of the same $9y$ plane, before and after the tilt correction.

and after correction, that we identified as necessary to analyze this effect. The measured angular tilt of $9y$ from the data is about 18 mrad. This value corresponds to the one assumed by the interdistances survey. The applied geometrical correction to the $9y$ hits is:

$$\begin{aligned} y'_9 &= \cos\theta \cdot y_9 \\ y'_9 &\sim (1-\theta^2/2)\cdot y_9 \\ \theta^2/2 &\sim 0.00017\,\mathrm{rad}^2 \;\Rightarrow\; \theta \sim 0.018\,\mathrm{rad}, \end{aligned} \tag{4.28}$$

where y_9 and y'_9 are the $9y$ hits before and after correction, while θ is the tilt angle (see fig. 4.44 for reference).

4.5.3 Hits and event efficiencies

For the analysis of the elastic μ-e events we used an algorithm of pattern recognition, analogous to that developed for the TB17 (see sec. 4.4.8). It has been extended to include in the selection of downstream multiplicities other topologies, with respect to the simple “222”, (that is two and only two hits

layers	σ_{res} (μm)	bad hits (%)	hit eff (%)	event eff ϵ (%)
$1y$	49	34	94.6	
$2x$	38	13	95.1	
$3y$	43	6	73.9	
$4x$	40	3	76.8	
$5y$	31	19	98.6	
$6x$	32	10	98.8	
$7y$	26	7	96.1	67.5
$8x$	25	5	96.7	54.4
$9y$	28	4	59.9	78.2
$10x$	40	65	59.2	25.0
$11y$	39	1	98.2	81.3
$12x$	25	1	98.4	88.6
$13y$	31	8	94.8	83.8
$14x$	41	1	94.3	79.5
$15y$	45	5	82.1	80.6
$16x$	48	16	83.4	85.2

Table 4.7: Layer residual widths, fiducial mask and hits, event efficiencies.

per layer), which in any case represents our golden selection mode. Since of the large number of inefficiency problems, we tried to evaluate:

- the hit efficiency per tracking module,
- the overall event efficiency.

Table 4.7 shows the hit efficiencies. We have made a fit through all the layers excluding those under investigation, by choosing one and only one hit per layer and determining the correct covariance matrix. We have evaluated how many times there are not hit on the reference plane within a tolerance window of $3\,\sigma$, with σ equal to the angular resolutions of the planes, estimated by the amplitudes of the residues. To clean the reference data sample used to determine the efficiency, a χ^2 cut was also applied to the tracks: $\chi^2_x + \chi^2_y < 26$, equal to a probability for the χ^2 with 8 degrees of freedom of the order of $1 \cdot 10^{-3}$.

As expected from the quality analysis appeared that the worst sensors was the $10x$ layer (fig. 4.32). This layer has been replaced during the data taking process. In general, we measured the efficiency of a silicon layer to be more than 99%. The values of these efficiencies, excluding the critical hits, were not evaluated using the strip mask we prepared. However, the low values certainly have an effect on the reconstruction of elastic events.

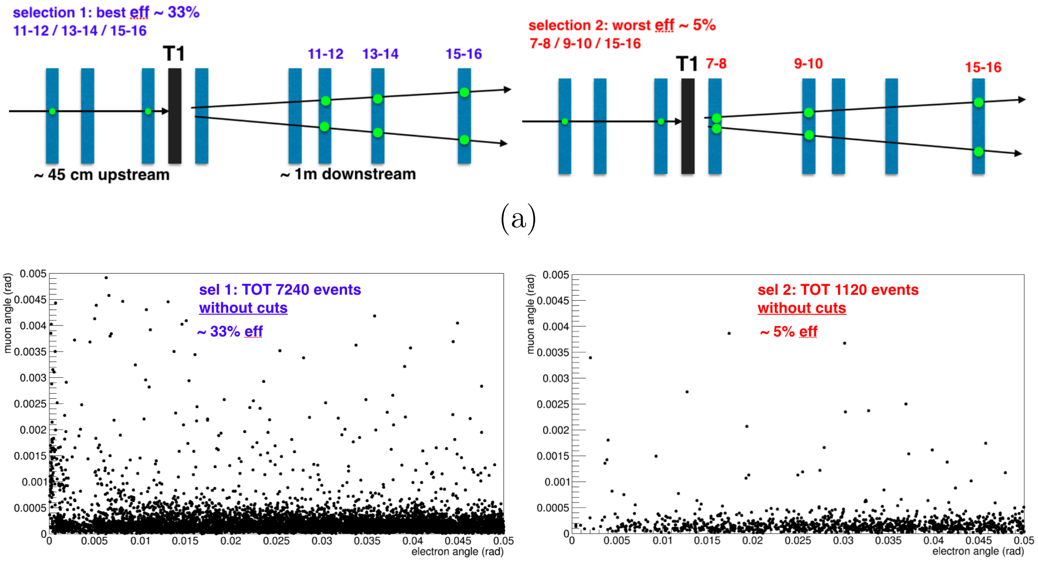

(a)

(b)

Figure 4.46: (a) Selections of different efficiencies on the same run. (b) Angular reconstruction θ_μ-θ_e related to the selections in (a).

In order to estimate the impact of the detection problems on the final physics analysis, we determined the event efficiency per layer. The estimation of the event efficiency is more complicated than the hit efficiency, because in order to avoid bias it is important to select with accuracy the reference sample.

For this reason we have chosen a limited topology for the input tracks (1 hits per layer) and for the output tracks: 2 and only 2 hits per layer, without conditions for the sensor under analysis. Table 4.7 shows the results of this multiplicity analysis. All layers have efficiency per event below 90%. Beyond the known low value of the efficiency expected for the $10y$, we detect a bad behavior also for the $7y$ and $8x$ layers, which have shown relatively high hits efficiency. These two layers are the locate immediately after the T1 target, at a distance of 10 cm. We understood the bad performance on event efficiency were due to the capability to discriminate two close hits. Our collaborators, who set up the TB18 apparatus, confirmed this hypothesis.

To quantitatively check the validity of these estimates, it was decided to divide the events of a large run into two categories of different event efficiency to analyze exactly in the same conditions. We selected $N_\mu = 18.4 \cdot 10^6$ incoming muons. We considered the coincidence of the three best layers response per view getting:

$$\begin{aligned}\epsilon_{max} &= \epsilon_{11u} \cdot \epsilon_{12x} \cdot \epsilon_{13y} \cdot \epsilon_{14v} \cdot \epsilon_{15y} \cdot \epsilon_{16x} \\ &= 0.81 \cdot 0.89 \cdot 0.84 \cdot 0.80 \cdot 0.81 \cdot 0.85 \sim 33\%\end{aligned} \tag{4.29}$$

and the three worst:

$$\begin{aligned}\epsilon_{min} &= \epsilon_{7y} \cdot \epsilon_{8x} \cdot \epsilon_{9y} \cdot \epsilon_{10x} \cdot \epsilon_{15y} \cdot \epsilon_{16x} \\ &= 0.68 \cdot 0.54 \cdot 0.78 \cdot 0.25 \cdot 0.81 \cdot 0.85 \sim 5\%\end{aligned} \tag{4.30}$$

as explained in fig. 4.46(a). We measured the best efficiency for double track detection to be about 33% (to note the absence of the second target). The pattern recognition algorithm was then applied by reconstructing the events of this same run, selected with these two sets of detectors. Results of the reconstruction are shown in fig. 4.46(b). The ratio R_{counts} between the candidates number identified in the two cases corresponds precisely to the ratio R_ϵ between efficiencies:

$$\begin{aligned}R_{\text{counts}} &= 7240/1120 = 6.5 \pm 0.3, \\ R_\epsilon &= 33\% \,/\, 5\% = 6.6.\end{aligned} \tag{4.31}$$

Considering the number of the incoming muons N_μ selected for this analysis, we can calculate the observed integral rate r_{tot} of the total events (signal + backgrounds) within 50 mrad corrected for the estimated inefficiency. For the sample with the best efficiency:

$$r_{\text{tot}} \sim \frac{7240/33\%}{18.4 \cdot 10^6} \sim 1.2 \cdot 10^{-3} \quad \text{for } \theta_e < 50\,\text{mrad}. \tag{4.32}$$

This event number per incoming muon matches the order of magnitude found with the preliminary GEANT4 simulation reported in sec. 3.5.2 of about 10^{-3}. In that case, the target was 20 mm of Beryllium, here we have 8 mm graphite. Scaling for the different thickness and scattering centers number, it obtains a factor 2 in favor of the MC. A detailed GEANT4 simulation is under construction to check these preliminary estimations and also the differential efficiencies as a function of the electron angle.

4.5.4 Final results

One of the most interesting results we obtained is the angular resolutions measured in TB17 and TB18 as shown in fig. 4.47. The muon energy in the two cases is similar: 160 GeV in 2017, 187 GeV in 2018. The thickness of the silicon layers is not significantly different. Figure shows how the angular

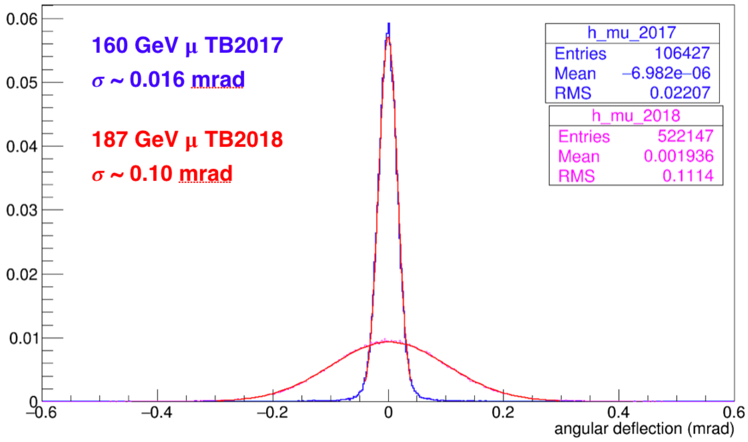

Figure 4.47: Comparison between the angular resolution for 2017 and 2018 test beams, by using muons of 160 GeV and of 187 GeV respectively.

deflections (determined as the difference between downstream and upstream directions) are substantially different. The widths of the distributions include the small contribution of the multiple scattering. The dominant effect is due to the intrinsic trackers resolution.

The relatively poor angular resolution identified in TB18 motivated us to remove the second target (T2) in the final phase of the data taking, in order to get a larger downstream arm. It was also essential for tracking the electrons to the calorimeter.

The calorimeter measured the energies of the scattering electron: details are reported in ref. [71].

To select the incoming muons sample, we applied a strong selection of one and only one hit for all upstream layer and all x/y view (first 3 tracking module). The aim was to safely clean the initial sample, considering the problems of this setup. The resulting number of incoming muons is $\sim 58.2 \cdot 10^6$.

Figure 4.48 shows a preliminary result about the μ-e angular correlation obtained by using the described pattern recognition method and the experimental cuts discussed below. With the same combinatorial method already used in TB17 to discriminate the muon from the electron, based on the best χ^2 to recognize the muon, we evaluated topologies with 3 hits per layer. It has not been possible so far to evaluate the efficiency of this algorithm. GEANT4 simulations are ongoing to estimate this efficiency, as well as that of possible alternative methods.

The region of small electrons angles seems to be scarcely populated. The reason is still under investigation. It is not clear because due to the cross section just few events are expected below 5-10 mrad. The integrated elastic

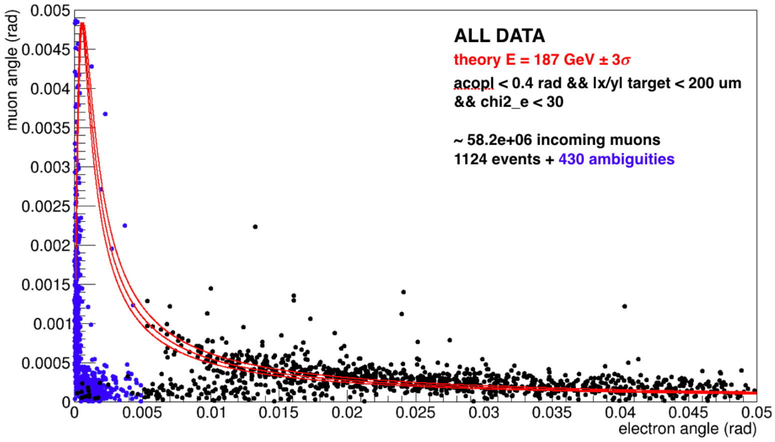

Figure 4.48: Angular correlation μ-e with kinematical cuts only (without using calorimeter data).

cross sections between 4.5 and 5.5 mrad is $\sim 2\ \mu$b, while between 39.5 and 40.5 mrad is $\sim 20.2\ \mu$b: so we expect an order of magnitude difference between counts around elasticity the curve in these two regions (μ-e events for $E_e > 1$ GeV). The layers inefficiencies, mentioned above, could partially explain this apparent lack, both there could be other possible inefficiencies in the tracking and pattern recognition algorithms.

In this analysis (fig. 4.48) only kinematic cuts had been applied as we now discuss:

- quality cut on track χ^2: $\chi_x^2 + \chi_y^2 < 30$;
- an interaction vertex cut of 200 μm to constraint incoming and outgoing directions at the target nominal position;
- a loose coplanarity cut of 0.4 rad with the definition A_2 in eq. (4.34).

We have tried different definitions of acoplanarity and also a common vertex constraint to the target that has demonstrated a good capability to reject pair background. Let's recall the definition of acoplanarity we gave in sec. 4.4.8:

$$A_1 = \frac{\pi}{2} - \arccos \frac{\vec{\mu}_i \cdot (\vec{\mu}_o \times \vec{e}_o)}{|\vec{\mu}_i||\vec{\mu}_o \times \vec{e}_o|}. \tag{4.33}$$

It is based on the scalar product between the incoming muon direction $\vec{\mu}_i$ and the plane generated by outgoing directions of muon $\vec{\mu}_o$ and electron $\vec{e}_o$. This variable is not particularly effective to reject e^+e^- pairs background. It doesn't consider that two particles are not back-to-back in the transverse

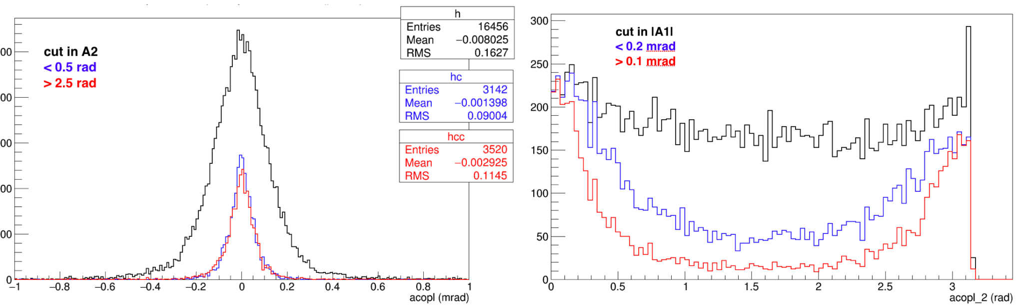

Figure 4.49: Acoplanarity definition A_1 (left) and A_2 (right).

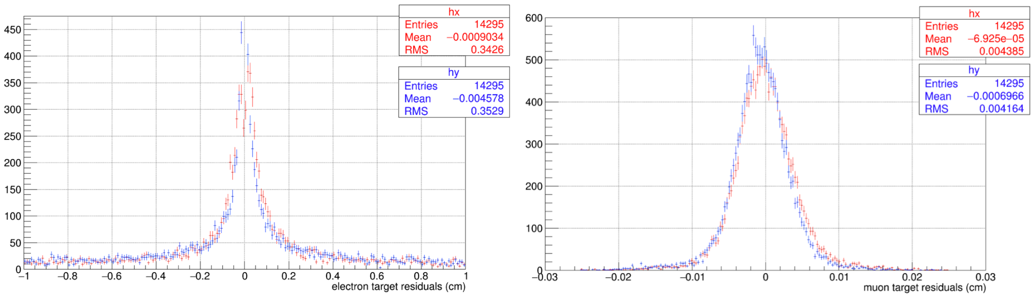

Figure 4.50: Distribution of residuals, in x (red) and y (blue) view, defined by the difference between outgoing (of muons on the left and electrons on the right) and incoming μ direction at the nominal position of the target.

plane, as one can expect for the momentum conservation. For this reason, we have introduced a second definition:

$$A_2 = \pi - \arccos \frac{(\vec{\mu}_i \times \vec{\mu}_o) \cdot (\vec{\mu}_i \times \vec{e}_o)}{|\vec{\mu}_i \times \vec{\mu}_o||\vec{\mu}_i \times \vec{e}_o|} \tag{4.34}$$

In this case, $A_2 \sim 0$ only for back-to-back particles. Figures 4.49 show the relative effects of the two definition. By using some analyzed samples we realized that $A_1 \sim 0$ for both the cases $A_2 \sim 0$ and $A_2 \sim \pi$, Therefore a cut in this second definition is more efficient on the background that still has good coplanarity in A_1.

We have then constructed the distributions of residuals defined as the differences between incoming muons and scattering muons and electrons at the nominal position of the target. Figure 4.50 show the related distributions for muons and electrons and demonstrated the good definition of this variable: the distribution are well centered to zero and the width for the muons of about 40 μm is in agreement with what can be expected from the intrinsic resolution.

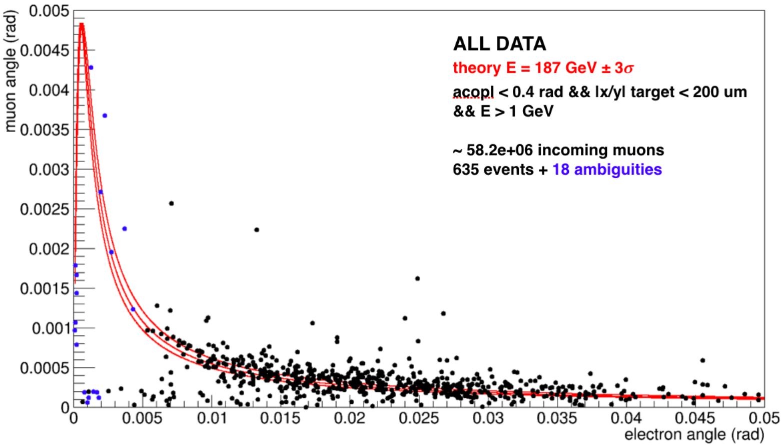

Figure 4.51: Angular μ-e correlation with all applied cuts (see text), kinematic and on the electron energy: $E_e > 1$ GeV.

Figure 4.51 shows the selection on the electron energy with $E_e > 1$ GeV, applied in addition to the previous kinematic cuts, in order to expose the elastic scattering signal in the MUonE region of interest ($\theta_e < 30$ mrad). The effect is what we expect that is a strong efficiency in rejecting the background at the low muon angles. Roughly the counting drop observable at 30 mrad corresponds to the cutting value for kinematics.

Finally we can evaluated if the candidates number is in agreement with the expectation from μe cross section. Considering:

- the total number of incoming muons ($\sim 58.2 \cdot 10^6$) under analysis corresponding to the first three months of data taking,
- the probability of elastic scattering $\sim 1.1 \cdot 10^{-4}$ for $E_e > 1$ GeV and 8 mm graphite, see sec. 2.4.2,
- the 3 best trackers of efficiency of 33%,

the expected integrated number of signal events (μe elastic scattering for $\theta_e \lesssim 30$ mrad) is of the order of $2 \cdot 10^3$. After all the preliminary cuts applied, we found a number of candidate signal events of about $6 \cdot 10^2$, so a factor 3 of difference. Which becomes about a factor 10, not considering the estimated efficiency.

This conclusion is in agreement with the one of the parallel and independent analysis in [71]: $\sim 3 \cdot 10^3$ signal candidate events for $E_e > 1$ GeV with respect to $\sim 5 \cdot 10^8$ incoming muons, i.e. an estimated signal rate of about 10^{-5} against the expected of the order of 10^{-4}.

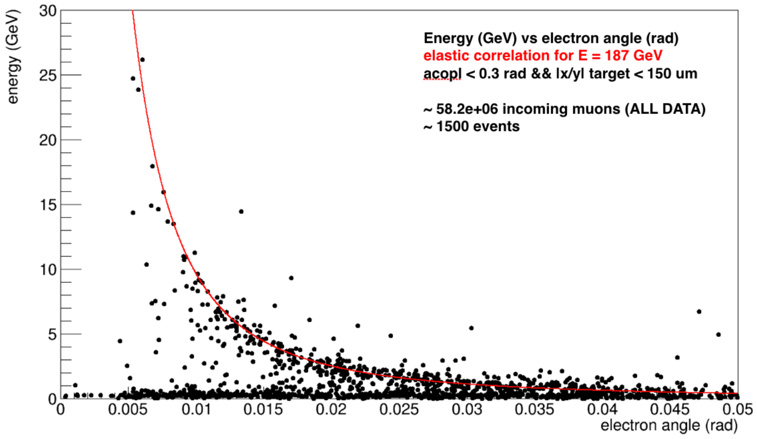

Figure 4.52: Correlation between electron energy E_e and scattering angle θ_e, with the predicted curve from kinematics.

However in these evaluations, we did not take in account the efficiency of the calorimeter, the pattern reconstruction efficiency, the effects of the acoplanarity cuts, vertex constraint and χ^2 selection cuts. And also the inefficiency due to geometrical acceptance because of the fact that the incoming muons impinge almost uniformly on all the sensors surface, causing a not quantified boundary effect.

Further analysis with the GEANT simulation could explain this lack of signal events, allowing to evaluate the efficiencies of all the selection variables.

Finally we show the preliminary analysis about the correlation between electron energy and angle, predicted by the kinematics. Figure 4.52 shows this results with all the applied cuts: many events collect around the kinematics prediction for 187 GeV incoming muons, qualitatively confirming the action of the downstream calorimeter.

Chapter 5

Extracting the anomaly

In this chapter we described the workflow to determine a_μ^{HLO} starting from the measurement of the running of α. Aim of the analysis is to verify the reliability of the method and assess the precision achievable in the determination of the a_μ^{HLO}. It paves the way to future works and more refined analysis on this fundamental aspect of the MUonE experiment. We will show results obtained in the leading order approximation. Moreover we discussed the effects of some experimental systematic errors on a_μ^{HLO}.

5.1 Fitting the LO cross section

5.1.1 Statistical exercises

As a first exercise we have determined the value of a_μ^{HLO} in the simplest case, generating simulated events by using the LO cross section with the running of $\alpha(t)$. The running is an high order effect, but has been factorized as an overall factor depending of the transferred momentum that modifies the LO cross section.

We want to fit the angular distribution of the elastic scattering events, collected in a fast-MC sample with muon beam energy of 160 GeV, using the analytical expression of the LO differential cross section as a function of θ_e:

$$f(\theta_e) = A \cdot \left(\frac{d\sigma}{d\theta_e}\right)_{LO} = A \cdot \frac{4\pi\alpha^2(t)}{\lambda(s, m_\mu^2, m_e^2)} \left(\frac{(s - m_\mu^2 - m_e^2)^2}{t^2} + \frac{s}{t} + \frac{1}{2}\right) \left|\frac{dt}{d\theta_e}\right|, \tag{5.1}$$

where A is a normalization constant, $dt/d\theta_e$ and $d\sigma/d\theta_e$ are given by eq. (2.64). The running of α is expressed as:

$$\alpha(t) = \frac{\alpha}{1 - \Delta\alpha(t)} = \frac{\alpha}{1 - \Delta\alpha_{\mathrm{lep}}(t) - \Delta\alpha_{\mathrm{had}}(t)} \tag{5.2}$$

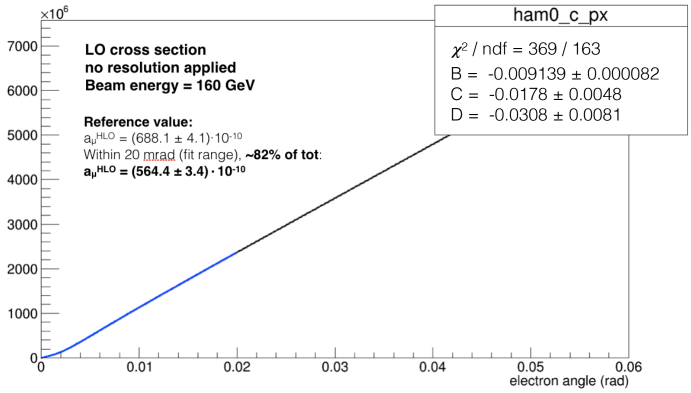

Figure 5.1: Fit result of the leading order cross section without resolution effects (black). Blue curve is the fitting function in eq. (5.1).

where α is the fine structure constant, $\Delta\alpha_{\text{lep}}(t)$ is the leptonic contribution (known with high precision), while $\Delta\alpha_{\text{had}}(t)$ has to be determined with the fit to calculate a_μ^{HLO} with the MUonE master formula (5.3):

$$a_\mu^{\text{HLO}} = \frac{\alpha}{\pi}\int_0^1 (1-x)\Delta\alpha_{had}[t(x)]dx. \tag{5.3}$$

To parametrize $\Delta\alpha_{\text{had}}(t)$ we have chosen a third-order polynomial with the constraint $\Delta\alpha_{had}(0) = 0$ as:

$$\Delta\alpha_{\text{had}}(t) = B\cdot t + C\cdot t^2 + D\cdot t^3. \tag{5.4}$$

This function has been proved to represent effectively the value of $\Delta\alpha_{\text{had}}$ can be determined with time-like measurements [44]. Other general parametrizations can be used, as proposed in [14].

With this model of the hadronic running, the fit function has 3 free parameters to be determined by fitting pseudo-data.

Figure 5.1 shows the results of the fit of an high-statistics sample (1/13 of the MUonE requested statistics) in the ideal case, without detector resolution effects. The fit returns:

$$\begin{aligned} B &= -0.009139 \pm 0.000082 \\ C &= -0.0178 \pm 0.0048 \\ D &= -0.0308 \pm 0.0081 \end{aligned} \tag{5.5}$$

The value of a_μ^{HLO}, calculated with the master formula in the interval $x \in [0.378, 0.936]$ using the fitted value of $\Delta\alpha_{\text{had}}$, returns:

$$a_\mu^{\text{HLO}}(\text{fit}) = (565 \pm 9)\cdot 10^{-10} \tag{5.6}$$

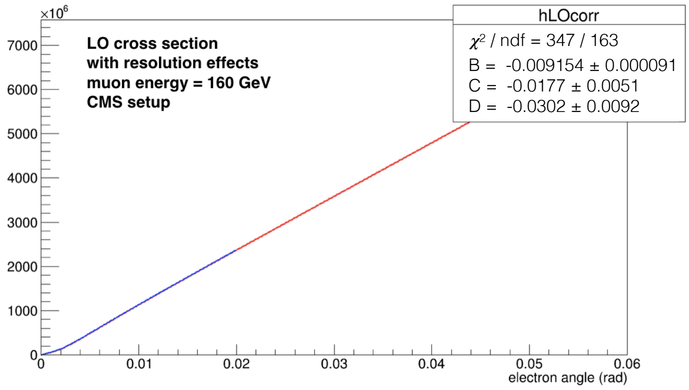

Figure 5.2: Fit result of the leading order cross section with experimental resolution effects (red). Blue curve is still the fitting function (5.1).

to be compared to the reference value:

$$a_\mu^{\mathrm{HLO}}(\mathrm{ref}) = (564.4 \pm 3.4) \cdot 10^{-10} \tag{5.7}$$

obtained integrating the reference $\Delta\alpha_{\mathrm{had}}$ function in the same interval. The integration interval corresponds to scattered electron energies in the observable range between about 1 GeV and 150 GeV (the maximum energy achievable by the electrons, considering a beam energy of 160 GeV).

The error associated to $a_\mu^{\mathrm{HLO}}(\mathrm{fit})$ is calculated by the error propagation of the statistical errors on the fit parameters.

As a second exercise we generated pseudo-experiments with the fast simulation considering the experimental resolution. In this case to fit data with the analytical model, requires the unfolding of the LO differential cross section [43].

The first step is to determine by MC the correction histogram h_{corr}^{MC} defined as:

$$h_{corr}^{MC} = \frac{h_{LO,s}}{h_{LO,0}}\bigg|_{MC}, \tag{5.8}$$

where $h_{LO,0}$ is the LO data distribution and $h_{LO,s}$ includes the resolution effects.

The unfolded LO cross section can be represented as the ratio of the histograms:

$$h_{LO}^{exp} = \frac{h^{exp}}{h_{corr}^{MC}}, \tag{5.9}$$

where h^{exp} is the result of an independent sample. Correction by ratios is the simplest unfolding procedure and is not free from possible bias [43], however it is suitable to solve this exercise.

Figure 5.2 shows the result of the fitting procedure applied to the data sample produced with fast-MC, for angular resolution achievable with the CMS 2S trackers. The values of the fit parameters are:

$$\begin{aligned} B &= -0.009154 \pm 0.000091 \\ C &= -0.0177 \pm 0.0051 \\ D &= -0.0302 \pm 0.0092. \end{aligned} \tag{5.10}$$

The corresponding value of a_μ^{HLO} is:

$$a_\mu^{\mathrm{HLO}}(\mathrm{fit}) = (563 \pm 10) \cdot 10^{-10}, \tag{5.11}$$

in agreement with $a_\mu^{\mathrm{HLO}}(\mathrm{ref})$ in eq. (5.7) within the errors. Remarkably this result has been obtained with 1/10 of the MUonE required statistics.

5.1.2 Uncertainty on the MCS model

We studied the systematic effect induced by the uncertainty on the knowledge of the multiple scattering. This is the systematic error that could be introduced by the GEANT4 model, expected to be of the order of 1% according to the 2017 test beam analysis. In order to study the effect, we produced MC samples with angular resolution uniformly modified by 1% on the whole particle energy range.

Figure 5.3(a) presents a relative comparison of the cross section calculated with the nominal resolution and the cross section calculated with the uniform systematic.

Figure 5.3(b) shows the effect of the systematics with respect to the ideal case by the ratio between the two curve in fig. 5.3(a). It shows a quadratic behavior. Fitting it with a second order polynomial in a range [10,20] mrad allows to extrapolate the correct behavior of the cross section for small angles. Considering the CMS 2S resolution the fitting function is

$$f_{syst} = 0.579\,\theta_e^2 + 10^{-6}. \tag{5.12}$$

Using this quadratic correction function (maximum correction is of the order of 10^{-4}), it is possible to correct bin-by-bin the experimental histogram h_{LO}^{exp} in eq. (5.9) and then to fit with the analytical model (5.1).

Figure 5.3(c) shows the final result of the fit performed after the correction of the systematic effect has been applied, using a data sample of 1/10 of the

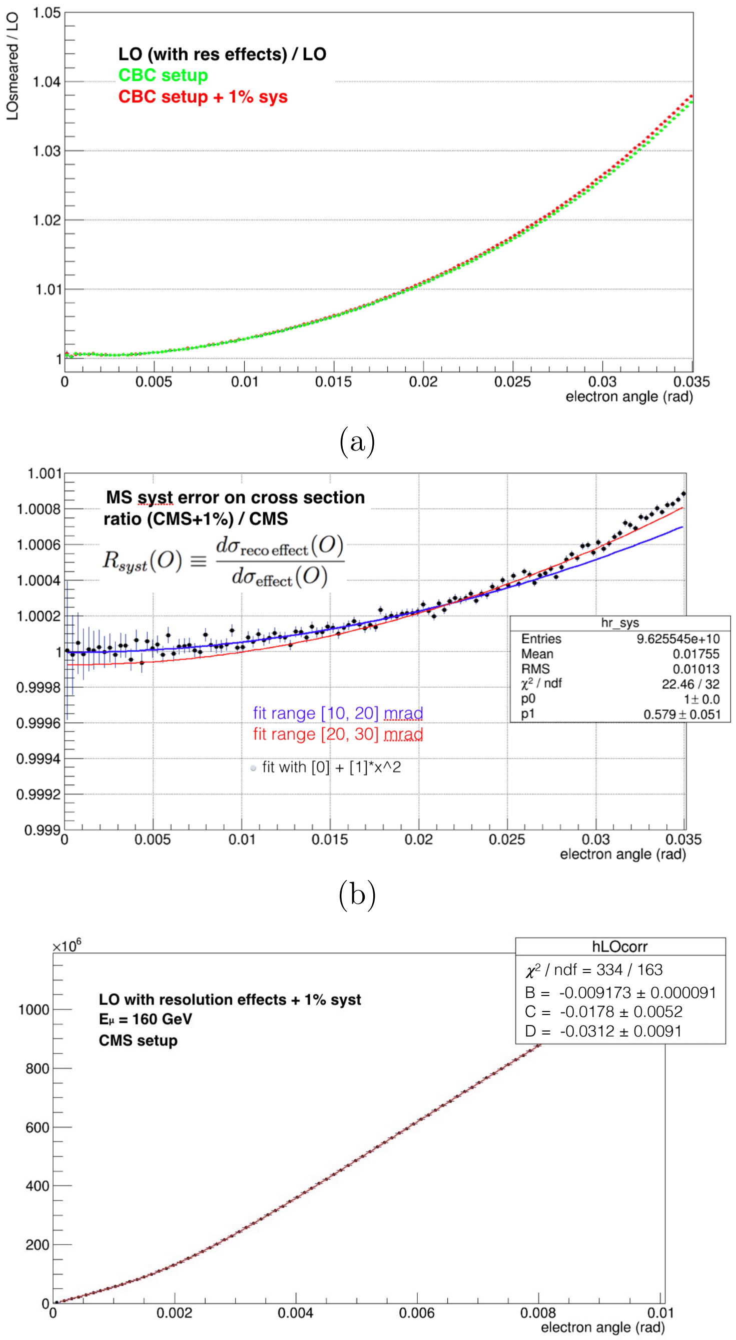

(a)

(b)

(c)

Figure 5.3: (a) Ratio between the LO cross section, convoluted with the experimental resolution, and the tree level cross section: in green the nominal CMS 2S resolution, in red with the +1% systematic. (b) Relative effect on the LO cross section of +1% mis-knowledge of the width of the MCS distribution. Parabolic fits determined in two different θ_e intervals are extrapolated to the full angular region. (c) Result of the fit using a MC sample with +1% of systematic on the MCS contribution.

full statistics. The fit value is in agreement with the reference value of a_μ^{HLO} in eq. (5.7) within the error:

$$a_\mu^{\text{HLO}}(\text{fit}) = (559 \pm 10) \cdot 10^{-10}. \tag{5.13}$$

5.2 Effect of the systematics

The ratio used to expose the hadronic running has been introduced in sec. 2.6.3:

$$\begin{aligned} R_{\text{signal}}(t) &\equiv \frac{d\sigma(\Delta\alpha_{\text{had}}(t) \neq 0)/dt}{d\sigma(\Delta\alpha_{\text{had}}(t) = 0)/dt} \\ &\sim \frac{|1 - \Delta\alpha_{\text{lep}}(t)|^2}{|1 - \Delta\alpha_{\text{lep}}(t) - \Delta\alpha_{\text{had}}(t)|^2} \\ &\propto |1 - \Delta\alpha_{\text{lep}}(t)|^2 \cdot \left[1 + 2\left(\Delta\alpha_{\text{lep}}(t) + \Delta\alpha_{\text{had}}(t)\right)\right]. \end{aligned} \tag{5.14}$$

At the numerator there is the cross section with the “full running”, while at the denominator there is only the leptonic contribution. From eq. (5.14) one can determine $\Delta\alpha_{\text{had}}(t)$ by:

$$\Delta\alpha_{\text{had}}(t) = 1 - \Delta\alpha_{\text{lep}}(t) - \frac{1 - \Delta\alpha_{\text{lep}}(t)}{\sqrt{R_{\text{signal}}(t)}}. \tag{5.15}$$

In order to evaluate the effects of the experimental systematic, we propose to consider an analogous ratio of cross sections defined as:

$$\begin{aligned} R_{\text{syst}}(t) \equiv \frac{d\sigma_{\text{syst}}/dt}{d\sigma_{\text{ref}}/dt} &\equiv \frac{d\sigma(\Delta\alpha'_{\text{had}}(t) \neq 0)/dt}{d\sigma(\Delta\alpha_{\text{had}}(t) \neq 0)/dt} \\ &\sim \frac{|1 - \Delta\alpha_{\text{lep}}(t) - \Delta\alpha_{\text{had}}(t)|^2}{|1 - \Delta\alpha_{\text{lep}}(t) - \Delta\alpha'_{had}(t)|^2} \\ &\propto |1 - \Delta\alpha_{\text{ref}}(t)|^2 \cdot [1 + 2(\Delta\alpha_{\text{lep}}(t) + \Delta\alpha'_{had}(t))] \end{aligned} \tag{5.16}$$

where at the denominator there is the reference cross section with “full running”, while at the numerator there is the differential cross section with the modified hadronic running by the systematic effect under study.

From eq. (5.16) we can determine the perturbed $\Delta\alpha'_{\text{had}}(t)$, as a function of t with:

$$\boxed{\Delta\alpha'_{\text{had}}(t) = 1 - \Delta\alpha_{\text{lep}}(t) - \frac{1 - \Delta\alpha_{\text{lep}}(t) - \Delta\alpha_{\text{had}}(t)}{\sqrt{R_{\text{syst}}(t)}}}. \tag{5.17}$$

Let's calculate $R_{\text{syst}}(t)$ as a function of θ_e. The differential cross section in θ_e is (eq. (2.64)):

$$\frac{d\sigma}{d\theta_e} = \frac{d\sigma}{dt}\frac{dt}{d\theta_e} = \frac{d\sigma}{dt}\frac{4m_e^2 r^2 \sin 2\theta_e}{\left(r^2\cos^2\theta_e - 1\right)^2}, \tag{5.18}$$

with

$$r = r(E_\mu) \equiv \frac{p_\mu}{E_\mu + m_e} = \frac{\sqrt{E_\mu^2 - m_\mu^2}}{E_\mu + m_e}, \tag{5.19}$$

where $E_\mu = E_\mu^{\text{beam}}$ while p_μ is the muon beam momentum. Using (5.18) and (5.16), the ratio $R_{\text{syst}}(t)$ can be written as a function of θ_e:

$$\begin{aligned} R_{\text{syst}}(\theta_e) &\equiv \frac{d\sigma_{\text{syst}}/dt}{d\sigma_{\text{ref}}/dt}\frac{(dt/d\theta_e)_{\text{syst}}}{(dt/d\theta_e)_{\text{ref}}} = R_{\text{syst}}[t(\theta_e)]\cdot\frac{(dt/d\theta_e)_{\text{syst}}}{(dt/d\theta_e)_{\text{ref}}} \\ &\sim \frac{\left|1-\Delta\alpha_{\text{ref}}[t(\theta_e)]\right|^2}{\left|1-\Delta\alpha_{\text{lep}}[t(\theta_e)]-\Delta\alpha'_{\text{had}}[t(\theta_e)]\right|^2}\frac{r_{\text{syst}}^2}{r_{\text{ref}}^2}\frac{\left(r_{\text{ref}}^2\cos^2\theta_e-1\right)^2}{\left(r_{\text{syst}}^2\cos^2\theta_e-1\right)^2}, \end{aligned} \tag{5.20}$$

where $\Delta\alpha_{\text{ref}}(t) = \Delta\alpha_{\text{lep}}(t) + \Delta\alpha_{\text{had}}(t)$ is the reference value of the running. Values r_{ref} and r_{syst} are different only if we want to evaluate the energy mis-calibration effect, because of the beam energy dependence $r = r(E_\mu^{\text{beam}})$. In case of other systematics (multiple scattering, beam spread), the cross section ratio in θ_e observable simply reads

$$R_{\text{syst}}(\theta_e) = R_{\text{syst}}[t(\theta_e)] \sim \frac{\left|1-\Delta\alpha_{\text{ref}}[t(\theta_e)]\right|^2}{\left|1-\Delta\alpha_{\text{lep}}[t(\theta_e)]-\Delta\alpha'_{\text{had}}[t(\theta_e)]\right|^2}. \tag{5.21}$$

In conclusion, from the cross section ratio $R_{\text{syst}}(\theta_e)$ we can estimate the effect of systematic biases or uncertainties on the extracted $\Delta\alpha_{\text{had}}(t)$.

5.2.1 Systematic related with the beam energy

Let's study the systematic error related to the mis-calibration ΔE of the energy scale with respect to the nominal value E_0. In this case R_{syst} is:

$$R_{\text{syst}} = \frac{d\sigma(E_0 + \Delta E)}{d\sigma(E_0)}, \tag{5.22}$$

from which we can extract $\Delta\alpha'(t)$, using (5.17).

Figures 5.4 show the effect of a mis-calibration of the beam energy of $\Delta E = \pm\, 5$ MeV on $E_0 = 150$ GeV (relative difference of $3.3 \cdot 10^{-5}$) on the LO differential cross section as a function of t and θ_e. The effect mainly affects the distribution for small θ_e values, i.e. large transferred momenta,

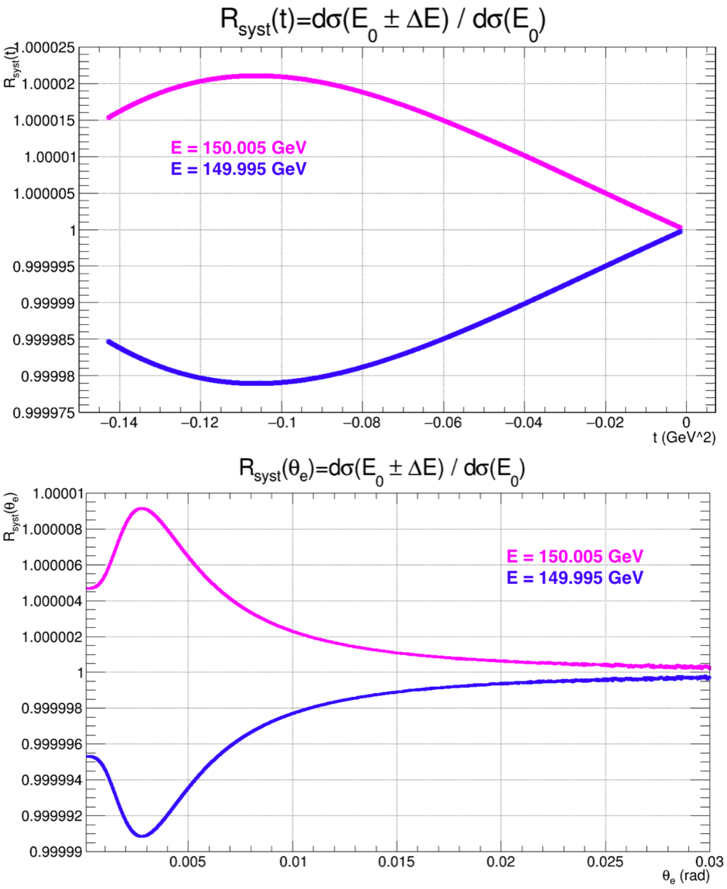

Figure 5.4: Beam scale mis-calibration on the differential cross sections in t (top) and θ_e (bottom): the effect in t is wider at a level above $1 \cdot 10^{-5}$ over almost the whole range.

with a pronounced peak of the order of 10^{-5} on θ_e and with maximum level of $2 \cdot 10^{-5}$ on the t differential cross section.

Let's see how the systematic effect propagates to $\Delta\alpha_{\mathrm{had}}(t)$ and then on the final value of a_μ^{HLO}.

Figures 5.5 (a) and (b) show the results of a single pseudo-experiment from the point of view of $\Delta\alpha_{\mathrm{had}}(t)$ and of the final integrand function of eq. (5.3) respectively. Together with the systematic due to the momentum shift of $+5$ MeV, we consider the statistical fluctuations, given the total luminosity (sec. 2.4). As expected, the results deviate significantly from the reference only at high $|t|$ (low electron scattering angles).

Figure 5.6 shows the systematic effect on a_μ^{HLO}, obtained with 3000 pseudo-experiments, considering an error on the energy scale of -5 and -2 MeV. The systematic error on a_μ^{HLO} due to an energy shift of ± 5 MeV agrees with

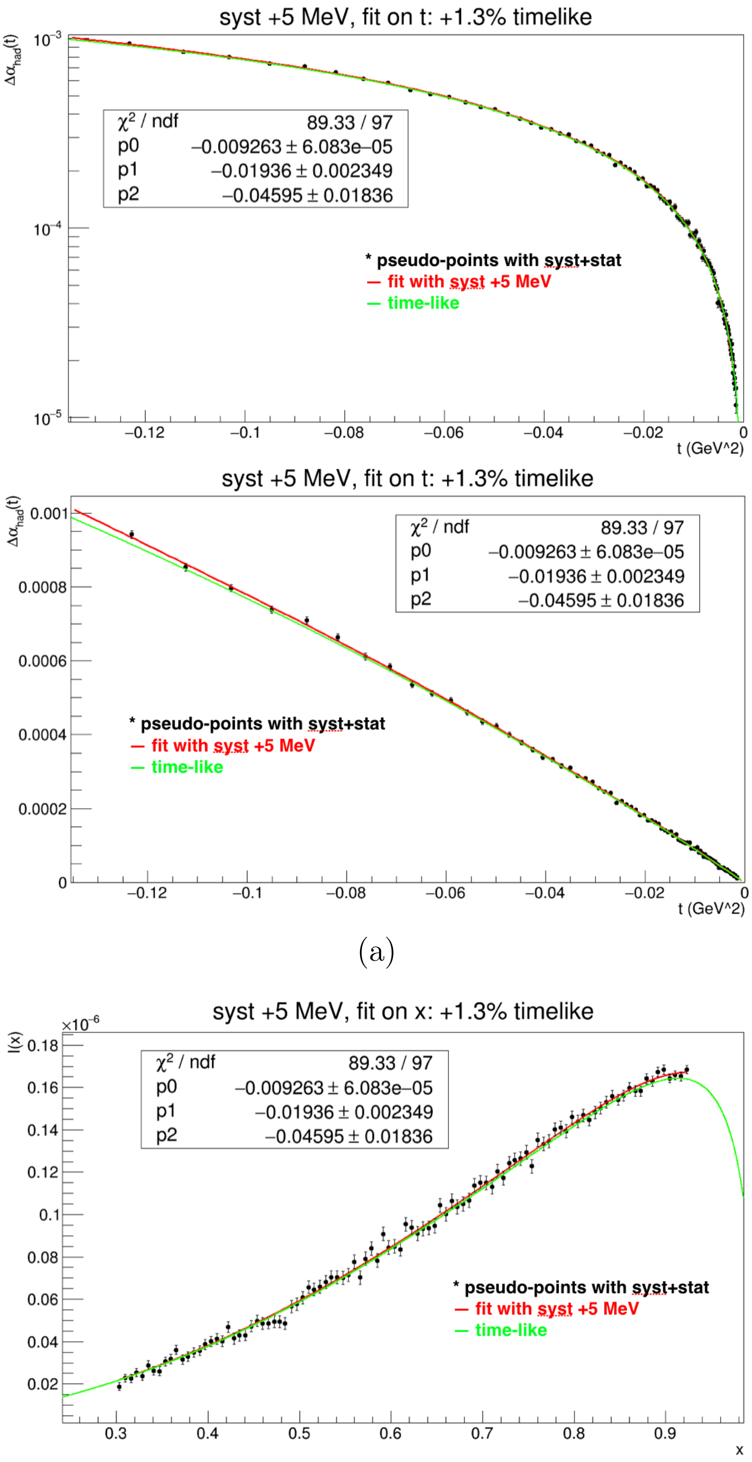

(a)

(b)

Figure 5.5: (a) Systematic effect on $\Delta\alpha_{\rm had}(t)$ due to an error of +5 MeV on the energy calibration in logarithmic and linear scale. (b) The same systematic effect on $I(x) = \alpha/\pi(1-x)\Delta\alpha_{\rm had}(t)$, integrand of the master formula in eq. (5.3).

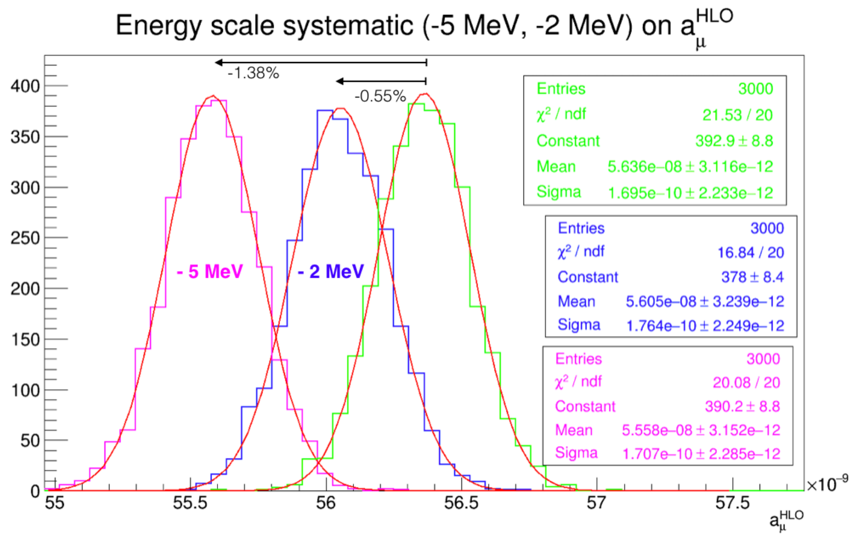

Figure 5.6: Distributions of a_μ^{HLO} obtained of 3000 pseudo-experiments with absolute error on the energy scale on -2 MeV (blue) and -5 MeV (magenta). In green the distribution of a_μ^{HLO} with statistical contribution only.

the previous approximate estimation. It corresponds to $\sim 1\%$ systematic error on a_μ^{HLO}.

To keep this systematic uncertainty at the level of the statistical precision of 0.3%, the beam energy scale must be known to 2-3 MeV, i.e. with a relative precision of $2 \cdot 10^{-5}$ on the energy scale.

Considering such precision request, it is not possible event by event to invert kinematics to estimate the incoming muon momentum, because of multiple scattering, intrinsic resolution effect and radiative corrections that take events off the elasticity curve. A well known process or a physical aspect given by the kinematics will be fundamental to fix the energy calibration. A condition has been identified that allows to invert the elastic kinematics univocally connected to the energy scale as stated in [14]. Let's discuss the principles underlying the proposed method.

From the elastic scattering kinematics, it can be demonstrated there is an equal scattering angle θ_{eq} condition that depends only on the incoming particle energy. Identifying this condition a posteriori from the data allows, from kinematics inversion, to measure the energy scale.

We start from the transverse momentum conservation:

$$p'_\mu \sin\theta_\mu = p'_e \sin\theta_e \tag{5.23}$$

with p'_e, p'_μ are the final-state electron and muon momenta, $E'_e(\theta_e)$ the electron energy and $E_\mu = E_\mu^{\rm beam}$ is the energy scale to be estimated. Imposing that $\theta_e = \theta_\mu \equiv \theta_{eq}$, one can obtain for the quantities after scattering:

$$\begin{aligned} p'_\mu &= p'_e \\ E'_e(\theta_{eq}) &= \frac{(E_\mu + m_e)^2 + m_e^2 - m_\mu^2}{2(E_\mu + m_e)} \\ E'_\mu(\theta_{eq}) &= \frac{(E_\mu + m_e)^2 + m_\mu^2 - m_e^2}{2(E_\mu + m_e)}. \end{aligned} \tag{5.24}$$

By using (5.24) and the expression of the electron scattering angle as a function of its energy

$$\cos\theta_e = \frac{1}{r}\sqrt{\frac{E'_e - m_e}{E'_e + m_e}}, \tag{5.25}$$

so the scattering angle θ_{eq} read as:

$$\cos^2\theta_{eq} = \frac{(E_\mu + m_e)^2}{(E_\mu + 2m_e)^2 - m_\mu^2}, \tag{5.26}$$

which depends only on the beam energy scale E_μ. By developing in m_e/E_μ:

$$\cos\theta_{eq} \sim \frac{E_\mu + m_e}{E_\mu + 2m_e} \quad \rightarrow \quad 1 - \frac{\theta_{eq}^2}{2} \sim 1 - \frac{m_e}{E_\mu} \tag{5.27}$$

from which we obtain

$$\theta_{eq} \sim \sqrt{\frac{2m_e}{E_\mu}}. \tag{5.28}$$

For $E_\mu = 150$ GeV, $\theta_{eq} \sim 2.51$ mrad and both the particle energies are $\sim$ 75 GeV.

Figure 5.7 shows the absolute angular difference $\Delta\theta_{eq}$ between the two equal-angle states corresponding to the modified and the nominal energy scale. We use these values to estimate whether the method has the sensitivity to distinguish two energies that differ from few MeV. It is necessary to discriminate scattering angles at $\Delta\theta_{eq} \sim 2 \cdot 10^{-5}$ mrad absolute level to achieve the requested precision of $\sim$ 2 MeV on the energy scale. Considering an angular resolution σ_θ in the equal angle region, we can estimate the required statistics as needed events number N_{eq} with:

$$\Delta\theta_{eq} = \frac{\sigma_\theta}{\sqrt{N_{eq}}} \quad \rightarrow \quad N_{eq} = \left(\frac{\sigma_\theta}{\Delta\theta_{eq}}\right)^2 = \left(\frac{\sigma_\theta}{k \cdot \Delta E}\right)^2, \tag{5.29}$$

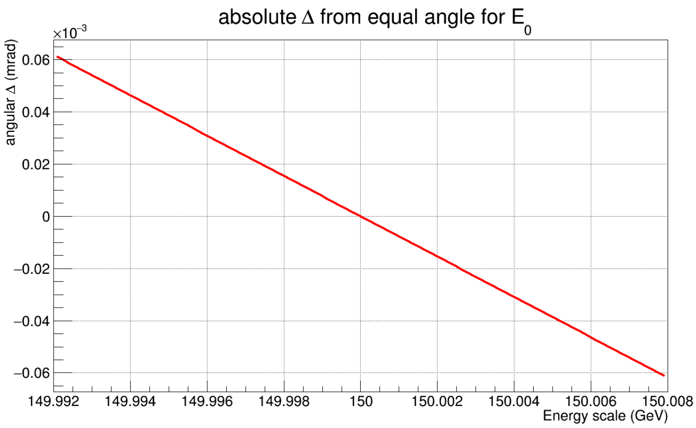

Figure 5.7: Angular sensitivity from eq. (5.26) of the equal angle method for the nominal value $E_0 = 150$ GeV. $\Delta = \Delta\theta_{eq}$ is the absolute difference between equal angle condition for $E_0 + \Delta E$ and E_0. In order to translate the ΔE request (MeV) in $\Delta\theta_{eq}$ (mrad) a very good approximation, by a simple fit of this behavior, is: $\Delta\theta_{eq} = -7.7 \cdot 10^{-6}\Delta E$, for 150 GeV.

where $k = 7.7 \cdot 10^{-6}$ mrad/MeV for $E_0 = 150$ GeV (fig. 5.7) and ΔE is the absolute request of precision on the energy scale. By assuming $\sigma_\theta = 0.03$ mrad as the angular resolution of the CMS trackers around few mrad, dominated by the intrinsic resolution, we get:

$$N_{eq} = \left(\frac{0.03\,\text{mrad}}{2 \cdot 10^{-5}\,\text{mrad}}\right)^2 \sim 2.3 \cdot 10^6\,\text{events}. \tag{5.30}$$

The differential cross section at $\theta_{eq} = 2.5$ mrad is $d\sigma/d\theta_e \sim 1$ μb/mrad: with a bin width of 1 mrad, the integrated cross section is about 1 μb. Multiplying by the instantaneous luminosity with a module only $\mathcal{L}_1 = 0.38$ nb^{-1}s^{-1}/40, the expected event rate in the equal-angle bin is $R_{eq} \sim 6.3$ s^{-1}. Therefore a measurement of the average beam energy with the required precision can be obtained within a time interval:

$$\Delta t = \frac{N_{eq}}{R_{eq}} \sim 3.6 \cdot 10^5\,\text{s}, \tag{5.31}$$

i.e. ~ 7 days, given a running cycle of about 60%. Such required time appears reasonable.

The method to measure the calibration energy essentially relies on the very precise measurement on the angular deflections, at a relative level of 10^{-5}. This request has a direct impact also on the precision about the trackers longitudinal alignment, that is about the sensors position. Considering a

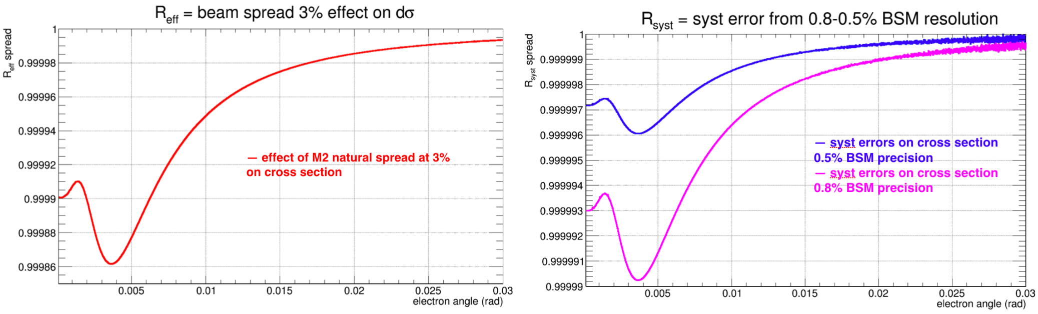

Figure 5.8: (left) Beam spread effect on the differential cross section as a function of θ_e. (right) Systematic error due to two different spectrometer (BMS) precisions on the momentum measurement.

tracking station of $L = 1$ m, a precision of 10^{-5} on the angles requires a systematic control within 10^{-5} m $= 10$ μm on the sensors longitudinal position. As we have seen in the test beams analysis, it is not possible to control precisely this aspect from the data. Only an optical survey, laser-based for instance, allows to check the longitudinal alignment at this precision level.

5.2.2 Beam energy spread

Another important aspect related to the M2 beam is the energy spread. The beam width of about 3-4%[1] directly affects the differential μe cross section. Still looking at fig. 5.4, the impact on the differential cross section is not symmetric for symmetric energy compared to the central value E_0. Such effect is at relative level of 10^{-4}.

In order to measure the beam energy profile, the MUonE collaboration proposed to use the beam momentum spectrometer (BMS) of COMPASS experiment [14] upstream the apparatus. This detector can reach a relative precision below 0.8% on the momentum measurement. The resulting systematic will arise from the spectrometer resolution knowledge.

Here we considered the worst case, that is the propagation on the final a_μ^{HLO} of the momentum measurement precision assuming no knowledge about the spectrometer resolution. According to the present study, the systematic error can be evaluated by:

$$R_{\text{syst}} = \frac{d\sigma(w_{beam} \oplus w_{BMS})}{d\sigma(w_{beam})}, \tag{5.32}$$

---

[1] From a private communication with J. Bernhard, coordinator of the M2 beam line, the natural spread at 160 GeV is 3.75%.

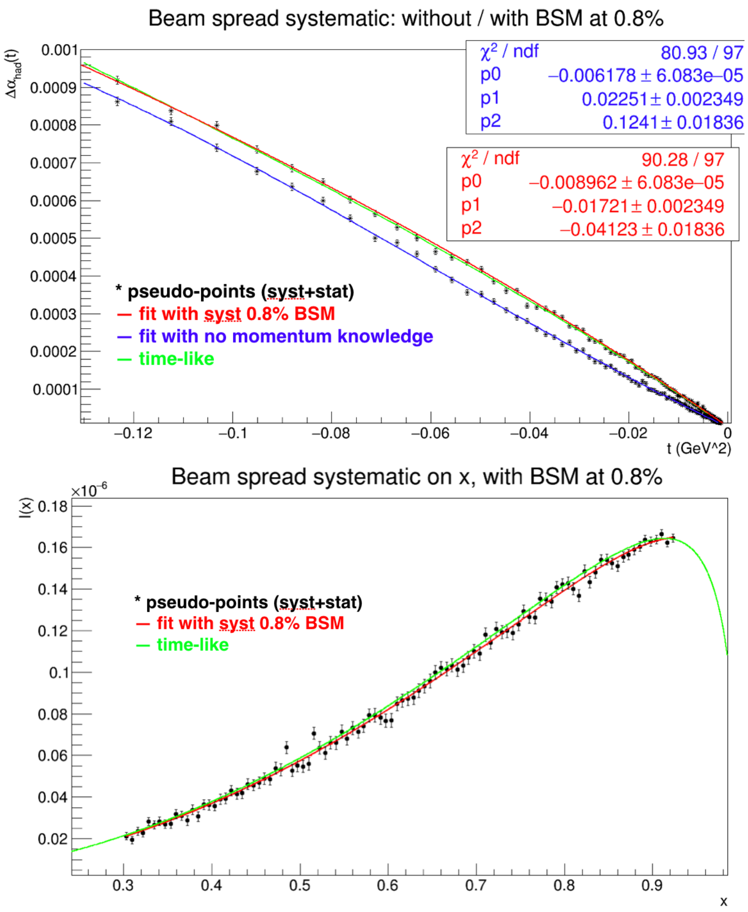

(a)

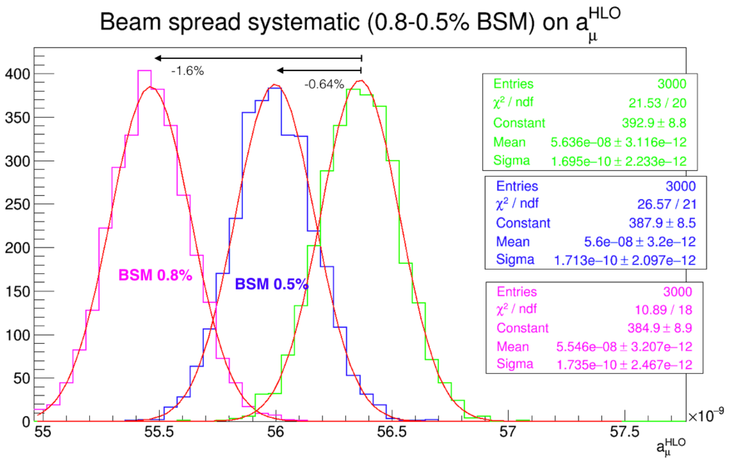

(b)

Figure 5.9: (a) $\Delta\alpha_{\rm had}(t)$ and the integrand of the master formula altered by BMS precision systematic at level of 0.8%. (b) Statistical distributions of 3000 pseudo-experiments on $a_\mu^{\rm HLO}$: comparison between two different BMS precisions. In green with the statistical contribution only.

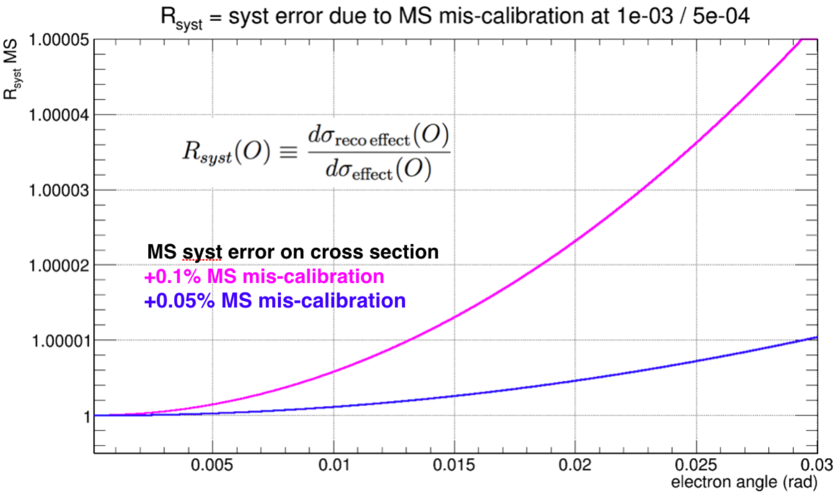

Figure 5.10: MCS systematic effect on the LO differential cross section: comparison between two different mis-knowledge.

where $w_{beam} \oplus w_{BMS}$ is the measured beam width by the spectrometer, considering the nominal spread w_{beam} and the precision w_{BMS} on the momentum measurement.

Figure 5.8 (left) show the relative effect of the natural spread on the cross section with respect to the case of monochromatic beam. Figure 5.8 (right) shows the relative impact of the BMS precision using R_{syst} from which we can extract modified value $\Delta\alpha'(t)$ in order to evaluate the related systematic error. As well as the energy scale effect, there are a peak at level of 10^{-5}, at low scattering angle, i.e. high $|t|$.

Figures 5.9(a) show the effect of 0.8% BSM precision on $\Delta\alpha_{\text{had}}(t)$ and on the integrand of master formula in eq. (5.3). In order to quantify the systematic shifts, the results of 3000 pseudo-experiments, using two different BMS precision of 0.8% and 0.5%, are shown in fig. 5.9(b).

Even if we do not assume any knowledge of the BMS resolution, a spectrometer of precision of about 0.5% gives a systematic shift below the percent level. Assuming to know the spectrometer resolution to 20-25%, the impact on a_μ^{HLO} should be negligible [14].

5.2.3 Multiple scattering

Now we considered systematic uncertainties of the MCS model at the level of +1%, +0.1% and +0.05%. Figure 5.3(b) shows that the relative effect on the cross section of the systematic uncertainty of +1% is less or of the order of 10^{-4}. Figure 5.10 shows that the effects of 0.1% or 0.05% are below 10^{-5}.

Figures 5.11 (a) and (b) show the effect of the multiple scattering systematic uncertainty on the hadronic running $\Delta\alpha_{\text{had}}(t)$ and on the integrand function of the master formula in eq. (5.3) respectively.

For the $+1\%$ systematic uncertainty, the fit to determine the hadronic running does not converge. Going to mis-calibration of 10^{-3} or less, the fits become reasonably good and give results close to the reference. In particular for a mis-calibration in the MCS model of the order of $5 \cdot 10^{-4}$, the systematic error due to multiple scattering is at the percent level on a_μ^{HLO}, as it is shown in fig. 5.12.

The required accuracy on the MCS model we think we can be reached by combining GEANT simulation and data-driven corrections, which has to determine possible systematic trend at large scattering angle, corresponding to the small energy region.

The studies about the systematics errors presented in this chapter will need to be updated in the light of the high order corrections to the cross section (sec. 2.6.3) by means of the final workflow presented in sec. 2.2.2, and recently in the Letter of Intent of the MUonE proposal [14].

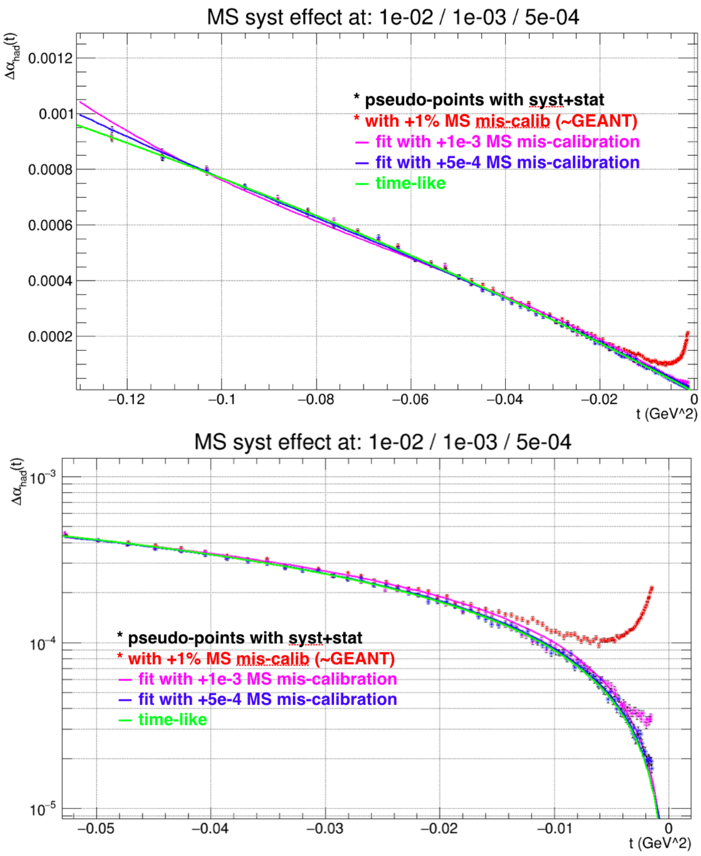

(a)

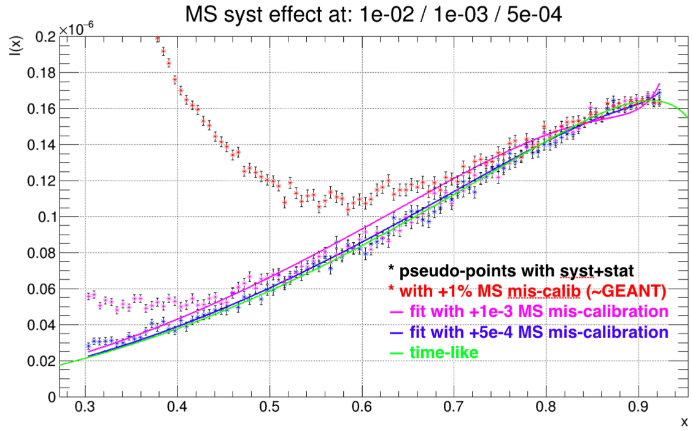

(b)

Figure 5.11: (a) Effect on the MCS systematic uncertainty of 1%, 0.1% and 0.05% on $\Delta\alpha_{\rm had}(t)$, in linear and log scale. (b) Same effects on the master formula integrand.

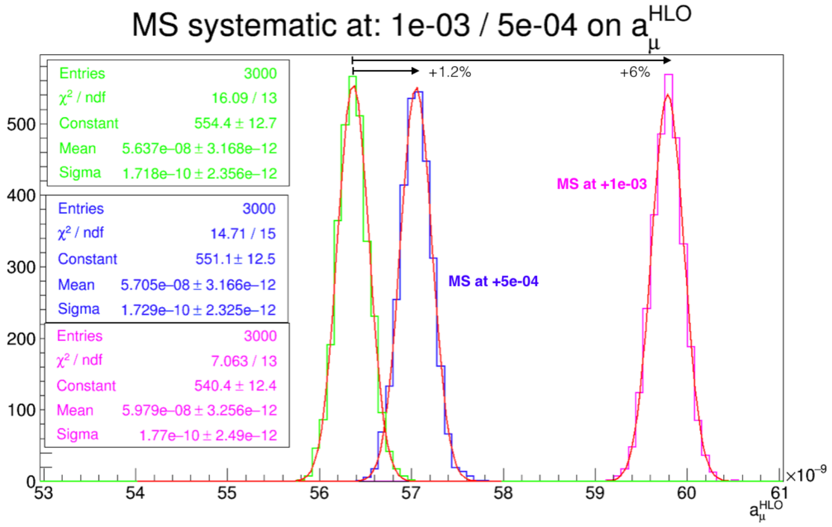

Figure 5.12: Distributions of a_μ^{HLO} obtained performed 3000 pseudo-experiments for systematic uncertainties of MCS model of $+0.1\%$ (magenta) and $+0.05\%$ (blue). In green the statistical contribution only.

Conclusions and outlook

The thesis concerns the feasibility study of the MUonE experiment. The proposed high precision experiment, to be performed at M2 beam at CERN, aims to measure the electromagnetic coupling α as a function of squared transferred momentum t using high energy muon elastic scattering on electron at rest. Knowing $\alpha(t)$ we can determine the hadronic contribution to the running and calculate the leading order hadronic contribution to the muon anomalous magnetic moment a_μ^{HLO}. The innovative method proposed by MUonE is complementary to the traditional time-like approach to determine a_μ^{HLO}. The MUonE collaboration aims to reach a precision of 0.3%, comparable to the time-like approach in two years of data taking.

To detect μe elastic scattering events, we developed the concept of a modular detector, consisting of independent and identical tracking stations. The work done for this thesis has contributed to the optimization of the tracking stations design by means of GEANT4 based simulation code. Each station will be equipped with a thin target of Beryllium and three tracking layers of Silicon strip detectors.

I contributed to the test beams performed at CERN to assess the performance of a detector prototype. I developed the tracking algorithm used for the alignment of the strip Silicon strip detectors and to the reconstruction of the scattering events. The results of these measurements allowed us to study the effect of multiple scattering of high energy electrons hitting on low Z material targets. The results have been submitted for publication [8, 9]. They show that GEANT4 multiple scattering models allow to reproduce the experimental data within 1-2%.

I proposed an analytical model to describe the angular resolution of the tracking station. It allowed me to develop a fast Monte Carlo used to generate large data sample. This instrument enabled us to study with high statistical precision the analysis workflow to determine a_μ^{HLO} and to evaluate the effects of the main systematic uncertainties on the observables.

I confirmed that MUonE can reach the statistical precision goal of 0.3%. In this work the most important experimental systematics have been identified and studied, in particular the effects due to multiple scattering, to the intrinsic resolution, and to the knowledge of the beam energy. I assessed the level of the main systematic uncertainties can be controlled to keep the systematic error on a_μ^{HLO} on the same level of the statistical error. The required precise knowledge of the average beam energy, to 5 MeV or better, is probably the most challenging constraint that emerged from this study.

I contributed to the Letter of Intent [14] submitted to the CERN SPSC by the MUonE collaboration beginning of June 2019. The plan is to performed a Pilot Run in 2021, to test the final version of the detector, of the DAQ and trigger system to then performed the experiment in the years 2022-2024.

The detector stations will be equipped with the 2S CMS strip sensors, developed by CMS collaboration for the upgrade of detector foreseen for Hi-Lumi phase of LHC. The CMS 2S sensors have revealed to be an ideal tracking detector providing a single hit resolution of 18 μm and allowing MUonE to reach the design angular resolution of 0.02 mrad on a detection scale of 1 m.

Appendix A

Monte Carlo

A.1 Correlations induced by MCS: a toy-MC study

In order to prove this relationship and derive other important properties that are useful in the data analysis of the first test beam data (2017) we built a simple toy-MC. Let's suppose the thickness indicated in fig. 3.1 represents the region between two consecutive trackers, that is the region between two hits. The angle ψ_{plane} of fig. 3.1 is the angle reconstructed using the hits in the two adjacent planes (the only one accessible), while θ_{plane} (of width θ_{MS}) is the true angle of the particle when leaving the second tracking plane.

So:

$$< y^2_{plane} >= L^2 < \psi^2_{plane} > \quad \rightarrow \quad \psi^{rms}_{plane} = \frac{1}{\sqrt{3}}\theta^{rms}_{plane} = \frac{1}{\sqrt{3}}\theta_{\mathrm{MS}}, \tag{A.1}$$

The measurable ψ_{plane} and the true θ_{plane} angular distributions have significantly different widths when leaving the scattering region. If the particles cross several regions, for example separated by the presence of a target, then the distribution of the incoming particles in the second region is the true one, although the only available for measurement is the reconstructed one. If the effect of the multiple scattering is large in the first part of the system, as in the case of the 2017 test beam, the difference between the two distributions is significant. In the TOY-MC, upstream station of 2017 test beam is divided in N steps and in each one scattering angle and y are calculated and used for next step (fig. A.1). Only angles are random, the angle generator is simply gaussian with mean=0 and sigma=θ_{MS} ((3.3)) for thickness L / N: lateral displacement (hits) and so theta distribution from hits are determined geometrically from random angles. Geant, in an extremely complex mode,

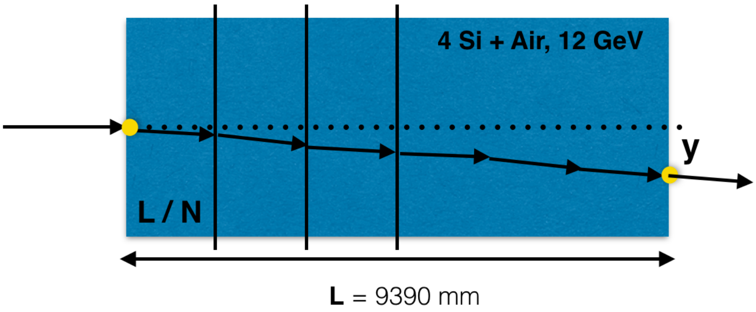

Figure A.1: Toy-MC to study correlations between lateral displacement (hits) and scattering angles.

acts in this way to simulate particles transport through matter. Figure A.2 shows what we expected: the width of the lateral displacement is reduced by a factor $\sqrt{3}$ compared to the true distribution one: $0.0953 \cdot \sqrt{3} \sim 0.165$ mrad.

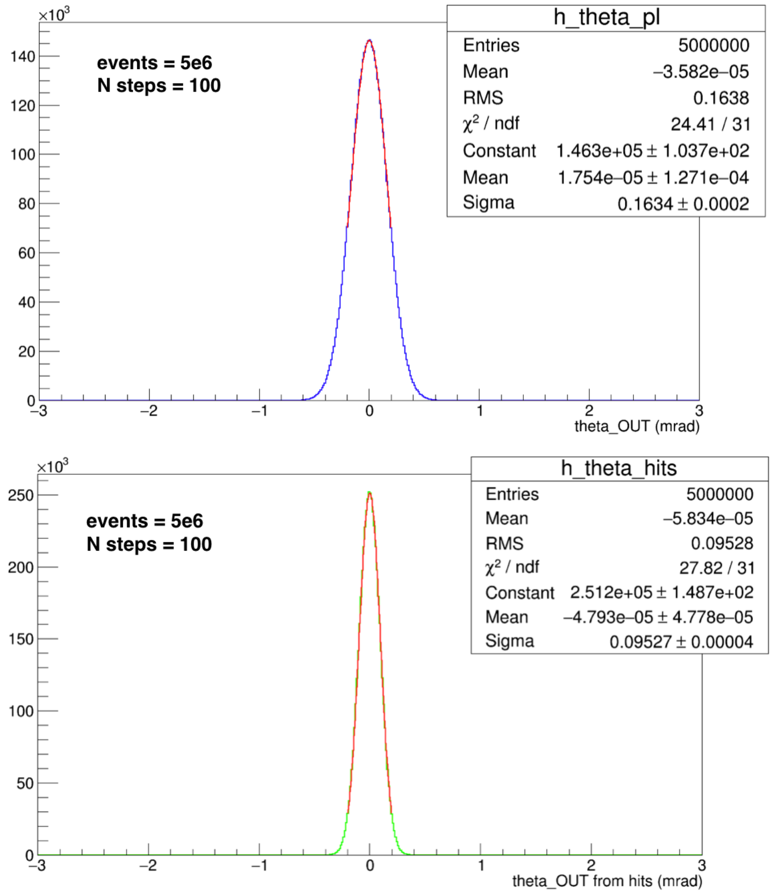

Figure A.2: Results of toy-MC: (top) true exit angle distribution, (bottom) reconstructed angle distribution from hits, that is lateral displacement.

Appendix B

Relativity

B.1 Summary

As useful reference, the most important relations about μe elastic scattering are summarized. Some of these have been introduced in chapter 2.

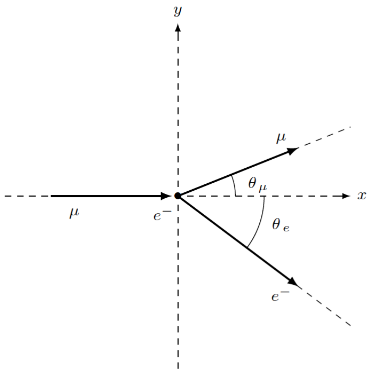

$$\mu^{\pm}(p_1) + e^-(p_2) \to \mu^{\pm}(p_3) + e^-(p_4)$$

- 4-momenta in the lab frame (electron rest frame):

$$\begin{aligned}
p_1 &= (E_\mu, \vec{p}_\mu) = (E_\mu, p_\mu, 0, 0)\\
p_2 &= (E_e, \vec{p}_e) = (m_e, 0, 0, 0)\\
p_3 &= (E'_\mu, \vec{p}'_\mu) = (E'_\mu, p'_\mu \cos\theta_\mu, p'_\mu \sin\theta_\mu, 0)\\
p_4 &= (E'_e, \vec{p}'_e) = (E'_e, p'_e \cos\theta_e, -p'_e \sin\theta_e, 0),
\end{aligned} \tag{B.1}$$

with (PDG values)

$$\begin{aligned}
m_e &= 0.000510998928\,\text{GeV}\\
m_\mu &= 0.1056583715\,\text{GeV},
\end{aligned} \tag{B.2}$$

where $p_\mu = |\vec{p}_\mu| \equiv p_\mu^{beam}$, $E_\mu \equiv E_\mu^{beam}$; after scattering $p'_\mu = |\vec{p}'_\mu|$ and $p'_e = |\vec{p}'_e|$.

- Mandelstam's invariants s, t and λ (Kallen or triangular function) in lab frame:

$$\begin{aligned} s &\equiv (p_1 + p_2)^2 = (p_3 + p_4)^2 = m_e^2 + m_\mu^2 + 2m_e E_\mu \\ t &\equiv (p_1 - p_3)^2 = (p_2 - p_4)^2 = 2m_e(m_e - E'_e) = 2m_e(E'_\mu - E_\mu) \\ \lambda(s, m_e^2, m_\mu^2) &\equiv (s - m_e^2 - m_\mu^2)^2 - 4m_e^2 m_\mu^2 = 4m_e^2(E_\mu^2 - m_\mu^2). \end{aligned} \tag{B.3}$$

- 4-momenta in the CM frame (applying momentum conservation and mass-shell relations):

$$\begin{aligned} p_1^* &= (E_\mu^*, p^*, 0, 0) \\ p_2^* &= (E_e^*, -p^*, 0, 0) \\ p_3^* &= (E_\mu^*, p^* \cos\theta^*, p^* \sin\theta^*, 0) \\ p_4^* &= (E_e^*, -p^* \cos\theta^*, -p^* \sin\theta^*, 0), \end{aligned} \tag{B.4}$$

where

$$\begin{aligned} E_\mu^* &= \frac{s + m_\mu^2 - m_e^2}{2\sqrt{s}} \\ E_e^* &= \frac{s + m_e^2 - m_\mu^2}{2\sqrt{s}} \\ p^* &= \frac{\sqrt{\lambda(s, m_\mu^2, m_e^2)}}{2\sqrt{s}} = \frac{p_\mu m_e}{\sqrt{s}} \\ &\boxed{t = -2p^{*2}(1 - \cos\theta^*) < 0}, \end{aligned} \tag{B.5}$$

$\sqrt{s}$ is CM energy, $\sqrt{|t|}$ the transferred momentum, p^* is the 3-momentum of particles in CM before scattering and λ function defined above.

- From (5), $\cos\theta^* = -1$ gives the max transferred momentum $|t|$, i.e. min $t < 0$ in $2 \to 2$ μ-e scattering:

$$|t|_{max} = (2p^*)^2 \to t_{min} = -4p^{*2} = -\frac{\lambda(s, m_\mu^2, m_e^2)}{s} = -4\frac{p_\mu^2 m_e^2}{s} \tag{B.6}$$

- LAB (electron rest frame) - CM boost:

$$\begin{aligned} \beta_{CM} &= v_e^* = \frac{p^*}{E_e^*} = \frac{p_\mu}{E_\mu + m_e}, \\ \gamma_{CM} &= \frac{E_e^*}{m_e} = \frac{E_\mu + m_e}{\sqrt{s}} \end{aligned} \tag{B.7}$$

where $p_\mu \equiv p_\mu^{beam}$ and $E_\mu \equiv E_\mu^{beam}$ defined in (1).

- Lorentz boost (7) along x axis, for the components of muon final momentum $\vec{p}'_\mu$:

$$\begin{aligned} p'_\mu \sin\theta_\mu &= p^* \sin\theta^* \\ p'_\mu \cos\theta_\mu &= \gamma_{CM}(p^*\cos\theta^* + \beta_{CM}E^*_\mu) \end{aligned} \tag{B.8}$$

- Angular relations LAB - CM, using this Lorentz boost:

$$\begin{aligned} \tan\theta_\mu &= \frac{p'^y_\mu}{p'^x_\mu} = \frac{\sin\theta^*}{\gamma_{CM}\left(\cos\theta^* + \beta_{CM}E^*_\mu/p^*\right)} \\ \tan\theta_e &= \frac{p'^y_e}{p'^x_e} = \frac{\sin\theta^*}{\gamma_{CM}\left(-\cos\theta^* + \beta_{CM}E^*_e/p^*\right)} = \frac{\sin\theta^*}{\gamma_{CM}\left(-\cos\theta^* + 1\right)} \end{aligned} \tag{B.9}$$

B.2 Kinematics correlations $2 \to 2$ scattering

- Energies and angles in t invariant:

$$E'_\mu = \frac{s + t - m_e^2 - m_\mu^2}{2m_e} = \frac{2m_eE_\mu + t}{2m_e} \tag{B.10}$$

$$E'_e = \frac{2m_e^2 - t}{2m_e}. \tag{B.11}$$

$$\cos\theta_\mu = \frac{2m_e^2(t - 2m_\mu^2) + 2m_eE_\mu(2m_eE_\mu + t)}{\sqrt{\lambda(s, m_e^2, m_\mu^2)}\sqrt{\lambda(s + t, m_e^2, m_\mu^2)}} \tag{B.12}$$

$$\cos\theta_e = \frac{-2m_e(E_\mu + m_e)t}{\sqrt{\lambda(s, m_e^2, m_\mu^2)}\sqrt{t^2 - 4m_e^2t}}. \tag{B.13}$$

- Correlation E'_μ / θ_μ:

$$\boxed{E'_\mu(\theta_\mu) = \frac{a \pm b\, p_\mu^2 \cos\theta_\mu}{d}}, \tag{B.14}$$

where

$$\begin{aligned} a &\equiv (E_\mu + m_e)(m_\mu^2 + m_eE_\mu) \\ b = b(\theta_\mu) &\equiv \sqrt{m_e^2 - m_\mu^2 \sin^2\theta_\mu} \\ d = d(\theta_\mu) &\equiv (E_\mu + m_e)^2 - p_\mu^2 \cos^2\theta_\mu. \end{aligned} \tag{B.15}$$

By reverting (2.4), one can write the useful inverse formula:

$$x = \left(1 - \sqrt{1 - \frac{4m_\mu^2}{t}}\right)\frac{t}{2m_\mu^2}. \tag{B.16}$$

- **Correlation E'_e / θ_e:**

$$\boxed{E'_e(\theta_e) = m_e \frac{(E_\mu + m_e)^2 + p_\mu^2 \cos^2\theta_e}{(E_\mu + m_e)^2 - p_\mu^2 \cos^2\theta_e} = m_e \frac{1 + r^2\cos^2\theta_e}{1 - r^2\cos^2\theta_e}} \tag{B.17}$$

with

$$r \equiv \frac{p_\mu}{E_\mu + m_e} = \frac{\sqrt{E_\mu^2 - m_\mu^2}}{E_\mu + m_e}. \tag{B.18}$$

- Inverse:

$$\cos\theta_e = \frac{1}{r}\sqrt{\frac{E'_e - m_e}{E'_e + m_e}}. \tag{B.19}$$

- Maximum muon scattering angle from (15):

$$\begin{aligned} \sin\theta_\mu < \frac{m_e}{m_\mu} \quad \rightarrow \quad \theta_\mu^{max} &= \arcsin\frac{m_e}{m_\mu} \sim 4.83635\,\text{mrad} \\ E'_\mu(\theta_\mu^{max}) &= \frac{a}{d(\theta_\mu^{max})} \\ E'_e(\theta_\mu^{max}) &= E_\mu + m_e - E'_\mu(\theta_\mu^{max}) \end{aligned} \tag{B.20}$$

- **Correlation between θ_μ and θ_e:**

$$\boxed{\sin\theta_\mu = \frac{p'_e \sin\theta_e}{p'_\mu} = \frac{\sqrt{E_e'^2(\theta_e) - m_e^2}\,\sin\theta_e}{\sqrt{(E_\mu + m_e - E'_e(\theta_e))^2 - m_\mu^2}}} \tag{B.21}$$

where scattering electron energy $E'_e(\theta_e)$ is given by (16) and $E_\mu = E_\mu^{beam}$. This simply formula holds only for $m_e < m_\mu$.

- From (16)(20), an equal angle condition exists, i.e. $\theta_{eq} \equiv \theta_e = \theta_\mu$:

$$\begin{aligned} p'_\mu &= p'_e \\ E'_e(\theta_{eq}) &= \frac{(E_\mu + m_e)^2 + m_e^2 - m_\mu^2}{2(E_\mu + m_e)} \\ E'_\mu(\theta_{eq}) &= E_\mu + m_e - E'_e(\theta_{eq}) \\ \cos^2\theta_{eq} &= \frac{(E_\mu + m_e)^2}{(E_\mu + 2m_e)^2 - m_\mu^2}. \end{aligned} \tag{B.22}$$

- From above formulae, some reference values for $E_\mu = E_\mu^{beam} = 150$ GeV:

$$
\begin{aligned}
&\boxed{E_{CM} \equiv \sqrt{s} \sim 405.541\,\mathrm{MeV}}\\
&\lambda(s, m_e^2, m_\mu^2) \sim 0.02350078\,\mathrm{GeV}^4\\
&E_\mu^* \sim 175.627\,\mathrm{MeV}\\
&E_e^* \sim 153.300\,\mathrm{MeV}\\
&p^* \sim 189.006\,\mathrm{MeV}\\
&\boxed{\gamma_{CM} \sim 369.877}\\
&\boxed{t_{min} \sim -0.142893\,\mathrm{GeV}^2} \to \sqrt{|t|_{max}} \sim 378.012\,\mathrm{MeV}\\
&E'_\mu(|t|_{max}) = E'_\mu(\mathrm{min}) \sim 10.1827\,\mathrm{GeV}\\
&E'_e(|t|_{max}) = E'_e(\mathrm{max}) \sim 139.818\,\mathrm{GeV}\\
&E'_\mu(\theta_\mu^{max}) \sim 19.0694\,\mathrm{GeV}\ \text{(at peak)}\\
&E'_e(\theta_\mu^{max}) \sim 130.931\,\mathrm{GeV}\ \text{(at peak)}\\
&\theta_e(\theta_\mu^{max}) \sim 0.70438\,\mathrm{mrad}\ \text{(at peak)}\\
&\theta_{eq}(\theta_e = \theta_\mu) \sim 2.51339\,\mathrm{mrad}\\
&E'_\mu(\theta_{eq}) \sim 75.0003\,\mathrm{GeV}\\
&E'_e(\theta_{eq}) \sim 75.0002\,\mathrm{GeV}
\end{aligned}
\tag{B.23}
$$

B.3 Differential cross sections in t, θ_e and θ_μ

- The differential unpolarized cross section at leading order (LO):

$$\boxed{\frac{d\sigma}{dt} = \frac{4\pi\alpha^2}{\lambda(s, m_e^2, m_\mu^2)}\left[\frac{(s - m_e^2 - m_\mu^2)^2}{t^2} + \frac{s}{t} + \frac{1}{2}\right]}, \tag{B.24}$$

where $\alpha = \alpha$ fine structure constant: $\alpha = 1/137.035999139$.

- For NLO vacuum polarization, the running of α is factorizable:

$$\alpha \to \alpha(t) = \frac{\alpha}{1 - \Delta\alpha_{lep}(t) - \Delta\alpha_{top}(t) - \Delta\alpha_{had}(t)} \tag{B.25}$$

- Cross section in θ_e (using (23) and chain rule):

$$\frac{d\sigma}{d\theta_e} = \frac{d\sigma}{dt}\frac{dt}{d\theta_e}. \tag{B.26}$$

From t expression in lab frame (3) and (16):

$$\begin{aligned} t = t_{ee} &= 2m_e \left(m_e - E'_e(\theta_e)\right) \\ &= 2m_e^2 \left(1 - \frac{1 + r^2 \cos^2\theta_e}{1 - r^2 \cos^2\theta_e}\right) \\ &= \frac{4m_e^2 r^2 \cos^2\theta_e}{r^2 \cos^2\theta_e - 1}. \end{aligned} \tag{B.27}$$

So deriving this formula in θ_e, the differential cross section (at LO) in the electron scattering angle is:

$$\boxed{\frac{d\sigma}{d\theta_e} = \frac{4m_e^2 r^2 \sin 2\theta_e}{\left(r^2 \cos^2\theta_e - 1\right)^2} \frac{d\sigma}{dt}} \tag{B.28}$$

- Cross section in θ_μ (using (23)):

$$\frac{d\sigma}{d\theta_\mu} = \frac{d\sigma}{dt}\frac{dt}{d\theta_\mu}. \tag{B.29}$$

In the same way[1], from (3):

$$\begin{aligned} t = t_{\mu\mu} &= 2m_e \left(E'_\mu(\theta_\mu) - E_\mu\right) \\ &= 2m_e \left(\frac{a \pm b\, p_\mu^2 \cos\theta_\mu}{d} - E_\mu\right), \end{aligned} \tag{B.30}$$

where coefficients a, $b = b(\theta_\mu)$, $d = d(\theta_\mu)$ are given by (15). The derivative in θ_μ is

$$\begin{aligned} \frac{dt}{d\theta_\mu} = \frac{\pm 2m_e p_\mu^2 \sin\theta_\mu}{d^2 b} & \left\{\mp 2ab\cos\theta_\mu + p_\mu^2 \cos^2\theta_\mu (m_\mu^2 - m_e^2)\right. \\ & \left. + (E_\mu + m_e)^2 \left[m_\mu^2 (1 - 2\cos^2\theta_\mu) - m_e^2\right]\right\} \end{aligned} \tag{B.31}$$

---

[1] For 2 → 2 scattering, from 4-momenta conservation $t = t_{ee} = t_{\mu\mu}$ holds, i.e. is valid at LO and also at NLO vacuum polarization (a subset of NLO radiative corrections).

Appendix C

Detector

C.1 Calorimeter

A calculation is proposed to estimate how much of an electromagnetic shower induced by a scattering electron, in the trackers section, will reach the final calorimeter. By considering the material budget of a CMS trackers, one can estimate the radiation length X_0 offered by a single station, using the values of tab. C.1:

$$\begin{aligned}\Delta D(X_0) = t_{mod} &= \frac{d}{X_0}\Big|_{Be} + \frac{d}{X_0}\Big|_{Si} + \frac{d}{X_0}\Big|_{Air} \\ &= \frac{1.5\,\text{cm}}{X_0}\Big|_{Be} + \frac{0.24\,\text{cm}}{X_0}\Big|_{Si} + \frac{100\,\text{cm}}{X_0}\Big|_{Air} \\ &\sim 0.0425_{Be} + 0.0256_{Si} + 0.00329_{Air} \\ &\sim 0.0714\,X_0 \text{ per station.}\end{aligned} \tag{C.1}$$

Mat.	X_0 (cm)	E_C (MeV)	R_M (cm)	Z/W (mol/g)	ρ (g/cm^3)
Be	35.28	113.7	6.6	$4/9.012 \sim 0.444$	1.848
Si	9.37	40.2	4.9	$14/28.09 \sim 0.498$	2.329
Air	$303.9\cdot10^2$	87.9	$73.3\cdot10^2$	$<$Z/A$>\sim 0.5$	$1.205\cdot10^{-3}$

Table C.1: Module materials parameters. X_0 is the radiation length, E_C the critical energy, R_M the Moliere radius, Z/W is the atomic number on atomic weight and ρ is the material density.

The position of the maximum of an electron induced electromagnetic shower can be estimated with:

$$\begin{aligned} t_{max} \sim \log\frac{E_0}{E_C} - 1 &\sim 0.9\,X_0 \;\; (E_0 = 500\,\mathrm{MeV}) \\ &\sim 1.6\,X_0 \;\; (E_0 = 1\,\mathrm{GeV}) \\ &\sim 3.9\,X_0 \;\; (E_0 = 10\,\mathrm{GeV}) \\ &\sim 9.0\,X_0 \;\; (E_0 = 100\,\mathrm{GeV}) \end{aligned} \tag{C.2}$$

given an average critical energy E_C (between Be and Si) of $\sim$ 77 MeV. For example, an electron of low energies ($E_e \lesssim 1$ GeV) and low angle ($\theta_e \lesssim 5$ mrad) could induce an e.m. shower before reaching the end of the stations. Such electron would pass through about ten stations, before leaving the geometric acceptance of the trackers. Such particles should be background, since at small angles signal electrons have high energy.

C.2 Silicon strip detectors and point resolution

A charged particle passing through the silicon bulk creates free charge carriers as electron-hole pairs. In the case of silicon, a small amount of energy ($\sim$ 3.6 eV) is enough to generate a pair. The current produced is measured by a series of strips (electrode). Together with this process, there is a certain probability of generation for higher energy electrons (delta-rays), some of which can travel inside the bulk even for hundreds of microns: this process sets a lower limit, within few μm, to the spatial precision achievable by silicon detectors.

The main design factors limiting the spatial resolution σ_x of an SSD are:

- the granularity: read-out pitch p, that is the physical distance between the strips;
- readout: digital (binary) or analogue.

For the digital readout, a threshold counter is used to indicate whether a strip was hit or not: in this case, the resolution is determined only by the readout pitch p. Since the distribution of particle hit positions in between strips can be assumed to be uniformly distributed, the standard deviation of the measurements, thus the spatial resolution, is given by the standard deviation of the uniform distribution:

$$\sigma_x = \frac{p}{\sqrt{12}} \qquad \text{(binary)}. \tag{C.3}$$

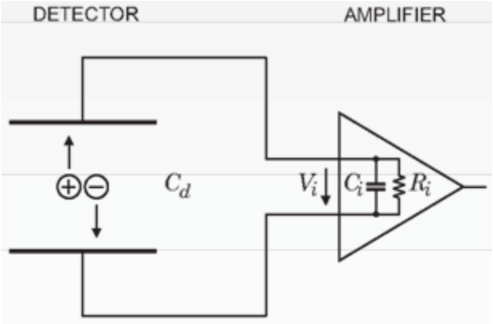

Figure C.1: SNR and Si detector capacitance.

This is an upper limit to the intrinsic point resolution. To improve it, one has to use analog readout what essentially means to measure the signal (s_i) of every strip. The mean of the strip positions x_i, weighted with the signals of the strips than gives a better measurement of the position, provided that more than one strip has been hit. Of course only strips whose signals exceed a certain threshold can contribute. Such a group of strips is called a strip-cluster. The weighted mean of the strip positions is referred to as Center of Gravity (CoG):

$$x_{CoG} = \frac{\Sigma s_i \, x_i}{\Sigma s_i} \tag{C.4}$$

and a sophisticated cluster algorithm è incaricato di determinarlo. The resolution than becomes dependent on the signal/noise ratio (SNR), because an error on s_i distorts the weighted mean. The larger SNR is, better resolutions can be achieved. So for analog readout, the intrinsic resolution reads:

$$\sigma_x \sim \frac{p}{SNR} \qquad \text{(analog)}. \tag{C.5}$$

The fact that more strips sharing the produced charge, leads to a significant resolution improvement. A further development is the well-known floating strip technique: the aim of intermediate strips is to improve this ability, i.e. the occurrence of single strip clusters should decrease, what is beneficial for the calculation of the cluster's center of gravity (CoG).

To a given signal in charge $Q_S = s_i$ (fig. C.1), collected from the strips, corresponds a voltage:

$$V_S = \frac{Q_S}{C_d + C_i}, \tag{C.6}$$

where C_d and C_i are the capacities of the Si sensor and the amplification stage. The read voltage therefore depends on the detector capacity and the amplification inevitably adds an input noise voltage V_N. So the signal-to-noise ratio (SNR or S/N) is defined as:

$$SNR = \frac{V_S}{V_N} = \frac{Q_S}{V_N(C_d + C_i)}. \tag{C.7}$$

To preserve a high SNR it is necessary to keep the collected charge high, with a bulk thickness not too small, and to limit the capacity, i.e. its action as a capacitor: it is therefore a trade-off between these requirements.

The intrinsic point resolution defines the intrinsic one on the angles, i.e. the observables of the experiment, according to the known relation:

$$\Delta\theta_i = \sqrt{2}\frac{\sigma_x}{L}, \tag{C.8}$$

where L is the module arm, i.e. in first approximation the distance between the extreme Si detectors within a single module. Then given a certain σ_x depending on the tracker design, the angular resolution can be optimized by varying L, depending on the total space available.

Bibliography

[1] F. Jegerlehner and A. Nyffeler, "*The Muon g-2*", Phys. Rept. **477** (2009) 1, `arXiv:0902.3360 [hep-ph]`.

[2] F. Jegerlehner, "*The Muon g-2 in Progress*", Acta Phys. Polon. B **49** (2018) 1157, `arXiv:1804.07409 [hep-ph]`.

[3] G. W. Bennett *et al.* [Muon g-2 Collaboration], "*Final Report of the Muon E821 Anomalous Magnetic Moment Measurement at BNL*", Phys. Rev. D **73** (2006) 072003, `hep-ex/0602035`.

[4] J. Grange *et al.* [Muon g-2 Collaboration], "*Muon (g-2) Technical Design Report*", `arXiv:1501.06858 [physics.ins-det]`.

[5] C. M. Carloni Calame, M. Passera, L. Trentadue and G. Venanzoni, "*A new approach to evaluate the leading hadronic corrections to the muon g-2*", Phys. Lett. B **746** (2015) 325, `arXiv:1504.02228 [hep-ph]`.

[6] G. Abbiendi *et al.*, "*Measuring the leading hadronic contribution to the muon g-2 via μe scattering*", Eur. Phys. J. C **77** (2017) no.3, 139, `arXiv:1609.08987 [hep-ph]`.

[7] J. Bernhard, "*The M2 beam and its implications for MuonE*", 1st MuonE Collaboration Meeting, `[indico.cern.ch]`.

[8] G. Abbiendi *et al.* [MUonE Collaboration], "*Results on Multiple Coulomb Scattering from 12 and 20 GeV electrons on Carbon targets*", submitted to JINST, `arXiv:1905.11677 [physics.ins-det]`.

[9] G. Ballerini *et al.*, "*A feasibility test run for the MUonE project*", Nucl. Instrum. Meth. A -in press- (2018), `10.1016/j.nima.2018.10.148`.

[10] M. Pesaresi *et al.*, "*Design and performance of a high rate, high angular resolution beam telescope used for crystal channeling studies*", JINST **6** (2011) P04006, `[ua9.web.cern.ch]`.

[11] M. Prest, G. Barbiellini, G. Bordignon, G. Fedel, F. Liello, F. Longo, C. Pontoni and E. Vallazza, "*The AGILE silicon tracker: An innovative gamma-ray instrument for space*", Nucl. Instrum. Meth. A **501** (2003) 280, [lnf.infn.it].

[12] A. Dainese *et al.* [QCD Working Group], "*Physics Beyond Colliders: QCD Working Group Report*," arXiv:1901.04482 [hep-ex].

[13] R. Alemany *et al.*, "*Summary Report of Physics Beyond Colliders at CERN*," arXiv:1902.00260 [hep-ex].

[14] G. Abbiendi [MUonE collaboration], "*Letter of Intent: the MUonE project*", CERN-SPSC-2019-026 / SPSC-I-252, [cds.cern.ch].

[15] J. J. Sakurai, "*Modern Quantum Mechanics*", Pearson, 2nd ed., 2010.

[16] G. E. Uhlenbeck and S. A. Goudsmit, "*Spinning electrons and the structure of spectra*", Nature **117** (1926) 264.

[17] P. A. M. Dirac, "*The quantum theory of the electron*", Proc. Roy. Soc. Lond. **A117** (1928) 610, 10.1098/rspa.1928.0023.

[18] W. Greiner, "*Relativistic Quantum Mechanics*", Springer Verlag, 2000.

[19] W. E. Lamb and R. C. Retherford, "*Fine structure of the hydrogen atom by a microwave method*", Phys. Rev. **72** (1947) 241, 10.1103/PhysRev.72.241.

[20] H. A. Bethe, "*The Electromagnetic shift of energy levels*", Phys. Rev. **72** (1947) 339, 10.1103/PhysRev.72.339.

[21] J. Schwinger, "*On Quantum-Electrodynamics and the Magnetic Moment of the Electron*", Phys. Rev. **73** (1948) 416, [aps.org].

[22] P. Kusch and H. M. Foley, "*The Magnetic Moment of the Electron*", Phys. Rev. **74** (1948) 250, 10.1103/PhysRev.74.250.

[23] C. M. Sommerfield, "*Magnetic Dipole Moment of the Electron*", Phys. Rev. **107** (1957) 328, 10.1103/PhysRev.107.328.

[24] S. Laporta and E. Remiddi, "*The Analytical value of the electron (g-2) at order* α^3 *in QED*", Phys. Lett. B **379** (1996) 283, hep-ph/9602417.

[25] D. Hanneke, S. Fogwell and G. Gabrielse, "*New Measurement of the Electron Magnetic Moment and the Fine Structure Constant*", Phys. Rev. Lett. **100** (2008) 120801, arXiv:0801.1134 [physics.atom-ph].

[26] M. Tanabashi *et al.* [Particle Data Group], "*Review of Particle Physics*", Phys. Rev. D **98**, 010001 (2018), `[pdg.lbl.gov]`

[27] A. Keshavarzi, D. Nomura and T. Teubner, "*Muon* $g-2$ *and* $\alpha(M_Z^2)$*: a new data-based analysis*", Phys. Rev. D **97** (2018) no.11, 114025, `arXiv:1802.02995 [hep-ph]`.

[28] T. Blum *et al.* [RBC and UKQCD Collaborations], "*Calculation of the hadronic vacuum polarization contribution to the muon anomalous magnetic moment*", Phys. Rev. Lett. **121** (2018) no.2, 022003 `arXiv:1801.07224 [hep-lat]`.

[29] F. Jegerlehner, "*Muon g-2 theory: The hadronic part*", EPJ Web Conf. **166** (2018) 00022 `arXiv:1705.00263 [hep-ph]`.

[30] F. Jegerlehner, "*Essentials of the Muon g-2*", Acta Phys. Polon. B **38** (2007) 3021, `hep-ph/0703125`.

[31] T. Blum, A. Denig, I. Logashenko, E. de Rafael, B. L. Roberts, T. Teubner and G. Venanzoni, "*The Muon (g-2) Theory Value: Present and Future*", `arXiv:1311.2198 [hep-ph]`.

[32] M. Davier, A. Hoecker, B. Malaescu and Z. Zhang, "*Reevaluation of the hadronic vacuum polarisation contributions to the Standard Model predictions of the muon* $g-2$ *and* $\alpha(m_Z^2)$ *using newest hadronic cross-section data*", Eur. Phys. J. C **77** (2017) no.12, 827, `arXiv:1706.09436 [hep-ph]`.

[33] A. Nyffeler, "*Precision of a data-driven estimate of hadronic light-by-light scattering in the muon* $g-2$*: Pseudoscalar-pole contribution*", Phys. Rev. D **94** (2016) no.5, 053006 `arXiv:1602.03398 [hep-ph]`.

[34] M. Steinhauser, "*Leptonic contribution to the effective electromagnetic coupling constant up to three loops*", Phys. Lett. B **429** (1998) 158, `hep-ph/9803313`.

[35] A. Anastasi *et al.* [KLOE-2 Collaboration], "*Measurement of the running of the fine structure constant below 1 GeV with the KLOE Detector*", Phys. Lett. B **767** (2017) 485. `arXiv:1609.06631 [hep-ex]`.

[36] D. W. Hertzog [Muon g-2 E821 Collaboration], "*The BNL muon anomalous magnetic moment measurement*", `hep-ex/0202024`.

[37] G. Venanzoni, "*The New Muon g-2 experiment at Fermilab*", Nucl. and Particle Phys. Proc. **273** (2016) 584, `arXiv:1411.2555 [physics.ins-det]`.

[38] M. Abe *et al.*, "*A New Approach for Measuring the Muon Anomalous Magnetic Moment and Electric Dipole Moment*", `arXiv:1901.03047 [physics.ins-det]`.

[39] K. Melnikov, "*Theory review of the muon g-2*", EPJ **118**, 01020 (2016), FCCP2015 `10.1051/epjconf/201611801020`.

[40] F. Jegerlehner, "*The anomalous magnetic moment of the muon*", Springer International Publishing, 2nd ed., 2017.

[41] M. Alacevich, C. M. Carloni Calame, M. Chiesa, G. Montagna, O. Nicrosini and F. Piccinini, "*Muon-electron scattering at NLO*", JHEP **1902** (2019) 155, `arXiv:1811.06743 [hep-ph]`.

[42] L. Gatignon, "*PBC conventional beams*", CERN-PBC-Note-2018-005, `[indico.cern.ch]`.

[43] O. Behnke *et al.*, "*Data analysis in high energy physics*", John Wiley & Sons, 2013.

[44] L. Pagani, "*A new approach to muon g-2 with space-like data: analysis and fitting procedure*", Master Degree in Physics, 2017, University of Bologna, `[amslaurea.unibo.it]`.

[45] M. Prydderch *et al.* [RAL and Imperial College], "*CBC3: A CMS micro-strip readout ASIC with logic for track-trigger modules at HL-LHC*", `[cern.ch]`.

[46] S. S. Nasr-Storey [CMS outer tracker Upgrade Collaboration], "*Recent developments in the CBC3, a CMS micro-strip readout ASIC for track-trigger modules at the HL-LHC*", Nucl. Instrum. Meth. A -in press- (2018), `https://doi.org/10.1016/j.nima.2018.11.005`.

[47] K. Uchida *et al.*, "*Results from the CBC3 readout ASIC for CMS 2S-modules*", Nucl. Instrum. Meth. A -in press- (2018), `10.1016/j.nima.2018.09.051`.

[48] CMS Collaboration, "*The Phase-2 Upgrade of the CMS Tracker*", Technical Report CERN-LHCC-2017-009, CMS-TDR-014. `[cds.cern.ch]`.

[49] LHCb Collaboration, "*LHCb Trigger and Online Upgrade Technical Design Report*", Technical Report CERN-LHCC-2014-016, LHCB-TDR-016. `[cds.cern.ch]`.

[50] A. Rose *et al.*, "*Serenity: An ATCA prototyping platform for CMS Phase-2*", Topical Workshop on Electronics for Particle Physics (TWEPP2018), 17-21 September 2018. `[hep.ph.ic.ac.uk]`.

[51] M. Fael, "*Hadronic corrections to μ-e scattering at NNLO with space-like data*", JHEP **1902** (2019) 027 `arXiv:1808.08233 [hep-ph]`.

[52] M. Fael and M. Passera, "*Muon-electron scattering at NNLO: the hadronic corrections*", `arXiv:1901.03106 [hep-ph]`.

[53] S. Di Vita, S. Laporta, P. Mastrolia, A. Primo and U. Schubert, "*Master integrals for the NNLO virtual corrections to μe scattering in QED: the non-planar graphs*", JHEP **1809** (2018) 016, `arXiv:1806.08241 [hep-ph]`.

[54] M. Passera, "*The Standard model prediction of the muon anomalous magnetic moment*", J. Phys. G **31** (2005) R75, `hep-ph/0411168`.

[55] R. Früwirth, M. Regler, R. K. Bock, H. Grote, D. Notz, "*Data Analysis Techniques for High-Energy Physics*", Cambridge University Press, 2nd ed., 2008.

[56] H. A. Bethe, "*Moliere's theory of multiple scattering*", Phys. Rev. **89** (1952) 1256, `[isu.edu]`.

[57] S. Goudsmith, J. L. Saunderson, "*Multiple scattering of electrons*", Phys. Rev. **57** (1940) 24, `[isu.edu]`.

[58] H. W. Lewis, "*Multiple scattering in an infinite medium*", Phys. Rev. **78** (1950) 526, `[umich.edu]`.

[59] V. L. Highland, "*Some practical remarks on multiple scattering*", Nucl. Instrum. Meth., **129** (1975) 497 `[cvut.cz]`.

[60] L. Urban, "*A Model for Multiple scattering in Geant4*", CERN-OPEN-2006-077, `[cds.cern.ch]`.

[61] V. N. Ivanchenko, O. Kadri, M. Maire, L. Urban, "*Geant4 models for simulation of multiple scattering*", J. Phys. Conf. **219** (2010) 032045, `[inspirehep.net]`.

[62] M. J. Berger *et al.* [NIST], "*Stopping-Power & Range Tables for Electrons, Protons, and Helium Ions*", NIST Standard Reference Database 124 (2017), [nist.gov].

[63] D. E. Groom, N. V. Mokhov and S. Striganov, "*Muon stopping power and range tables 10 MeV - 100 TeV*", Atomic Data and Nuclear Data Tables, **76**, No. 2, (2001), [pdg.lbl.gov].

[64] M. Bonanomi, "*Study and validation of an innovative experiment to measure the hadronic contributions to the running of α_{em}*", Master Degree in Physics, 2018, University of Milano-Bicocca.

[65] G. Barbiellini, G. Fedel, F. Liello, F. Longo, C. Pontoni, M. Prest, M. Tavani and E. Vallazza, "*The AGILE silicon tracker: Testbeam results of the prototype silicon detector*", Nucl. Instrum. Meth. A **490** (2002) 146, [lnf.infn.it].

[66] P. Abbon *et al.* [COMPASS Collaboration], "*The COMPASS experiment at CERN*", Nucl. Instrum. Meth. A **577** (2007) 455, hep-ex/0703049.

[67] N. Ellis, "*Trigger and data acquisition*", CERN Yellow Report CERN-2010-001, 417-449, arXiv:1010.2942 [physics.ins-det].

[68] M. Pentia, G. Iorgovan and A. Mihul, "*Multiple scattering error propagation in particle track reconstruction*", Rom. J. Phys. **40** (1995) 181, hep-ph/9406006.

[69] R. Frühwirth, "*Application of Kalman filtering to track and vertex fitting*", Nucl. Instrum. Meth. A **262** (1987) 444, [psu.edu].

[70] P. Billoir, "*Progressive track recognition with a Kalman-like fitting procedure*", Comp. Phys. Com. **57** (1989) 390.

[71] M. Soldani, "*MUonE: a high-energy scattering experiment to study the g-2*", Master Degree in Physics, 2019, University of Insubria. [cds.cern.ch].

[72] A. B. Arbuzov, D. Haidt, C. Matteuzzi, M. Paganoni and L. Trentadue, "*The Running of the electromagnetic coupling alpha in small angle Bhabha scattering*", Eur. Phys. J. C **34** (2004) 267, hep-ph/0402211.

[73] G. Abbiendi *et al.* [OPAL Collaboration], "*Measurement of the running of the QED coupling in small-angle Bhabha scattering at LEP*", Eur. Phys. J. C **45** (2006) 1, hep-ex/0505072.

[74] M. Boronat, C. Marinas, A. Frey, I. Garcia, B. Schwenker, M. Vos and F. Wilk, "*Physical limitations to the spatial resolution of solid-state detectors*", IEEE Trans. Nucl. Sci. **62** (2015) no.1, 381 `arXiv:1404.4535 [physics.ins-det]`.

[75] V. Blobel, "*Software alignment for tracking detectors*", Nucl. Instrum. Meth. A **566.1** (2006) 5, `[desy.de]`.

[76] K. Banzuzi *et al.*, "*Performance and calibration studies of silicon strip detectors in a test beam*", Nucl. Instrum. Meth. A **453** (2000) 536.

Impressioni

> "Tutto quello che ho imparato, l'ho imparato perché ho amato."
> (*Lev Tolstoj*)

Ho avuto la fortuna ed il privilegio di far parte di questa proposta di esperimento, riuscendo a partecipare ai vari aspetti della sua costruzione. Lo devo ai primi due personaggi che ho incontrato in dipartimento a Bologna, Umberto e Domenico.

Nel corso del tempo, ho osservato la lenta costruzione del consenso e della conoscenza all'interno del gruppo. L'incontro (e lo scontro) dei singoli caratteri nella ricerca di una sintesi. La fatica e lo sconforto di un codice che si ostina a non funzionare, insieme alla fiducia ed alla sorpresa nel vedere all'opera la relatività. Le giornate che si aprono con qualche certezza e finiscono con i dubbi che ti inseguono fino alla mattina successiva. La fede nel sentire ci sia una soluzione anche se non la si vede, senza la quale un'idea a questo stadio sarebbe soffocata dalla pressione al conformismo.

Su tutto, l'imbarazzante bellezza di questa disciplina, che riesce a rivestire di precisione e rigore la lucida follia delle persone che vi lavorano. Ho appreso tanto dalle persone che ho conosciuto e dal loro modo di lavorare. Credo sia un mestiere che si impari per testimonianza, con costanza e pazienza, come nelle vecchie botteghe artigiane.

Vorrei ringraziare Clara per avermi dato l'opportunità della borsa di studio al CERN e per l'incrollabile dedizione verso questa disciplina. Senza retorica, è un onore poter lavorare con lei. L'estate al CERN è stata una lunga ed entusiasmante giornata di lavoro. È un posto strano, un eremo, in mezzo a campagne incantevoli. Con un grosso e costoso giocattolo sotto terra.

Ringrazio Giovanni per l'insegnamento all'attenzione del dettaglio e per le discussioni sincere. Probabile che in questo lavoro di tesi ci siano non più di 1/10 dei particolari che avrebbe voluto. Ringrazio ed apprezzo Graziano per aver mostrato la necessità di gettare il cuore oltre l'ostacolo. Domenico per i consigli e l'aiuto fornito nella redazione della tesi. I ragazzi del gruppo LHCb di Bologna e le loro indicibili sconcezze. Il gruppo di Insubria per le chiacchierate in canteen al CERN e le lunghe discussioni con Mattia. Le analisi, gli eventi che sembrano non esserci. Come da una serie di numeri disordinati, si possa vedere all'opera la relatività. Un mistero. Difficile non essere credenti.

In particolare ringrazio Umberto. Non dimenticherò le lunghe lotte per sfangare uno ad uno i problemi che abbiamo incontrato. Le moderate bestemmie per far girare GEANT. La correzione paziente di tutti gli inevitabili errori di programmazione. Le birre a fine giornata. La legge di Murphy all'opera: se una cosa può andare male, lo farà e nel modo peggiore. Lo stupore, alla fine, nel vedere che le cose iniziano a tornare. Per poi andare, ancora, chissà dove.

Lo ringrazio per le riflessioni metafisiche. Perché, anche se non ce lo diciamo più, facciamo in fondo della filosofia. Ogni giorno, ogni volta che parte una simulazione o si accende un rivelatore. Lo ringrazio per la ricerca estenuante della chiarezza e della sintesi nella scrittura e nella comunicazione scientifica. Trovo sia uno degli aspetti più belli della fisica. È un atto di amore nei confronti di chi legge ed ascolta. Tutti gli inevitabili errori ed imprecisioni nella stesura di questo lungo documento sono da imputare totalmente al sottoscritto. Lo ringrazio infine per il calore e l'umanità, che sembra inizino ad essere così rari.

Vorrei continuare a scrivere, per documentare e poter un giorno, rileggendo, ricordare. Sono d'altronde un ossessivo, appassionato di fotografia. Ho bisogno di fissare istantanee. Impressioni. Per la paura che queste possano svanire. Non so dove mi porterà la mia strada. So che mi è piaciuto molto percorrere quest'ultimo tratto.

Dedico questa tesi a Martina. Ogni parola, ogni figura. Per tutto il tempo che le ho rubato. E per tutto l'amore che lei, in cambio, mi ha restituito.